Three-Dimensional Topology of the Magnetic Field in the Solar Corona

Daniel Thomas Lee

A thesis submitted in partial fulfilment
of the requirements for the degree of
Doctor of Philosophy

Jeremiah Horrocks Institute for Maths, Physics and Astronomy
University of Central Lancashire

November 2018

Declaration

Type of Award: Doctor of Philosophy

School: Physical Sciences and Computing

I declare that while registered as a candidate for the research degree, I have not been a registered candidate or enrolled student for another award of the University or other academic or professional institution.

I declare that no material contained in the thesis has been used in any other submission for an academic award and is solely my own work.

No proof-reading service was used in the compilation of this thesis.

Daniel Thomas Lee

November 2018

Abstract

This thesis investigates the topology of the magnetic field in the solar corona, due to a variety of source configurations and types. To fully understand the complex behaviour of the Sun's magnetic field, it is important to have a complete description of the features present in its structure.

The magnetic topologies due to network source configurations are investigated using both the point source description and the continuous source description. A series of case studies involving an emerging bipole in a hexagonal arrangement to simulate a supergranular cell are studied. This has a particular focus on the behaviour of coronal nulls located in the topology, and a particular case may form the underpinning of a model for polar plumes.

A new topological feature, called a null-like point, is defined by relaxing the definition of a magnetic null point. Separatix-like surfaces, originating from null-like points, allow quasi-separatrix layers to be found in magnetic topologies due to continuously distributed sources. The squashing factor, Q, is mapped across the source configuration, highlighting the locations of the quasi-separatrix layers.

Finally, an algorithm is developed which automatically detects and classifies magnetic events local to X-ray bright points (XBPs). Significant peaks are identified in the gradients of flux curves (positive, negative and absolute flux) local to XBP footpoints, allowing instances of flux emergence and cancellation to be identified and linked to the onset and demise of the XBPs studied. The algorithm correctly classifies 90% of all emergence and cancellation events related to the studied XBPs.

Contents

List of Tables

List of Figures

Acknowledgements

I am profoundly grateful to my supervisor, Daniel Brown, for his constant support, patience and guidance throughout my studies, and for sharing his experience. Thanks to all of the research students and staff of the Jeremiah Horrocks Institute at the University of Central Lancashire for creating a department that feels like home.

I would like to thank my mother, Karen Lee, for her continual support, belief, and for encouraging me to stay engaged in hobbies as well as work.

I also want to thank my father, David Lee, for his support and especially his financial aid during the closing months, along with all of my family, for unending encouragement, enthusiasm, chocolate and cake.

Heartfelt thanks go to my brother-in-solar, Andrew Walker, for coffee breaks, useful (and useless) discussion and for giving me an example to follow, and to Ben MacFarlane, for discussion, counsel and almonds.

My sincere thanks to my friends who made our Dungeons & Dragons group one of the most enjoyable games I have ever created and played, which we lovingly named PhD&D. Andrew Walker, Chris Kaye, Jordan Thirlwall, Jowy Quaintance, Rebecca Wardman, Simon Smalley, Steven Bourn.

Finally, I would like to thank Rebecca Wardman, for supporting me throughout this project, especially during the write-up phase, and for introducing five hungry mouths into my life; Jarvis, Rocket, Quill, Snakey and Parker.

Chapter 1

Introduction

The Sun is responsible for all life on Earth, providing both heat and light to the planet. As technological advances are being made on unprecedented scales, and civilisation further supplants itself into the information age, near-Earth space is becoming increasingly populated with satellites to facilitate social and industrial needs. The Sun, however, is also responsible for kicking out large amounts of energetic particles, accelerated by coronal mass ejections and solar flares. These particles can be dangerous for the electronics aboard such a satellite, and the radiation can be hazardous for high-altitude flights. To better protect the advancing collection of equipment from space weather, one must endeavour to better understand the mechanisms which cause it.

The creation of telescopes and increases in computational power have allowed bigger and better models for dynamic activity on the Sun to be produced. Magnetohydrodynamics is at the core of solar research and helps bring together both observational and theoretical solar physics. Whilst problems remain to be solved, such as coronal heating or the nature of reconnection in three-dimensions, many physical properties of solar activity are now well documented.

This thesis focuses on the topology of potential magnetic fields, derived from a variety of source configurations and types, and the bifurcations which take place in

these topologies as the system evolves. The work uses the solution for a potential magnetic field as this is the simplest to solve mathematically, therefore requiring the least computational resources. By relaxing the definition of a magnetic null point, this thesis defines an additional topological feature, called a null-like point (NLP). The squashing factor, Q, is used to help interpret the behaviour of NLPs and provides insight into the structure of quasi-separatrix layers (QSLs) which originate from the NLPs. Finally, a sample of X-ray bright points (XBPs) is collected by identifying and tracking these features as they rotate across the solar disc. An algorithm is developed, which automatically detects and classifies magnetic events (such as flux emergence or cancellation) in photospheric magnetogram data of the region local to the XBP. These events are then related to the onset and demise of the bright point structures.

This chapter serves as an introduction to the properties of the Sun, and the overarching physical and mathematical principles required for the study of potential magnetic fields. The end of this chapter outlines the work contained throughout the thesis.

1.1 Solar Structure

The Sun has significantly different properties depending on the radial distance from the Sun's core. When the properties change, a new layer of the Sun is defined, and these are split into broad regions; the solar interior and the solar atmosphere. Figure 1.1 shows several regions of both the solar interior and the solar atmosphere, along with some examples of the Sun's dynamic features. Whilst the solar atmosphere can be viewed using a variety of instruments, the solar interior is obscured from view by the solar surface, the photosphere. However, one field of solar research, helioseismology, is used to infer the properties of the solar interior, which is sub-divided into three distinct regions; the core, the radiative zone and the convection zone (Priest

2014). The magnetic field is thought to be generated at the interface between the radiative zone and convection zone, called the tachocline (Harra & Mason 2004; Dwivedi & Parker 2007). The solar atmosphere consists of the photosphere, chromosphere, transition region and the corona. This project focuses on the dynamics and structure of the solar atmosphere.

1.1.1 Solar Interior

The interior of the Sun is categorised into three distinct regions where different physical processes dominate. These are the core, radiative zone and the convection zone, and each plays an important role for energy transport within the Sun. The solar interior is also incredibly dense, where due to absorption and re-emission, a single photon can take around 150,000 years to get from the interior to the surface (Priest 2014).

The Core

The solar core is the region at the heart of the solar interior and extends out to around one-quarter of the solar radius ($0.25\mathrm{R}_{\odot}$). With a density of 1.6×10^5 kg m^{-3} and a temperature of 15,000,000 K, the pressure within the core is so intense that nuclear fusion occurs. This process primarily occurs through the proton-proton (PP) chain,

$$4^1\mathrm{H} \rightarrow\ ^4\mathrm{He} + 2e^+ + 2v + 26.7\mathrm{MeV}, \tag{1.1}$$

where four protons are fused together to produce a single helium nucleus, releasing energy which heats the core to temperatures of 15,000,000 K. The PP chain is believed to be the dominant form of nuclear fusion in all Sun-like stars (Priest 2014; Green & Jones 2015), though it should be noted that other processes such as the CNO cycle also contribute small amounts to the Sun's energy (Dwivedi & Parker 2007).

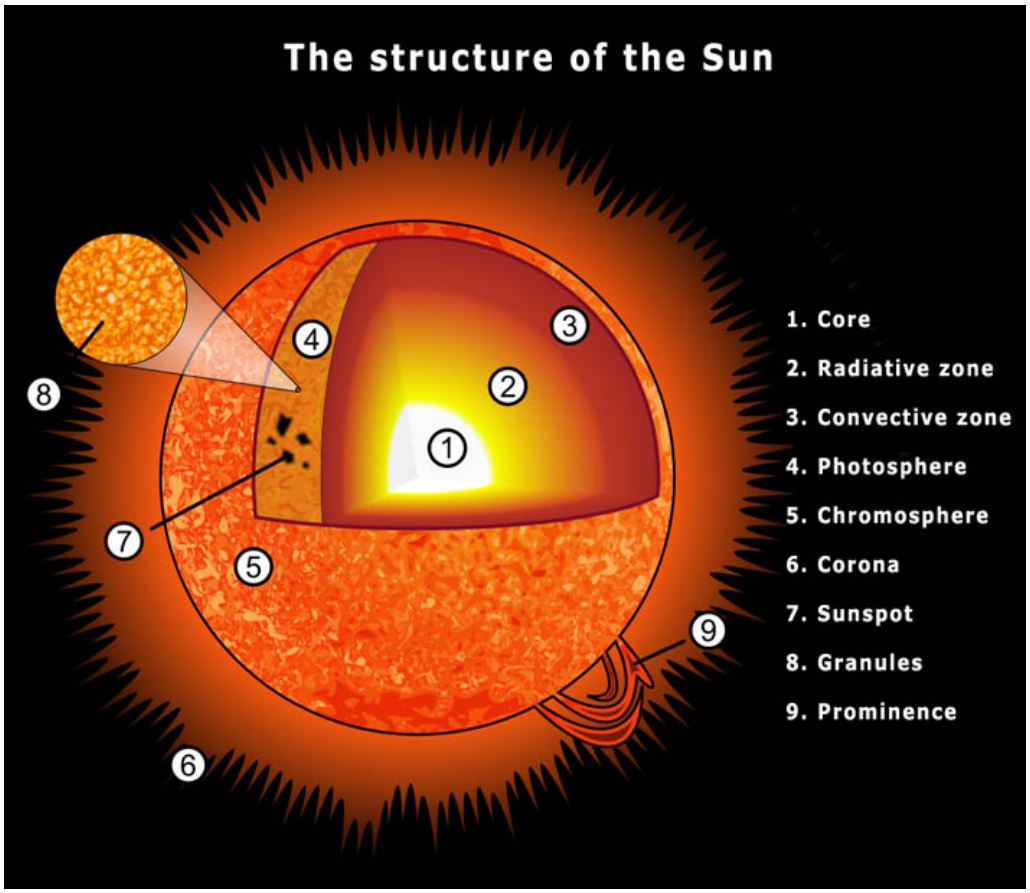

Figure 1.1: Diagram illustrating the structuring of different layers within the solar interior and atmosphere, along with some of the key features of these layers.

Radiative Zone

The radiative zone spans the distance from $0.25R_\odot$ out to $0.7R_\odot$ and forms the next layer out from the core. The temperature of the radiative zone is around 15,000,000 K at the boundaries of the core, dropping to 1,500,000 K at the base of the convection zone. The typical density of the radiative zone is around 1.5×10^4 kg m^{-3}, and decreases as a function of radius throughout the region. Here, radiative diffusion is the dominant form of energy transport. Within the radiative zone, opacity increases as a function of solar radius, and a single photon can be absorbed and re-emitted multiple times over many thousands of years before finally reaching the outer boundary of the radiative zone and diffusing out into the next layer. At

this boundary ($0.7R_\odot$), the opacity of the solar interior becomes so great that the heated plasma becomes buoyant and begins to rise, diffusing into the convection zone (Priest 2014).

Convection Zone

The convection zone starts around $0.7R_\odot$ and continues up to the solar surface at $1.0R_\odot$. Here, convection is the dominant form of energy transport due to convective instabilities arising from a large temperature gradient. A simple convective process is where a large blob of plasma gains some energy and rises, before transferring that energy, subsequently cooling, and falling back down to collect more. Where the convection zone reaches the base of the photosphere, density drops to as little as 8.0×10^{-5} kg m^{-3}. Typical temperatures in the convection zone are around 1,000,000 K, as temperature continues to decline with increasing distance from the core (Priest 2014).

The Tachocline

Together the core and the radiative zone rotate as a solid body, whereas the convection zone experiences differential rotation (Lang 2001; Dwivedi & Parker 2007). Where the change in energy transport mechanism occurs, so too does a difference in rotational paradigm, which creates a thin shear layer. This shear layer is called the tachocline and sits at approximately $0.713R_\odot$. The tachocline is responsible for the Sun's magnetic field and generates it through a physical process called the solar dynamo. Study of the solar dynamo is still an open field of research as the process is not fully understood. It is suggested that the magnetic field is generated by dynamo action in a cyclic way, since a simple MHD oscillation would require a large velocity oscillation which is not present in the Sun. Whilst this project does not study the solar dynamo, it is logical to consider its existence when one wishes to study the

solar magnetic field (Priest 2014).

1.1.2 Solar Atmosphere

The solar atmosphere has a range of temperatures and densities (figure 1.2), which allow four distinct layers to be described: the photosphere, chromosphere, transition region and corona. Here, photons produced by the PP chain (equation 1.1) can escape into space. The photosphere is the surface layer of the Sun, which is responsible for emitting most of the solar radiation. It is optically thick in the majority of spectral lines, thus the photosphere is often imaged across the continuum part of the spectrum (figure 1.3a). Above the photosphere sits the chromosphere, which is optically thin across the continuum, except for a collection of spectral lines (e.g., He II, H_α). Above the chromosphere is the very narrow transition region, which is again optically thin across the majority of the spectrum so proves very difficult to image directly. It can be seen in the C IV line, but this also captures parts of the upper photosphere, or in He II which mainly captures the chromosphere. Finally, extending above the transition region and out into space is the corona. It is optically thin across the spectrum but can be captured by the spectral lines of some ions. Whilst a range of ions have coronal spectral lines, typical satellite filters capture those of heavily ionised iron (FE IX, FE XII, FE XVI, FE XXIII).

Photosphere

The visible surface layer of the Sun is referred to as the photosphere. The photosphere has a depth of around 500 km, and emits most of the Sun's visible light, along with some ultraviolet and infrared light. The temperature also drops off rapidly from 15,000,000 K in the core, to just 5,800 K at the photosphere with a density of 1×10^{-3} kg/m^{-3} (figure 1.2). Figure 1.3a is an image of the photosphere at around 6,000 K captured using a narrow waveband around 6,173 Å, while figure 1.3b is a

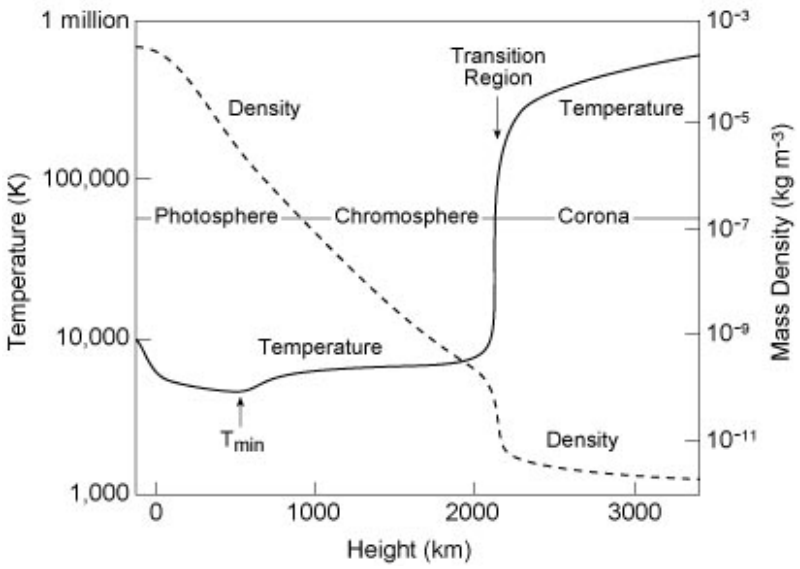

Figure 1.2: Plot showing the change in temperature and density with radial distance from the photosphere. Image credit: Eugene Avrett, Smithsonian Astrophysical Observatory.

line-of-sight magnetogram image of the same region. The photospheric structure is heavily influenced by convective motions within the solar interior. Granulation and super-granulation are the direct results of this effect (Foukal 2004; Stix 2004; Bhatnagar & Livingston 2005). In the centre of a granule, hotter, less dense material rises quickly towards the top of the photosphere, where it then cools and is pushed outwards, before sinking back down and forming inter-granular lanes. Granulation presents itself most visibly in high-resolution continuum images from ground-based instruments, and the boundaries of supergranular cells are visible in line-of-sight magnetogram images (figure 1.4).

Several other features are also present in the photosphere. Strong concentrations of magnetic flux around 100 Mm across are called active regions. They grow as flux emerges over two weeks forming two opposing regions. Sunspots (figure 1.5) are associated with active regions and appear as dark patches on the solar surface in continuum images, the visible manifestation of intense magnetic flux tubes emerging

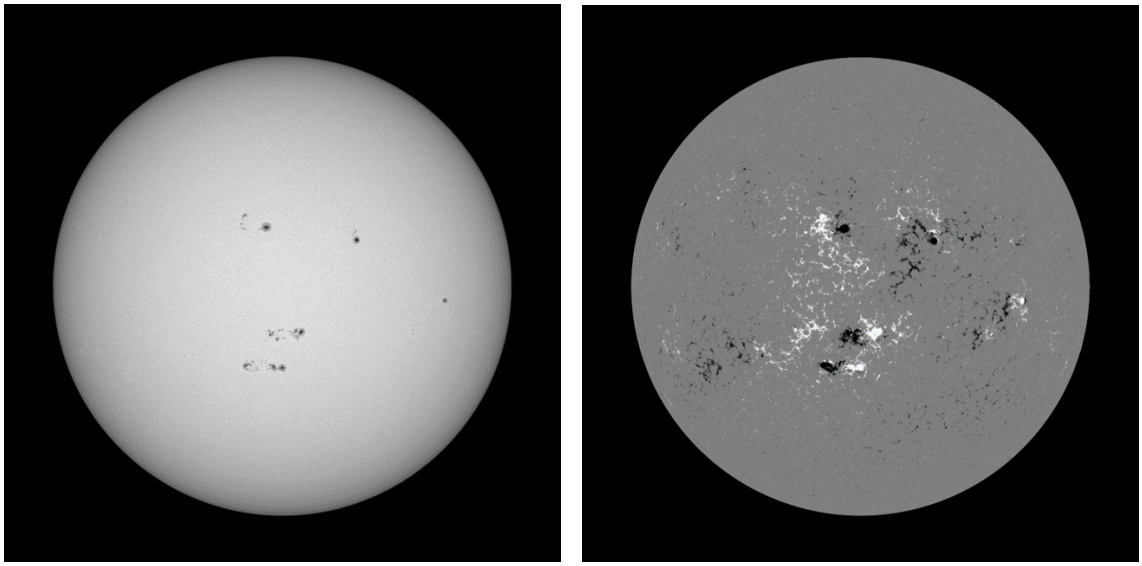

(a) (b)

Figure 1.3: a) Continuum image of the photosphere taken with the HMI instrument aboard SDO. Several sunspots are visible as dark blemishes on the solar disc. b) Line of sight magnetogram taken with the HMI instrument aboard SDO. Active regions are where the flux is most concentrated, in the same locations as the sunspots in image a. Images courtesy of helioviewer.org , taken June 8^{th}, 2014.

from the solar interior (Priest 2014).

Chromosphere

The next layer outwards from the Sun's core is the chromosphere. The chromosphere extends from 500 km above the solar surface, to approximately 2,000 km above the surface and has a density ranging from 1×10^{-7} kg/m^{-3} to 1×10^{-10} kg/m^{-3} (figure 1.2). The temperature of the chromosphere at its base is 4,300 K, but this steadily increases with height to temperatures upwards of 25,000 K, before reaching the base of the transition region. Figure 1.6 shows an image of the chromosphere and transition region at a waveband centred on 304 Å emitted by He II at around 50,000 K. At a height of 2,000 km, the temperature increases dramatically through

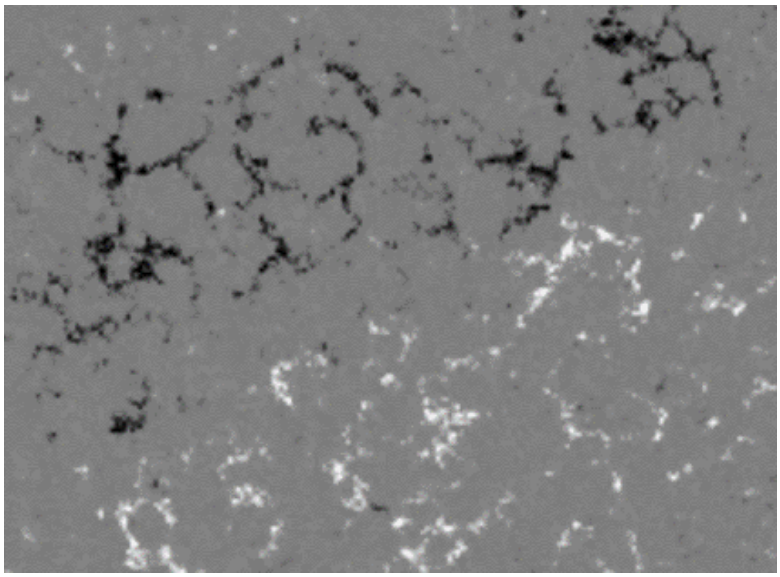

Figure 1.4: HMI line-of-sight magnetogram image of the solar corona, clearly showing the structure of the supergranular lanes, captured July 5^{th}, 2015. Image courtesy of helioviewer.org.

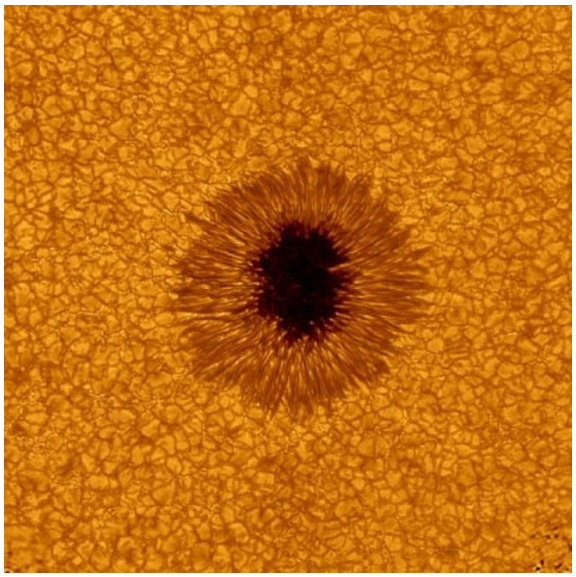

Figure 1.5: Image of a sunspot taken in July, 2010. The granulation effect is highlighted by the network of dark, inter-granular lanes and the bright granular cores throughout the region. Image Credit: Big Bear Solar Observatory.

the transition region to a coronal value around 1×10^6 K (figure 1.2).

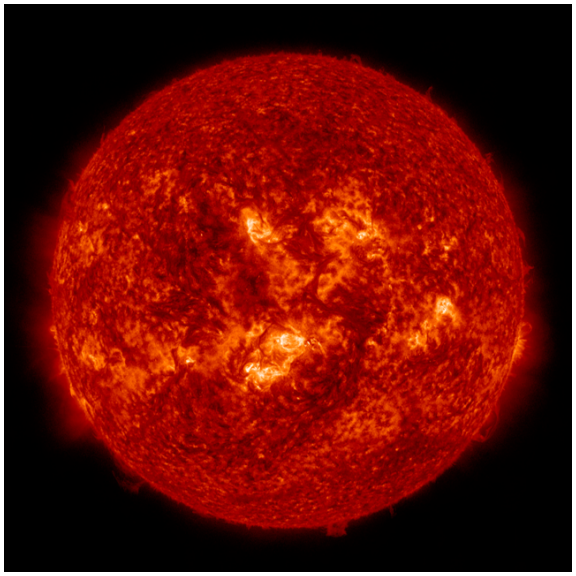

Figure 1.6: Image of the chromosphere taken at 304 Å with the AIA instrument aboard SDO. Large brightenings are visible in the vicinity of the active regions (figure 1.3b), and elongated dark regions are prominences sitting in the atmosphere. Image courtesy of helioviewer.org, taken June 8^{th}, 2014.

Transition Region

The transition region is a thin layer no more than a few 100 km thick. It exists wherever chromospheric plasma is heated up to coronal temperatures before rising higher into the atmosphere. Typical transition region densities are 1×10^{-10} kg/m^{-3}, with temperatures ranging between chromospheric and coronal values (Priest 2014). It is difficult to capture an image of the transition region, though some select wavelengths allow glimpses of transition region components. Figure 1.7 captures C IV emissions at the 1600 Å waveband, which is heated to around 10,000 K. Whilst this mostly captures carbon ions in the upper photosphere, it also collects emissions from the transition region components.

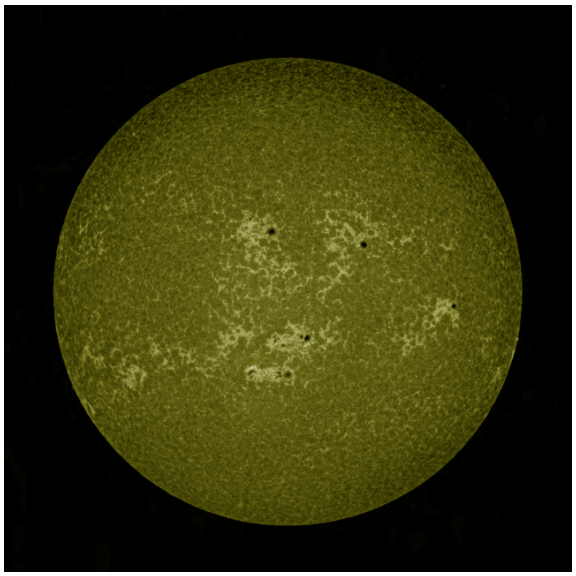

Figure 1.7: Image of the upper photosphere and hints of the transition region taken at 1600 Å with the AIA instrument aboard SDO. Hot, coronal loops of plasma are much brighter than the surrounding material and are the coronal extension of active regions in the photosphere. Images courtesy of helioviewer.org, taken June 8^{th}, 2014.

Corona

Extending above the transition region and into space is the solar corona. Its boundary may be defined as where the Alfvén speed (60 km s^{-1}) matches that of the solar wind, also known as the Alfvén radius. Hence, as the solar wind varies, so too does the definable corona. The depths of the chromosphere and transition region are then negligible when one considers the whole solar atmosphere. In the corona, density drops to 1×10^{-12} kg/m^{-3} making it the least dense layer of the solar atmosphere. However, the plasma is further heated with temperatures in the 1,000,000s K (figure 1.2).

The corona contains magnetically closed loops of hot plasma, called coronal loops, which have their footpoints rooted in the photosphere. These hot loops of plasma are often best observed in images taken at 171 Å at around 600,000 K as illustrated by figure 1.8a, which also captures the quiet corona and hints of the upper

transition region. Typical magnetic field strengths in the corona vary from a few gauss in quiet Sun regions up to a few hundred gauss above active regions. In the corona, the plasma beta (as defined in section 1.3.4) is much less than one, which has the result that the magnetic field dominates. This means that the plasma is essentially 'frozen in' to the magnetic field, where it is able to move along magnetic field lines, but not perpendicular to them (Priest 2014). Thus, in the corona, we can indirectly observe the magnetic field through the motions of the plasma, as it traces out the magnetic field structures. Bright hot loops of plasma exist in the corona above active regions with temperatures in the range of 3 - 5 million K.

The corona may be viewed directly in soft X-rays and extreme ultra-violet (EUV) since there is little emission from the lower regions at these wavelengths (Golub & Pasachoff 2009; Priest 2014). Figure 1.8b shows the corona at a wavelength of 193 Å which is dominated by emissions from FE XII at 1,000,000 K (predominantly capturing active regions), but also includes FE XXIV which is material in solar flares heated to 20,000,000 K. Small, intense brightenings, called X-ray bright points, are observed, along with the large, dark patchwork of coronal holes from which the fast solar wind blows out into space along open magnetic field lines (Golub & Pasachoff 2009; Priest 2014). The corona was first observed during a solar eclipse, resembling a glowing halo around the moon. The solar disc may also be artificially occulted so that the coronal plasma can be studied, such as in a coronagraph (figure 1.9).

1.2 Dynamic Activity on the Sun

This section looks at some of the Sun's dynamic behaviour, occurring both in the photosphere and the corona. Solar activity can often be considered as falling into two categories, the quiet Sun and the active Sun. Whilst this project studies magnetic topologies which may arise in regions of the quiet Sun, a brief introduction is given to the active Sun, followed by a discussion of quiet Sun phenomena.

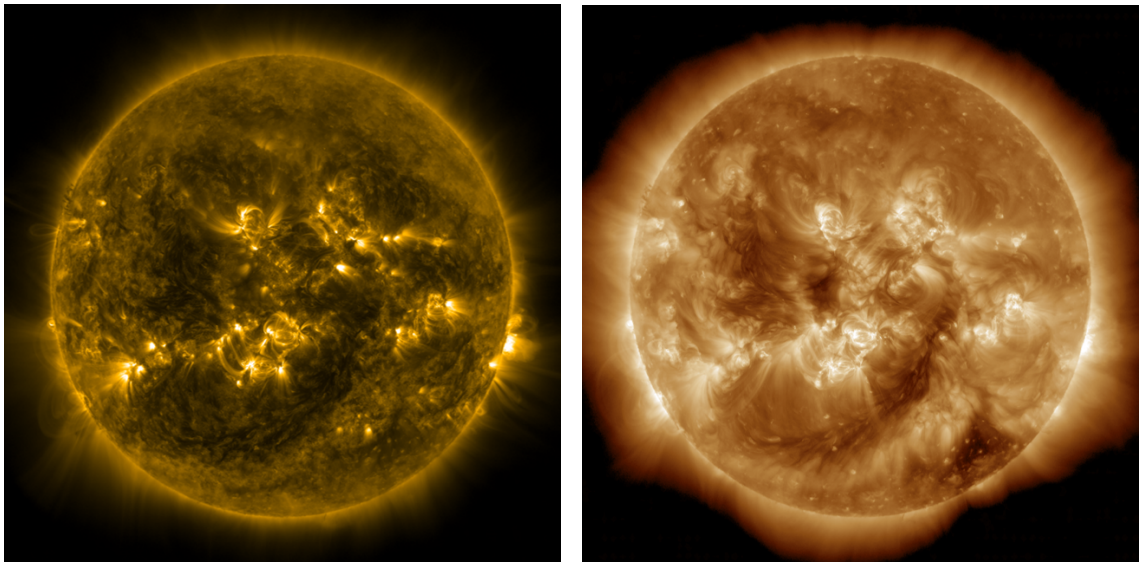

(a) (b)

Figure 1.8: Image of the solar corona measured at a) 171 Å and b) 193 Å as captured by the AIA instrument aboard SDO, courtesy of helioviewer.org. Both images taken June 8^{th}, 2014.

1.2.1 The Active Sun

Telescopes first recorded dark regions on the sun as early as 1610 (Priest 2014), and later these blemishes would be called sunspots. Sunspots are the visible fingerprint of active regions upon the solar surface, which are regions where intense flux tubes emerge through the photosphere and out into the corona (figure 1.10). Some large active regions can have a magnetic flux density as large as 3 kG, occasionally strong enough to modify the convective patterns around them.

The number of sunspots present is not constant (figure 1.11), but rather it changes over time from periods of large sunspot counts (solar maxima) to much lower numbers of sunspots (solar minima). The periodicity of this cycle was then determined to be roughly eleven years in duration (Schwabe 1843), however, the duration between any two peaks or troughs can vary widely (Priest 2014). The

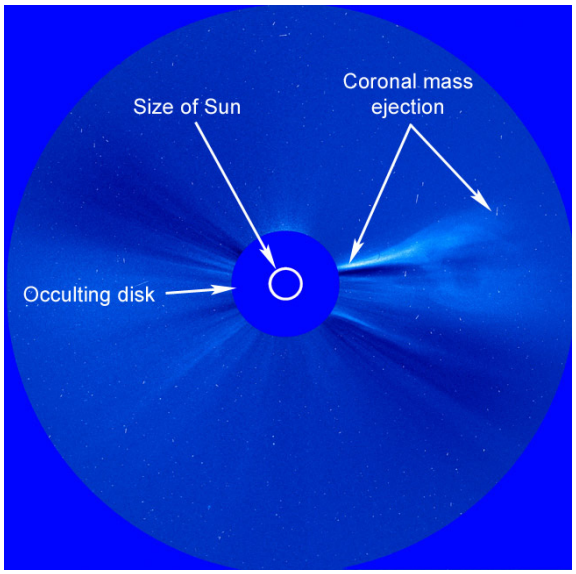

Figure 1.9: Annotated coronagraph image from the Stereo A spacecraft showing the size of the Sun, a coronal mass ejection, and the occulting disk. Image Credit: NASA.

polarity of the Sun's magnetic field also changes with the solar cycle. This 'flipping' of the magnetic field has a cycle of around 22 years (Hale & Nicholson 1925).

As the number of sunspots increases, so too does the frequency of violent space weather events. Active regions are responsible for causing significant space weather events; solar flares and coronal mass ejections (CMEs) are often born of active region fields. Solar flares send large amounts of radiation out into space, and the first was observed in 1859 by Richard Carrington (Priest 2014). They are observed as rapid brightenings in Hα and X-rays, but also at other wavelengths. Coronal mass ejections (CMEs) were first observed with the OSO-7 satellite (Tousey 1973) and are events which blast large amounts of plasma out into the solar wind. Those that occur close to active regions may be associated with a solar flare. When the events coincide, it is a result of the violent energy release of the reconnection process, not one event acting as a trigger for the other (Harrison 1996).

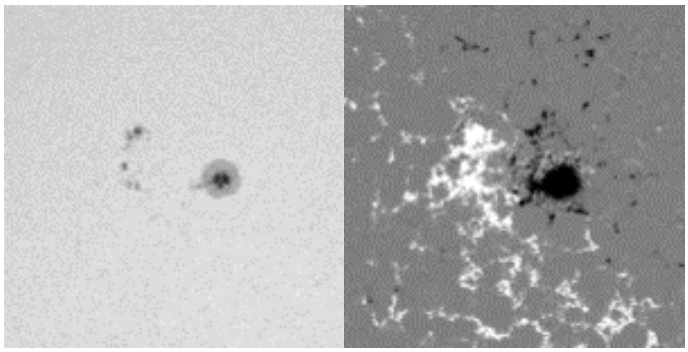

Figure 1.10: Two images of the solar photosphere. A sunspot is visible in the HMI continuum image (left), with its magnetic footprint shown in the HMI line of sight magnetogram (right). Both images taken June 8^{th}, 2014.

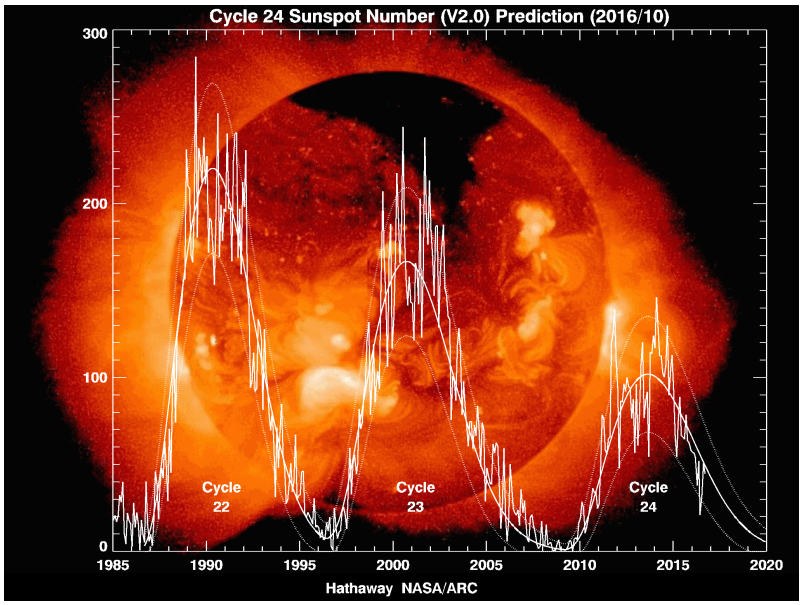

Figure 1.11: Chart showing the change in the number of sunspots over time for the three most recent solar cycles. Image Credit: David Hathaway / NASA

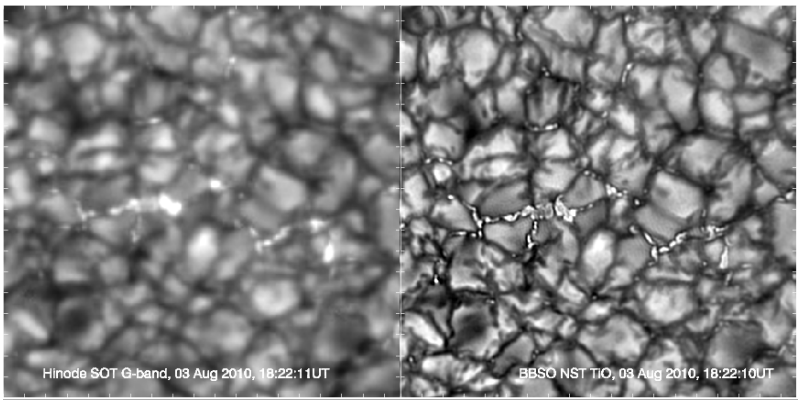

Figure 1.12: Images of photospheric granulation as captured by Hinode/SOT (left) and NST (right) on August 3^{rd}, 2010 (Image Credit: Big Bear Solar Observatory). Both images are of the same region, where NST clearly has a higher spatial resolution across the 19" by 19" area, displaying numerous bright features within the dark inter-granular lanes.

1.2.2 The Quiet Sun

The Magnetic Carpet

Photospheric magnetic features exist on a variety of scales, and the overall photospheric behaviour is largely governed by convective motions in the plasma. Granulation is present across the photospheric surface, where they appear most vividly in continuum images (figure 1.12). Typical granules are 1 Mm in diameter, bounded by dark intergranular lanes of cooler material which can be as much as 0.3 Mm wide. Typically, granules have lifetimes of 5 to 10 minutes and form from the merger or fragmentation of existing granules. Granules were found to exist within larger structures called supergranules (Hart 1954), and later found to move with them (Title et al. 1989).

Measurements for the size of supergranular cells vary with instrumentation, yet a typical supergranule would be 30 Mm across, whilst they can grow to sizes as large as 70 Mm. Supergranules have an average lifetime of 36 hours, much longer than the

granules found within them. New supergranules, like granulation, may be formed from the fragmentation of larger supergranules, whilst others emerge from the lanes between existing supergranular structures. Convective motions are again responsible for supergranular structures, with hot plasma rising at the centre of the cell before following a horizontal outflow. The horizontal motions provide the clearest picture of supergranulation through tracking of the motions or Doppler measurements near the solar limb. Supergranular cell boundaries are where the most intense flux tubes concentrate. Whilst the interior of the cell has the most flux, most of it forms closed structures before reaching the upper atmosphere. Cell interiors can have a magnetic flux density up to 300 G and are not unipolar in nature, but rather a mix of varying polarity magnetic flux elements.

Within the supergranular boundaries, small bipolar regions of magnetic flux, called ephemeral regions, may emerge and are visible on magnetograms (Harvey & Martin 1973). From their emergence, the two islands of magnetic flux begin to drift away from one another towards the boundaries of the cell. The standard model assumes that they fragment during this time, before merging with the flux at the supergranular boundaries. Ephemeral regions have lifetimes of around 24 hours, and from observations made with SOHO's MDI instrument, it was established that two ephemeral regions may emerge per 100 Mm^2 per day (Hagenaar et al. 2008). Whilst present, they may contribute as much as 90% of the flux in the cell interior, and sometimes manifest as X-ray bright points in the corona where strong increases in X-ray (Vaiana et al. 1970) and EUV emissions are detected.

X-ray Bright Points

X-ray bright points (XBPs) appear as small, intense brightenings in X-ray and EUV emissions in the solar corona (figure 1.13). They were first observed in X-ray images taken by an Aerobee rocket flight carried out in 1969 (Vaiana et al. 1970), later

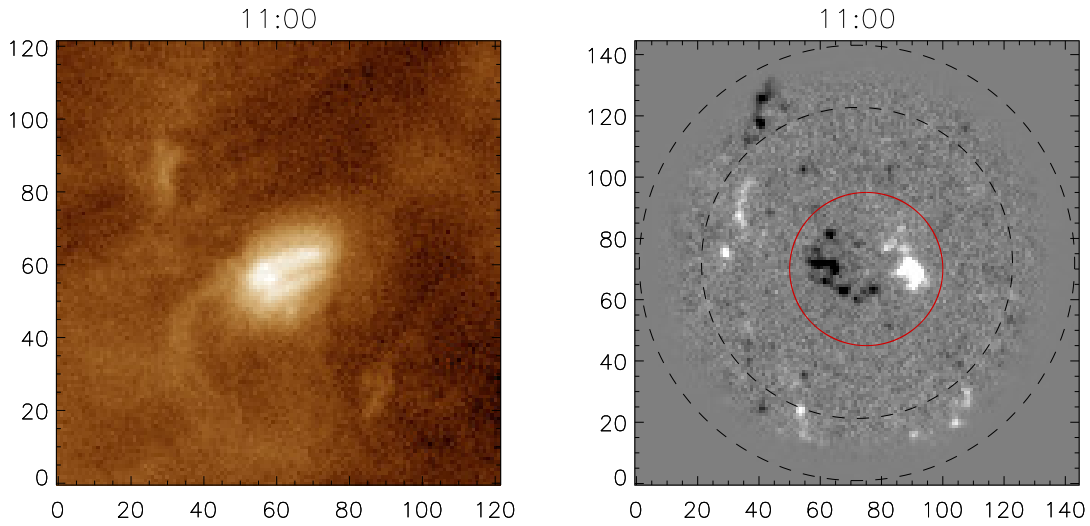

(a) (b)

Figure 1.13: a) Image of an X-ray bright point captured by AIA and b) associated magnetic foot points captured by HMI.

being observed in radio (Habbal et al. 1986) and EUV emissions (Kankelborg et al. 1996), and their magnetic structure was studied using the TRACE satellite (Brown et al. 1999).

The properties of XBPs have been well studied (Golub et al. 1974, 1976a; Brown et al. 2002). Typically, X-ray bright points have diameters of 22 Mm and a brighter core of 4 Mm (Golub et al. 1974, 1979). Average XBP lifetimes span around 8 hours (Golub et al. 1976a), but some can live longer than 48 hours. Bright points can be considered as falling into one of two classes. The first have lifetimes of less than 2 days with a distribution across the entire solar disc, while the second have much longer lifetimes and are typically found within 30 degrees of the solar equator (Golub et al. 1976a; Priest 2014). The maximum area of an X-ray bright point is proportional to its lifetime (Golub et al. 1974) as given by the relation,

$$A_{max} = 2.5 \times 10^7 \tau, \tag{1.2}$$

where τ is measured in hours and A_{max} is measured in km^2. Hence, larger bright points exist over longer timescales. Typical photospheric flux measures for an XBP are in the range 10^{19} and 10^{20} Mx (Golub et al. 1976b; Priest et al. 1994), and flaring may cause them to increase in intensity by an order of magnitude (Golub et al. 1974). As many as 1,500 new bright points may emerge each day, across the solar cycle (Golub et al. 1974; Brown et al. 2001b). XBPs are distributed across the entire solar disc and together may contain as much of the photospheric magnetic flux as an active region (Golub et al. 1976b). However, the number of bright points present was found to be anticorrelated with the solar cycle (Priest 2014). In the 1990's, the NIXT survey allowed the complex loop structures of the XBPs to be observed for the first time (Parnell et al. 1994), which exist on scales of 9 Mm.

1.3 Solar Magnetohydrodynamics

Magnetohydrodynamics (MHD) describes how a plasma interacts with a magnetic field by coupling some simplified versions of Maxwell's equations with Ohm's law, an equation of motion, an equation of state and the induction equation (Priest & Forbes 2000; Priest 2014). Whilst this project focuses on a particular solution of the set of equations, namely magnetohydrostatics (MHS), a basic understanding of the fundamental equations of MHD should be established.

1.3.1 Magnetohydrodynamics

Maxwell's Equations

Maxwell's equations are given by,

$$\boldsymbol{\nabla} \times \mathbf{B} = \mu \mathbf{j} + \frac{1}{c^2} \frac{\partial \mathbf{E}}{\partial t}, \tag{1.3}$$

$$\boldsymbol{\nabla} \, . \, \mathbf{B} = 0, \tag{1.4}$$

$$\boldsymbol{\nabla} \times \mathbf{E} = -\frac{\partial \mathbf{B}}{\partial t}, \tag{1.5}$$

$$\boldsymbol{\nabla} \ . \ \mathbf{E} = \frac{\rho^*}{\epsilon}, \tag{1.6}$$

where $\mathbf{B}$ is magnetic induction (though in solar physics it is often referred to simply as the magnetic field), $\mathbf{E}$ is the electric field, ρ^* is the charge density, $\mathbf{j}$ the current density, μ is magnetic permeability and ϵ is permissivity of free space.

However, equation 1.3 can be simplified to,

$$\mathbf{j} = \boldsymbol{\nabla} \times \frac{\mathbf{B}}{\mu}, \tag{1.7}$$

which is illustrated when approximating the current displacement by,

$$\frac{E_0}{c^2 t_0} \approx \frac{V_0^2}{c^2} |\boldsymbol{\nabla} \times \mathbf{B}|, \tag{1.8}$$

where c represents the speed of light and $V_0 \ll c$. Thus, the current displacement term vanishes from equation 1.3.

Ohm's Law

Ohm's law states that a plasma in a magnetic field is also subjected to an electric field. In addition to the electric field ($\mathbf{E}$) which acts on a material at rest, there is another electric field ($\mathbf{v} \times \mathbf{B}$) which acts on a material in motion. Ohm's law states that the total electric field is proportional to the current density by,

$$\mathbf{j} = \sigma(\mathbf{E} + \mathbf{v} \times \mathbf{B}), \tag{1.9}$$

where σ is the electrical conductivity and $\mathbf{v}$ is the plasma velocity. It is often convenient to rearrange this equation and to write it as,

$$\mathbf{E} = -\mathbf{v} \times \mathbf{B} + \frac{\mathbf{j}}{\sigma}, \tag{1.10}$$

such that **E** is now the subject. However, within solar physics, use of this equation often involves consideration of such large length scales that the current term becomes negligible. Hence,

$$\mathbf{E} \approx -\mathbf{v} \times \mathbf{B}, \tag{1.11}$$

is an approximation of Ohm's law that is often used to find the electric field.

The Induction Equation

The induction equation describes the behaviour of a magnetic field. It can be obtained by first eliminating the electrical parameters, **E** and **j**, from Maxwell's equations (1.3 and 1.5) and Ohm's Law (1.9) to give,

$$\frac{\partial \mathbf{B}}{\partial t} = \boldsymbol{\nabla} \times (\mathbf{v} \times \mathbf{B}) + \boldsymbol{\nabla} \times (\eta \boldsymbol{\nabla} \times \mathbf{B}), \tag{1.12}$$

where $\eta = 1/\mu\sigma$ is the magnetic diffusivity, which typically has a value of 1 $\mathrm{m}^2\ \mathrm{s}^{-1}$ in coronal plasma with a temperature of 10^6 K. Then, using a vector identity and equation 1.4, the induction equation can be written,

$$\frac{\partial \mathbf{B}}{\partial t} = \boldsymbol{\nabla} \times (\mathbf{v} \times \mathbf{B}) + \eta \nabla^2 \mathbf{B}, \tag{1.13}$$

where η has been assumed to be uniform since, in many solar applications, η may not vary much over typical length scales.

Plasma Equations

The plasma motions can be used to describe the evolution of a magnetic field by relating the two. The velocity term, **v**, in the induction equation 1.13 allows such a relation to be established. Plasma motions can be described by equations of motion, mass continuity and an equation of state. The equation of motion can be defined when the plasma is electrically neutral,

$$n_+ - n_- \ll n, \tag{1.14}$$

where n_+ and n_- represent the number densities of positive and negative ions respectively and $n = n_+ + n_-$ is the total number density. Thus, the charge density, $\rho^* \approx 0$, which has the consequence that equation 1.6 reduces to $\boldsymbol{\nabla} \cdot \mathbf{E} \approx 0$.

Typically, the solar atmosphere satisfies the condition of charge neutrality, which allows plasma motions to be described by the coupling of a pressure gradient,

$$-\boldsymbol{\nabla} p, \tag{1.15}$$

where p represents plasma pressure, the Lorentz force,

$$\mathbf{F}_1 = \mathbf{j} \times \mathbf{B}, \tag{1.16}$$

and the combined forces of gravity and viscosity,

$$\mathbf{F}_2 = \mathbf{F}_g + \mathbf{F}_v, \tag{1.17}$$

where F_g and F_v represent gravity and viscosity respectively. Thus, the equation of motion is given by,

$$\rho \frac{d\mathbf{v}}{dt} = -\boldsymbol{\nabla} p + \mathbf{j} \times \mathbf{B} + \mathbf{F}_2, \tag{1.18}$$

where ρ represents the mass density of the plasma.

Mass conservation of the plasma is then described by,

$$\frac{\partial \rho}{\partial t} + \boldsymbol{\nabla} \cdot (\rho \mathbf{v}) = 0. \tag{1.19}$$

This has the consequence that if additional matter enters the region, the density of the plasma will increase so that equation 1.19 is satisfied.

Finally, an equation of state is used the describe the pressure of the gas. The perfect gas law is expressed as,

$$p = \frac{k_B}{m} \rho T, \tag{1.20}$$

where k_B is the Boltzmann constant ($k_B = 1.381 \times 10^{-23}$ J deg^{-1}), m is the mean particle mass and T represents temperature in degrees kelvin.

1.3.2 Energy Equations

To complete the description of an MHD process, the energy of the system must also be considered. The energy equation is given by,

$$\rho T \frac{ds}{dt} = -\mathcal{L}, \tag{1.21}$$

where s is the entropy per unit mass of the plasma and $\mathcal{L}$ is the energy loss function,

$$\mathcal{L} = \boldsymbol{\nabla} \cdot \mathbf{q} + L_r - \frac{j^2}{\sigma} - F_H. \tag{1.22}$$

Here, $\mathbf{q} = -\kappa \boldsymbol{\nabla} T$ is heat flux due to particle conduction (where κ is the thermal conduction tensor), $L_r = \rho^2 Q(T)$ is net radiation function for an optically thin plasma (such as the corona), j^2/σ is Ohmic dissipation and F_H is the sum of all other heating sources.

When considering the internal energy per unit mass, the energy equation (equation 1.21) may be rewritten as,

$$\rho \frac{de}{dt} - \frac{p}{\rho} \frac{d\rho}{dt} = -\mathcal{L}, \tag{1.23}$$

where e represents the internal energy. This internal energy can then be expressed as,

$$e = \frac{p}{(\gamma - 1)\rho}, \tag{1.24}$$

where γ is the ratio of specific heats which typically has a value between 1 and 5/3 for a partially ionised plasma.

Using the equation for internal energy (equation 1.24) to subsitute for e in equation 1.23, the energy equation (equation 1.21) may then be written as,

$$\frac{\rho^\gamma}{\gamma - 1} \frac{d}{dt} \left(\frac{p}{\rho^\gamma} \right) = -\mathcal{L}. \tag{1.25}$$

Often, it is useful to find the total energy of the system, by considering the contributions of kinetic, magnetic and internal energy. To study the kinetic energy,

the equation of motion (equation 1.18) is modified using the relation,

$$\frac{d}{dt} \equiv \frac{\partial}{\partial t} + \mathbf{v} \,.\, \boldsymbol{\nabla}, \tag{1.26}$$

which gives the total derivative for time variations that follow the motion. Thus, equation 1.18 may be rewritten as,

$$\rho \frac{\partial \mathbf{v}}{\partial t} + \rho(\mathbf{v} \,.\, \boldsymbol{\nabla})\mathbf{v} = -\boldsymbol{\nabla} p + \mathbf{j} \times \mathbf{B} + \mathbf{F}_2. \tag{1.27}$$

The equation for kinetic energy is given by the scalar product of $\mathbf{v}$ with equation 1.27,

$$\frac{\partial}{\partial t}\left(\frac{1}{2}\rho v^2\right) + \boldsymbol{\nabla} \,.\, \left(\frac{1}{2}\rho v^2\right)\mathbf{v} = -\mathbf{v} \,.\, \boldsymbol{\nabla} p + \mathbf{v} \,.\, (\mathbf{j} \times \mathbf{B}) + \mathbf{v} \,.\, \mathbf{F}_2. \tag{1.28}$$

To derive the magnetic energy equation, consider an equation for the divergence of the Poynting flux,

$$\boldsymbol{\nabla} \,.\, \left(\mathbf{E} \times \frac{\mathbf{B}}{\mu}\right) = -\mathbf{E} \,.\, \left(\boldsymbol{\nabla} \times \frac{\mathbf{B}}{\mu}\right) + \frac{\mathbf{B}}{\mu} \,.\, (\boldsymbol{\nabla} \times \mathbf{E}),$$

which is transformed using equations 1.5 and 1.7 to give,

$$\boldsymbol{\nabla} \,.\, \left(\mathbf{E} \times \frac{\mathbf{B}}{\mu}\right) = -\mathbf{E} \,.\, \mathbf{j} - \frac{\partial}{\partial t}\left(\frac{B^2}{2\mu}\right), \tag{1.29}$$

where equation 1.10 shows that $\mathbf{E} \,.\, \mathbf{j} = j^2/\sigma + \mathbf{v} \,.\, (\mathbf{j} \times \mathbf{B})$.

Next, the equation for internal energy is also rewritten using equation 1.26 to give,

$$\frac{\partial}{\partial t}\left(\frac{p}{\gamma - 1}\right) + \boldsymbol{\nabla} \,.\, \left(\frac{\gamma p}{\gamma - 1}\mathbf{v}\right) = -\mathcal{L} + \mathbf{v} \,.\, \boldsymbol{\nabla} p. \tag{1.30}$$

Finally, combining the equations for kinetic energy, magnetic energy and internal energy (equations 1.28, 1.29 and 1.30 respectively) gives,

$$\frac{\partial}{\partial t}\left(\frac{1}{2}\rho v^2 + \frac{B^2}{2\mu} + \frac{p}{\gamma - 1}\right) +$$
$$\boldsymbol{\nabla} \,.\, \left(\left(\frac{1}{2}\rho v^2\right)\mathbf{v} + \frac{\mathbf{E} \times \mathbf{B}}{\mu} + \left(\frac{\gamma p}{\gamma - 1}\right)\mathbf{v}\right) = F_H - \boldsymbol{\nabla} \,.\, \mathbf{q} + \mathbf{v} \,.\, \mathbf{F}_2 - \rho^2 Q(T), \tag{1.31}$$

which is called the total energy equation.

1.3.3 Summary of MHD Equations

The following equations are a complete set for describing MHD processes. The primary variables $\mathbf{B}$, $\mathbf{v}$, p, ρ and T can be obtained from use of,

$$\frac{\partial \mathbf{B}}{\partial t} = \boldsymbol{\nabla} \times (\mathbf{v} \times \mathbf{B}) + \eta \nabla^2 \mathbf{B}, \qquad \text{(induction equation)}$$

$$\rho \frac{d\mathbf{v}}{dt} = -\boldsymbol{\nabla} p + \mathbf{j} \times \mathbf{B} + \mathbf{F}_2, \qquad \text{(equation of motion)}$$

$$\frac{\partial \rho}{\partial t} + \boldsymbol{\nabla} \cdot (\rho \mathbf{v}) = 0, \qquad \text{(equation of mass continuity)}$$

$$\frac{\rho^\gamma}{\gamma - 1} \frac{d}{dt} \left(\frac{p}{\rho^\gamma} \right) = -\mathcal{L}, \qquad \text{(energy equation)}$$

and an equation of state such as,

$$p = \frac{k_B}{m} \rho T. \qquad \text{(perfect gas law)}$$

The secondary variables, $\mathbf{E}$ and $\mathbf{j}$, then follow from,

$$\mathbf{E} = -\mathbf{v} \times \mathbf{B} + \frac{\mathbf{j}}{\sigma}, \qquad \text{(Ohm's law)}$$

$$\mathbf{j} = \boldsymbol{\nabla} \times \frac{\mathbf{B}}{\mu}, \qquad \text{(Ampère's law)}$$

whilst the magnetic field $\mathbf{B}$ is subject to the solenoidal condition,

$$\boldsymbol{\nabla} \,.\, \mathbf{B} = 0.$$

1.3.4 Magnetohydrostatics

MHS is a powerful tool for studying solar structures which evolve slowly over long timescales and is a particular solution to Maxwell's equations for MHD. By assuming that any motion in the plasma is slow, the system damps to equilibrium faster than the magnetic field and the plasma are moving. It then follows that typical relaxation timescales are shorter than the typical timescales over which the magnetic footpoints evolve and hence one may assume that $|\mathbf{v}|$ is so small that $\partial/\partial t$ terms can be approximated by zero. The core assumption of MHS is then that the plasma is in

equilibrium and there are no motions in the plasma ($\mathbf{v} = \mathbf{0}$). When considering an MHS equilibrium, the equation of motion 1.18 may be simplified such that,

$$\mathbf{0} = -\boldsymbol{\nabla} p + \mathbf{j} \times \mathbf{B} - \rho g \, \hat{\mathbf{z}}. \tag{1.32}$$

The magnetic field is then described by equation 1.32, together with equations 1.7, 1.4 and 1.20.

Force-Free Solution

In some circumstances, equation 1.32 can be further simplified. Consider a case where the magnetic field is both uniform and purely vertical above a locally plane part of the solar surface. Here, gravity acts along the negative z-axis, $\mathbf{B} = B_0 \, \hat{\mathbf{z}}$ and $\mathbf{j} = 0$ since, for this case, $\boldsymbol{\nabla} \times \mathbf{B} = 0$. Thus, the Lorentz force is eliminated from the equation of motion (equation 1.32) such that,

$$0 = -\frac{\partial p}{\partial z} - \rho g, \tag{1.33}$$

where p and ρ are functions of z along a given field line. This can be solved and integrated to give,

$$p = p_b \exp\left(- \int_0^z \frac{dz}{H(z)} \right), \tag{1.34}$$

where p_b is the base pressure at $z = 0$ and $H(z)$ is the pressure scale-height given by,

$$H(z) = \frac{p}{\rho g}, \tag{1.35}$$

which represents the height over which pressure falls by a factor of e. An order of magnitude comparison of ∇p with ρg from equation 1.32 gives the pair of equations,

$$\nabla p \approx \frac{p_0}{l_0}, \tag{1.36}$$

$$\rho g \approx \rho_0 g_0, \tag{1.37}$$

where l_0 is the length-scale considered. If the height of the structures studied are much less than the pressure scale-height ($l_0 \ll H(z)$) then it follows from equation 1.35 that,

$$l_0 \ll \frac{p_0}{\rho_0 g_0},$$

which rearranges to give,

$$\rho_0 g_0 \ll \frac{p_0}{l_0},$$

and from equations 1.36 and 1.37 this shows that in magnitude,

$$\rho g \ll \nabla p. \tag{1.38}$$

Hence, when considering structures much smaller than a pressure scale height, the gravitational force in equation 1.32 can be neglected by comparing it with the pressure gradient. Thus equation 1.32 becomes,

$$\mathbf{0} = -\boldsymbol{\nabla} p + \mathbf{j} \times \mathbf{B}. \tag{1.39}$$

Furthermore, the plasma beta gives the ratio between plasma pressure (p_0) and magnetic pressure (B_0^2) such that,

$$\beta \equiv \frac{2\mu p_0}{B_0^2}. \tag{1.40}$$

When $\beta \ll 1$, the Lorentz force dominates the pressure gradient, thus the pressure gradient becomes negligible. Hence, equation 1.32 becomes,

$$\mathbf{0} = \mathbf{j} \times \mathbf{B}, \tag{1.41}$$

which is called the force-free solution. Consequently, equation 1.41 implies that the two vectors, $\mathbf{j}$ and $\mathbf{B}$, are parallel to one another. Thus, the magnetic field can now be related to the current density through multiplication by a scalar, a,

$$\mathbf{j} = a\mathbf{B}, \tag{1.42}$$

which together with equation 1.41 gives that,

$$\boldsymbol{\nabla} \times \mathbf{B} = \alpha \mathbf{B}, \tag{1.43}$$

where $\alpha = a\mu$ and is therefore a scalar. However, from the equation,

$$\mathbf{B} \cdot \nabla \alpha = 0, \tag{1.44}$$

it also follows that α must be constant along field lines (Priest 2014).

Potential Field Solution

The potential solution arises when the current density throughout the field reduces to zero ($\mathbf{j} = \mathbf{0}$). When $\mathbf{j}$ vanishes, equation 1.42 requires a to also reduce to zero. Consequently, α is then eliminated simplifying equation 1.43 to,

$$\boldsymbol{\nabla} \times \mathbf{B} = \mathbf{0}. \tag{1.45}$$

Hence, equations 1.4 and 1.45, together with the vector identity for the curl of the curl,

$$\nabla^2 \mathbf{B} \equiv \boldsymbol{\nabla}(\boldsymbol{\nabla} \cdot \mathbf{B}) - \boldsymbol{\nabla} \times (\boldsymbol{\nabla} \times \mathbf{B}), \tag{1.46}$$

give the vector Laplace equation,

$$\nabla^2 \mathbf{B} = \mathbf{0}. \tag{1.47}$$

From 1.45 it then follows that the magnetic field may be represented by,

$$\mathbf{B} = \nabla \psi, \tag{1.48}$$

where ψ is a magnetic, scalar potential, since,

$$\boldsymbol{\nabla} \times \nabla \psi = 0, \tag{1.49}$$

from the vector identity for the curl of a gradient. Thus, once a solution for ψ is found, equations 1.4 and 1.45 are automatically solved. This has the benefit of making the potential field solution computationally cheap and quick to obtain compared with more cumbersome force-free solutions.

1.4 Magnetic Topology

When one wishes to study a magnetic field, often it is useful to consider the geometrical structures of which it is comprised. Together, these structures form the topological skeleton, which can be considered as the coupling of two different categories, the magnetic skeleton and the quasi-skeleton (Priest 2014). Magnetic topology is used to investigate how the coronal magnetic field may be structured and configured, along with providing insights into how the field evolves over time. Studies have focused on configurations of particular sets of sources, such as the topologies from the three source case (Brown & Priest 1999), topologies from four magnetic sources (Maclean et al. 2006a) and in particular a pair of bipolar regions (Beveridge et al. 2002; Maclean et al. 2006b), along with a mixed polarity field (Schrijver & Title 2002). This section will outline some of the main features of each.

1.4.1 The Magnetic Skeleton

One of the key features of a magnetic skeleton are linear null points (Lau & Finn 1990), where the magnetic field vanishes ($\mathbf{B} = \mathbf{0}$). A null point may be classified as either positive or negative, where the classification is dependent upon the eigenvalues derived from the Jacobian matrix of the linearised field about the null (Priest & Titov 1996).

The Jacobian Matrix of a magnetic field $\mathbf{B}$ is the matrix which contains all of the first-order partial derivatives of $\mathbf{B}$ and is given by,

$$\mathbf{J_B} = \begin{bmatrix} \frac{\partial B_x}{\partial x} & \frac{\partial B_x}{\partial y} & \frac{\partial B_x}{\partial z} \\ \frac{\partial B_y}{\partial x} & \frac{\partial B_y}{\partial y} & \frac{\partial B_y}{\partial z} \\ \frac{\partial B_z}{\partial x} & \frac{\partial B_z}{\partial y} & \frac{\partial B_z}{\partial z} \end{bmatrix}. \tag{1.50}$$

The eigenvalues of the Jacobian matrix, $\mathbf{J_B}$, may then be found by finding the values of λ which satisfy,

$$|\mathbf{J_B} - \lambda \boldsymbol{I}| = 0, \tag{1.51}$$

where $\boldsymbol{I}$ is the 3×3 identity matrix.

Given that there is zero divergence in the magnetic field, as required by equation 1.4, the sum of the eigenvalues must be equal to zero. Whilst other solutions exist, the generic linear case is where two eigenvalues are of one sign (say positive), and the third eigenvalue of the opposite sign (say negative).

From a null point, field lines can be defined called the spine and the fan (Priest & Titov 1996) as shown in figure 1.14a. When there are two positive eigenvalues, the corresponding eigenvectors form a fan of field lines which diverge from the null point, while the spine is formed from the eigenvector of the third eigenvalue and is directed towards the null point. In the contrasting case, where two eigenvalues are negative, the converse holds. Further descriptions may also be given to null points such as prone, and upright, depending on the orientation of its spine field lines (Maclean et al. 2005).

From these field lines, separatrix surfaces can be traced, across which there exist discontinuities in the field line mappings (Seehafer 1986). For example, a fan separatrix surface serves to divide the volume into different regions of magnetic connectivity. As the separatrix surfaces are extended from the null point, they form a complex structure of walls and domes as in figure 1.14b. The region where two separatrix surfaces intersect is called a separator field line (Lau & Finn 1990), the foot points of which may connect to nulls or boundaries (Longcope & Cowley 1996a; Priest & Titov 1996). Thus, separators bound four distinct regions of connectivity. This makes the separator a prominent region where plasma elements can change their connectivity, resulting in the transfer of flux from one domain to another, called reconnection.

Separatrix surfaces do not have to form new domains of connectivity however. An open separatrix surface may exist such that two spine field lines form bounds on the surface, which may then intersect a boundary in a non-closed curve (Priest

2014). Field lines on either side of this surface will occupy the same domain, yet the mapping is still discontinuous across the surface. In this case, reconnection may still occur across the separatrix, but instead, it simply transfers flux from one part of the magnetically connected domain to another part of the same domain.

The topological structures and behaviour produced from a model with three magnetic sources have been completely classified (Brown & Priest 1999). Here, changes in the source positions lead to drastic changes in the configuration of the magnetic skeleton. Such a change is a type of bifurcation, which are explored further in section 1.5. In the case of three magnetic sources, all of the nulls lie in the photospheric plane. However, this is not a requirement of their description. When a fourth source of magnetic flux is added, null points can be found off the plane and are hence called coronal null points. Figure 1.15 depicts such a situation, where the coronal null is connected to those in the plane by a collection of separator field lines.

Much of the solar activity that affects the Earth is rooted in the solar corona and is thought to be driven by magnetic reconnection (Priest 2014). As reconnection may occur at both separator field lines and null points (Longcope 1996; Priest & Titov 1996; Longcope & Beveridge 2007), a single coronal null may, therefore, be related to multiple sites where reconnection can occur in the corona. It has been suggested that the number of coronal nulls drops off exponentially with height from the solar surface (Schrijver & Title 2002), potential field extrapolations from magnetogram images suggest 96% of nulls exist in the plane of the sources (Close et al. 2004), whilst other studies have considered the distribution of coronal null points (Edwards & Parnell 2015; Freed et al. 2015). Thus, understanding the behaviour of coronal null points is vital to further understand the mechanisms which lead to solar flares and coronal mass ejections.

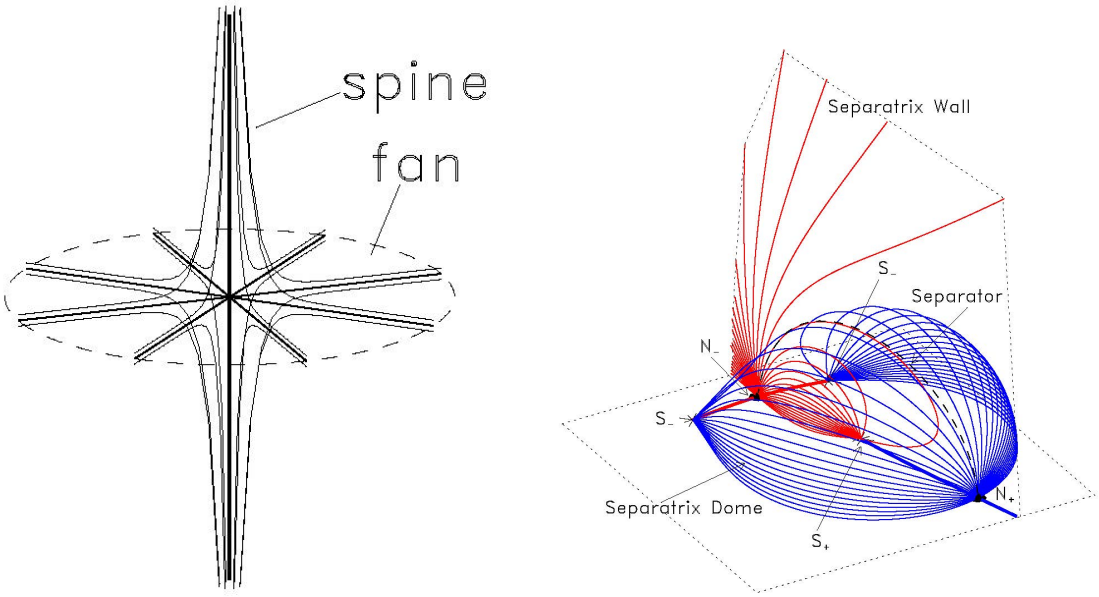

(a) (b)

Figure 1.14: a) Example of the spine and fan field line configuration local to a linear magnetic null point (Brown & Priest 2001a). Bold lines represent spine field lines, along with those that sit in the plane of the fan surface. Field lines are shown travelling towards the null point, along the spine field lines, before they radiate out away from the null along the fan surface. b) The magnetic skeleton of the three-source intersected state (Brown & Priest 2001a). Positive and negative sources are labelled S_+ and S_- respectively. Null points are presented as bold black dots, with positive and negative nulls labelled N_+ and N_- respectively. Solid lines represent field lines in a fan separatrix surface, bold lines illustrate spine field lines, and dashed lines are used for magnetic separators.

1.4.2 The Quasi-Skeleton

The quasi-skeleton is composed of a tangled network of quasi-separatrix layers (QLSs). Across the surface of a QSL, field line connectivities have a steep but finite gradient; QSLs do not have a discontinuous field line mapping from one foot-point to another (Mandrini et al. 1995; Priest & Démoulin 1995; Démoulin et al.

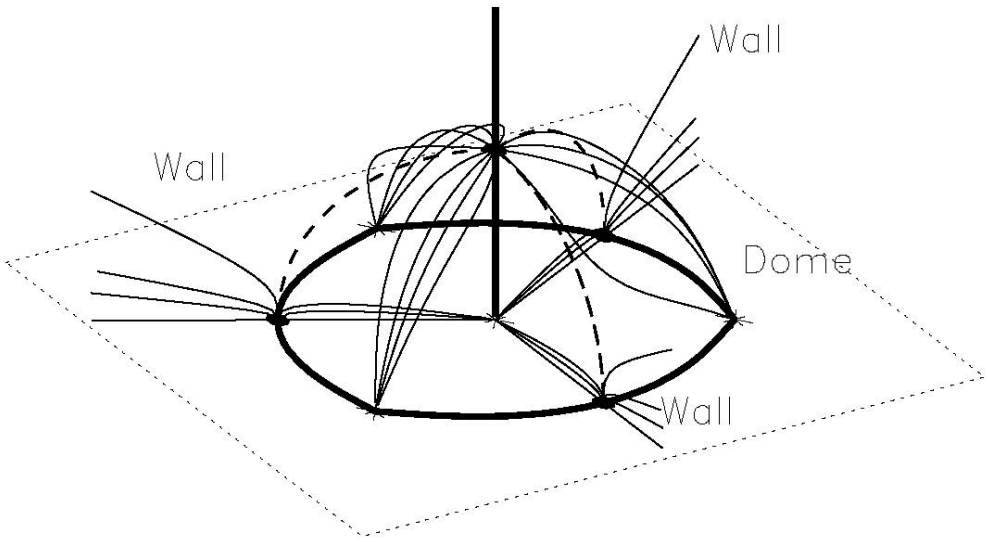

Figure 1.15: Diagram of the four-source coronal null state. Spine field lines are represented by bold lines, while fan field lines are thin. Three walls intersect the coronal dome, creating three separators (dashed lines), linking the coronal null to each of the planar null points (Brown & Priest 2001a).

1996, 1997). Null points often feature in topological skeletons, forming a myriad of separatrix surfaces. However, where there are no null points present, there are also no separatrices, hence the field line mapping between footpoints can be described continuously (Schindler et al. 1988). Yet in the absence of nulls, QSLs may still be present and a method for their detection was found (Priest & Démoulin 1995). This detection method was later built upon in the form of a squashing factor, Q, which calculates the divergence in the footpoints of field lines such that regions with values of $Q \gg 1$ are QSLs (Titov et al. 1999; Titov 2007; Titov et al. 2009). The squashing factor is explored in more detail in section 3.4.

Where two QSLs intersect, they form a quasi-separator, which provides another site for reconnection to occur. The study of reconnection in quasi-separatrix layers was first described as magnetic flipping (Priest & Forbes 1992), but later termed quasi-separator reconnection (Priest & Démoulin 1995). Studies have shown that

current sheets can also form along quasi-separators where there are smooth, large-scale motions in the footpoints (Aulanier et al. 2005). Since then, QSLs have also been considered in the context of solar flares where slip-running reconnection occurs (Aulanier et al. 2006).

By considering the quasi-skeleton, the complex structures formed by a collection of quasi-separatrix layers and quasi-separators can be studied. However, a more complete description of a magnetic topology is found when both the quasi-skeleton and the magnetic skeleton (consisting of magnetic null points, separatrix surfaces and magnetic separators) are simulated for a model topology arising from a magnetic configuration.

1.5 Bifurcation Theory

Here, ideas of how a system can change due to arbitrary changes in key parameters are explored. First, a mathematical description of bifurcations is provided, which is then contextualised when considering a magnetic skeleton.

1.5.1 Mathematical Descriptions of Bifurcations

Consider a system depending on some parameter λ,

$$\dot{x} = f(x, \lambda), \tag{1.52}$$

defined by an ordinary differential equation. At critical values of λ, the behaviour of the system may change drastically and non-smoothly. These changes are called bifurcations and lead to distinct changes in the configuration of various topological features such as equilibrium points. There are two classifications, global and local bifurcations. A local bifurcation is one which results in a change of stability of an equilibrium point and/or the number of equilibrium points, where one of the eigenvalues of the Jacobian matrix of the system at the equilibrium is equal to zero

at the moment of bifurcation. Two types of local bifurcation, which are common in magnetic topology, are turning point bifurcations and pitchfork bifurcations. A turning point bifurcation may occur when a mixed-stability equilibrium point forms at the moment of bifurcation, which then splits into two distinct equilibrium points that are stable and unstable respectively. A pitchfork bifurcation occurs where a single equilibrium point changes stability at the moment of bifurcation and splits to create two additional equilibrium points with the same stability as the original equilibrium point. Both of the local bifurcation processes discussed are also permissible in reverse (Guckenheimer & Holmes 1986; Glendinning 1994). Global bifurcations may be characterised as changes which occur in the phase space of the system. Global bifurcations in magnetic topologies may be spine-fan bifurcations or separator bifurcations, though there are many others.

Turning Point Bifurcation

A turning point bifurcation is a form of local bifurcation which can be exampled by the differential equation,

$$\dot{x} = \lambda - x^2. \tag{1.53}$$

The equilibrium points of such a system occur when $\dot{x} = 0$, thus are found by solving,

$$\lambda - x^2 = 0. \tag{1.54}$$

Hence, when $\lambda < 0$ there are no real solutions to equation 1.54, thus there are no equilibrium points (figure 1.16a). The bifurcation occurs when $\lambda = 0$, where a single equilibrium point exists at $x = 0$ (figure 1.16b). In the case where $\lambda > 0$, $x = \pm\sqrt{\lambda}$, such that two real solutions are found (figure 1.16c). The solution for $x = +\sqrt{\lambda}$ is stable (figure 1.16c), meaning that solution trajectories local to the equilibrium point tend towards it, as indicated by the arrows in figure 1.16c. However, the solution for $x = -\sqrt{\lambda}$ is unstable (figure 1.16c), so the equilibrium point repels local

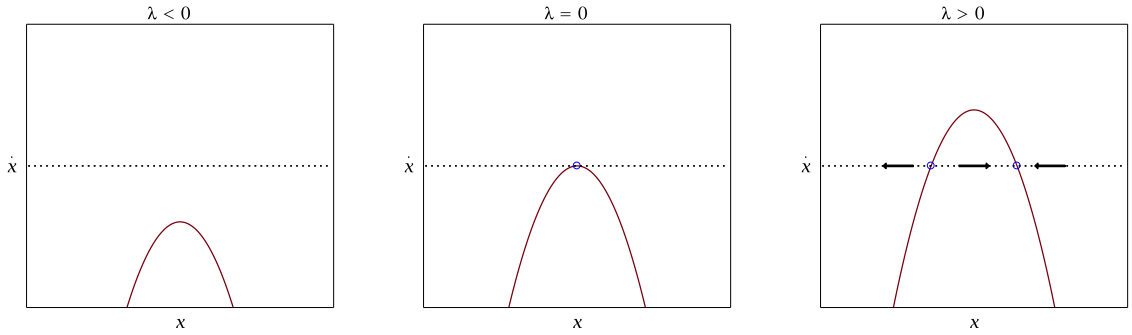

Figure 1.16: Plots showing the solutions for the equilibrium points of the turning point bifurcation for different values of λ. The dotted line represents where $\dot{x} = 0$, blue circles give the position of the equilibria, and the red line is $f(x, \lambda)$. The solution is increasing where $f(x, \lambda)$ is positive, but is decreasing where $f(x, \lambda)$ is negative. Arrows are used to indicate the stability of the equilibria, where local trajectories will be attracted towards stable equilibria, or repelled away from unstable equilibria.

solution trajectories.

Figure 1.17 shows how the value of x varies with the parameter λ at the equilibrium points, which is called the bifurcation diagram for this system. Real equilibria exist when $\lambda \geq 0$, with two equilibria for $\lambda > 0$. The equilibrium point where $x > 0$ is stable (solid line), whilst the negative value of x is an unstable equilibrium (dashed line).

Pitchfork Bifurcation

The pitchfork bifurcation is another local bifurcation which can be represented by,

$$\dot{x} = x(\lambda - x^2). \tag{1.55}$$

The equilibrium points for this system can be obtained by solving the equation,

$$x(\lambda - x^2) = 0. \tag{1.56}$$

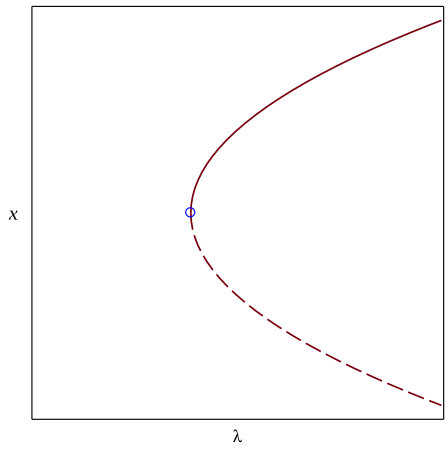

Figure 1.17: Bifurcation diagram for the turning point bifurcation. The solid line is the stable solution, while the dashed line is the unstable solution. The blue circle indicates the moment of bifurcation, where $\lambda = 0$.

In contrast to the turning point bifurcation, a stable equilibrium at $x = 0$ is found for $\lambda < 0$ (figure 1.18a). Again, the bifurcation occurs at $\lambda = 0$ (figure 1.18b), where a single equilibrium point exists at $x = 0$. For $\lambda > 0$ three equilibria exist, two stable and one unstable (figure 1.18c). The stable equilibria exist at $x = \pm\sqrt{\lambda}$, where the unstable equilibrium exists at $x = 0$, as shown in figure 1.19.

The bifurcation diagram for this system is shown in figure 1.19, showing how the value of x varies with the parameter λ at the equilibrium points. In this system, real equilibria exist for all real values of λ. When $\lambda < 0$, a single, stable equilibrium point exists at $x = 0$. When $\lambda > 0$, there are three equilibrium points, two of which are stable, but one is unstable. The unstable equilibrium point exists at $x = 0$, but the equilibrium points for the positive and negative values of x are both stable.

Heteroclinic Connection

One type of global bifurcation which often occurs in potential magnetic fields involves a heteroclinic connection. Whilst local bifurcations relate to properties local to equilibrium points, global bifurcations consider the connectivity of the streamlines.

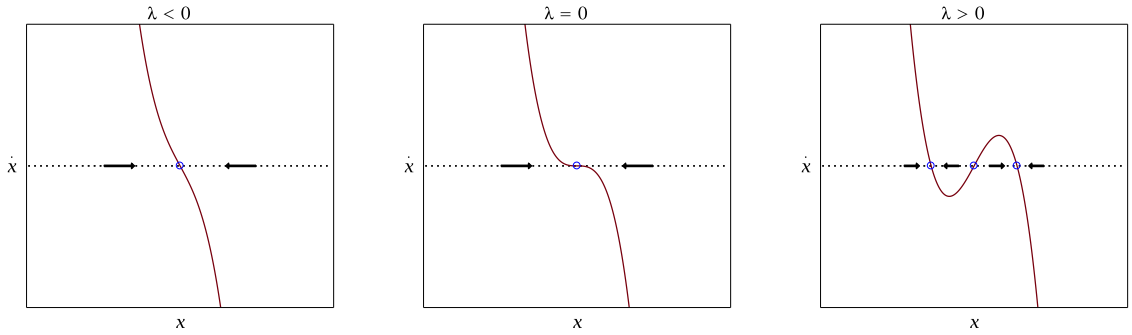

Figure 1.18: Plots showing the solutions for the equilibrium points of the pitchfork bifurcation for different values of λ. The dotted line represents where $\dot{x} = 0$, blue circles give the position of the equilibria, and the red line is $f(x, \lambda)$. The solution is increasing where $f(x, \lambda)$ is positive, but is decreasing where $f(x, \lambda)$ is negative. Arrows are used to indicate the stability of the equilibria, where local trajectories will be attracted towards stable equilibria, or repelled away from unstable equilibria.

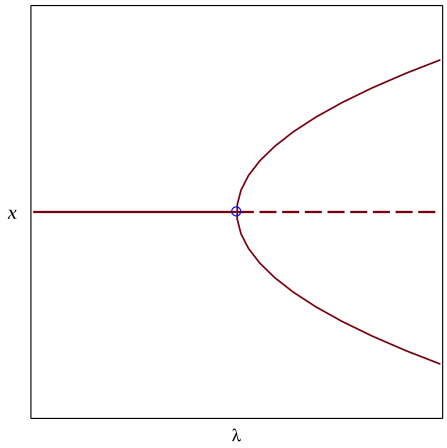

Figure 1.19: Bifurcation diagram for the pitchfork bifurcation. The solid lines represent stable solutions and the dashed line represents the unstable solution. The blue circle indicates the moment of bifurcation, where $\lambda = 0$.

Consider the pair of equations,

$$\dot{x} = \lambda + x^2 - xy, \tag{1.57}$$

and

$$\dot{y} = y^2 - x^2 - 1. \tag{1.58}$$

Here, equilibrium points exist when $\dot{x} = 0$ and $\dot{y} = 0$.

First, consider the case when $\lambda = 0$. Here, equilibria exist at (0 , 1) and (0 , -1), such that both the saddle nodes are now joined by a heteroclinic connection (figure 1.20b). Since the two equilibrium points are saddle nodes, the trajectory joining them is also a separatrix. However, small perturbations to the parameter λ break this connection.

Next, consider when $\lambda < 0$ (figure 1.20a), there is no heteroclinic connection between the saddle nodes, hence streamlines extend from $x = -\infty$ to $x = +\infty$. The equilibrium points are no longer aligned with one another on the y-axis, the lower equilibrium point now sits in the region where $x > 0$, but the upper equilibrium point is in the region $x < 0$.

The final case where $\lambda > 0$ (figure 1.20c) has the result that streamlines travel from $x = +\infty$ to $x = -\infty$. This case also differs to when $\lambda < 0$ when one considers the position of the equilibria. Here, the lower equilibrium point is instead in the region where $x < 0$, but the upper equilibrium point is in the region $x > 0$. Streamline connectivity is then determined to be dependent upon the sign of λ, giving that $\lambda = 0$ is the bifurcation point of the system.

1.5.2 Topological Bifurcations of a Magnetic Field

Where topological features of the magnetic skeleton are unaffected by small changes in the boundary conditions, they are referred to as being topologically stable. However, if an arbitrary change in the boundary conditions cause the topology to change, it is topologically unstable. Such a change in the topology may be due to either a local or a global bifurcation.

A bifurcation which affects the number of null points in a topology, or changes

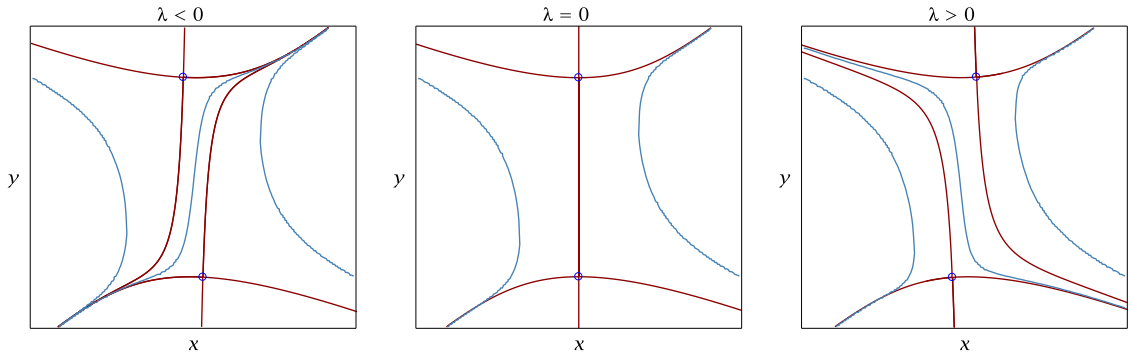

Figure 1.20: Figures showing the solution trajectories for the equilibrium points of the heteroclinic connection bifurcation for different values of λ. Blue circles represent equilibrium points and red lines are separatrices originating at the equilibrium points. Blue lines show example trajectories which do not originate at the equilibria.

the stability of a null point, is called a local bifurcation. Null points are always created, or destroyed, in pairs. In the context of the bifurcations presented in section 1.5.1, a pitchfork bifurcation may result in a single first-order null point, becoming a third-order null point at the moment of bifurcation where it then splits, forming three first-order null points. A turning point bifurcation can also create or destroy a pair of null points, occurring for example when two first-order nulls coalesce and annihilate one another.

Global bifurcations are observed as changes to the configuration of the separatrix surfaces in a topology, such that the number of separators present may change, but without changes in the number of nulls present, which is characteristic of a local bifurcation. A global separator bifurcation occurs when a stable magnetic separator is created (or destroyed) as the result of two fan surfaces touching at the moment of bifurcation, which is a three-dimensional equivalent of the heteroclinic connection bifurcation in two dimensions. A global spine-fan bifurcation is one which observes the spine of one null cross the fan plane of another, but at the moment of

bifurcation, the spine of one null lies in the fan of the other null (Brown & Priest 1999). This connection is an x-line structure, which looks like an x-point in the two-dimensional plane perpendicular to the spine. The bifurcation process itself serves as a heteroclinic connection bifurcation, changing the connectivity of the field lines.

1.6 Solar Observations

As early as 2000 BC, Chinese astronomers recorded their observations of a solar eclipse (Priest 2014). The first telescopes were invented in the early 17th century, and observations of sunspots were prominent enough that a period of prolonged minima in their number was recorded, later termed the Maunder minimum. In the modern age, ground and space-based telescopes now survey the Sun twenty-four hours a day, providing continuous observations and vast amounts of data on everything from active regions to energetic particle events. One such mission is the Solar Dynamics Observatory (SDO), which is used in Chapter 4 of this thesis.

1.6.1 Solar Dynamics Observatory

The Solar Dynamics Observatory (SDO), displayed in figure 1.21, was launched on February 11th, 2010, returning science data from May 1st, 2010. It was the first mission launched as part of NASA's Living with a Star program and served as the spiritual successor to both the Solar and Heliospheric Observatory (SOHO) and the Transition Region and Coronal Explorer (TRACE) missions. SDO's design intent was to predict solar activity both as a forecast for space weather phenomena along with solar activity levels in future solar cycles (Pesnell et al. 2012). The focus of SDO is to monitor solar variations which impact life on Earth, termed space weather, and to strive towards predictive and forecasting capabilities. To accomplish this, the generation and structure of the solar magnetic field must be

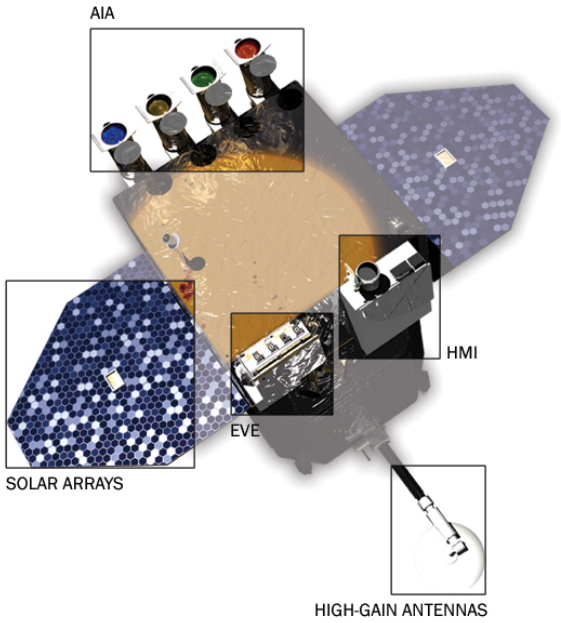

Figure 1.21: Diagram of the SDO with key scientific instruments highlighted (Image Credit: NASA).

studied extensively, alongside how the stored magnetic energy is released as the solar wind into the heliosphere. The mission was designed to last five years but has been prepared with enough resources to remain operational for a further five years beyond. SDO has three instruments aboard it, the Atmospheric Imaging Assembly (AIA), the Extreme Ultraviolet Variability Experiment (EVE) and the Helioseismic and Magnetic Imager (HMI). AIA consists of an array of four telescopes which observe the solar atmosphere. EVE is designed to measure variations in total solar ultraviolet emission, with the intent to provide scientists with extreme ultraviolet (EUV) emissions at a 10-second cadence. However, EVE is not used in this project and thus is not discussed in greater detail. Further information on the EVE instrument can be found in the instrument overview publication (Woods et al. 2012). The HMI instrument is designed to map magnetic and velocity fields at the solar photosphere using helioseismic techniques.

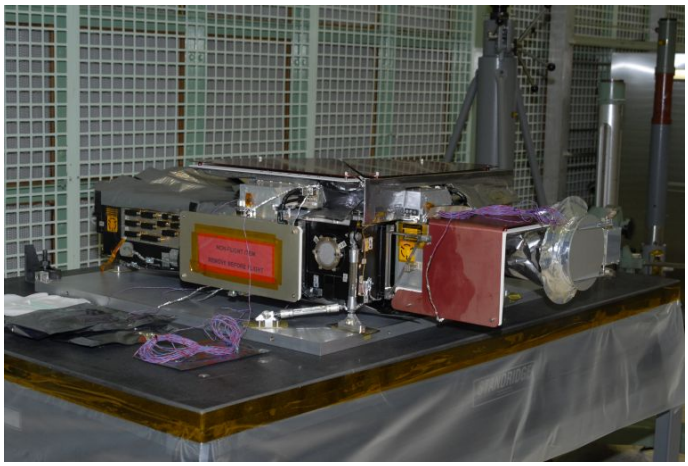

Figure 1.22: Photograph of the HMI instrument, prior to its installation aboard SDO (Image Credit: NASA).

1.6.2 Helioseismic and Magnetic Imager

The Helioseismic and Magnetic Imager (HMI), seen in figure 1.22, instrument aboard the SDO was based on the Michelson Doppler Imager (MDI) from the SOHO satellite (Scherrer et al. 1995) and designed to use helioseismic techniques with observations of the near-photospheric magnetic field to study the solar interior (Schou et al. 2012). It was constructed by the Lockheed Martin Solar and Astrophysics Laboratory (LMSAL), who also constructed the AIA instrument, hence they share a number of identical components. The instrument has two 4096 × 4096 pixel CCD cameras with 0.5-arcsecond pixels. HMI has an overall cadence of 45 seconds for Doppler shift, intensity and line-of-sight magnetic-field measurements, using the FE I (6173 Å) wavelength. It is known as a filtergraph, which means that it derives physical parameters from a combination of images taken at different wavelengths and polarizations.

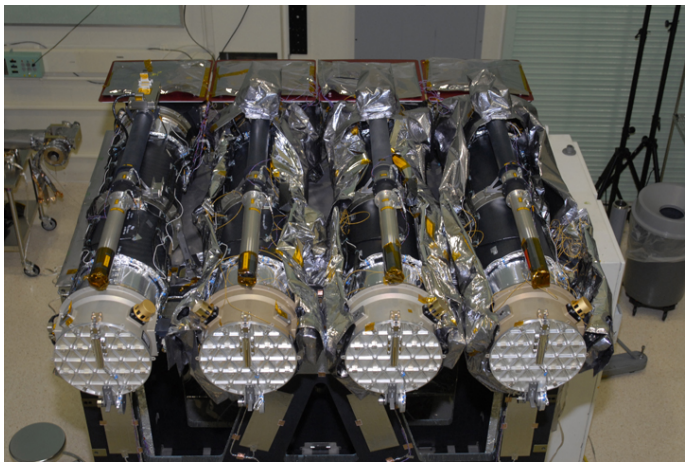

Figure 1.23: Photograph of the AIA instrument, prior to its installation aboard SDO (Image Credit: NASA).

1.6.3 Atmospheric Imaging Assembly

The Atmospheric Imaging Assembly (AIA) instrument, shown in figure 1.23, collects full-disc images across all the regions of the solar atmosphere in UV and EUV wavelengths, in order to advance the understanding of the physical processes behind solar variability (Lemen et al. 2012). In total, the array of four telescopes collects seven EUV wavelengths, six of which are highly ionised FE emission lines, and the other is the HE II line. The temperature range of the EUV emissions covers 60,000 K up to 20,000,000 K, allowing the entire upper portion of the solar atmosphere to be observed. One of the four telescopes also collects images from C IV (1600 Å) and the nearby continuum (1700 Å). The 4096 × 4096 CCD cameras have a resolution of 0.6 arcseconds per pixel, collecting images at a 12-second cadence.

1.7 Thesis Summary

This thesis studies the topological behaviour of the magnetic field in the solar corona. Section 1.3 discusses the equations of magnetohydrodynamics, in particular, the equations pertaining to the solution for a potential magnetic field. The potential

magnetic field solution is used throughout this thesis when modelling the topologies of magnetic fields. Section 1.4 has discussed the features of the magnetic skeleton prevalent in potential field topologies. Section 1.5 provides descriptions of the bifurcation processes through which a magnetic topology changes state. These are seen throughout chapter 2 of this thesis, in the complex topologies which arise from configurations similar to network flux distributions. Finally, section 1.6 discusses the SDO satellite and the instruments aboard it. These instruments have provided all the data used in the final chapter of this thesis, for the study of magnetic events which occur in regions local to X-ray bright points.

Chapter 2 of this thesis presents a study of the topological differences in systems of discrete and continuous sources of magnetic flux. The complex topologies which arise are explored both in terms of their components and the bifurcations which allow them to transition from one state to another. Sources are configured in a supergranular-like manner, forming a crude hexagonal boundary which contains two other sources. At least one coronal null point is present in each of the studied and one of the case studies has three coronal nulls, resulting in a topological structure which is qualitatively similar to the open-separatrix case discussed by Priest (2014). One case exhibits behaviour where a coronal null point is initially enclosed by a separatrix dome originating from a planar null point. As the configuration evolves, the spine of the coronal null bifurcates through the fan of the enclosing dome which opens the previously enclosed flux to the background magnetic field. This may form a basis for a flux breakout model applicable to polar plumes.

Chapter 3 of the thesis defines a new topological feature, the null-like point. Null-like points are locations where x-line structures intersect the photospheric plane in the absence of a null point, protruding into the coronal volume. Trajectories in separatrix-like surfaces, originating from the null-like points, provide insight into the locations and structures of quasi-separatrix layers within the topology. The

squashing factor, Q, of the source configurations is mapped in order to highlight the presence of these structures. It is demonstrated that inclusion of null-like points and their associated separatrix-like surfaces is needed to fully understand the topology generated from continuous source distributions.

Chapter 4 outlines two algorithms. The first is based on McIntosh & Gurman (2005) and detects X-ray bright points SDO/AIA data, tracking identified features over subsequent observations to form a catalogue of XBPs. The second, developed in this chapter, automatically detects and classifies magnetic events local to X-ray bright points such as flux emergence and cancellation. The algorithm is applied to a sample of XBPs from the catalogue, with selection criteria based on the XBP's lifetime and its position relative to the centre of the solar disc. The detected magnetic events are compared with the times detected by the first algorithm to establish the cause of the onset and demise of the bright points.

Chapter 2

Network Topologies: Comparing Discrete and Continuous Source Models

This chapter studies the magnetic skeleton of source configurations when solving for a potential magnetic field. It will focus on a particular set of magnetic source configurations in two different regimes. One where the sources are defined to be points of magnetic flux emerging through a planar photosphere, the other where the sources are continuously distributed following some pre-designated profile. First, the two methods are outlined, along with some of the flaws present in both models. This is followed by a series of case studies that aim to model the types of magnetic field that might be found in intergranular lanes, about a supergranular cell.

2.1 Principles of Magnetic Charge Topology

The principles of magnetic charge topology were first presented by Baum & Bratenahl (1980), later being termed *'magnetic charge topology'* (MCT) by Longcope (1996). MCT makes two approximations in order to calculate the topology of a

magnetic field. First, the coronal field is assumed to be potential, which is a particular solution of a force-free field. This may be a valid assumption, provided the velocities in the plasma are much smaller than the Alfvén speed, as is required for a force-free field. The potential field solution then produces a topology which is robust to small perturbations in α. The field may then be considered to evolve through a series of static equilibria, as governed by the equations of magnetohydrostatics (section 1.3.4). This first approximation is certainly feasible in regions of the quiet-Sun, but almost certainly breaks down during the eruptive phase of a solar flare.

Secondly, magnetic sources are described by discrete points upon the photospheric plane ($z = 0$), where each source has a radius of zero. This approach is used as an approximation of continuously distributed sources; at the solar surface, discrete points of magnetic flux are not observed. However, provided the source has a sufficiently small radius, an observer at a large distance may perceive the source to be a single point. At the point sources themselves, $\boldsymbol{\nabla} \cdot \mathbf{B} = 0$, but $\mathbf{B}$ becomes infinite in violation of the divergence theorem. This problem is resolved by placing the sources on a surface that is external to the volume modelled. These surfaces can then be removed from the volume, hence $\boldsymbol{\nabla} \cdot \mathbf{B} = 0$ is then preserved everywhere in the simulated volume. Together, these assumptions allow the magnetic field to be calculated analytically at any point in the volume. It can be described by the equation,

$$\mathbf{B}(\mathbf{r}) = \sum_i \varepsilon_i \frac{\mathbf{r} - \mathbf{r}_i}{\mid \mathbf{r} - \mathbf{r}_i \mid^3}, \tag{2.1}$$

where, $r = x\hat{\mathbf{x}} + y\hat{\mathbf{y}} + z\hat{\mathbf{z}}$ and $r_i = x_i\hat{\mathbf{x}} + y_i\hat{\mathbf{y}} + z_i\hat{\mathbf{z}}$ is the position of source i with flux ε_i. The magnetic topology can be described from this equation and the source configuration.

Brown & Priest (1999) used MCT to completely classify the magnetic topology generated by configurations of three discrete sources. The work presented here will use six magnetic sources, placed in a hexagonal configuration to represent the

boundary of a supergranular cell. Two additional sources will then be placed internal to this hexagonal configuration. First, for completeness, the artificial case where the internal sources are of the same charge will be considered. Then, an alternate scenario follows where internal sources of opposing charges are used to represent an emerging bipole. Three cases will be considered for each set of interior sources where the boundary sources are varied in charge, representative of the supergranular network.

2.2 Modelling Point Sources of Magnetic Flux

The Interactive Data Language (IDL) has been used for all the programs which generate magnetic topology from point sources. First, point sources of flux are defined with arbitrary intensities upon the $z = 0$ plane. However, at the sources, the field becomes infinite, hence the divergence theorem (equation 1.4) no longer holds. This is then justified by considering the sources as locations on the coronal boundary, where flux passes through the photospheric surface, so that they may be 'cut out' of the coronal volume. Thus they can be considered not to be true monopoles, and the divergence theorem (equation 1.4) holds everywhere else in the volume. Next, the locations of null points are found as outlined in section 2.2.1. The structure of the spine and fan field lines about the null point can be determined as outlined in section 2.2.2. The magnetic separators are then found by scanning all the field lines of the topology for regions where they diverge from one another, as outlined in section 2.2.3.

2.2.1 Finding Magnetic Null Points

Null points are defined as locations where the magnetic field vanishes; at a magnetic null point, the components of the magnetic field go to zero. Since the force-free

model requires that the divergence of the magnetic field be equal to zero (equation 1.4), the Jacobian matrix ($\mathbf{M}$) local to a magnetic null point will be symmetric (in the potential field model only). This yields three real eigenvalues of which at least one will typically be of each sign (Cowley 1973; Yeh 1976; Longcope 1996) together with a set of eigenvectors. These parameters then define the configuration of the fan surfaces and spine field lines about the null.

To locate magnetic null points, the volume is divided into a grid, with the magnetic field calculated at the corners of each grid-cell. Nullclines are defined as surfaces where one of B_x, B_y, or $B_z = 0$. These nullclines are then located in the grid by searching for the cells where the sign of field components (B_x, B_y and B_z) flip. The cells which contain two or more nullclines are then divided across a smaller sub-grid, and the process is then repeated to find cells containing all three nullclines. Through linear interpolation, an approximate location of where the nullclines cross is found, which is used as a starting point for the Newton-Raphson method. This double process is used because the form of the magnetic field needs a good initial guess for the Newton-Raphson scheme to converge, and the gridding method provides confidence that all of the null points in the volume are found.

The iterative Newton-Raphson method is then used, which, in one dimension, is given by,

$$x_{k+1} = x_k - \frac{f(x_k)}{f'(x_k)}, \tag{2.2}$$

where x_k is the approximate position of a root of $f(x^*) = 0$ for iteration k (i.e $x_k \rightarrow$ equilibrium, as $k \rightarrow \infty$).

However, the three-dimensional, iterative Newton-Raphson method must be used here, where the derivative of the magnetic field local to the null point is given by the Jacobian Matrix, $\mathbf{J_B}(\boldsymbol{r}_k)$. This may then be expressed as,

$$\boldsymbol{r}_{k+1} = \boldsymbol{r}_k - \left(\mathbf{B}(\boldsymbol{r}_k)\mathbf{J_B}(\boldsymbol{r}_k)^{-1}\right), \tag{2.3}$$

where $\boldsymbol{r}_k = x_k\hat{\mathbf{x}} + y_k\hat{\mathbf{y}} + z_k\hat{\mathbf{z}}$ is the approximate position of the null point for iteration

k and $\mathbf{B}(\boldsymbol{r}_k)$ is the measure of the magnetic field at position $\boldsymbol{r}_k$.

This process is iterated until the approximated position of the null point has converged to within an area of radius 1×10^{-4}. However, if the position falls outside of the identified grid cell, the result is rejected.

2.2.2 Finding Spine and Fan Field Lines

The field lines, $\mathbf{r}(s)$, for the spine and separatrix surfaces are obtained by integrating,

$$\frac{d}{ds}\mathbf{r}(s) = \frac{\mathbf{B}[\mathbf{r}(s)]}{|\mathbf{B}[\mathbf{r}(s)]|}, \tag{2.4}$$

by starting from a footpoint $\mathbf{r}(0)$. Once the magnetic null points have been located in the volume, their spine and fan structures can be generated. The Jacobian matrix is given by,

$$\mathbf{J_B} = \begin{bmatrix} \frac{\partial B_x}{\partial x} & \frac{\partial B_x}{\partial y} & \frac{\partial B_x}{\partial z} \\ \frac{\partial B_y}{\partial x} & \frac{\partial B_y}{\partial y} & \frac{\partial B_y}{\partial z} \\ \frac{\partial B_z}{\partial x} & \frac{\partial B_z}{\partial y} & \frac{\partial B_z}{\partial z} \end{bmatrix}, \tag{2.5}$$

which is the matrix of all first-order partial derivatives of the magnetic field. This is evaluated at the nulls points and its eigenvalues and eigenvectors are calculated. For linear null points, two of the eigenvalues will be of one sign, and one of the other sign. Suppose here that the eigenvalue λ_1 is of opposite sign to the eigenvalues λ_2 and λ_3. The eigenvector $\boldsymbol{v}_1$ associated with eigenvalue λ_1 relates to the spine of the null point and is used to determine the pair of starting points for the spine field lines by,

$$\boldsymbol{s}_1 = \boldsymbol{r}_k \pm \delta_r \boldsymbol{v}_1, \tag{2.6}$$

where $\boldsymbol{r}_k = x_k\hat{\mathbf{x}} + y_k\hat{\mathbf{y}} + z_k\hat{\mathbf{z}}$ is the position of the null point, δ_r is a small radius about the null (typically 2.5×10^{-2}). Using the remaining eigenvectors, together with the ratio of the eigenvalues corresponding to the fan surface,

$$\delta_\lambda = \frac{\lambda_y}{\lambda_z}, \tag{2.7}$$

the start points for field lines in the fan surface are then calculated using,

$$\boldsymbol{f}_2 = \boldsymbol{r}_k \pm \delta_\lambda \delta_r \boldsymbol{v}_2, \tag{2.8}$$

and,

$$\boldsymbol{f}_3 = \boldsymbol{r}_k \pm \delta_\lambda^{-1} \delta_r \boldsymbol{v}_3. \tag{2.9}$$

These four initial points in the fan surface form the semi-major and semi-minor axis of an ellipse about the null. The separatrix surface is then populated with trajectories by spacing start point along this ellipse. A fourth-order Runge-Kutta method is then used to integrate along the length of the field lines in the separatrix surfaces, until they reach a source or one of the bounding surfaces of the volume.

2.2.3 Finding Magnetic Separators

The next step is to find the magnetic separators within the topology. First, each of the trajectories in the fan surfaces are scanned for adjacent field lines which diverge significantly from one another. Suppose there are two adjacent field lines, $\boldsymbol{P}$ and $\boldsymbol{Q}$. For each point, i, along each line take the difference,

$$\boldsymbol{m} = \boldsymbol{P}_i - \boldsymbol{Q}_i, \tag{2.10}$$

where the vector $\boldsymbol{m}$ then gives the difference in position between the two points. The distance, d, between them is found by,

$$d = \left(m_x^2 + m_y^2 + m_z^2\right)^{\frac{1}{2}}, \tag{2.11}$$

where m_x, m_y and m_z are the x, y and z co-ordinates respectively. If $d > d_{crit}$ (typically $d_{crit} = 0.2$), the midpoint, $\boldsymbol{M}_i$, between the two field lines is then found from,

$$\boldsymbol{M}_0 = \frac{1}{2}\left(\boldsymbol{P}_i + \boldsymbol{Q}_i\right). \tag{2.12}$$

A field line is then calculated from the point $\boldsymbol{M}_0$, where the end point of the line, $\boldsymbol{M}_n$, is then compared to the end points of the field lines $\boldsymbol{P}$ and $\boldsymbol{Q}$. The nearest

field line is then replaced by the new field line, $\boldsymbol{M}$, and the process is repeated until one of two conditions are met.

The first condition requires a midpoint field line to pass within some small radius δ_r of a null point (typically $\delta_r = 0.025$). When this occurs, the midpoints and associated field lines are then traced backwards, using an average of the field lines calculated. This field line is then stored as a separator. The alternative condition is that the process has gone through more than a critical number of cycles. In this event, the search for a separator is abandoned, assuming that the region of the fan surface is simply sparsely populated due to the configuration of the eigenvalues of the null point. This issue is further discussed in section 2.2.4.

2.2.4 Flaws in the Model

While the assumptions of MCT are sound for the scenario considered, some issues arise. Under certain configurations, the field lines of a separatrix surface may not spread to cover the surface evenly. Using an elliptical ring of starting points reduces this, but when $\lambda_2 \gg \lambda_3$ the field lines become bunched in the direction of $\boldsymbol{v}_2$ and cover less of the separatrix surface. A solution may be found by increasing the number of field lines calculated within the fan surface. However, whilst improving the image provided of the surface in previously 'bare' areas, many of the additional field lines cluster together making the surfaces less transparent. Alternatively, many field lines could be generated, and the surface the scanned to find if the field lines are too packed together. In this case, selective rejection of field lines could be performed to remove the nearest neighbours and reduce the bunching. In cases where this issue presents, efforts have been made to find a balance between the two extremes.

Previously, the ability of a potential field to represent the topology of a force-free field has been disputed (Hudson & Wheatland 1999). One of the main problems for solving linear force-free fields is that the length scales for which the solutions hold

decreases as α (see equation 1.43) increases (Gary 1989). It was later concluded that, provided one is close enough to the sources being considered, potential fields are topologically comparative to their force-free counterparts (Brown & Priest 2000).

2.3 Modelling Continuously Distributed Magnetic Sources

Magnetic sources at the photosphere are not observed as discrete points, but rather are continuously distributed across an area. It may not always be appropriate to assume a source to be a discrete point, such as the large concentrations observed in an active region.

In the continuous source model, each source is in the photospheric plane, $z = 0$, with flux distributed across each shape. Though continuous sources of flux may be defined upon any of the bounding surfaces of the volume.

Unlike the point source model, the solution for a magnetic field in the continuous source regime is not analytic. Instead, the magnetic field must be calculated by numerically solving Poisson's equation across the volume. Equation 1.48 describes the magnetic field in terms of a scalar potential. To determine the scalar potential, first consider the parabolic equation,

$$\nabla^2 \psi = \frac{\partial \psi}{\partial t}. \tag{2.13}$$

If the boundary conditions remain constant and the divergence theorem (equation 1.4) holds for the volume, then $\partial\psi/\partial t \to 0$ as $t \to \infty$. This gives an eliptical equation where the scalar potential is satisfied by,

$$\nabla^2 \psi = 0, \tag{2.14}$$

which is known as Poisson's equation. This means that the elliptical, partial differential equation, can be solved as a parabolic equation when the boundary conditions

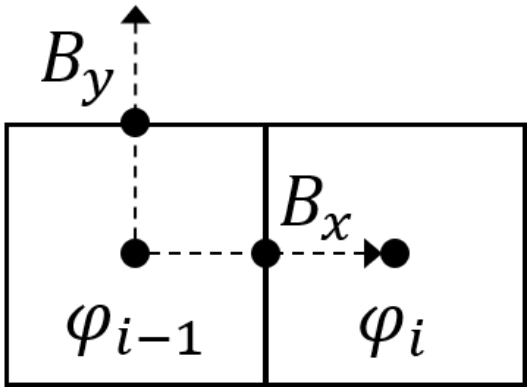

Figure 2.1: Figure of neighbouring grid cells in the magnetic field. At the centre of each cell is a scalar potential, ψ_i.

remain constant since the elliptic solution is approached as $t \to \infty$, though this can be terminated once the field has relaxed to some numerically deep level.

An alternating direction-implicit (ADI) method (Morton & Mayers 2005) is then employed to solve Poisson's equation in each of the axes across the grid. The three-dimensional volume is thus considered in a series of one-dimensional layers consisting of grid squares (figure 2.1). If each cell has a width δ, this provides the scalar potentials, ψ_i, ψ_j and ψ_k throughout the volume, at the centre of each grid cell such that the magnetic field is defined on the face of each grid cell by,

$$\mathbf{B}_x = \frac{\partial \psi}{\partial x} = \frac{\psi_i - \psi_{i-1}}{\delta_x},$$
$$\mathbf{B}_y = \frac{\partial \psi}{\partial y} = \frac{\psi_j - \psi_{j-1}}{\delta_y},$$
$$\mathbf{B}_z = \frac{\partial \psi}{\partial z} = \frac{\psi_k - \psi_{k-1}}{\delta_z}.$$

2.3.1 Boundary Conditions

In order to preserve the divergence theorem (equation 1.4), the flux entering and leaving the numerical volume must be balanced. As the cases presented in this chapter arise from unbalanced configurations of magnetic sources, boundary conditions are configured to allow flux to enter or leave the volume, thus able to reach an

assumed balancing source outside the box. This is described by,

$$\int_s \mathbf{B} \,.\, \hat{\mathbf{n}}\, ds = \int_v \nabla^2 \psi \, dv, \tag{2.15}$$

where s is the closed surface that bounds the volume v, $\mathbf{B}$ has been prescribed and $\hat{\mathbf{n}}$ is a unit vector normal to the surface. However, we also have that $\nabla^2 \psi = 0$ from Poisson's equation (equation 2.14), such that equation 2.15 becomes,

$$\int_s \mathbf{B} \,.\, \hat{\mathbf{n}}\, ds = 0. \tag{2.16}$$

The boundary conditions used in this thesis belong to several cases. When discussing each case, it is assumed that the prescribed flux has been distributed only across the $z = 0$ surface and that the rest are scaled such that equation 2.16 holds in each case.

The first such case is when the flux is assumed to be contained in a closed system within the volume. Here, the sum of the flux on the plane is equal to zero. Thus, the accompanying five surfaces need no flux to be distributed across them, so each of their grid cells is given a value of 0.

Alternatively, the flux in the plane may be unbalanced. Here, the normal field for each point on the bounding surfaces is estimated using the analytical expression of the magnetic field (equation 2.1), where each value on the $z = 0$ boundary assumed to be a point source. This is then scaled to ensure that the flux that enters or leaves through the other five boundaries is balanced with that on the $z = 0$ plane.

Finally, when the flux in the plane is unbalanced, the balancing flux may be distributed across just one of the other surfaces. This approach is often adopted when calculating the Q-map of a configuration (section 3.4). Here, the balancing flux is distributed across the upper plane ($z = n$) of the volume in one of two methods. The first method divides the balancing flux across the entire surface, such that it is uniformly distributed across the entire area. The alternate method defines a circular source of flux with a large radius, placed in the upper plane and centred on the origin.

2.3.2 Continuous Source Flux Distribution

Continuously distributed sources are defined for a number of different source shapes. One commonly used source shape is the circular source where the flux is distributed by,

$$F_{circ} = \begin{cases} \epsilon \left(\cos\left(\frac{\pi r_n}{r}\right) + 1 \right), & \text{if } r_n \leq r, \\ 0, & \text{if } r_n > r, \end{cases} \tag{2.17}$$

where r_n is the radius of a point from the source centre, ϵ is the peak flux value in arbitrary units, and r is the total radius of the source. This distributes the flux such that its peak is at the centre of the source, it drops off as a function of cosine with radius r and the distribution is smooth (figure 2.2a). Hence, when $r_n = 0$, $F_{circ} = 2\epsilon$ and when $r_n = r$, $F_{circ} = 0$ such that F_{circ} is continuous and the derivative of F_{circ} is continuous everywhere.

Another source shape which is used in this thesis is the cigar source. Here, two points are chosen, p_1 and p_2, as the start and end points of the cigar respectively, which is then formed from a line connecting the two points. The co-ordinates of the points p_1 and p_2 are then (x_1, y_1) and (x_2, y_2) respectively. The flux distribution is defined by the set of equations,

$$A = \frac{x_n w_x + y_n w_y}{(w_x^2 + w_y^2)^{\frac{1}{2}}}, \tag{2.18}$$

$$B = (x_n^2 + y_n^2 - A^2)^{\frac{1}{2}}, \tag{2.19}$$

and,

$$F_{bar} = \begin{cases} \epsilon \left(\cos\left(\frac{\pi B}{r}\right) + 1 \right), & \text{if } B \leq r, \text{ and } 0 < A < (w_x^2 + w_y^2)^{\frac{1}{2}}, \\ 0, & \text{elsewhere,} \end{cases} \tag{2.20}$$

where $w_x = x_2 - x_1$ and $w_y = y_2 - y_1$, giving the length of the bar in the x and y directions respectively, while x_n and y_n give the distance along the cigar in the x and

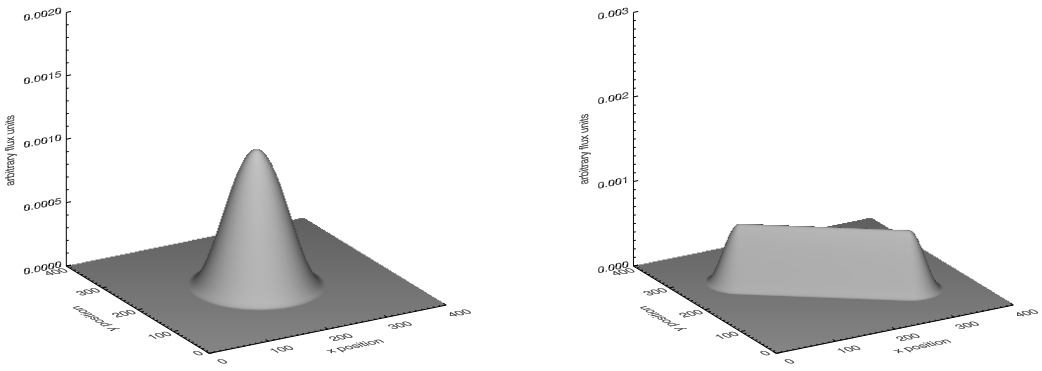

(a) (b)

Figure 2.2: Surface plots of the flux distribution for a) the circular source and b) the cigar source.

y directions respectively, by treating p_1 as the origin (0,0). The parameter r is the 'radius' of the cigar's bar about its centre-line. Together these equations distribute the flux such that it peaks along the centre-line of the cigar, reducing as a function of cosine (figure 2.2b). The rounded edges at the endpoints are added using the distribution profile of the circular source, but with the altered criteria given by,

$$F_{ends} = \begin{cases} \epsilon \cos\left(\dfrac{\pi r_n}{r}\right) + 1, & \text{if } r_n \leq r, \text{and either } A \leq 0 \text{ or } A \geq (w_x^2 + w_y^2)^{\frac{1}{2}}, \\ 0, & \text{if } r_n > r, \end{cases} \tag{2.21}$$

where the parameters r, w_x and w_y are as defined for equation 2.20.

2.4 Hexagonal Case Study

2.4.1 Point Source Setup

The following simulations consist of eight point sources placed in the $z = 0$ plane, at the positions given in table 2.1. Six of these sources (S1 - S6) form a roughly

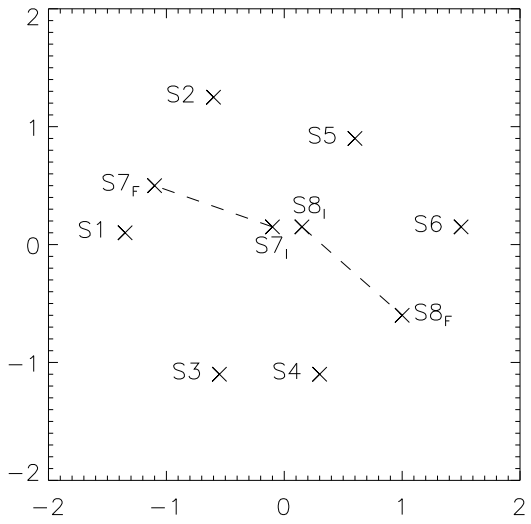

Figure 2.3: Figure showing the initial and final configurations of the magnetic sources, with the path of the internal sources indicated by the dashed line. For discrete sources, these coordinates are the exact source positions. For the continuous source cases, these positions give the centre points of the circular sources.

hexagonal pattern to represent a super-granular cell boundary (figure 2.3). The other two sources (S7 and S8) are placed internal to this boundary and are moved outwards, towards the boundary through a series of static equilibria to simulate the situation shortly after flux emergence. A variety of paths were used for the progression of the interior sources, however, it has been found that the choice of path does not introduce any significant alternative topological structures to those that are presented here. Whilst the parameter values at which bifurcations occurred and the creation of null points changed, the types of bifurcations and nulls found remained the same. For the purpose of these simulations, all sources used have a strength $\varepsilon = \pm 0.5$. The region modelled in these cases typically spans to ± 2 in the x and y directions, and from 0 to 2 in the z direction. However, these lengths are dimensionless and can be scaled to whichever real length is required.

Boundary Discrete-Source Parameters			
Source	**x**	**y**	**ϵ**
S1	-1.35	0.10	-0.50
S2	-0.60	1.25	-0.50
S3	-0.55	-1.10	-0.50
S4	0.30	-1.10	-0.50
S5	0.60	0.90	-0.50
S6	1.50	0.15	-0.50
S1′	-1.35	0.10	0.50
S2′	-0.60	1.25	0.50
Internal Discrete-Source Parameters			
Source	**x**	**y**	**ϵ**
$S7_I$	-0.10	0.15	0.50
$S7_F$	-1.10	0.50	0.50
$S8_I$	0.15	-0.15	0.50
$S8_F$	1.00	-0.60	0.50
$S7'_I$	-0.10	0.15	-0.50
$S7'_F$	-1.10	0.50	-0.50

Table 2.1: Table containing the parameters for the configuration of the discrete sources used for the hexagonal case study. S′ represents sources which are identical, save for the sign of their associated flux. S_I and S_F represent the initial and final positions of the internal sources respectively. Only one of S or S′ is present in each of the cases considered. The x and y columns represent the coordinate where the source is placed, while ϵ is used to represent the flux prescribed to the source.

2.4.2 Continuous Source Setup

Whilst topologies produced from point sources of magnetic flux are computationally cheap, they may not provide a complete picture of the magnetic skeleton for a topology. However, numerically solving Poisson's equation (equation 2.14) requires additional computer resources, which over many iterations may significantly increase the duration of a simulation.

The continuous source models presented in the case studies use the same coordinates as the point source cases for prescribing the source positions (table 2.1). The circular sources of flux used to recreate the discrete models are centred on these coordinates, with flux distributed in a radius of $r = 0.15$ about these points.

2.5 Case Study: Three Coronal Null Points

This pair of models considers an arguably artificial case. Here, each of the sources which form the hexagonal boundary are negative, but the two sources of flux placed centrally in the cell interior are positive. However, typical magnetic elements which emerge in the centre of a supergranular cell are bipolar.

2.5.1 Point Source Model

The initial configuration places the six negatively charged boundary sources (S1 - S6) on the $z = 0$ plane, surrounding two internal positive sources (S7 and S8). This creates seven null points in the photospheric plane, and a single coronal null point which sits above the centre of the configuration (figures 2.4a, 2.5a). The coronal null point's (CN1) fan plane extends down towards the photosphere, creating a dome that encompasses the two positive sources (S7 and S8), where its footpoints connect to the negative sources (S1 - S6). Six of the planar nulls have spines which connect to negative sources and sit towards the boundary of the configuration. The fans of

each of these null points form separatrix walls, which intersect the dome produced by the coronal null point, providing locations for six separator field lines. However, one planar null (N5), which exists in the region between the two central positive sources, has one spine field line terminate at each of the positive sources. The fan of this null extends towards the height of the coronal null but is bound within the coronal dome. Thus, the central null has a fan which forms a dome internal to the coronal dome structure. This pairing is analogous to the enclosed state found by Brown & Priest (1999), but is found here in a coronal context. One consequence of this is that the fan surface of any null point which exists between two sources at which the separatrix dome has footpoints, intersects both the separatrix dome and the coronal dome. Three nulls are positioned such that their fan surfaces behave in this way. Thus, the topology has a total of nine separator field lines.

The separation between the coronal dome and the enclosed dome has been emphasised in figures 2.6a and 2.6b. Here, the central sources have been unbalanced so that S7 has $\epsilon = 0.4$ and S8 has $\epsilon = 0.6$. This unbalancing reduces the height to which the enclosed dome extends, such that the field lines generated about the null point have a clearer coverage of the shape of the surface. Figure 2.6b also provides a clearer view of the separator network.

As the positive sources are moved closer to the boundary sources, the coronal null (CN1) begins to move close to the boundary too, in a similar direction to the positive source S8 (figure 2.4b). This causes some of the separators to begin to bunch up, until they become tightly pinched together. A turning point bifurcation then occurs in the coronal volume, producing two new coronal nulls CN2 and CN3 (figures 2.5b, 2.7). One of the new nulls, CN2, forms a second coronal dome, connecting to sources S1, S2, S3 and S5, with one spine field line connecting down to the positive source S7, and the other extending to the top of the coronal volume. The spine field lines of this coronal null, together with those of the original coronal null (CN1), now bound

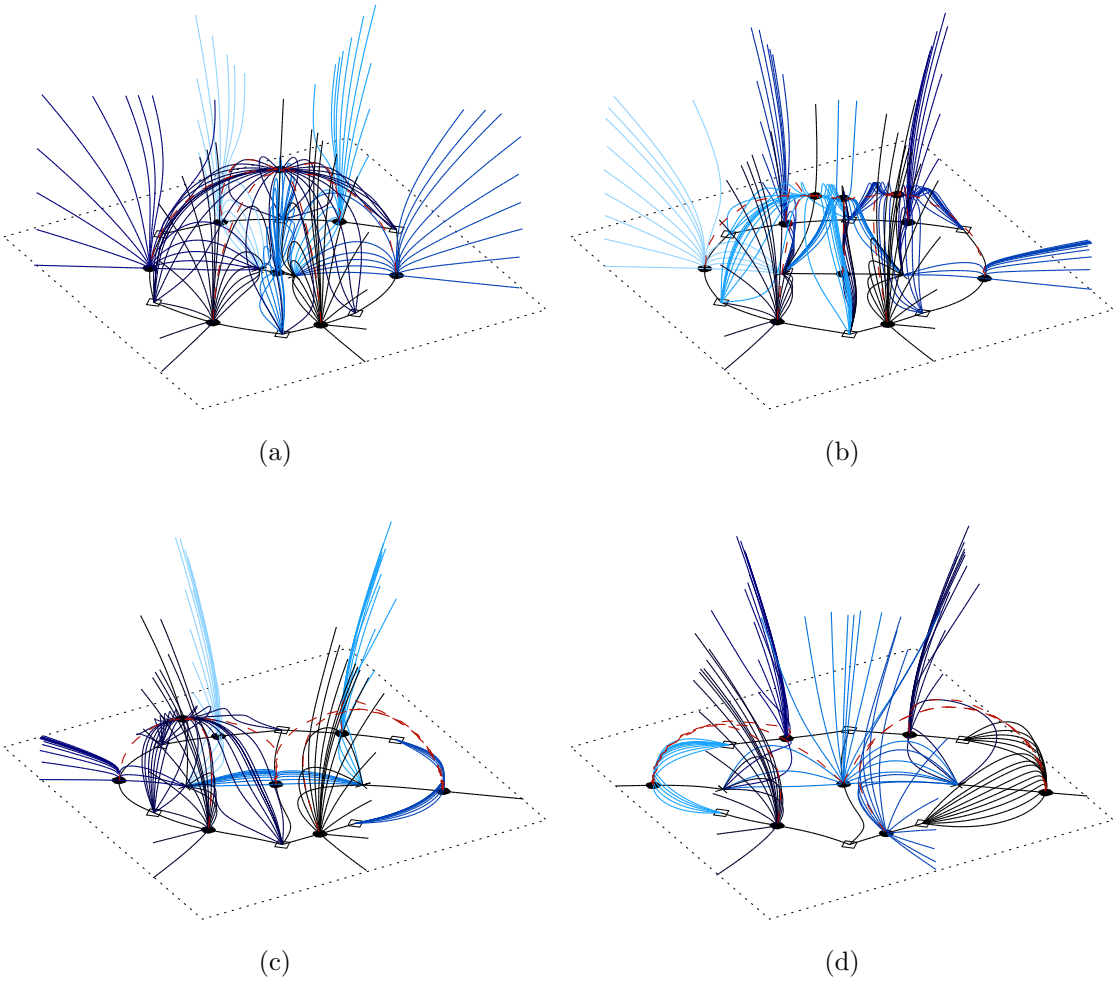

Figure 2.4: Different topological states which arise from the source configuration of the three coronal null points case. Null points are solid black circles, diamonds represent negative sources, and crosses represent positive sources. Black lines are used for the spines of null points, whilst field lines which exist in the fan surface of a null are coloured unique to each null point present. Magnetic separators are given by red-dashed lines.

the fan surface of the central coronal null (CN3), which radiates out to the boundary of the volume, and down to the two positive sources (S7 and S8) in the photospheric plane. The spine field lines of the central coronal null, CN3, reach down to the photosphere, connecting at sources S3 and S5, bounding the fan surface generated

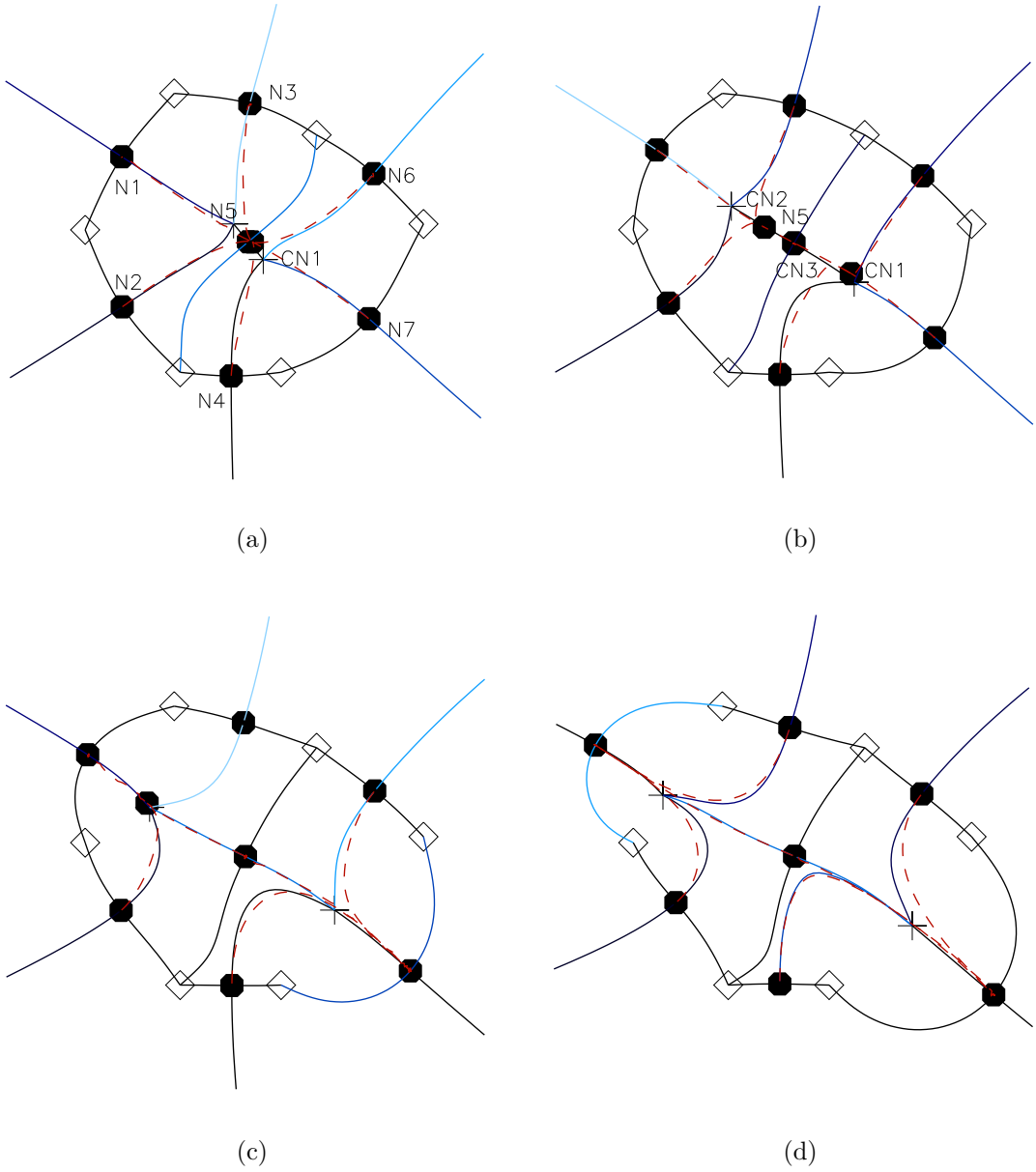

(a) (b)

(c) (d)

Figure 2.5: States of the magnetic skeleton in the $z = 0$ plane, arising from the source configuration used in the three coronal null points case. Null points have been labelled as 'N' and coronal nulls labelled as 'CN'.

from the central planar null N5, which now forms a separatrix wall. Each of the coronal domes is now intersected by four separatrix walls, and the two central fan surfaces, of N5 and CN3, also intersect in a separator field line. Hence, the coronal

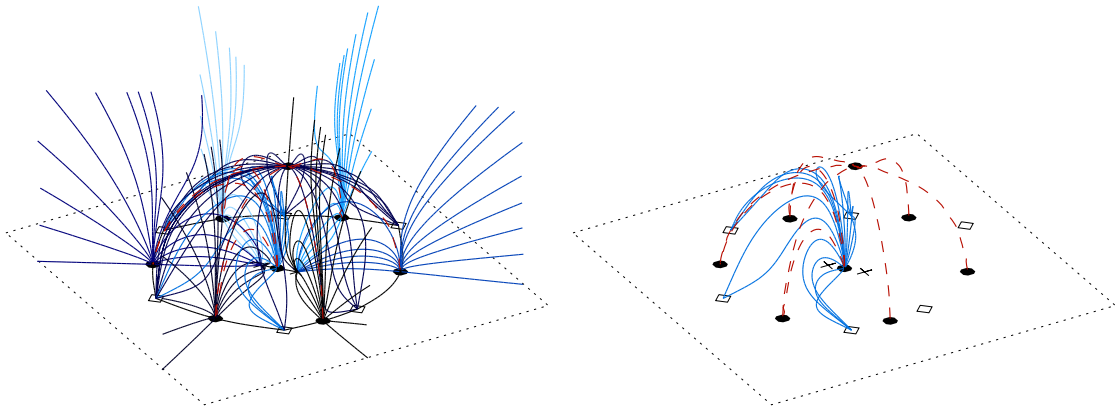

(a) (b)

Figure 2.6: The sources S7 and S8 from the three coronal null points case, have been modified here such that the pair no longer have equal amounts of flux passing through them. This emphasises the dome structure produced by the null which sits between the two central sources.

turning-point bifurcation has not introduced any additional magnetic separators into the topology, where the total remains at nine. This new structure is now analogous to the touching state presented by Brown & Priest (1999). Here, the two coronal domes meet at the spine of the central coronal null CN3, and the fan of the central planar null N5, forming an example of a coronal touching-state. This topology is also qualitatively similar to the 'open separatrix surface' case (Platten et al. 2014; Priest 2014). However, in the open separatrix surface case, the spines of the coronal nulls CN1 and CN2 only act as bounds on the open surface. In this case, they also bound the separatrix surfaces of two planar nulls, which further divide the volume into additional domains of connectivity, such that the 'open' separatrix surface is actually 'closed' in this case. The open separatrix surface case is explored further in section 3.8.

The height of the coronal nulls above the $z = 0$ plane then begins to decrease as the sources are moved further towards the boundary (figures 2.4c, 2.5c). Whilst

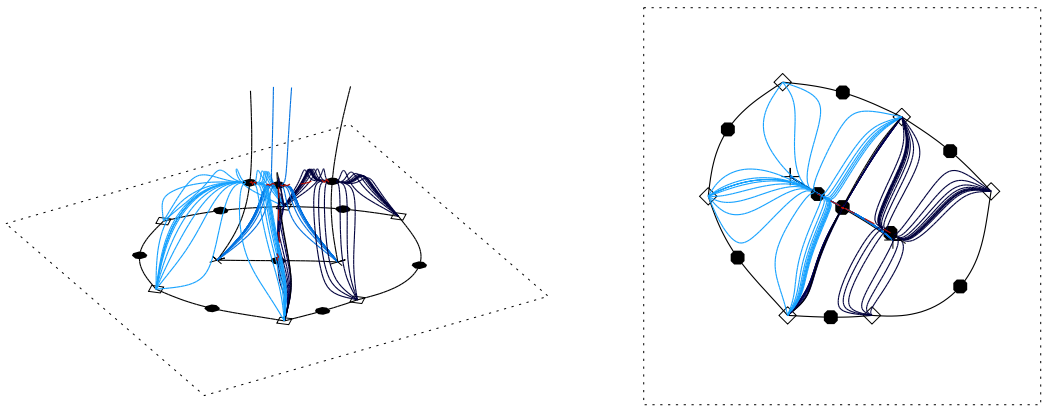

(a) (b)

Figure 2.7: Only the separatrix surfaces of the coronal nulls and the planar null N5 are displayed from the three coronal null points case, a) with a view of the topological structure and b) a projection of the skeleton onto the $z = 0$ plane.

the spines of the coronal nulls CN1 and CN2 begin to recede away from the centre, the fan wall of CN3 spreads to cover a larger area, but remains bounded. The three coronal nulls now undergo a series of pitchfork bifurcations with planar null points. First, CN1 coalesces with the planar null N7 (and a mirror coronal null in the $z < 0$ volume), through a pitchfork bifurcation, now forming a separatrix dome intersected by three separatrix walls. A separator field line which connected CN1 and N7 is also eliminated through this process. Next, a pitchfork bifurcation eliminates the central coronal null CN3 as it coalesces with N5, again removing the separator which connected them. The separatrix wall of the central null now has footpoints connecting to both positive sources (S7 and S8), where before they connected to the negative sources S3 and S5. Finally, the third coronal null, CN2, is also eliminated through a pitchfork bifurcation, the resulting topology mimicking that produced on the other side of the configuration.

Both the separatrix domes are intersected by three separatrix walls, for a total

of six separator field lines, where each null point in the topology is connected to at least one other null (figures 2.4d, 2.5d). Brown & Priest (1999) presented a double-intersected state which arises from four point-sources of flux in a potential field. The final state found under this eight-source configuration is similar to the double-intersected state, thus is referred to as the separate three-separator-state.

2.5.2 Continuous Source Model

In this model, the continuous sources have been placed in the same position as the positive sources used in the previous section (2.5.1). This initial topology (figure 2.8a) has an immediate difference to its point source counterpart. In the point source case, a null point is located between the two central positive sources. However, in the continuous source regime, these two sources overlap one another, resulting in the distribution of magnetic flux across the region where the null point was previously located. Thus, the criteria for a null point no longer hold. The absence of this central planar null reduces the number of separator field lines by three, as the internal dome shown by figure 2.6 is no longer present. Otherwise, the topology matches that found in the point source case.

As the central sources are moved towards the boundary, the central positive sources no longer overlap one another, so the planar null point between the pair is now located (figure 2.9). The fan of this null point produces a separatrix dome, enclosed within the coronal dome, which is qualitatively the same as found previously in the point source case (figure 2.6). Now, the components which make up the magnetic skeleton of this topology are identical to those in the point source case shown in figure 2.4b. This is followed by a turning point bifurcation in the coronal volume, creating two new coronal null points as shown in figure 2.8b, which is qualitatively similar behaviour to that found in the point source case.

As the sources are moved further apart, towards the boundary, the bifurcation

behaviour of the system qualitatively mimics that found in the point source case. First, a pitchfork bifurcation takes place as the central coronal null coalesces with the central planar null (figure 2.8c), annihilating the coronal null and leaving a single planar null. This is followed by the two remaining coronal null points coalescing with nulls on the boundary, where they are annihilated through a pitchfork bifurcation, again leaving a null point in the plane (figure 2.8d).

2.5.3 Discussion

Both regimes found that the initial configuration had a single coronal null point. After a turning point bifurcation takes place in the coronal volume, there are then three coronal null points present. When the system has this topological state (figures 2.4b, 2.8b), it closely resembles a topology presented by Priest (2014) which has a central 'open separatrix surface'. However, in this case, the 'open separatrix surface' is closed. This is because the fan surfaces, belonging to the planar nulls that are located between the boundary sources, meet at the spine field lines which form a bound on the surface. The open separatrix surface is further explored in section 3.8.

This case study has highlighted the similarities between the continuous and point source models. In fact, the point source model is an appropriate approximation of the continuous source case, except for when continuous sources overlap. The remaining case studies discussed in this chapter will not present an entire continuous source model alongside the point source models. Instead, comparisons will simply be made between the two cases.

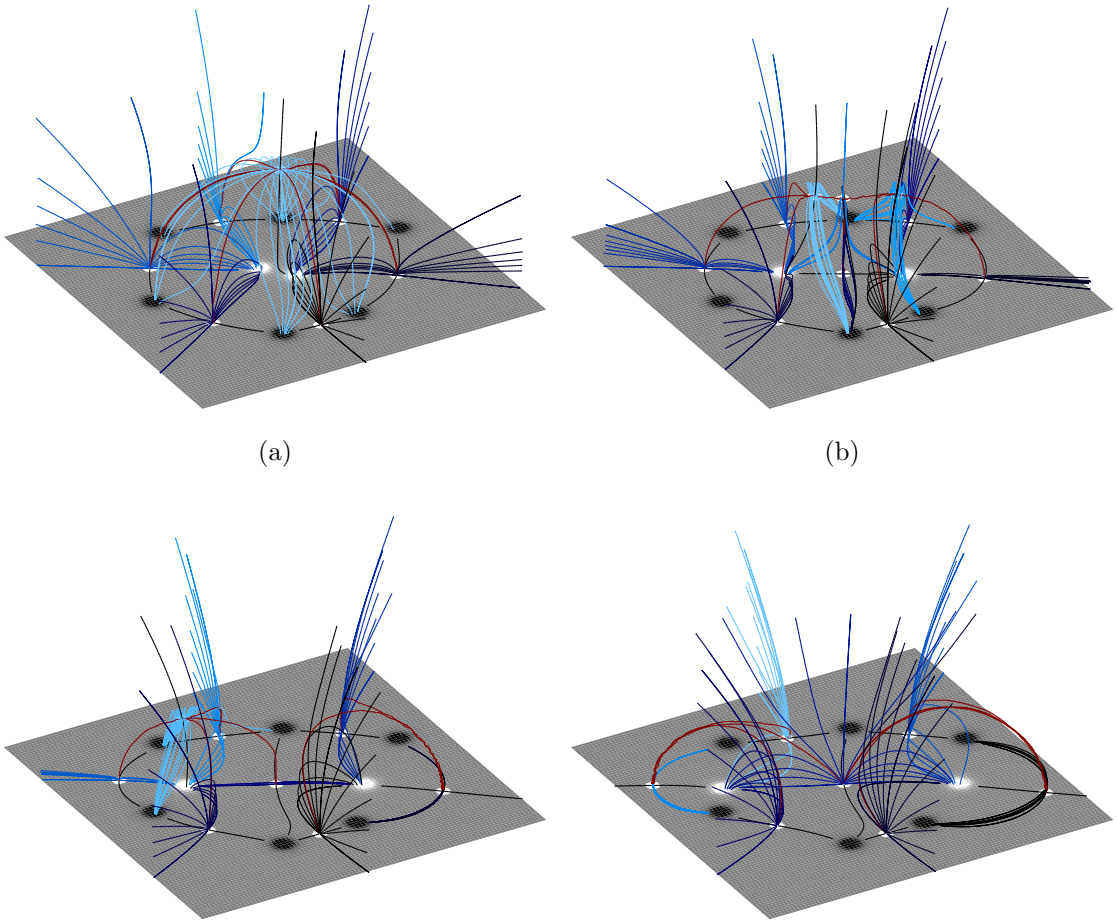

(a) (b)

(c) (d)

Figure 2.8: Different topological states which arise from using source configuration from the three coronal null points case. Null points are solid white circles, and regions where positive (negative) flux is passing through the $z = 0$ surface are represented as white (black) diffuse regions. Black lines are used for the spines of null points, whilst field lines which exist in the fan surface of a null are coloured unique to each null point present. Magnetic separators are given by red lines.

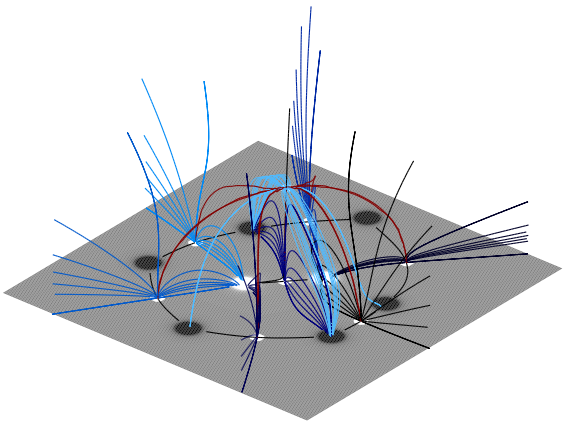

Figure 2.9: Figure showing the null point between the two central positive sources, and the separatrix dome produced by its fan surface for the three coronal null points case.

2.6 Case Study: Bipole Emergence with Six Negative Boundary Sources

The following scenarios are an approximation of the standard flux emergence case. Here, a pair of opposite polarity sources is emerged within the cell interior. Whilst typically, magnetic elements moving towards a cell boundary will fragment during their journey, the sources used here remain 'whole' throughout.

2.6.1 Point Source Case

This configuration uses only the negative sources, S1 - S6, as the boundary sources. The internal sources used are the negative S7′ and the positive S8. This starting configuration has a topology with a single coronal null, CN1, and seven planar nulls (figures 2.10a, 2.11a). The fan surface of the coronal null CN1 creates a coronal dome with footpoints at sources S1, S3 - S6 and S7′, while the spine field lines project down to the source S8 and out to infinity. This dome is then intersected by the fan planes of planar nulls N1, N2, N4 - N7, where six separator field lines are

defined, and each of these fans is bounded by the spine field lines of CN1. Each of the planar nulls is prone, with spine field lines terminating at negative sources. The fan surface of the null N3 is the only one not to intersect the coronal dome of CN1. Instead, its fan surface is analogous to that found in the detached state, such that the source S2 only has connectivity with the balancing source at infinity. Overall, the topology resembles a single detached state, with a multiply-intersected coronal dome, consisting of seven prone-planar nulls, a single coronal null and six separators.

The first bifurcation observed as sources S7′ and S8 are repositioned is a spine-fan bifurcation (figures 2.10b, 2.11b, 2.12). Here, the fan of null N2 slips past the spine of null N1, such that source S1 is no longer connected to source S8, producing a second detached state. This consequently removes a location for a separator field line, reducing the total to five. However, another spine-fan bifurcation then occurs between the fan of null N3 and the spine of null N5. Now the fan from N3 also intersects with the coronal dome, allowing some connectivity between source S2 and S8. After both bifurcations occur, the number of components producing the magnetic skeleton remains the same, only the configuration has changed. Thus, there are still six separator field lines, in a topology consisting of a multiply-intersected coronal dome, and a single detached state.

As the sources are placed further apart, the coronal null CN1 drops in height until it is eliminated through a pitchfork bifurcation with the planar null N7 (figures 2.10c, 2.11c, 2.13). The separator which previously connected the two is eliminated, and the fan surface of the null now forms a separatrix dome, with footpoints at each of the negative sources except S1. The walls which previously intersected the coronal dome now intersect the separatrix dome of N7, with separators connecting them to N7 rather than CN1. As only one separator has been eliminated, there are now five separators in the topology.

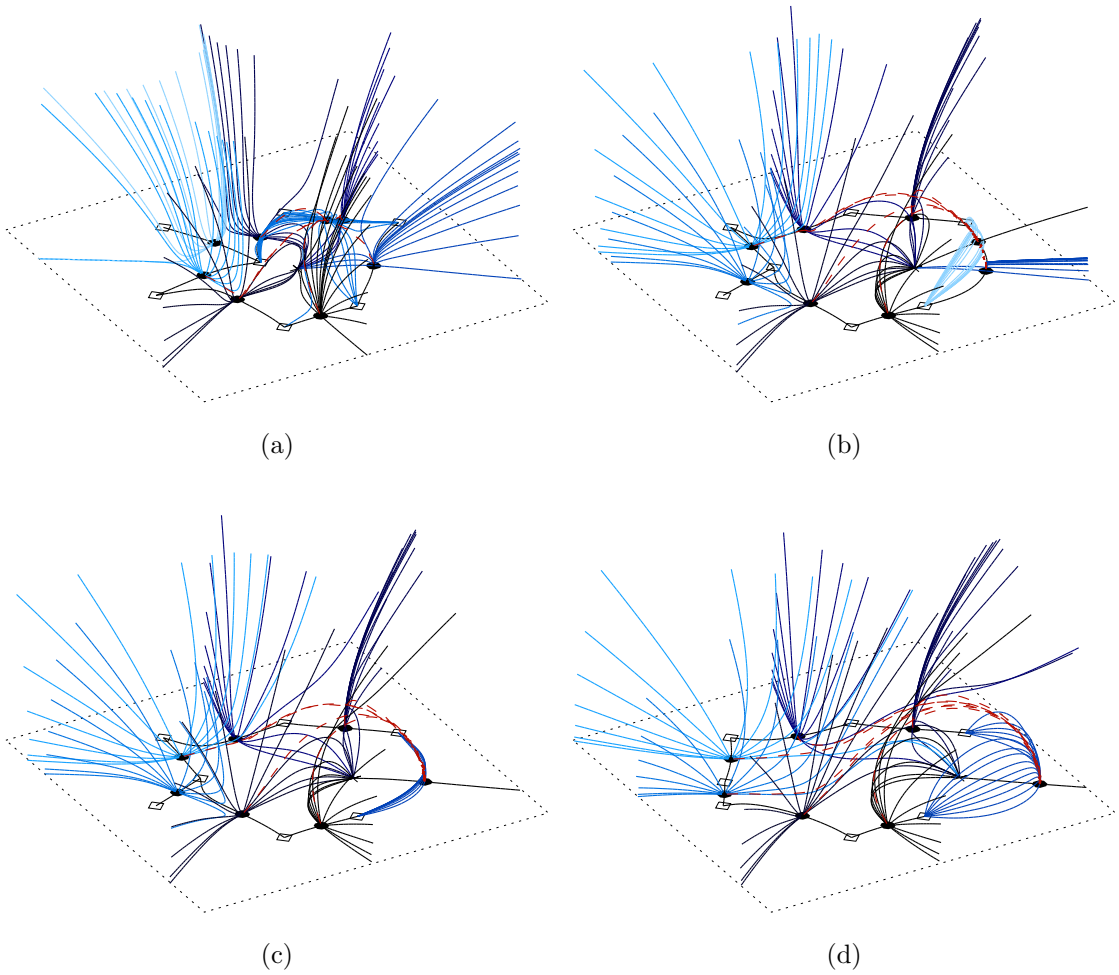

(a) (b)

(c) (d)

Figure 2.10: Different topological states which arise from using the six negative boundary source configuration. Null points are solid black circles, diamonds represent negative sources, and crosses represent positive sources. Black lines are used for the spines of null points, whilst field lines which exist in the fan surface of a null are coloured unique to each null point present. Magnetic separators are given by red-dashed lines.

The final bifurcation of this case is another spine-fan bifurcation (figures 2.10d, 2.11d, 2.14). Previously, the fan of null N2 flipped past the spine of null N1 in such a bifurcation. Now the two nulls have the same bifurcation process happen in reverse, as the fan of N2 again flips past N1's spine so that it intersects the separatrix dome

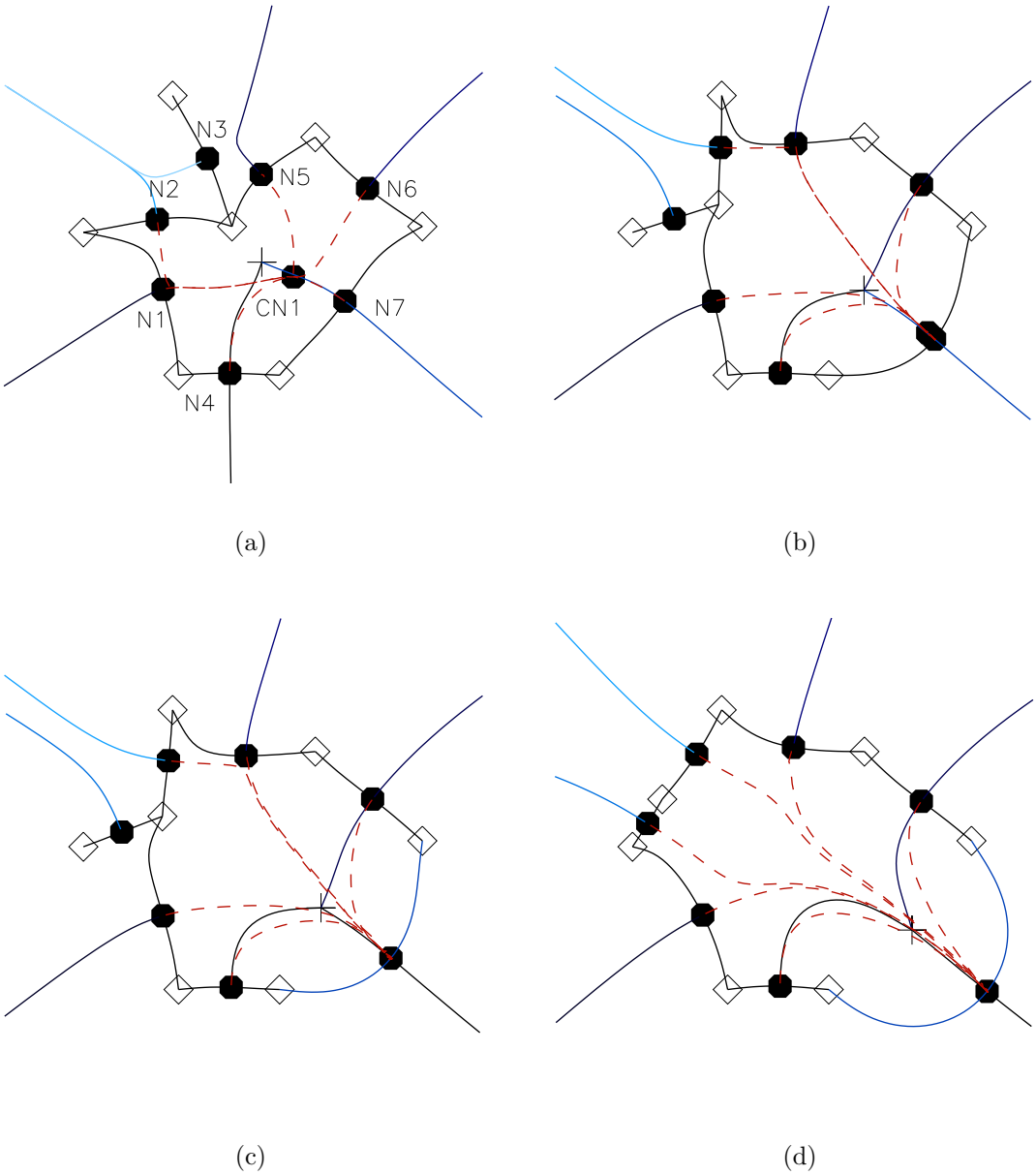

Figure 2.11: States of the magnetic skeleton in the $z = 0$ plane, arising from the six negative boundary source case. Null points have been labelled as 'N' and coronal nulls labelled as 'CN'.

of N7. This creates an additional separator, for a total of six in the topology. The final state is of a multiply-intersected dome, with seven prone planar nulls.

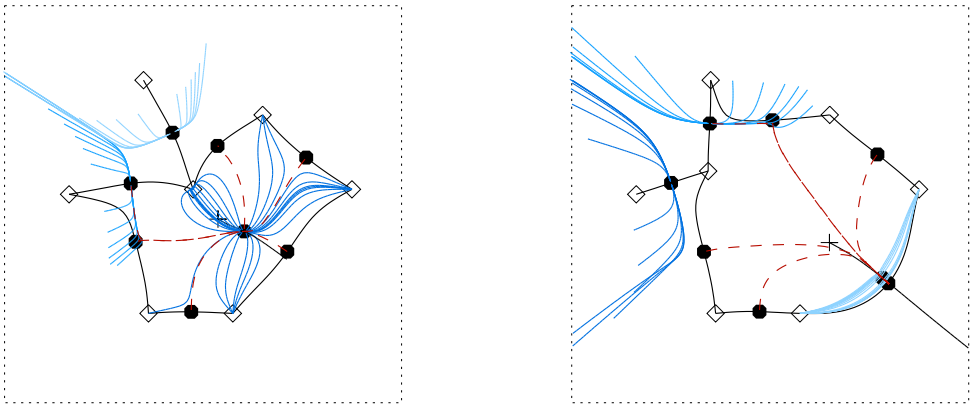

(a) (b)

Figure 2.12: A partial topology for the six negative boundary source case has been produced with only field lines in the surfaces of N2, N3 and CN1 displayed. a) Initially N2 shares a separator with CN1 while N3 does not. After a pair of spine-fan bifurcations, b) N2 no longer has shares a separator with CN1 and forms a detached state, where the fan surface of N3 now intersects the coronal dome, with a separator along the intersection.

2.6.2 Continuous Source Model

When the source configuration was applied to the continuous source regime, the bifurcation behaviour of the system was found to be qualitatively the same as in the point source model. Figure 2.15 shows the key states of the topology as the central sources are moved. The topology at the start of the scenario is shown in figure 2.15a, which matches the structure found in the point source case. Figure 2.15b shows the topology after the first spine-fan bifurcation occurs. Again, it is found that the coronal null point begins to drop in height until it eliminates with one of the planar nulls. The resultant topology is shown in figure 2.15c and the topology is shown in its final state in figure 2.15d.

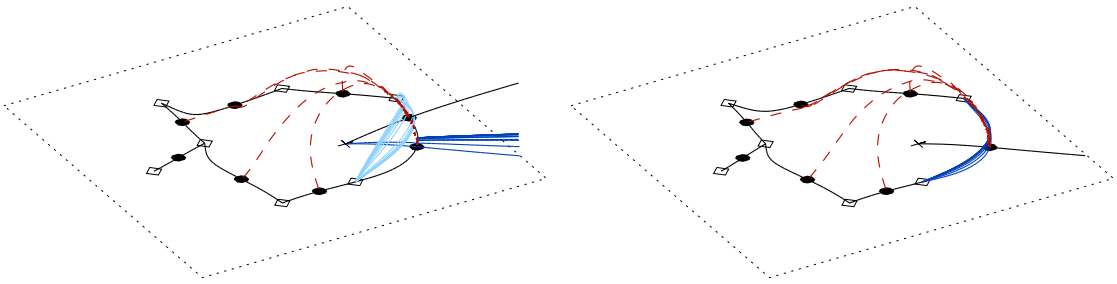

(a) (b)

Figure 2.13: Partial topological structure of the six negative boundary source case where only fan field lines of N7 and CN1 have been displayed. a) As the coronal null drops in height, b) it is eliminated through a pitchfork bifurcation with the planar null N7.

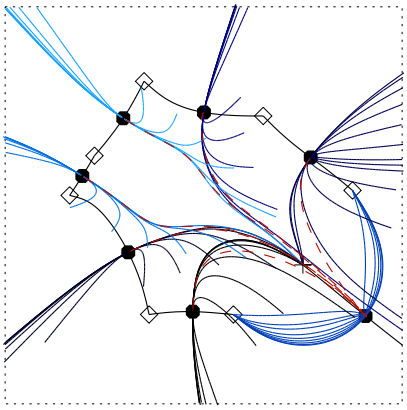

Figure 2.14: The final topological state of the six negative boundary source case, viewed from above.

2.6.3 Discussion

The cases explored here found that the topologies had only a single coronal null point present. These scenarios found that the bifurcations relating to the coronal null point where analogous to those found in the previous cases considered in section 2.5. The discrete source case here was found to be qualitatively similar to the continuous

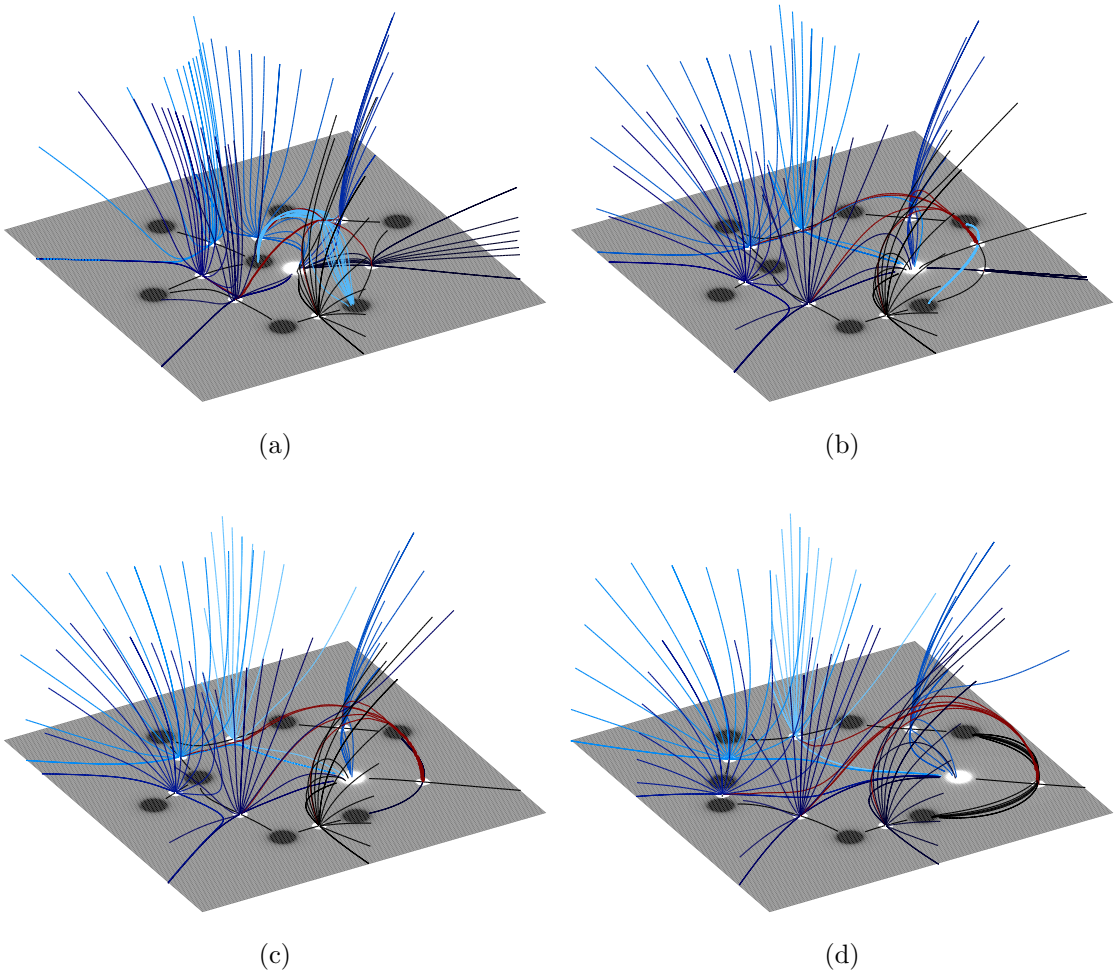

(a) (b)

(c) (d)

Figure 2.15: Different topological states which arise from using the six negative boundary source configuration, in the continuous source regime. Null points are solid white circles, negative sources are coloured in black, and positive sources are coloured white. Black lines are used for the spines of null points, whilst field lines which exist in the fan surface of a null are coloured unique to each null point present. Magnetic separators are given by solid red lines.

source case, except for when the central continuous sources overlapped one another.

2.7 Bipole Emergence with Five Negative and One Positive Boundary Sources

2.7.1 Point Source Model

This case studies a topology which starts out with seven planar null points and a single coronal null (figures 2.16a, 2.17a). They arise from a configuration of five negative sources (S2 - S6) and a single positive source (S1′) positioned as the boundary sources. Again, S7′ and S8 are placed in the hexagonal interior. The spine field lines of the coronal null CN1 extend vertically, one to the positive photospheric source and the other to infinity. The fan surface of the coronal null again forms a coronal dome, with footpoints at sources S3 - S6 and S7′. The fan surfaces of planar nulls N2 - N7 form separatrix walls, and those of nulls N2, N3, N5, N6 and N7 intersect the coronal dome producing five separators. The spines of each of these nulls each connect to a negative source, as do the spine field lines of the null N4. However, the fan of N4 cannot cross the spines of nulls N2 and N5, hence is deflected away to intersect with the separatrix dome produced by the fan of null N1. The walls of nulls N2 and N5 also intersect this surface, for a total of three separators along it. The dome produced by N1 has footpoints at sources S2, S3, S5 and S7′, again not projecting past the spines across the interior. Thus, the topology comprises a single multiply-intersected separatrix dome, separate to a multiply-intersected coronal dome (figure 2.16a), despite the two sharing footpoint sources. In total there are eight separator field lines in the topology.

The first type of bifurcation to occur is a spine-fan bifurcation (figures 2.16b, 2.17b). Here the spine of N4 flips through the fan of N5, changing its footpoints from S2-S5 to S2-S7′. The fan of N5 now reaches out to infinity, rather than into the surface of N1. Hence a separator is removed from the topology. However, as

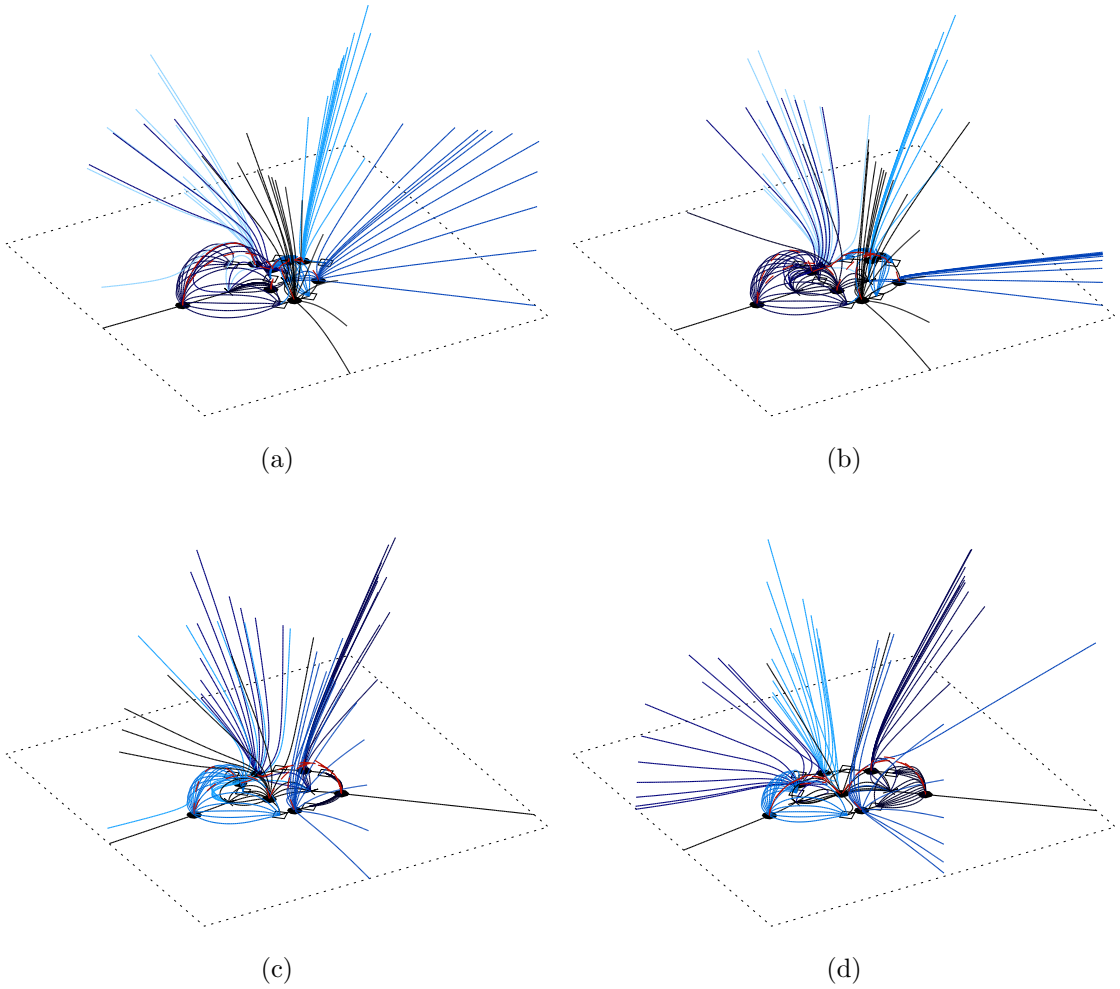

Figure 2.16: Different topological states which arise from using the five negative boundary source configuration. Null points are solid black circles, diamonds represent negative sources, and crosses represent positive sources. Black lines are used for the spines of null points, whilst field lines which exist in the fan surface of a null are coloured unique to each null point present. Magnetic separators are given by red-dashed lines.

the sources S7′ and S8 are repositioned further from one another, a second spine-fan bifurcation occurs between the same null pair. In contrast to the previous bifurcation, it is the spine of null N5 which now flips through the fan of null N4. The fan of null N4 now intersects the coronal dome produced by CN1, instead of

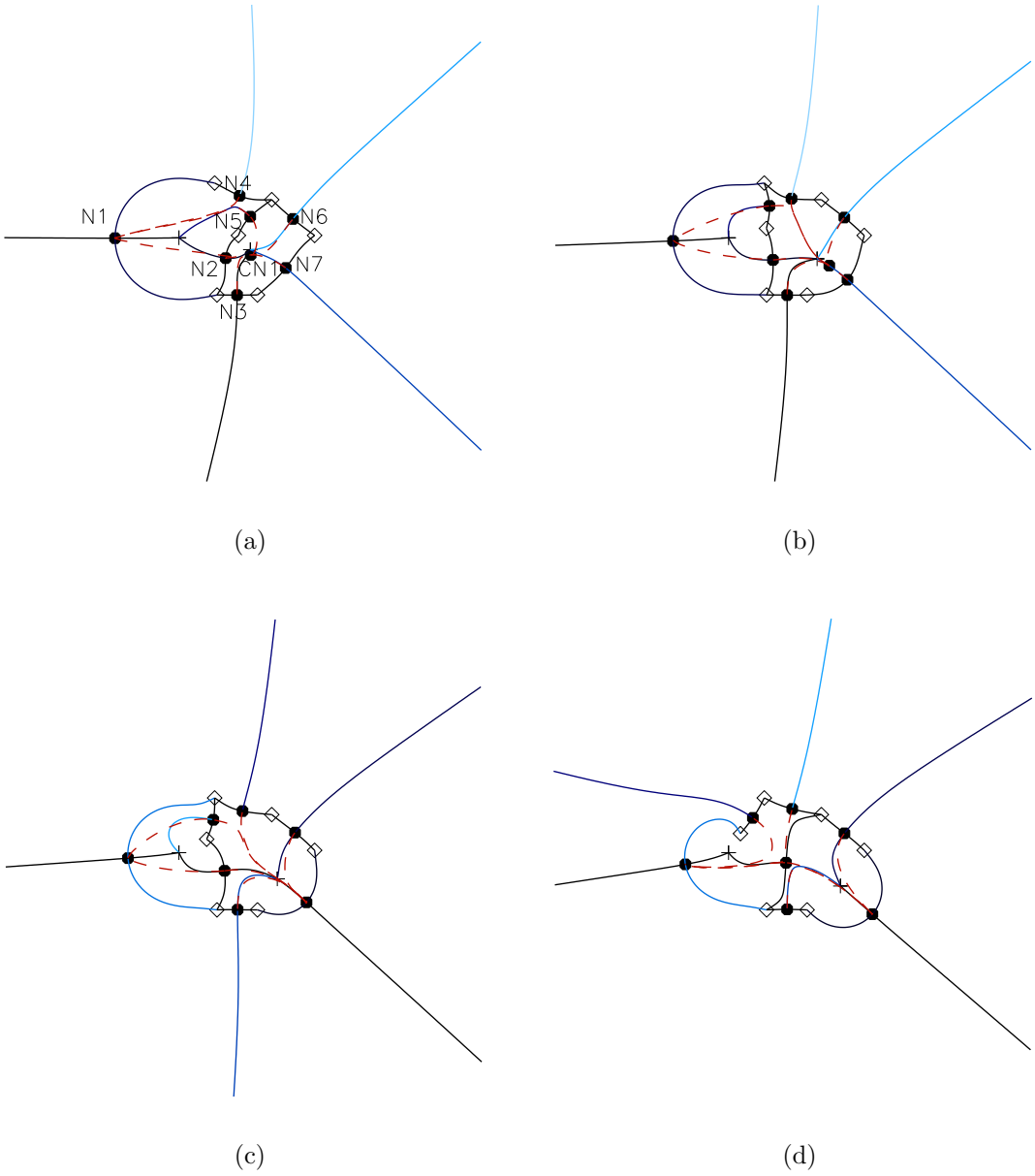

Figure 2.17: States of the magnetic skeleton in the $z = 0$ plane, arising from the five negative boundary source case. Null points have been labelled as 'N' and coronal nulls labelled as 'CN'.

extending out to the edge of the volume, adding an additional separator to the network, connecting N4 to CN1. Together, these processes have illustrated how a spine-fan bifurcation may both create and destroy a magnetic separator.

Next, the coronal null CN1 is destroyed through a pitchfork bifurcation with the null N7 (figures 2.16c, 2.17c). As in the previous case, this eliminates the separator connecting the two, and the null left in the plane forms a separatrix dome. This dome is intersected by each of the walls which previously intersected the coronal dome, hence only a single separator is removed from the topology.

In the final stage of this case, three further bifurcations occur (figures 2.16d, 2.17d). Firstly, the fans of nulls N1 and N4 interact through a fan-fan bifurcation. As the two surfaces become closer together, they finally flip through one another such that the surface of N4 no longer intersects that of N1, and the separator between the two is destroyed. However, this also changes the footpoints of the dome produced from N1, as it no longer has footpoints at source S2 as the domains of connectivity are restructured. Following this, the spine of null N2 and the fan of null N4 then interact with one another through a spine-fan bifurcation. This alters the footpoints of the fan of N4 from connecting to source S8, to now connect to source S1, resulting in the fan of N4 intersecting that of N1 once more. Thus, a separator is created, reforming the connection between N1 and N4. The spine of N2 then undergoes another spine-fan bifurcation, now with the fan of N5, which now also changes its connectivity from having footpoints at S8, to having them at S1. This process eliminates the separator connecting N5 to N7 but produces one connecting N5 to N1. Through this series of bifurcations, three separators have been eliminated, but two have been created. This topology now exists as two separate multiply-intersected domes, produced from the collection of fan surfaces of seven planar null points, with six separator field lines present. Each of the two separatrix domes connects to three of the negative sources and contain one of the positive sources, where both are bound by the spine field lines of null N2.

2.7.2 Continuous Source Model

For completeness, this source configuration was also modelled under the continuous source regime. Here, as found previously, the continuous source model produces qualitatively similar behaviour to the point source model. The key states of the topology are presented in figure 2.18, where at each stage the topology matches that of its point-source counterpart. In the interest of brevity, the specific description is not provided here.

2.7.3 Discussion

These cases found that the topologies had only a single coronal null point present, which is similar to the cases discussed in section 2.6. The bifurcations relating to the coronal null point where again analogous to those found in the previous cases considered in sections 2.5 and 2.6. However, as the topology evolves, it separates into two separate smaller states. Qualitative differences between the discrete and continuous source cases were again only present when the central sources of flux overlapped one another.

2.8 Bipole Emergence with Four Negative and Two Positive Boundary Sources

2.8.1 Point Source Model

This configuration presents the most complex skeleton of topological structures of all the studied cases (figures 2.19a, 2.20a). Under the initial configuration, the fan of null N1 forms a large separatrix dome, with footpoints at each of the negative boundary sources S3 - S6. This has the consequence that flux from sources S1′, S2′, S7′ and S8 is completely contained within its structure. Locally, these sources form

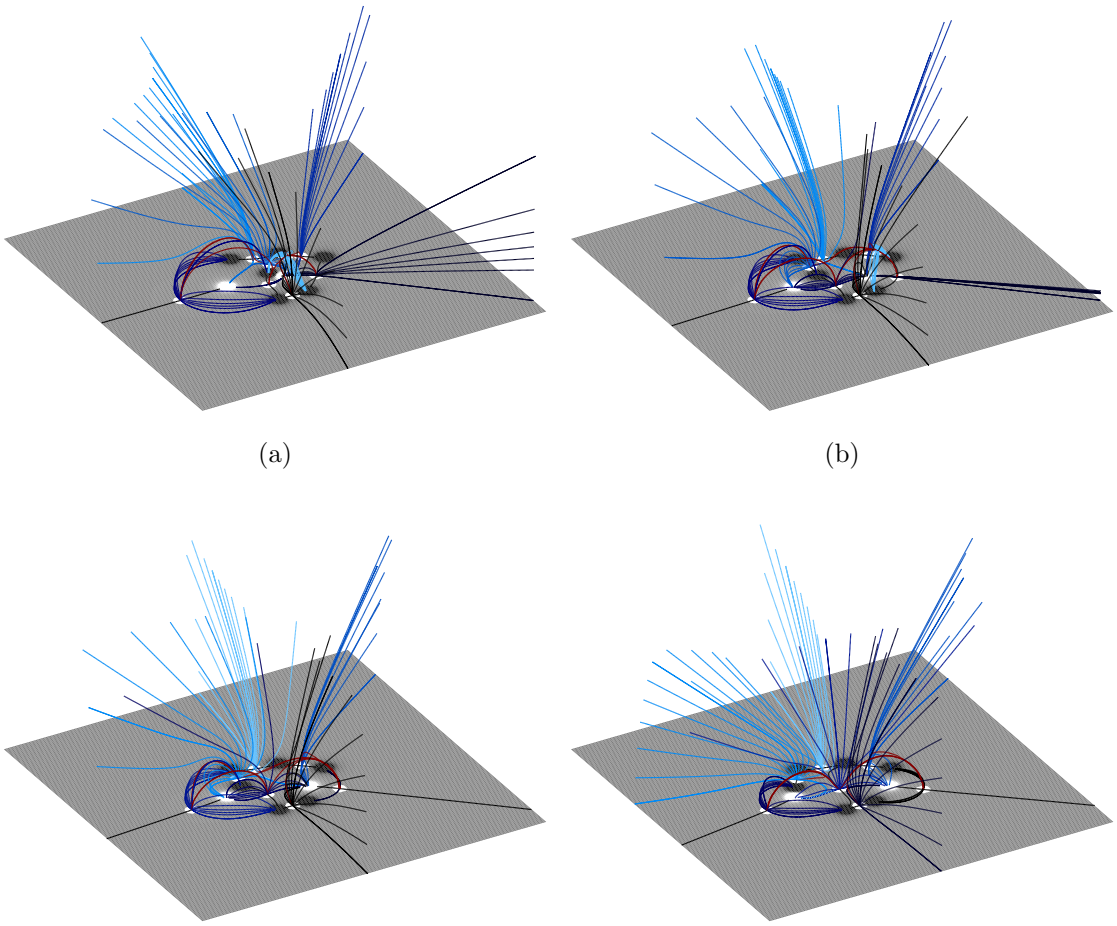

(a) (b)

(c) (d)

Figure 2.18: Different topological states which arise from using the five negative boundary source configuration, in the continuous source regime. Null points are solid white circles, negative sources are coloured in black, and positive sources are coloured white. Black lines are used for the spines of null points, whilst field lines which exist in the fan surface of a null are coloured unique to each null point present. Magnetic separators are given by solid red lines.

their own network of topological structures. The first component considered is the coronal null point CN1, which has a fan surface that projects a coronal dome down to the photospheric plane with footpoints at S3 - S6 and S7′. The spine field lines of this coronal null both end at photospheric sources of flux, namely S8 and S1′.

The spines of CN1 serve as bounds for the fans of nulls N3 and N5, which in turn have spine field lines that terminate at negative sources. Given the imbalance of the system, these fans would typically form separatrix walls extending out of the volume, bound by the spine of the coronal null. However, locally the imbalance is such that they instead form closed surfaces, bound by the coronal spine, thus producing an additional two coronal domes contained within the dome on N1, and intersecting the coronal dome of CN1. Null point N2 is also involved in this closed network, as it too forms a separatrix dome with footpoints at S7′, along with S5 and S6, but forms an enclosed structure with the fan of N1 (figure 2.21a). This complicated network splits the flux from S7′ into three domains of connectivity. One domain is contained by the intersection of the fan surfaces of the coronal null CN1, along with N3 and N5, allowing the connectivity of flux between S7′ and S8. Here, two separators exist connecting N3 to CN1, and N5 to CN1. Next, the fans of N2 and N5 form a domain for the flux to connect to S2′, and their intersection also forms a separator. Finally, the intersection of the surfaces from N2, N3 and N5 forms the region where flux may connect to S1′. However, no additional separators are defined as the fans of N3 and N5 do not intersect, but rather meet along the spine field line of the coronal null CN1 (figure 2.21b). The remaining nulls, N4, N6 and N7 form separatrix walls. Each of them intersects the contained coronal dome, along with the dome of N1, providing six separators. The fan of N6 also intersects the dome of N2, for an additional separator in the topology. In total, there are four separatrix domes, a single coronal dome and three separatrix walls. These are produced from seven photospheric nulls and a single coronal null. Together, the intersections of their surfaces produce ten separators within the topology.

Spine-fan bifurcations are the first to occur in this case studied (figures 2.19b, 2.20b). Here, the spine of N1 flips past the fan of N2, which serves to alter the enclosed state such that the enclosed dome now occupies the opposite side of the

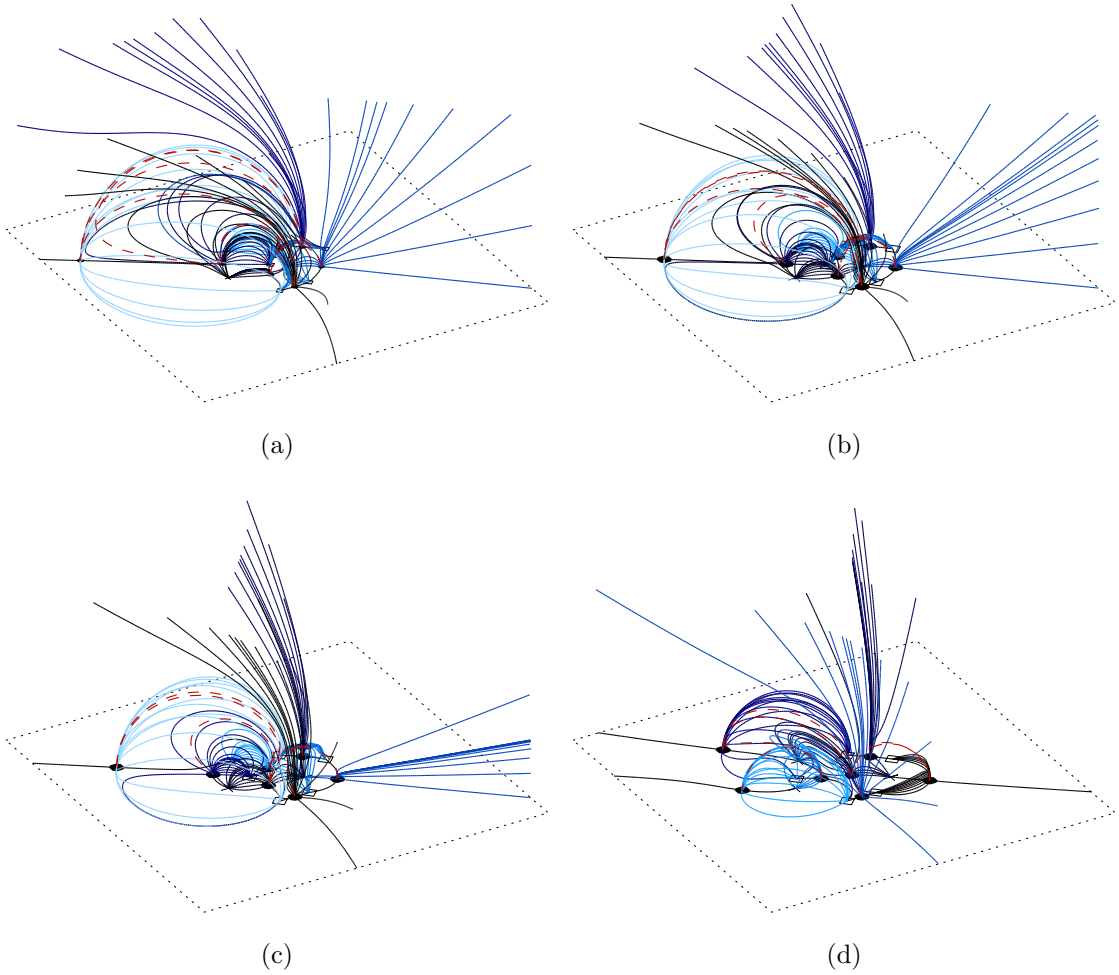

Figure 2.19: Different topological states which arise from using the four negative boundary source configuration. Null points are solid black circles, diamonds represent negative sources, and crosses represent positive sources. Black lines are used for the spines of null points, whilst field lines which exist in the fan surface of a null are coloured unique to each null point present. Magnetic separators are given by red-dashed lines.

structure. Hence, the footpoints of the fan of N2 now connect to sources S3 and S7′. The separators which previously intersected the fan of N2 are eliminated, replaced by ones in the intersection with the fan of N3 (figure 2.22). All of the separators which previously intersected with N1 are preserved through this change. The spine

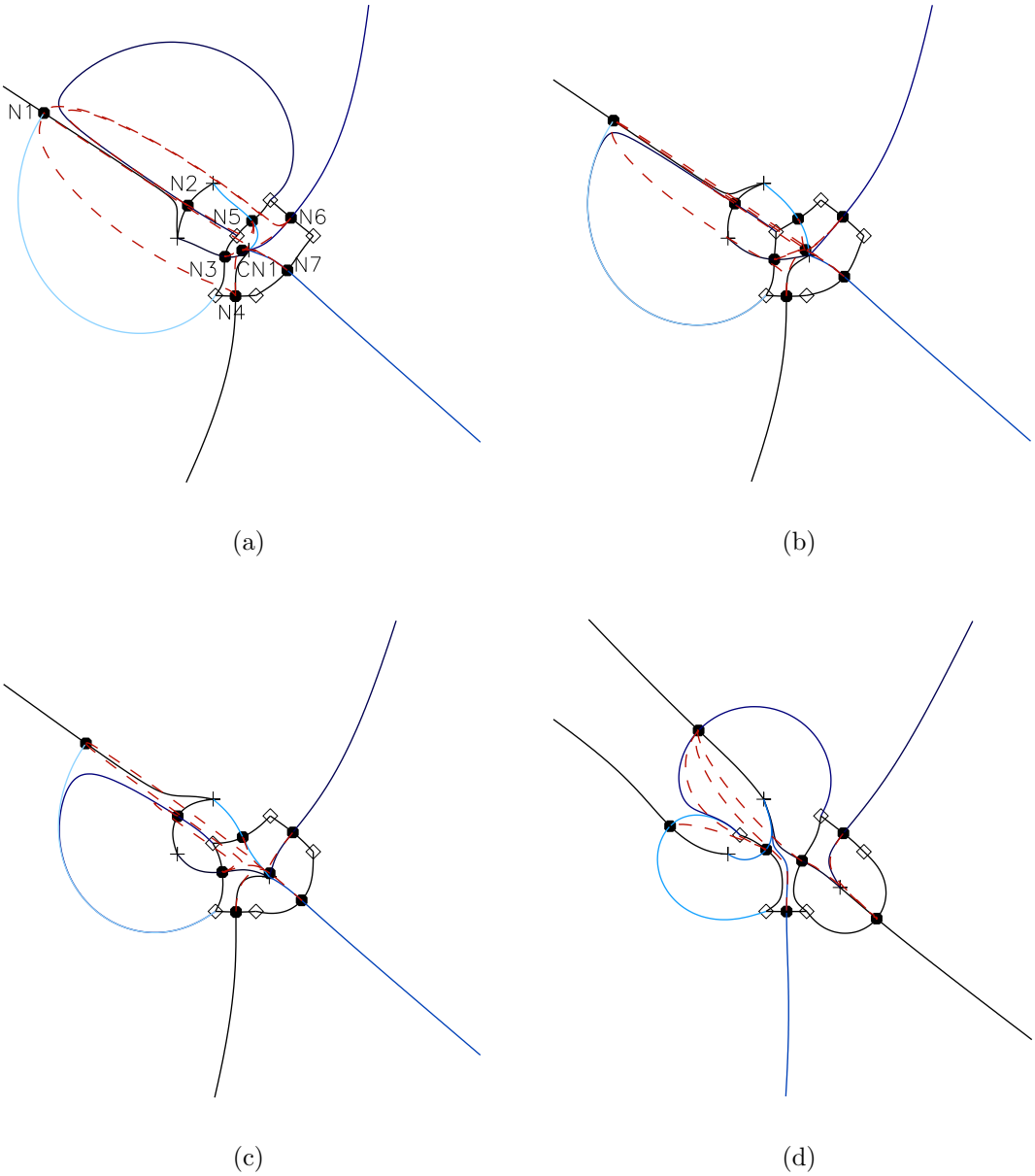

Figure 2.20: States of the magnetic skeleton in the $z = 0$ plane, arising from the four negative boundary source case. Null points have been labelled as 'N' and coronal nulls labelled as 'CN'.

of the coronal null CN1 which terminates at source S1′ also undergoes a spine-fan bifurcation, flipping through the fan of N2 and connecting to source S2′, preserving all of the separators along it. This leaves nine separators in the topology, as the

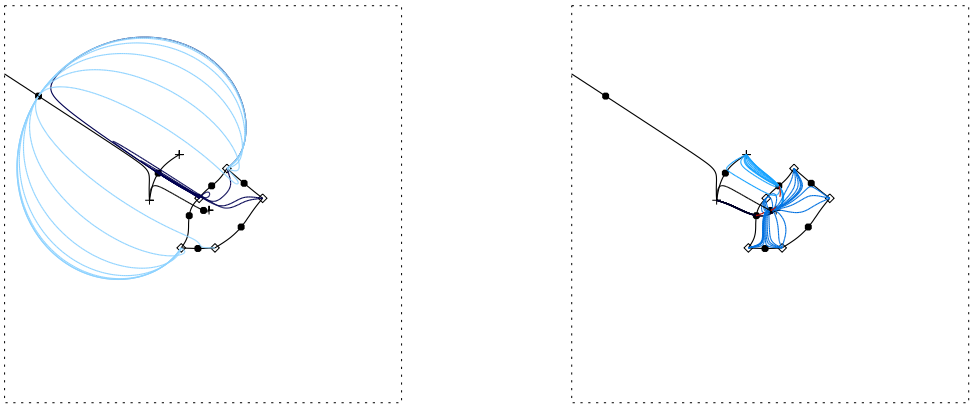

(a) (b)

Figure 2.21: Figues showing select topological features for the four negative boundary source case. a) The fan structures of nulls N1 and N2 have been displayed to illustrate the enclosed-state in which they exist. The dome of N1 completely encloses the network shown in part b), whilst the dome of N2 is distinctly separate to that of CN1. b) Partial magnetic skeleton of the four negative, oppositely-charged case. Fan field lines which exist in the surfaces of nulls N3, N5 and CN1 are displayed. Together, the spine of CN1 and the fans of N3 and N5 form a closed dome structure, which intersects with the fan of CN1 in two magnetic separator field lines.

enclosed dome from N2 now is a simple intersected dome, with just a single wall intersecting its surface.

The next bifurcation to occur involves the spine of the coronal null CN1 bifurcating through the fan of the null N1 through a spine-fan bifurcation (figures 2.19c, 2.20c, 2.23). Whilst the process is the same as those above, this has a larger consequence on the structures present in the topology. Prior to the bifurcation, the spine of the coronal null bounds numerous separatrix surfaces (N3, N4, N5, N6, N7). As the spine line from CN1 to source S2′ terminates at a photospheric source, the fans of N3 and N5 form closed dome structures, meeting at the spine field line. When

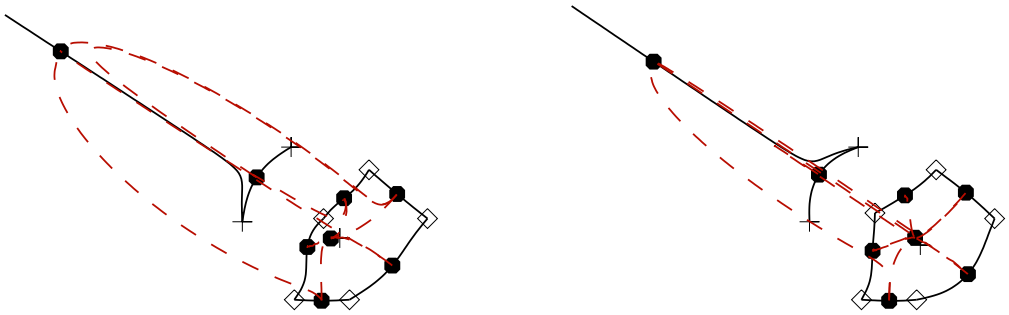

(a) (b)

Figure 2.22: The separator network of the four negative boundary source case, a) before the spine-fan bifurcations have occurred, and b) after the spine-fan bifurcations.

the spine line bifurcates through the fan surface, these surfaces are brought through with it, no longer bound to the interior of the dome of N1. Likewise, this change in position now prevents the fans of N4, N5 and N6 from intersecting with the separatrix dome. Thus, three separators are eliminated, and two new ones formed, for a new total of eight separators in the magnetic skeleton. The dome of N1 is now intersected by the newly opened fans of N3 and N5, the surface of CN1 has preserved the 5 separators along it, and the surface of N2 still represents the intersected state with only the surface of N3 interacting with it.

Finally, the coronal null CN1 is eliminated through a pitchfork bifurcation with the planar null N7, which destroys the separator connecting the two (figures 2.19d, 2.20d). The planar nulls then undergo seven spine fan bifurcations and this eliminates two more of the separators. The null N7 is intersected by the fans from N5 and N6, with footpoints at S4 - S6, forming a double-intersected state. The wall from N4 now only intersects the dome of N1, which is also intersected by the separatrix walls of N3 and N5. The null N2 forms a separatrix dome, which exists in

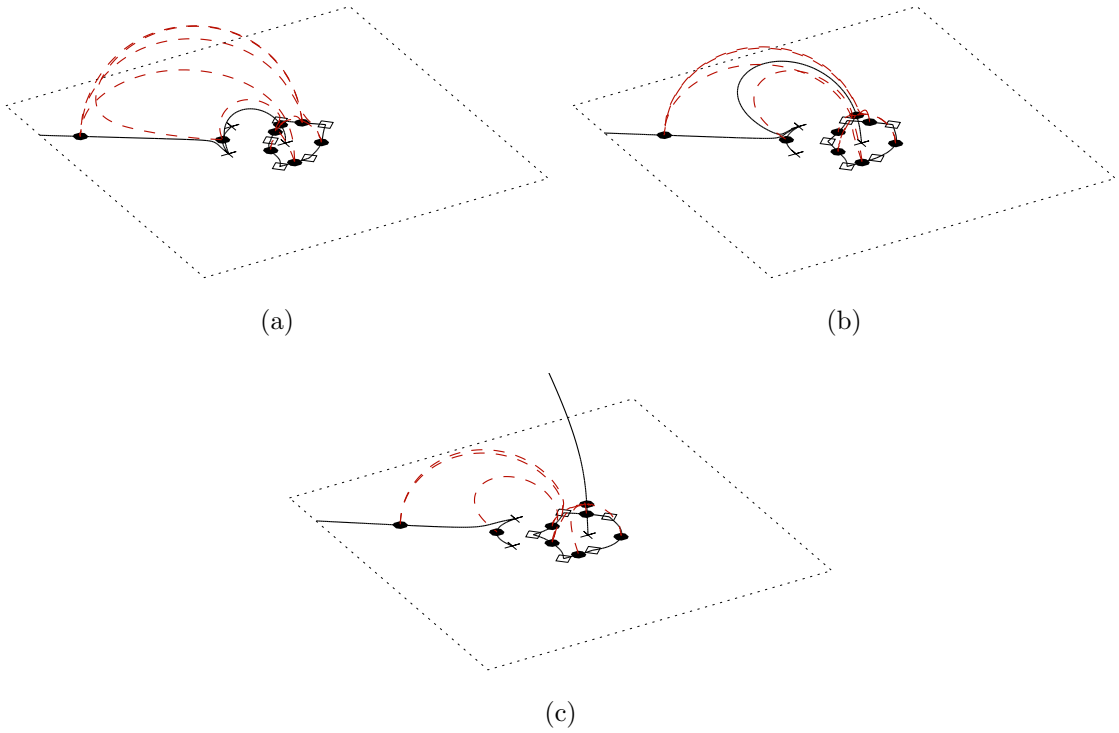

Figure 2.23: In the four negative boundary source case, the eruption of the spine field line of CN1 through the fan of N1 is explored by considering the separator networks. a) The initial topological state, with the spine of the coronal null bound within the large dome of N1. b) The topological state after the spine-fan bifurcation of the enclosed domes. Note how the spine of the coronal null has become more elongated. c) Topological state after the spine of the coronal null has bifurcated through the fan of N1, where it is now open to the coronal background.

the separate state from the dome of N1, intersected only by the wall of N3. Hence the topology consists of three separate domes, each with a different number of fan surfaces intersecting it.

2.8.2 Continuous Source Model

Again, when the source configuration is modelled in the continuous source regime, qualitatively similar behaviour is found. The core topological state of the continuous source model is presented in figure 2.24. It should be noted that the same bifurcation behaviour is seen throughout the process, including the bifurcation of the coronal null spine with the planar dome fan.

2.8.3 Discussion

Again, the cases explored here consisted of topologies with only a single coronal null point present. However, the topology due to four negative and two positive boundary sources had numerous differences to all the other cases which have been considered in this chapter (sections 2.5, 2.6, 2.7).

Here, a system was presented where the topology consisted of a coronal dome confined within a planar dome. A bifurcation occurs where a spine field line of the coronal null point bifurcates through the fan plane of the planar dome (figure 2.23). This bifurcation opens the previously enclosed, compact topology of the coronal dome network, to the larger background field throughout the volume. This interaction is relatable to the magnetic breakout model (Antiochos 1998), such as for a polar plume (figure 2.25) or X-ray jet (Moreno-Insertis et al. 2008; Pariat et al. 2009; Kumar et al. 2018).

2.9 Cigar-shaped Sources of Magnetic Flux

In magnetograms of the photosphere, such as those produced by the HMI instrument aboard SDO, magnetic sources and sinks rarely appear as small discs. Often, these fragments exist as much more dispersed shapes of flux. Thus, use of source

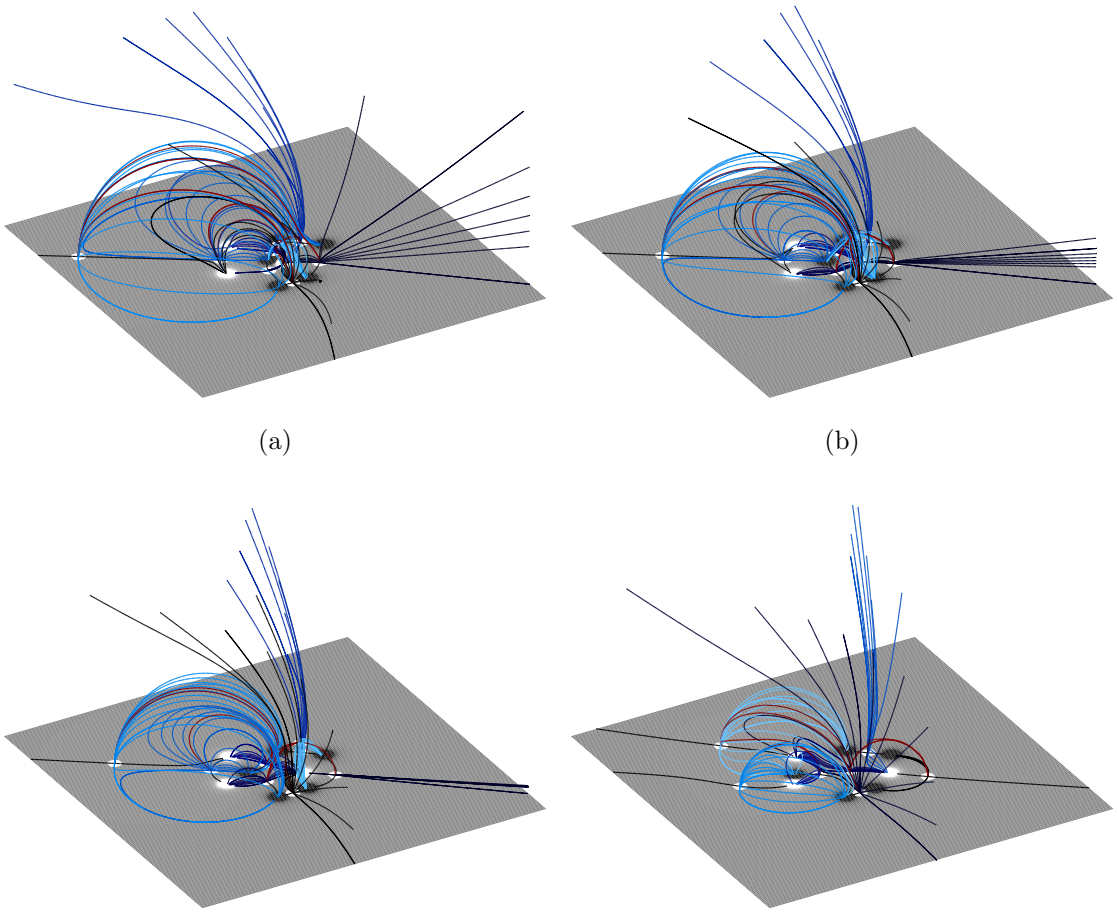

(a) (b)

(c) (d)

Figure 2.24: Different topological states which arise from using the four negative boundary source configuration, in the continuous source regime. Null points are solid white circles, negative sources are coloured in black, and positive sources are coloured white. Black lines are used for the spines of null points, whilst field lines which exist in the fan surface of a null are coloured unique to each null point present. Magnetic separators are given by solid red lines.

shapes which are more characteristic of the photospheric fragments should be considered. Here, a number of cigar-shaped sources are applied to two of the source configurations that have already been explored.

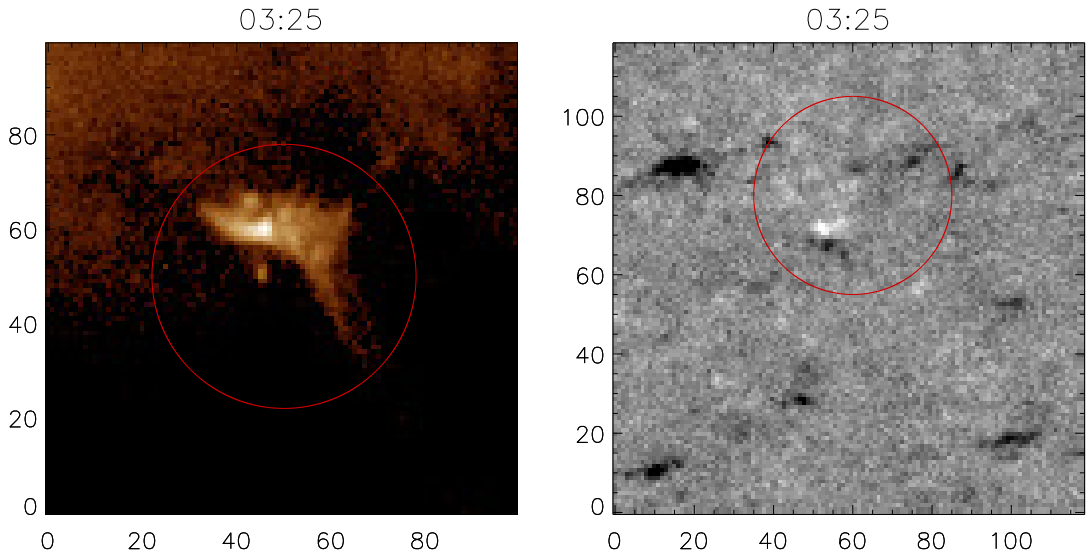

(a) (b)

Figure 2.25: Images captured showing a) image of polar plumes towards the south pole of the Sun, captured with SDO/AIA in the 193 Å waveband and b) line-of-sight magnetic field at the photosphere for the same region with SDO/HMI at 03:25 on January 6^{th}, 2018. The red circles indicate a) the polar plume structure and b) the region where the footpoints of the plume are located.

2.9.1 Six Negative Boundary Sources

The scenario with three coronal null points (section 2.5) is further developed here. Four of the negative boundary sources (S3 - S6) have been replaced with two 'cigar' shaped sources of flux (figure 2.26), and the resultant topologies have been found (figure 2.27). In order to preserve the unbalanced system flux, both of these additional sources have a total flux of -1.0 arbitrary units, with their parameters shown in table 2.2. The cigars each have a width of $w = 0.15$, and the semi-circular ends of the cigars have a radius of $r = 0.15$. The circular sources used in this configuration also have a radius of $r = 0.15$.

Boundary Continuous-Source Parameters					
Source	$\mathbf{x}_1$	$\mathbf{y}_1$	$\mathbf{x}_2$	$\mathbf{y}_2$	$\boldsymbol{\epsilon}$
C1	0.60	0.90	1.50	0.15	-1.00
C2	-0.55	-1.10	0.30	-1.10	-1.00

Table 2.2: Table containing the parameters for the configuration of the cigar-shaped sources used for the hexagonal case study. The x_1 and y_1 denote the start point of a cigar, with x_2 and y_2 representing the end points. The total flux distributed across the source is given by ϵ.

Again, the topology of the system changes through the same bifurcations as those seen in the point source case (sections 2.5.1, 2.5.2). First, a turning point bifurcation introduces two new coronal null points into the topology, where the fan surface of one forms a coronal dome and that of the other projects a wall down to the photospheric plane and out of the coronal volume. Thus, the triple-intersected-touching coronal dome state is recovered. Next, the coronal nulls eliminate through pitchfork bifurcations with nulls in the plane, where the magnetic skeleton now consists of a pair of intersected separatrix domes.

Replacing two of the sources with a single larger source serves to eliminate the null point that would otherwise be present between them. Previously, a separatrix wall from a null point between S5 and S6 would intersect the separatrix dome in the final state of the simulation. However, the absence of the null means that no separatrix surface is present, thus there are fewer separators in the resulting magnetic skeleton.

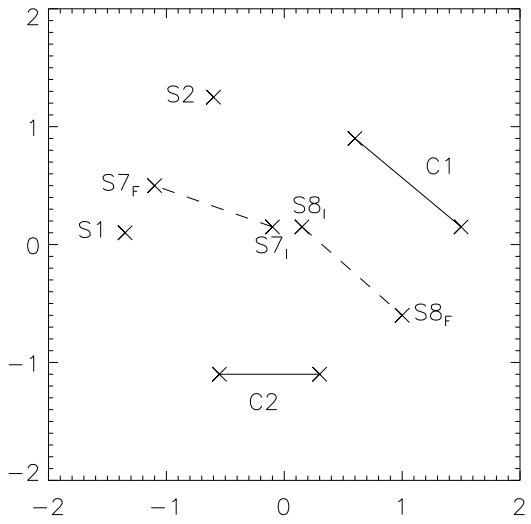

Figure 2.26: Figure showing the initial and final configurations of the magnetic sources for the six negative boundary source case using cigar shaped sources. The path of the internal sources is indicated by the dashed line. These positions give the centre points of the circular sources, and the endpoints of the cigars which have been indicated by the solid line connecting two points.

2.9.2 Breakout Model with Cigar-shaped Sources

This scenario aims to recreate the topological structures produced by the source configuration presented in section 2.8. The positions of the cigar-shaped sources used are given in table 2.3, along with a modified position for $S7'_F$ which prevents it crossing the cigar C3. The circular source S8 is moved using the same positions as in 2.8. Again, the cigars each have a width of $w = 0.15$, and their semi-circular ends have a radius of $r = 0.15$. The source positions are shown in figure 2.28.

In the initial configuration, the topology which arises from the sources (as shown in figure 2.29a) is similar, but not identical to that found previously in section 2.8. This model has three fewer planar nulls than the previous scenario, due to the positioning of the cigar sources. However, this is to be expected given the position and distribution of the cigar sources. This serves to also remove three of

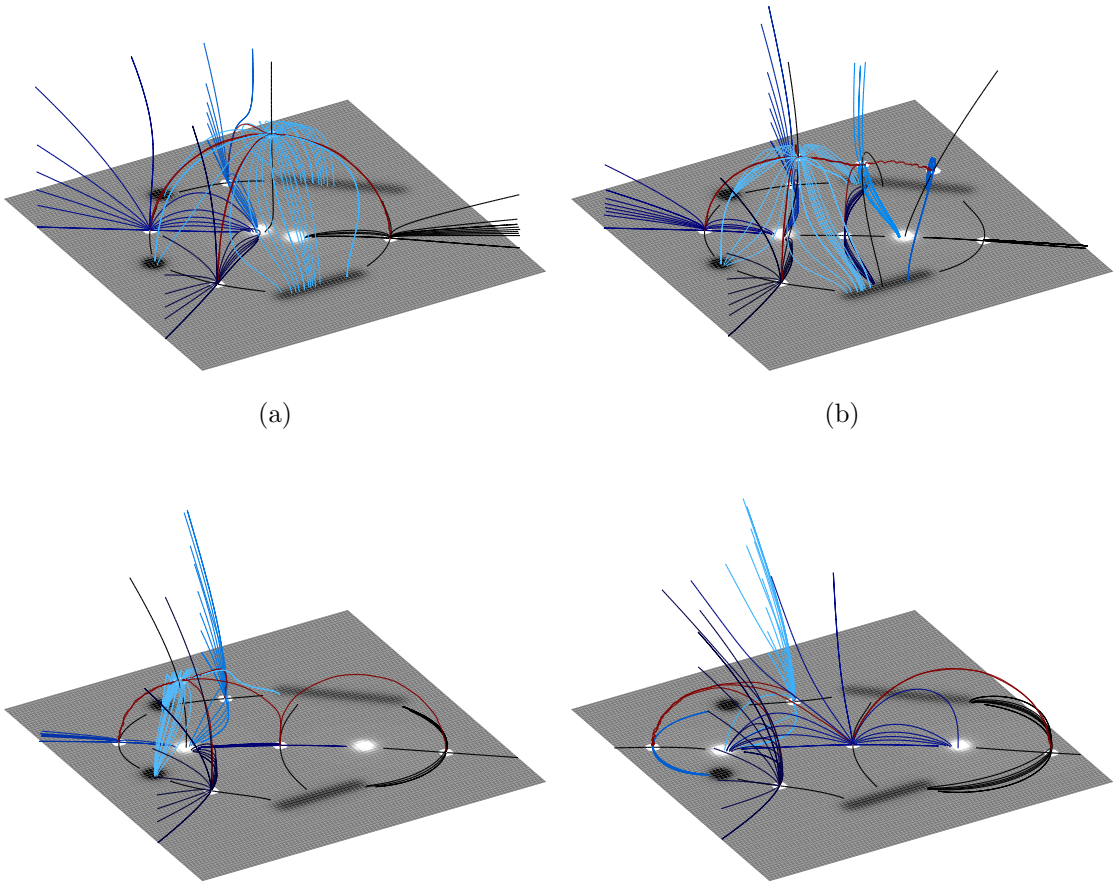

(a) (b)

(c) (d)

Figure 2.27: Different topological states which arise from using the source configuration of the three coronal null point case, with two cigars of flux. Null points are solid white circles, and regions where positive (negative) flux is passing through the $z = 0$ surface are represented as white (black) diffuse regions. Black lines are used for the spines of null points, whilst field lines which exist in the fan surface of a null are coloured unique to each null point present. Magnetic separators are given by red lines.

the separatrix walls from the structure, but the compact, internal structure involving the coronal null point and the two enclosed fan surfaces is preserved.

The key topological states of this system are presented in figure 2.29. At each

Continuous-Source Parameters					
Source	$\mathbf{x}_1$	$\mathbf{y}_1$	$\mathbf{x}_2$	$\mathbf{y}_2$	$\boldsymbol{\epsilon}$
C1	0.60	0.90	1.50	0.15	-1.00
C2	-0.55	-1.10	0.30	-1.10	-1.00
C3	-1.35	0.10	-0.60	1.25	1.00
$S7'_F$	-0.55	0.30	n/a	n/a	-0.50

Table 2.3: Table containing the parameters for the configuration of the cigar-shaped sources used for the magnetic breakout study. The x_1 and y_1 denote the start point of a cigar, with x_2 and y_2 representing the end points. The total flux distributed across the source is given by ϵ.

stage, the topology produced here is qualitatively similar to its counterpart in the point source regime, except for features which arise from the three missing nulls points. However, the 'break out' behaviour found previously, as discussed in section 2.8.3, is retained.

Figure 2.30 shows how the spine of the coronal null bifurcates through the separatrix dome of the distant planar null. Initially, the spine of the coronal null connects down to the photospheric plane in both directions (figure 2.30a). As the sources are moved further apart, the spine begins to elongate, stretching into the volume contained by the overarching separatrix dome (figure 2.30b). The sources then pass the critical point, where the spine of the coronal null bifurcates through the fan of the enclosing dome, dragging the fan surfaces of the two enclosed planar nulls with it (figure 2.30c). Similar to previously discussed instances, this serves to open the enclosed topology to the background coronal volume.

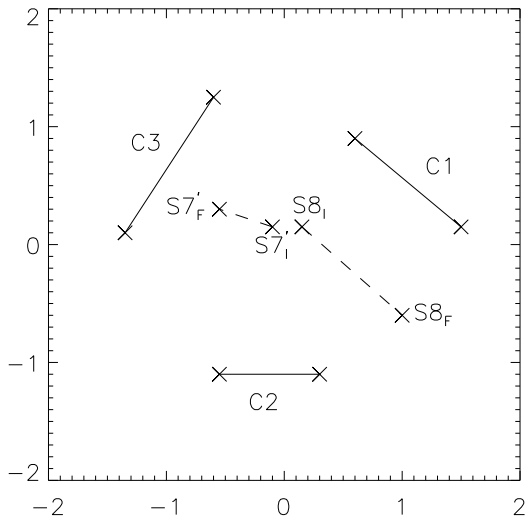

Figure 2.28: Figure showing the initial and final configurations of the magnetic sources for the breakout model using cigar shaped sources. The path of the internal sources indicated by the dashed line. These positions give the centre points of the circular sources and the endpoints of the cigars which have been indicated by the solid line connecting two points.

2.9.3 Discussion

Replacing circular sources of flux with cigar-shaped sources serves to more closely represent the features that one might observe in a magnetogram image of the solar photosphere. Here, two models that had previously been explored using both point and continuous sources where revisited. The only difference found between the two regimes was in the number of null points present. However, this is to be expected when the number of distinct sources is reduced. That the bifurcation and topological behaviour was otherwise preserved, suggests that the earlier models give good representations of more realistic configurations.

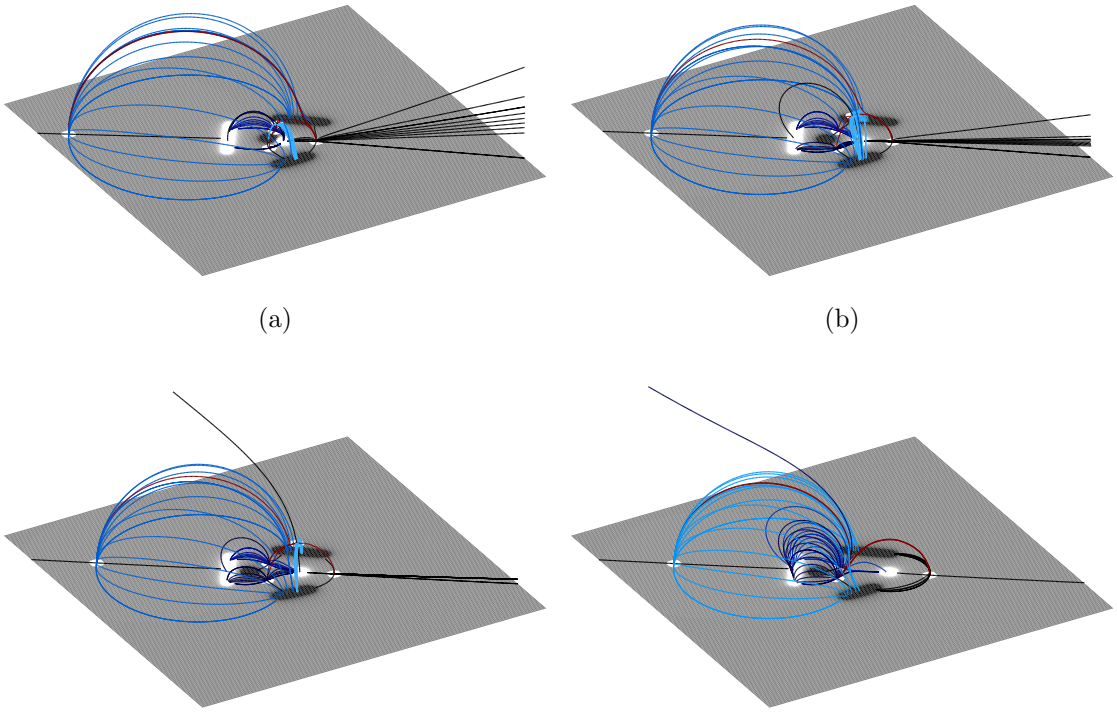

(a) (b)

(c) (d)

Figure 2.29: Different topological states which arise from using the cigar source breakout model. Null points are solid white circles, and regions where positive (negative) flux is passing through the $z = 0$ surface are represented as white (black) diffuse regions. Black lines are used for the spines of null points, whilst field lines which exist in the fan surface of a null are coloured unique to each null point present. Magnetic separators are given by red lines.

2.10 Discussion

This study has found that the topologies of potential magnetic fields of point-source models match those of their continuous source counterparts, provided that the continuous sources can be considered as circular sources of flux and are distinct from one another. In scenarios where the continuous sources are better described as more distributed flux concentrations, such as the cigar-shape, some null points present in

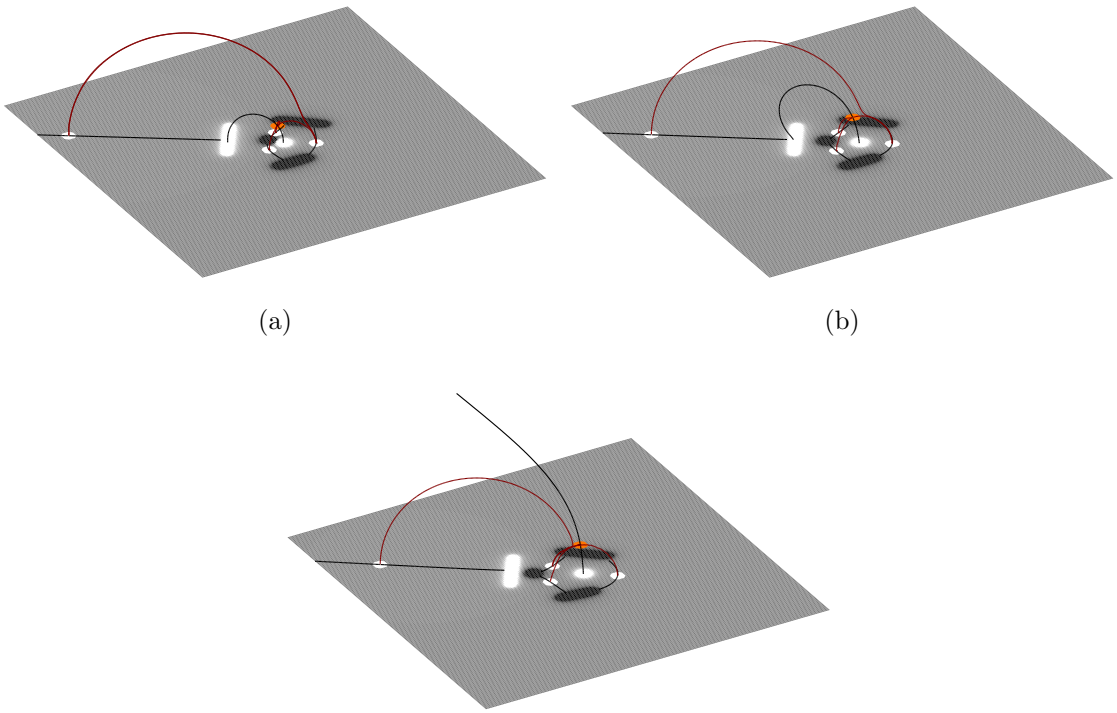

(a) (b)

(c)

Figure 2.30: In the cigar source, magnetic breakout case, the eruption of the spine field line of CN1 through the fan of N1 is explored by considering the separator networks. a) The initial topological state, with the spine of the coronal null bound within the large dome of N1. b) The topological state after the spine-fan bifurcation of the enclosed domes. Note how the spine of the coronal null has become more elongated. c) Topological state after the spine of the coronal null has bifurcated through the fan of N1, where it is now open to the coronal background.

the topology produced from point sources are absent. However, much of the core topological behaviour is returned. When two continuously distributed sources overlap, the null point which existed between them vanishes. This process is studied further in Chapter 3 of this thesis.

The study had a particular focus on topologies where coronal null points were present. A state which resembled a topology with an 'open separatrix surface',

previously found by Platten et al. (2014) and Priest (2014), but the open surface was bound on both sides by the separatrix surfaces of planar null points. This topological feature is explored further in section 3.8, where the inclusion of null-like points in the topology finds that the surface is maybe not as open as previously thought. It was also found that states analogous to those found previously (Brown & Priest 1999; Beveridge et al. 2002) existed throughout many of the cases considered, but also with a coronal equivalent of the enclosed state. Section 2.8 presented a transition between an enclosed, touching and then separate state, produced from a coronal dome and a separatrix dome.

Finally, a case was presented where a coronal dome was bound within a separatrix dome. During the scenario, the spine of the coronal null bifurcates with the fan of the separatrix dome through a spine-fan bifurcation. This then allows the spine of the coronal dome to extend out into the coronal volume, with a separator defined along its length. This scenario may be applicable as a characteristic model to a polar plume, where closed flux opens up to extend out into the coronal volume. Such a bifurcation in a topology presented here may provide the mechanism for the opening of the field. It would be interesting to explore this further by comparing to magnetic flux configurations observed at the base of polar plumes.

Chapter 3

Defining Null-like Points

3.1 Introduction

This chapter will address one of the issues that arose from Chapter 2, namely the vanishing of a null point when it is covered by two overlapping, continuously-distributed magnetic sources. A definition is provided for a new topological feature, the null-like point (NLP), which can be identified in the region where two sources overlap, and more generally in the distributed source regime. From these NLPs, surfaces with separatrix-like behaviour can be calculated which provide additional insight into the connectivity of the magnetic field lines within the volume.

Section 3.2 provides a brief introduction on the properties and behaviour of Quasi-Separatrix Layers, as the surfaces generated from the null-like points are a class of QSL. Section 3.3 defines null-like points by relaxing the definition of a magnetic null point and discusses some other properties which may also arise. Section 3.4 discusses the mathematics behind calculating the squashing factor, an identifier of QSLs, and also how it is applied in the context of this work. Section 3.5 will introduce two additional continuous source distributions which will be used later in this chapter. A series of case studies are then presented which consider the changes NLPs introduce into the magnetic skeleton. Section 3.6 describes the setup

of these case studies. Section 3.7 places four circular sources of magnetic flux in the photospheric plane, with possible overlaps between pairs of like-charged sources. This provides an initial understanding of how to relate an NLP to the Q-map of a configuration. Section 3.8 considers the previously discussed open-separatrix surface (Priest 2014), revealing a more complete picture of the magnetic skeleton through NLPs. Section 3.9 applies the method to various configurations of segmented annuli, providing an understanding of how the signatures of an NLP in a Q-map may vary. Finally, section 3.10 provides a discussion on the key results of this chapter.

3.2 Quasi-Separatrix Layers

Studies of solar flares found that the separatrix surfaces of magnetic null points are not always associated with the flaring site (Demoulin et al. 1994), but rather that there was a strong correlation between these sites and steep gradients in the field line connectivities (Mandrini et al. 1995; Démoulin et al. 1997). Priest & Démoulin (1995) later provided a definition for these regions, naming them quasi-separatrix layers. Quasi-separatrix layers (QSLs) are an important feature of the magnetic skeleton, where the connectivity of field lines changes rapidly over small scales but is not discontinuous as at a separatrix surface (Mandrini et al. 1995; Priest & Démoulin 1995; Démoulin et al. 1996, 1997). QSLs intersect one another at quasi-separators, which provide locations for reconnection to occur in a similar measure to separators (Priest 2014). However, QSLs are regions where reconnection can occur in the absence of separatrices, separators and null points (Priest & Démoulin 1995), hence it is important to know if they are present in a given topology, particularly in the context of energy release in a solar flare (Mandrini et al. 1995; Démoulin et al. 1997; Titov & Démoulin 1999a,b).

3.3 Defining Null-like Points

Linear magnetic null points were first defined by Lau & Finn (1990) as regions where the magnetic field vanishes ($\mathbf{B} = 0$). In three dimensions, this means,

$$B_x = B_y = B_z = 0, \tag{3.1}$$

where B_x, B_y and B_z are the components of the magnetic field in the x, y and z directions respectively.

If two sources of the same polarity are close together, there is usually a null point located between them (figure 3.1a). However, when the two sources of magnetic flux overlap, the null point between them vanishes (figure 3.1b) as equation 3.1 no longer holds ($B_z \neq 0$). In the absence of the null point, an x-line structure may persist within the overlap of the two sources. In principle, this could be extended to multiple overlapping sources with multiple x-line structures.

Within the boundary of a continuously distributed source, the magnetic field will never vanish completely. Thus, to locate these x-line structures, the definition of a magnetic null point is relaxed such that:

$$B_x = B_y = 0, \tag{3.2}$$

$$B_z \neq 0. \tag{3.3}$$

There are then three cases to consider, regarding the eigenvalues μ_1 and μ_2 of the Jacobian matrix of the magnetic field components in the B_x and B_y system only, along with the sign of B_z.

Suppose first that μ_1 and μ_2 are of opposite sign. One of these eigenvalues, say μ_2, will have a sign aligned with the direction of the B_z component. This configuration is sufficient to preserve the x-point configuration in the x-y plane. Here, a location where these conditions are met is called a prone null-like point (NLP), serving as the signature of an x-line structure in the photospheric plane.

An NLP also has a separatrix-like surface associated with it in the plane of the eigenvector $\boldsymbol{v}_2$ and $B_z\hat{\mathbf{z}}$. This is calculated by first finding the eigenvalues of the NLP. Then, a line which traces the separatrix in the $z = 0$ plane associated with μ_2 and $\boldsymbol{v}_2$ is found. From this line, selected points are then chosen as the starting points for calculating a set of field lines along this separatrix. This starting separatrix is traced until it reaches the edges of the source it is located in. The separatrix-like surface formed from these field lines is a QSL, though not all QSLs will be separatrix-like surfaces.

The intersection of a separatrix-like surface with another separatrix surface produces a separator-like field line, while the intersection of two QSLs produces a quasi-separator. Spine field lines of NLPs are not shown as they terminate immediately since the NLP lies in the spine-terminating source region.

Next, consider the case where the eigenvalues μ_1 and μ_2 are of the same sign, but the B_z component has opposite sign. A location where these conditions hold is defined as an upright NLP, where the associated separatrix-like surface is bound to the photospheric plane, and the spine-like field lines propagate out into the coronal volume.

The final scenario is where the eigenvalues μ_1, μ_2 and the sign of B_z are all the same. This situation arises at local absolute maxima in the flux distribution across a continuous source. Here, these features are called source-like points (SLPs), and act as a two-dimensional source or sink in B_x and B_y, whilst being non-stationary in B_z. They have similarities with point sources.

Some of these topological features are illustrated by the source configurations shown in figures 3.1a and 3.1b. In figure 3.1a, the two sources are distinct from one another, and a null point is found between them. The nullclines for this configuration (where $B_x = 0$ and $B_y = 0$) have been plotted over the region, indicating the presence of two SLPs at the centre of the sources. In figure 3.1b, the location of the

null point has now been covered by the overlapping sources. However, the nullclines still intersect at the point where the null point was located, and here a null-like point is now located. The two SLPs that where previously found are still present, though their position has moved with the position of the sources. Figures 3.2a and 3.2b show the dispersion of magnetic field lines around a null point, and around a null-like point respectively, where magnetic sources have been placed as shown in figure 3.1. Here, the structure of the field lines has connotations with the idea of magnetic flipping (Priest & Forbes 1992; Priest & Titov 1996) in QSLs. Consider the structure of the field lines shown in figure 3.2a. Field lines which start closer to the edges of the circular sources are initially inclined towards the separatrix surface of the null point which lies between the two sources. As the field lines get close to this surface, they are deflected upwards, where the separation between them is greatly reduced. This shows the discontinuous mapping of the field lines. Now consider the field lines shown in figure 3.2b. Similar behaviour is exhibited by these field lines as they get close to the location of the NLP, and the separatrix-like surface associated it, where the field lines begin to bunch together. While the field line mapping is no longer discontinuous, there is a region of rapid change in field line connectivity, which is characteristic of QSLs.

3.4 Calculating the Squashing Factor

Closed magnetic field lines in the solar atmosphere connect to two oppositely charged sources of magnetic flux in the photosphere. The positions of the footpoints at the photospheric surface can then be described by $\mathbf{r}_{\pm} = (x_{\pm}, y_{\pm})$ dependent on the polarity to which they connect. The footpoints can then be related to one another by the mapping,

$$\prod_{+-} : \mathbf{r}_{+} \rightarrow \mathbf{r}_{-}, \tag{3.4}$$

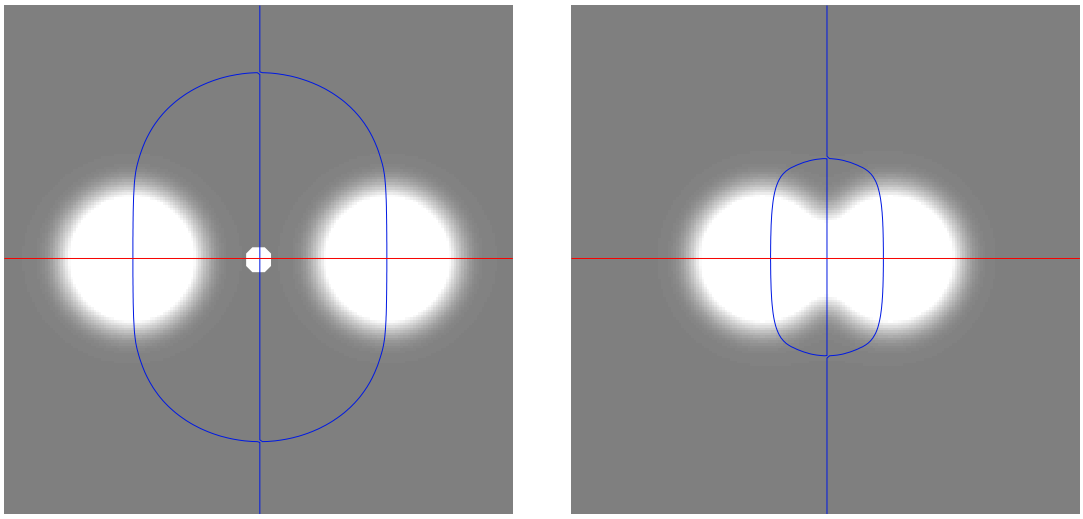

(a) (b)

Figure 3.1: a) Planar plot of two separate positive sources of flux, where the white dot indicates the position of the null point. Nullclines are also plotted to show the x-points in the x-y plane. The blue line gives the B_x nullcline and the B_y nullcline is shown in red. b) Planar plot of two circular sources of flux which now overlap, where the previous null has now vanished, though the B_x and B_y nullclines still intersect at the point where the null was previously located.

which maps the connection from the positive foot point $\mathbf{r}_+$ to the negative footpoint $\mathbf{r}_-$ (Titov et al. 1999). The inverse mapping would be represented as $\prod_{-+}$ for the connection in the opposite direction. These mappings can also be expressed as a function of the footpoints,

$$(X_-(\mathbf{r}_+), Y_-(\mathbf{r}_+)) \equiv \prod_{+-}(\mathbf{r}_+), \tag{3.5}$$

where an inverse is also definable.

Using this notion, Priest & Démoulin (1995) defined the function,

$$N(\mathbf{r}_\pm) = \left(\left(\frac{\delta X_\mp}{\delta x_\pm} \right)^2 + \left(\frac{\delta X_\mp}{\delta y_\pm} \right)^2 + \left(\frac{\delta Y_\mp}{\delta x_\pm} \right)^2 + \left(\frac{\delta Y_\mp}{\delta y_\pm} \right)^2 \right)^{\frac{1}{2}} \equiv N_\pm, \tag{3.6}$$

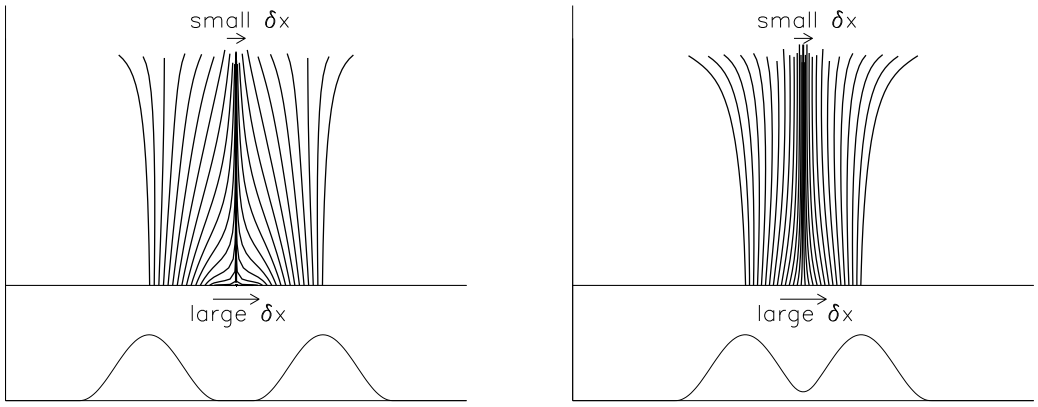

(a) (b)

Figure 3.2: a) Schematic showing the field line spread produced from field lines with footpoints on the continuous sources, when positioned apart as in figure 3.1a. The flux distribution along the x-axis is shown in the same frame, below the field line locations. b) Displays the same information as subfigure (a), but for the configuration where the sources overlap as shown in figure 3.1b.

which identified QSLs as regions where footpoints had a value $N_{\pm} \gg 1$. However, this result varied such that one field line may be attributed two values for N dependent on the direction of the mapping. Titov et al. (1999) refined this definition of a QSL by calculating a squashing factor, Q, by describing the mappings in terms of their derivatives, represented by the Jacobian matrices,

$$D_{+-} = \begin{bmatrix} \frac{\delta X_-}{\delta x_+} & \frac{\delta X_-}{\delta y_+} \\ \frac{\delta Y_-}{\delta x_+} & \frac{\delta Y_-}{\delta y_+} \end{bmatrix} \equiv \begin{bmatrix} a & b \\ c & d \end{bmatrix}, \tag{3.7}$$

and

$$D_{-+} = \begin{bmatrix} \frac{\delta X_+}{\delta x_-} & \frac{\delta X_+}{\delta y_-} \\ \frac{\delta Y_+}{\delta x_-} & \frac{\delta Y_+}{\delta y_-} \end{bmatrix} = \Delta_+^{-1} \begin{bmatrix} d & -b \\ -c & a \end{bmatrix}, \tag{3.8}$$

where,

$$\Delta_+ = (ad - bc) \equiv det(D_{+-}). \tag{3.9}$$

Titov et al. (1999) then consider the mapping of an orthonormal vector basis $(\hat{\mathbf{u}}_+, \hat{\mathbf{v}}_+)$ to a non-orthonormal vector basis $(\mathbf{u}_-, \mathbf{v}_-)$ in corresponding planes, where $\mathbf{u}_- = D_{+-}\hat{\mathbf{u}}_+$, and $\mathbf{v}_- = D_{+-}\hat{\mathbf{v}}_+$. By studying the geometry of this mapping, and using the definition of the norm (equation 3.6), Titov et al. (1999) define Q as,

$$Q = \frac{N_+^2}{|\Delta_+|}, \tag{3.10}$$

where $N_+ \equiv (a^2 + b^2 + c^2 + d^2)^{\frac{1}{2}}$ and $|\mathbf{u}_-|/|\mathbf{v}_-| \approx Q$ for $Q \gg 1$. Titov et al. (1999) state that since N_+ is the diagonal of the rectangular formed by $\mathbf{u}_-$ and $\mathbf{v}_-$, there is the additional property that $Q \geq 2$, which is in agreement with the results presented later in this chapter (sections 3.7 - 3.9).

Q then allows QSLs to be identified as regions where $Q \gg 1$ (Titov et al. 1999). Thus Q serves to characterise the magnetic connectivity of the volume, rather than the field line mappings. This definition for Q is also invariant, in that the same value is retrieved regardless of the direction of the mapping.

The definition of the squashing factor, Q, has been applied to other scenarios in a planar geometry (Titov et al. 2002; Titov & Hornig 2002) and has been generalised for a global geometry (Titov 2007), though it is the definition provided by equation 3.10 that is used in this thesis. Under the principles of MCT (section 2.1), the squashing factor has been calculated and used to aid the interpretation of topologies with null-like points. Q is calculated for each cell in the volume which has a source defined on it (i.e where $B_z \neq 0$). From each cell, four field lines are calculated with start points in the centre of each bounding edge of the cell (figure 3.3). These start points form one set of footpoints and the end set is obtained from where the field lines next touch the photospheric surface or leave the volume. Suppose the start points originate at a positive source in the plane, with the grid cell centred on co-ordinates (x, y). Let δx be the length of the cell parallel to the x-axis, and δy the length parallel to the y-axis. Thus define,

$$x_1 = x - \frac{\delta x}{2}, \quad x_2 = x + \frac{\delta x}{2}, \quad y_1 = y - \frac{\delta y}{2}, \quad y_2 = y + \frac{\delta y}{2},$$

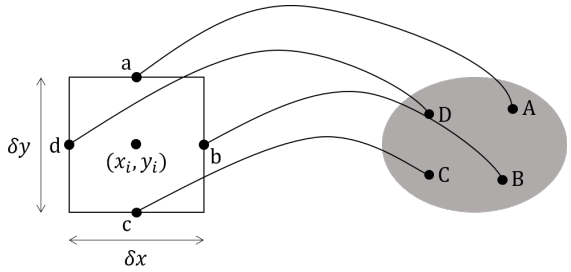

Figure 3.3: Mapping of the field lines from four footpoints in the origin source to the destination source. Points a, b, c and d represent $(x_i, y_i + \delta y)$, $(x_i + \delta x, y_i)$, $(x_i, y_i - \delta y)$ and $(x_i - \delta x, y_i)$ respectively.

where start points for the test field lines are then given by,

$$s_+ = \{(x_1, y), (x_2, y), (x, y_1), (x, y_2)\}. \tag{3.11}$$

The start points then map to the corresponding end points as,

$$(x_1, y) \to (X_1, Y_1),$$
$$(x_2, y) \to (X_2, Y_2),$$
$$(x, y_1) \to (X_3, Y_3),$$
$$(x, y_2) \to (X_4, Y_4).$$

The derivatives are then found by,

$$\begin{aligned}
\frac{\partial X_-}{\partial x_+} &= \frac{X_2 - X_1}{\delta x} = a, \\
\frac{\partial X_-}{\partial y_+} &= \frac{X_4 - X_3}{\delta y} = b, \\
\frac{\partial Y_-}{\partial x_+} &= \frac{Y_2 - Y_1}{\delta x} = c, \\
\frac{\partial Y_-}{\partial y_+} &= \frac{Y_4 - Y_3}{\delta y} = d,
\end{aligned}$$

where N_+ follows from equation 3.6, Δ_+ from equation 3.9 and hence Q from equation 3.10. Q then serves to identify regions where QSLs may be present.

3.5 Additional Continuous Source Shapes

Here, an additional pair of magnetic source shapes are described, the annulus and the broken annulus shapes. First, the distribution of flux about the annulus is defined by,

$$D_n = \begin{cases} \cos\left(\frac{\pi(r_n - r)}{\frac{w}{2}}\right) + 1, & \text{if } r_n - r < \frac{w}{2}, \\ 0, & \text{elsewhere,} \end{cases} \tag{3.12}$$

where r is the radius of the annulus and w is the width of the annulus. The parameter r_n is the radius at position n given by,

$$r_n = \sqrt{\frac{(x_n - x_c)^2}{x_\alpha^2} + \frac{(y_n - y_c)^2}{y_\alpha^2}}, \tag{3.13}$$

where x_n is the x coordinate at a position n, x_c is the x coordinate of the annular origin and x_α is the scaling factor along the x-axis, with y_n, y_c, and y_α following similarly. The distribution of flux about the annulus is then varied by the equations,

$$V_n = p + q\cos\left(\pi + \pi\theta_n\right), \tag{3.14}$$

where $p + q = 1$, $q \leq 0.5$ and θ_n is the angle from the origin of the annulus as given by,

$$\theta_n = \operatorname{atan}\left(\frac{y_n}{x_n}\right). \tag{3.15}$$

The flux distribution in the annulus may be rotated on the plane by modifying equation 3.15 to give,

$$\theta_n = \operatorname{atan}\left(\frac{y_n}{x_n}\right) + \theta_\delta, \tag{3.16}$$

where θ_δ is the rotation of the annulus about the origin expressed in radians. These equations are then combined with the arbitrary flux ϵ to give,

$$F_n = \varepsilon D_n V_n, \tag{3.17}$$

or more generally,

$$F = \varepsilon DV. \tag{3.18}$$

The distribution of the magnetic field about the annulus is shown by figure 3.4a, for the case where $p = 0.6$ and $q = 0.4$.

A broken annulus of flux consisting of m discrete arcs is built in a piecewise manner. First, m discrete-point pairs are defined by,

$$p_k = \frac{k\pi}{m} + \theta_\delta \pm \frac{\theta_w}{2}, \tag{3.19}$$

where k is an integer between 1 and m and θ_w is the angle subtended by the arc from the origin. The flux is again varied along the arcs by equation 3.14, with the additional constraint that $p = q = 0.5$, i.e,

$$\bar{V}_n = \begin{cases} 0.5 + 0.5\cos\left(\pi + \pi\theta_n\right), & \text{if } p_k \leq \theta_n \leq p_{k+1}, \\ 0, & \text{elsewhere,} \end{cases} \tag{3.20}$$

which causes the flux to tend to zero at the ends of the arc. The flux distributed about each arc is then given by,

$$F_n = \frac{\varepsilon}{m} D_n \bar{V}_n, \tag{3.21}$$

and is illustrated by figure 3.4b.

3.6 Case Study Setup

The following topological cases have been produced with the same modelling assumptions as those described in sections 2.1, 2.2 and 2.3 for point source and continuous source topologies respectively. Artificial symmetries in the source configurations have been removed by perturbing source positions slightly, to avoid symmetric cases. Where a case has an imbalance of magnetic flux in the photospheric plane, a balancing source is assumed to exist at infinity (Inverarity & Priest 1999). For discrete source models, the balancing source at infinity is on the $x-y$ plane since all sources exist on this plane. In models which use continuously distributed sources,

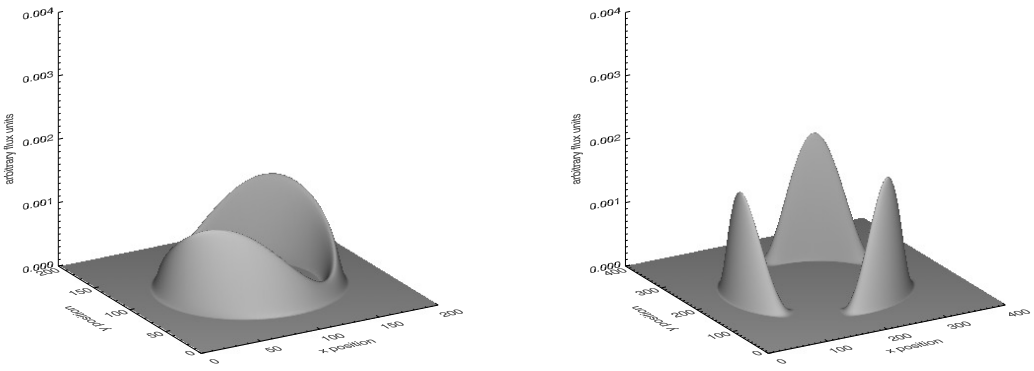

(a) (b)

Figure 3.4: Surface plots of a) the annulus source and b) the segmented annulus source flux distributions.

the magnetic flux of the balancing source is distributed across each cell of the bounding surfaces, which simulates the effect of the source placed at infinity on the $x - y$ plane.

The first case considered arises from four distinct sources of magnetic flux, initially in the discrete source regime, with a comparison to the continuous regime. The parameters for all of the sources used in this case study are shown in table 3.1. Where continuous sources are used, they are centred on these points, and have their flux distributed over a radius of $r = 0.28$ about this point. The model is then adapted to include NLPs, and topological differences are identified. Next, a series of configurations where two positive sources are contained within the boundary of an annulus of flux is studied. One topological state found has an open separatrix surface, as termed by Priest (2014). However, the inclusion of NLPs in the topology suggests that the surface may not be as open as previously suggested.

Non-Overlapping Source Parameters			
Source	**x**	**y**	ϵ
S1	0.40	-0.20	0.50
S2	-0.40	-0.21	0.50
S3	-0.01	0.50	-0.50
S4	0.01	1.25	-0.50
Positive Overlapping Source Parameters			
Source	**x**	**y**	ϵ
$S1_O$	0.18	-0.20	0.50
$S2_O$	-0.18	-0.21	0.50
Negative Overlapping Source Parameters			
Source	**x**	**y**	ϵ
$S3_O$	-0.01	0.72	-0.50
$S4_O$	0.01	1.08	-0.50

Table 3.1: Table containing the parameters for the configuration of the discrete and continuous sources used for the four-source case study. S_O represents sources which have been repositioned so that they overlap one another. Here, ϵ is used to represent the flux prescribed to each source.

3.7 Case Study: Four-Source Topologies

This first case study uses topologies produced from four sources of magnetic flux. In each configuration, two of the sources are positive and two are negative. Each magnetic source has the same absolute flux (0.5 arbitrary units), thus the cases considered here exist in a state of flux balance. Whilst such an occurrence is not typical of the solar surface, these cases provide the initial steps towards locating

NLPs and formulating a foundation for their properties. Discrete source topologies and continuous source topologies are produced under the same initial conditions and compared to one another.

3.7.1 Discrete Sources

Initially, the four-source case is modelled by a configuration of four discrete sources of magnetic flux positioned in two source pairs (figure 3.5a), using the parameters for sources S1 - S4 shown in table 3.1. A magnetic null point exists in the region between each pair of like-charged sources. The resulting topology is shown in figure 3.5b. Here, each of the two null points gives rise to a separatrix surface and a single magnetic separator exists, connecting the two null points where the separatrix surfaces intersect. This gives a topology similar to the intersected state as presented by Brown & Priest (1999); the main difference between this topology and the three-source intersected state is the additional source of flux. The two positive sources are then positioned closer to one another (figures 3.6a, 3.6b), now using sources $S1_O$ and $S2_O$ instead of S1 and S2, and the resulting topology is qualitatively the same as the initial topology. It is clear that discrete sources of flux will not 'overlap' unless they are placed at the same coordinates. Hence, the magnetic null point between the positive source pair is preserved, as expected, preserving the topology of the magnetic skeleton as the positive sources are repositioned.

3.7.2 Continuous Sources

This simulation is subject to same initial conditions as the discrete source case discussed in section 3.7.1, except continuous sources have been used to distribute the magnetic flux across the $z = 0$ plane. Each of the sources is defined with a radius of $r = 0.28$, centered on the same coordinates as the discrete sources (figure 3.5a). As there is flux balance in the photospheric plane ($z = 0$) for all of the cases in

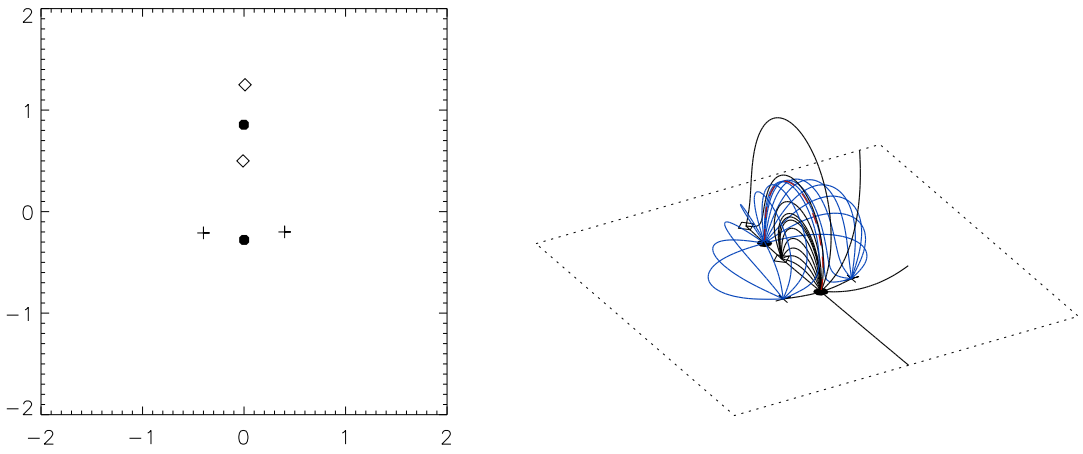

(a) (b)

Figure 3.5: Configuration and topology of the discrete, four-source case. a) The positions of the magnetic sources when they are apart from each other. Crosses mark the positions of the positive sources, diamonds are negative sources and dots are null points. b) The magnetic skeleton produced by this source configuration, showing a separatrix dome, intersected by a separatrix wall, producing a separator.

this study, the other five surfaces which bound the volume need no flux distributed across them, so each of their grid cells is given a value of 0. Thus, the divergence theorem (equation 1.4) is preserved.

Initially, each of the sources is separate from each other, and the topology of the magnetic skeleton (figure 3.7a) is the same as its counterpart in the discrete source case (figure 3.5b). However, as the two positive sources are repositioned closer to one another, they begin to overlap, causing the null point between them to vanish (figure 3.7b). This changes the topology such that there is now only a separatrix dome present, where the separatrix wall and associated separator have been eliminated by the source overlap.

Chapter 2 studied the bifurcation processes that occur when two magnetic null points interact. In the case considered here, there is no such interaction taking place,

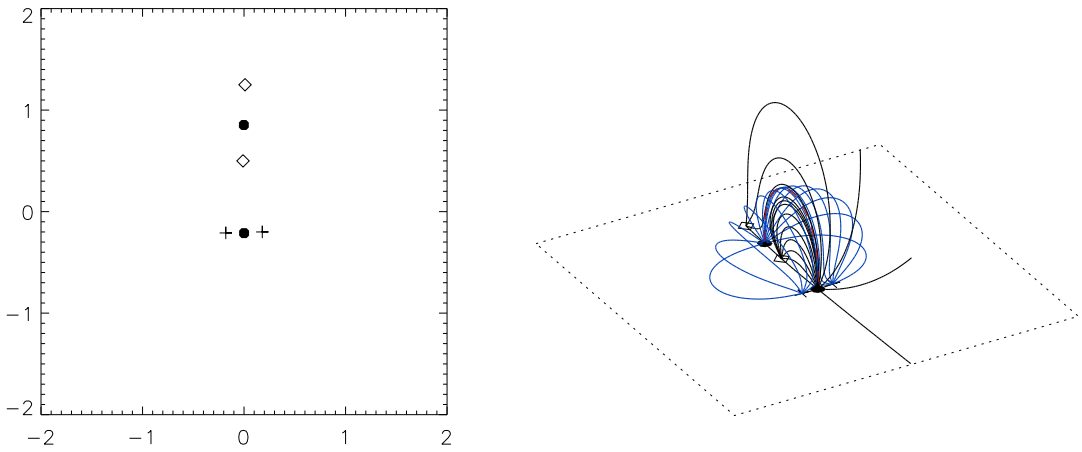

(a) (b)

Figure 3.6: a) The configuration of the sources when the positive sources are close to each other. Crosses mark the positions of the positive sources, diamonds are negative sources and dots are null points. b) The topology produced by this configuration.

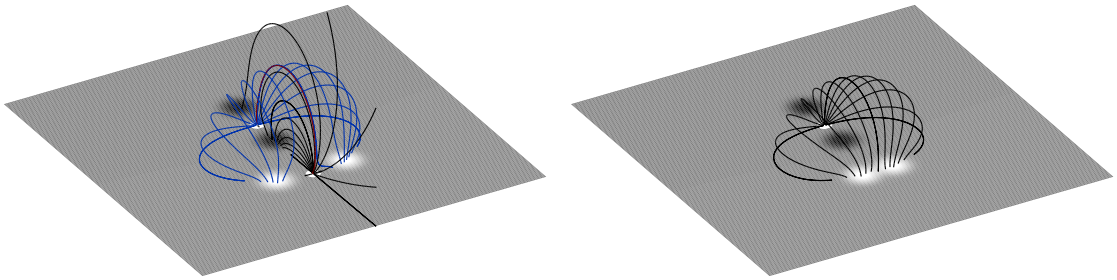

(a) Initial Configuration (b) Final Configuration

Figure 3.7: A four-source topology with circular sources of magnetic flux. (a) None of the sources overlap and each pair has a null point between them. (b) The positive sources now overlap. When compared to figure 3.6b, it is clear that the null point is lost in the overlap.

as only a single null is located between the two positive sources. Hence, the removal of the null point is the result of the overlapping flux, as the definition of the null point no longer holds (i.e. $B_z \neq 0$).

3.7.3 Continuous Sources with Null-like Points

The topology is then adapted to include locations of both true null points and NLPs. Figure 3.8 shows the configuration of the magnetic sources in the $z = 0$ plane, where positive flux is shown by white regions and negative flux is represented by black regions. Nullclines where $B_x = 0$ (blue) and $B_y = 0$ (red) are plotted over the region, and where these nullclines cross indicate points where $B_x = B_y = 0$. One such location is between the two negative sources where $B_z = 0$, so a true null point is found. There are three such locations in the overlapping positive sources, two (blue) are at the source centres and correspond to source-like points. The remaining (red) location corresponds to a null-like point. This is co-located with an x-line structure. From this NLP, a separatrix-like surface is extended which forms a wall structure, which replicates the behaviour of the previously existing null point (figure 3.9). This surface intersects the dome of the null between the negative sources, connecting the null to the NLP in a separator-like field line. Thus, the topology of figure 3.7a is preserved, using a separatrix-like surface and a separator-like field line.

The distribution of the flux in the region local to the NLP is also considered. If the two sources combined are considered to form a single magnetic footprint, then along the major axis of the footprint, one finds a local minimum in the flux distribution where the NLP has been detected. Next, the minor axis of the footprint is considered, where it is revealed that a local maximum is present in the flux measure at the location of the NLP. Together, these two features form a saddle in the flux measure (figure 3.10). In this case, the NLP is also located at this saddle.

This simplistic configuration illustrates the importance of NLPs in a continuous source regime, as they complement the magnetic skeleton produced by the magnetic sources and reveal topological-like features that might otherwise be missed.

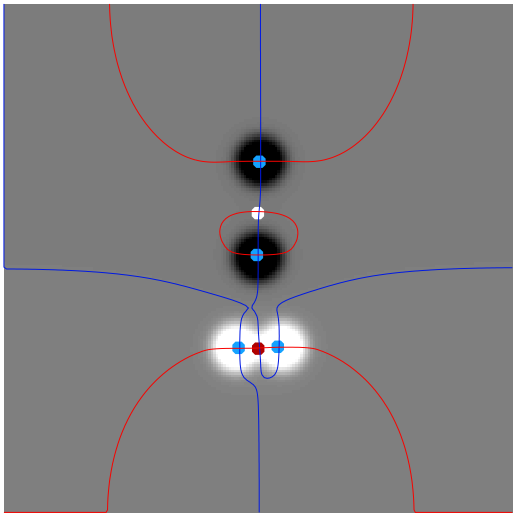

Figure 3.8: Planar plot of the four-source configuration. White dots mark magnetic null points, red dots indicate NLPs and blue dots show SLPs. Nullclines are plotted as blue and red lines representing $B_x = 0$ and $B_y = 0$ respectively.

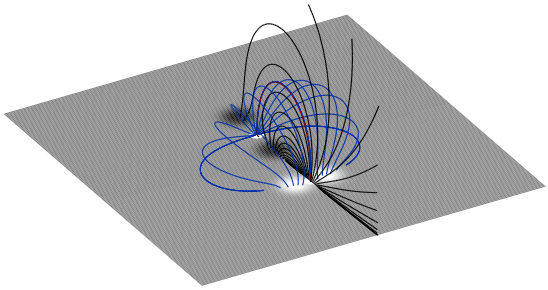

Figure 3.9: A four-source topology with the positive circular sources overlapping. Here, null-like points have been included, and one has been located in the overlap of the positive sources. The combination of the separatrix and separatrix-like surface form the complete magnetic skeleton and exist in a structure analogous to that found in section 3.7.1.

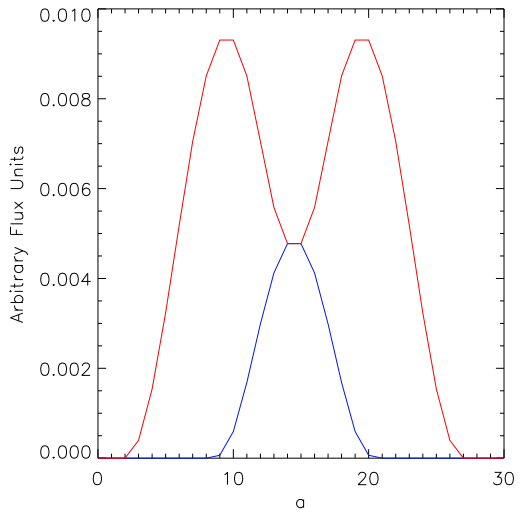

Figure 3.10: Flux measure against arbitrary distance along the overlapping sources. The red line shows the flux along the major axis combined source. The blue line gives the flux along the minor axis of the overlapping sources. The local minima of the red line and the local maxima of the blue line coincide, indicating a saddle point in the distribution.

3.7.4 Using a Squashing Factor to Identify a Null-Like Point

Although an NLP can be located by its definition, calculation of the squashing factor, Q, provides further evidence for the role of the NLP in defining the separatrix-like surface. The definition of the squashing factor was presented by Titov et al. (1999) for finding the location of quasi-separatrix layers (QSLs) and was outlined in section 3.4. Here, it is used as an accompaniment to the definition of the NLP to demonstrate that these are locations where an x-line protrudes through the base of the simulation.

The squashing factor is calculated from four field lines per grid cell which has $B_z \neq 0$. It is repeated for all source cell elements to produce a Q-map showing how Q varies across the sources. First for the non-overlapping case (figure 3.11a), using sources S1 - S4 from table 3.1, two distinctive features are present on the 'Q-maps'

for the configuration. The first is a diffuse region where the value of Q gradually increases to a peak, located on each source where it is closest to the other source of the same polarity, whilst the other feature presents as a distinctive line, often only one grid cell across, of a sudden increase in the squashing factor. The diffuse regions indicate the presence of a magnetic null point, with field lines starting close to the null point diverging from one another more than those which originate from cells further away. However, the Q-map does not map the null point itself, as this is not located within the boundary of a source. The peaks in Q coincide with the locations where the separatrices extending from the null points meet the photospheric plane. Where the surfaces bisect grid cells, the field lines generated at the cells exist in different domains of connectivity and thus will have a greater divergence than field lines in the same connective domain. Thus, the presence of both the null points and their associated surfaces are clearly distinguishable in the non-overlapping case in figure 3.11a.

Next the Q-map is generated for the configuration where the (lower) positive sources overlap (figure 3.11b), using sources $S1_O$, $S2_O$, S3 and S4 from table 3.1. Here, an NLP is present in the overlapping region of the two positive sources. Its presence is indicated by the increase in the Q value, though this signature is less intense than that found about a null point. There is also a diffuse region extended about the signature of the null point between the two negative sources. Here, a long tail of increased Q extends away from the null point, across the negative sources. This tail follows the path of the separatrix-like wall, which extends from the NLP, indicating its presence. The signature of the separatrix dome from the null point is present across the negative sources, as a curve of high Q across the sources.

The case where the negative sources overlap, but the positive ones do not, is shown in figure 3.11c, using sources S1, S2, $S3_O$ and $S4_O$ from table 3.1. Here, the presence of a null point between the two positive sources is clearly illustrated, as is

the associated separatrix wall, where it connects down to the negative sources. A gradual diffuse region about the overlap of the negative sources now indicates the presence of the NLP in the overlap. The associated separatrix-like surface is seen across the positive sources as a diffuse, curved region, following the path of the dome. Comparing figures 3.11a and 3.11c suggests that this is the correct analysis, as the separatrix dome and the separatrix-like dome produce similar signatures respective to their natures.

Finally, the case where both the source pairs overlap is studied for completeness (figure 3.11d), using sources $S1_O$ - $S4_O$ from table 3.1. Here, the Q-map supports the presence of both NLPs and their associated separatrices which are indicated by the diffuse regions across the sources.

The magnetic skeleton of the final two cases (negative overlap and both polarity overlap) strongly resembles the previous skeletons shown in figures 3.7a and 3.9, with one dome and one wall present in each. In the negative overlapping case, the dome originates from the NLP between the negative sources, making it a separatrix-like surface. The wall which is present in this case comes from the null point between the two positive sources. For the case where both source pairs overlap, both structures are separatrix-like surfaces, originating from null-like points in the source overlapping regions. In each case, a magnetic separator-like field line traces the intersection of the two surfaces.

3.7.5 Unmatched Flux Pair

In this study, the sources are positioned in the same configuration as the previous section (3.7.2). However, the flux of each source has been modified such that positive source S2 now has more flux distributed across it than its partner S1. The negative sources are still equal in flux but have additional flux distributed across them in order to preserve flux balance. The new source parameters used here are

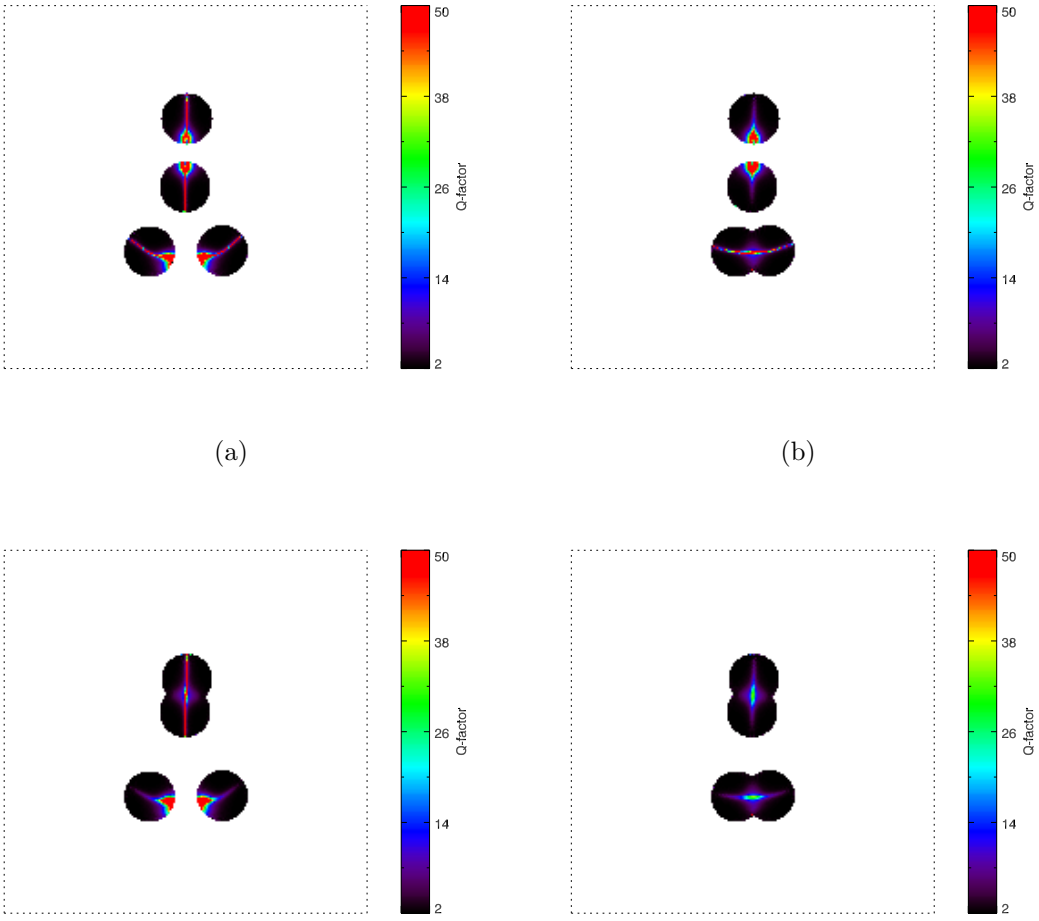

Figure 3.11: Q-maps for the four-source case when a) no sources overlap, b) the positive source pair overlap, c) the negative source pair overlap and d) both source pairs overlap.

shown in table 3.2. Despite these changes, there are still four SLPs, a single null point and one NLP present (figure 3.12). However, the path of the nullclines has changed such that the NLP and the SLP of the weak positive source are now closer together than in the balanced system. The aim here is to demonstrate the robustness of the previous result, that the Q-map indicates the presence of the NLPs and their associated separatrix-like surfaces, and show that it is not a product of some

Unmatched Flux Case Source Parameters			
Source	**x**	**y**	**ϵ**
$S1_O$	0.18	-0.20	0.50
$S2_O$	-0.18	-0.21	0.70
S3	-0.01	0.50	-0.60
S4	0.01	1.25	-0.60

Table 3.2: Table containing the parameters for the configuration of the continuous sources used for the four-source, unmatched flux case study. S_O represents sources which have been repositioned so that they overlap one another. Here, ϵ is used to represent the flux prescribed to each source. Assigned source numbers are the same as those used in table 3.1.

arbitrary symmetry.

Figure 3.13 shows that the magnetic skeleton of the resultant topology has the same components as that found under the previous configuration. The most distinct, qualitative difference is the curvature of the NLP's fan-surface due to the modified strengths of the sources.

Finally, study of the Q-map (figure 3.14) shows similar features to those in figure 3.11b. The key distinction here is the signature of the separatrix-like surface along the upper-most negative source. The signature is now curved, following the line of the separatrix-like surface, confirming that this signature indeed indicates the presence of the surface and is not an artefact of the calculation.

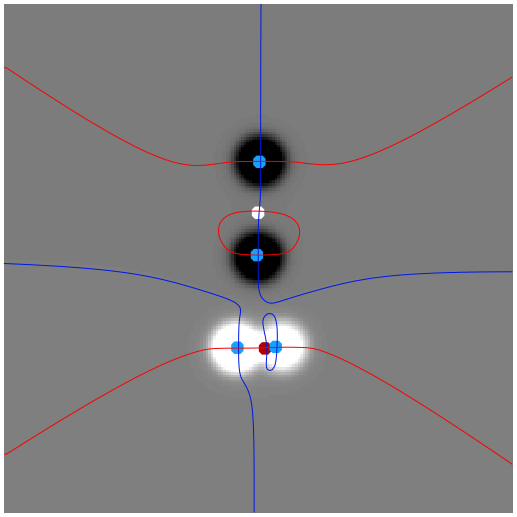

Figure 3.12: Planar plot of the source configuration for the unmatched positive pair. White dots mark null points, red dots are NLPs and blue are SLPs. Nullclines have been plotted over the region, where the blue and red lines represent $B_x = 0$ and $B_y = 0$ respectively.

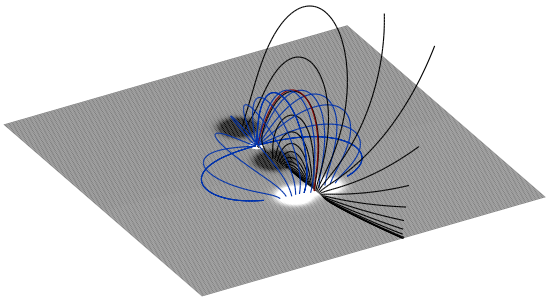

Figure 3.13: Topology of the magnetic skeleton in the four-source unmatched case.

3.8 Case Study: An Open Separatrix Surface

This case considers a configuration which produces an open separatrix surface (Priest 2014), which resembles a heliospheric curtain from the potential field source surface regime (Platten et al. 2014) (figure 3.15a).

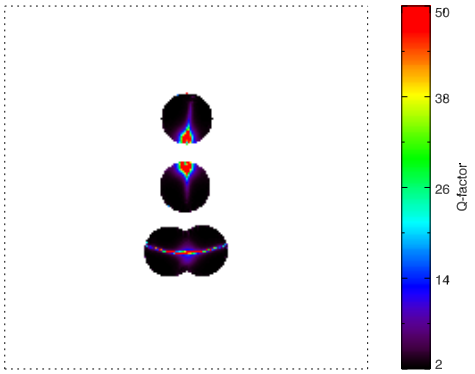

Figure 3.14: Q-map of the unmatched positive source configuration.

3.8.1 The Standard Topological Case

An annulus of negative magnetic flux (-3.0 arbitrary units of flux) encloses two circular sources of positive magnetic flux (0.5 arbitrary units each, producing 1.0 arbitrary units of flux in total). This configuration has an imbalance of flux distributed across the photospheric plane ($z = 0$). For the visualisation of the topology due to this source configuration, boundary conditions follow the description outlined in section 2.3.1, where the normal field for each point on the bounding surfaces is approximated using the analytical expression for the magnetic field (equation 2.1). However, when producing the Q-maps of the source configurations, the boundary conditions are then set such that the flux imbalance is distributed uniformly across the upper plane ($z = n$) bounding the volume, as discussed in section 2.3.1.

The magnetic skeleton consists of three coronal null points and a single photospheric null point. Two of the coronal nulls have fan surfaces which project down to the photospheric plane, forming the two coronal domes. The spines of these nulls are upright, extending down to the photosphere, and up into the corona. These spines also bound the fan surface of the 'central' coronal null such that it forms the open separatrix surface. The spine field lines of the central coronal null then project

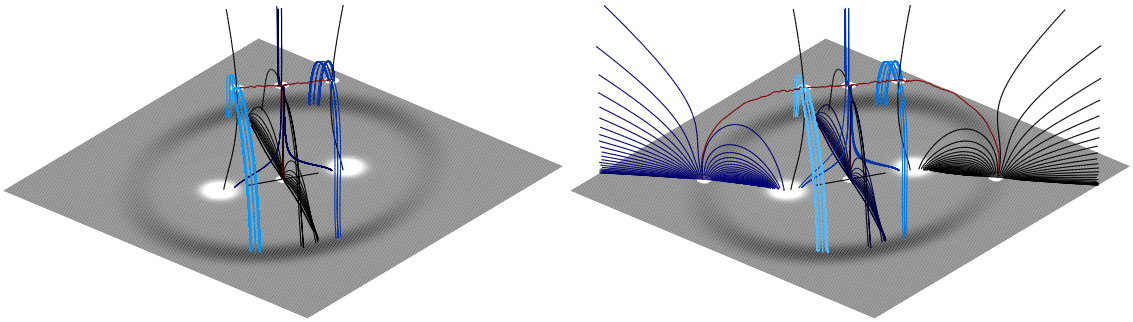

(a) (b)

Figure 3.15: Topology of the open-separatrix surface case when NLPs are a) excluded from the model and b) included in the model.

down to the photospheric surface, each connecting to the annulus of flux. Together, these spine field lines bound the separatrix wall of the planar null point, despite the appearance that they are offset (plotting 15,000 field lines from this null shows a warped separatrix wall structure, not a separatrix dome). The fan of the planar null then intersects the fan of the central coronal null in a separator field line, of which there are three in total as the central coronal null points fan also intersects each of the coronal domes. Thus, each null point has one separator field line connecting it to the central coronal null. This topology has three domains of connectivity, two of which are internal to the coronal domes, meaning that the volume exterior to the domes is a single connective domain. This would mean that footpoint motions of a field line may move it from one side of the open separatrix surface to the other, without undergoing reconnection or crossing a separatrix surface.

3.8.2 Annulus of flux with Null-like Points

The initial condition and configuration of the sources used in this scenario are the same as those used for the case in section 3.8.1. However, this scenario locates the null-like points and focuses on the changes they introduce to the topology. Two

null-like points are found within the annulus, along with their fan field lines (figure 3.15b) which define the QSL, in the form of separatrix-like walls. Each of these walls intersects the coronal domes which are present, with a separator-like field line running along each intersection.

Figure 3.16a shows the positions of the null point, null-like points and source-like points within the source configuration, along with the B_x and B_y nullclines in the region. Mapping the squashing factor for this configuration shows a band of increased Q internal to the source annulus (figures 3.16b, 3.16c). A mask has been applied to the Q-map as shown in figure 3.16c. The mask removes cells where the field lines have connected to the $z = n$ surface at the top of the volume, as these are not representative of the field lines connectivities since they do not terminate at another source in the photospheric plane $z = 0$. This band illustrates where the footpoints of the coronal domes meet the $z = 0$ which agrees with previously observed results (Masson et al. 2009). At the locations of the NLPs, an increase in Q can be seen in the Q-map but this is somewhat masked by the coronal dome marker. The increase in Q due to the separatrix-like surfaces crossing the circular sources is also not as apparent here as it was in figure 3.11. The reasons for diminished signatures in the Q-maps are discussed further in section 3.10.

When NLPs are considered, the open separatrix surface discussed in section 3.8.1 is not as open as previously thought. The motion of a field line from one side of the open separatrix surface to the other would see it cross either the 'open separatrix' or a QSL generated by one of the NLPs. Whilst field lines on either side would still be within the same domain of connectivity as one another, motions across the QSL would cause them to undergo slip-running reconnection or magnetic flipping (Aulanier et al. 2006; Priest 2014).

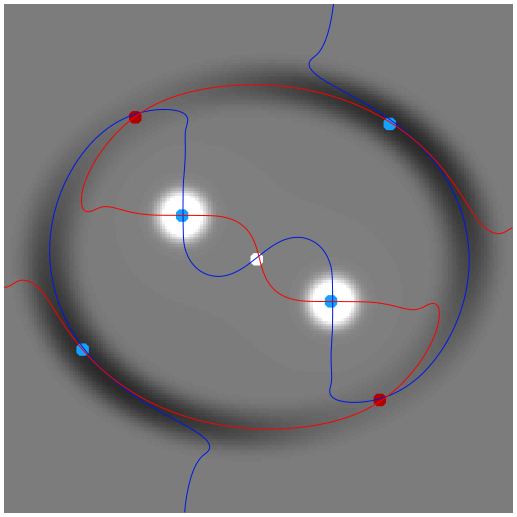

(a)

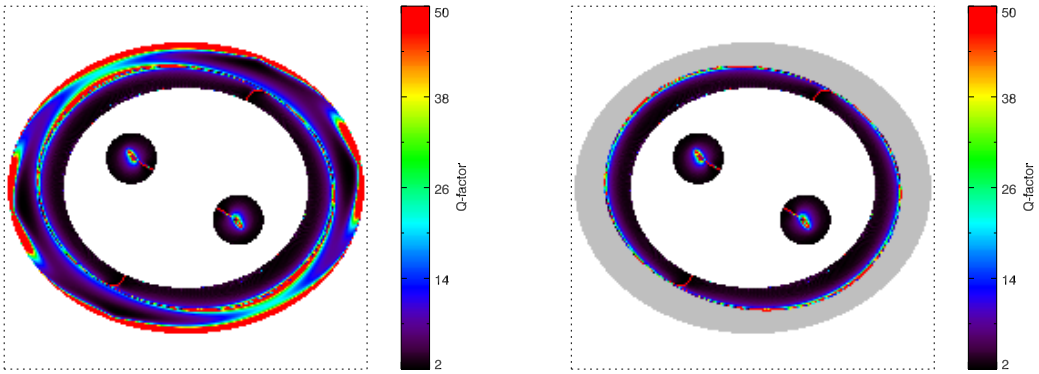

(b) (c)

Figure 3.16: a) Planar plot of the open-separatrix case, where white dots mark null points, red dots are NLPs and blue dots give SLPs. Nullclines for the configuration are overplotted, blue and red lines are $B_x = 0$ and $B_y = 0$ respectively. b) Complete Q-map for the open-separatrix surface case. c) Masked Q-map of the source configuration. Where all four test field lines of a grid cell leave the volume, that cell has been shaded grey.

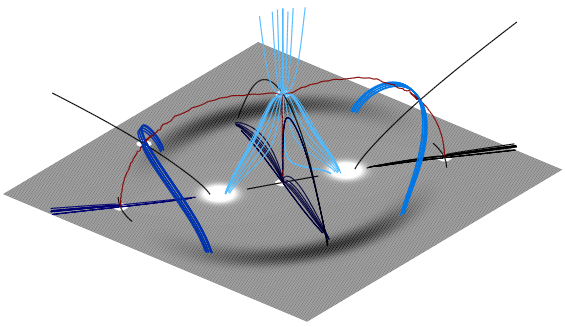

Figure 3.17: Topology of the magnetic skeleton which arises from the segmented annulus configuration with no source overlap.

3.9 Case Study: Segmented Annuli of Flux

The configuration of the elliptical source can be further developed by breaking it into several arcs of flux. By changing the angular extent of each arc, sources can be made to overlap or separate. This illustrates that where an NLP is found, removal of flux from that region allows a null point to be found instead.

3.9.1 No Source Overlap

The first topology studied has a configuration which consists of two circular sources of magnetic flux surrounded by two distinct arcs of flux (figure 3.17). Though no NLPs are present in the magnetic skeleton of this configuration, it is a useful comparative case for later scenarios where the arcs of flux overlap. Here, the topology arises from a total of six null points; there are three planar nulls and three coronal nulls (figures 3.17, 3.18a). Along with the null points, four source-like points are identified where the B_x and B_y nullclines intersect within the boundaries of the sources (figure 3.18a). The null points produce six separatrix surfaces and divide the volume into six domains of connectivity. The intersection of the surfaces produces a total of five separator field lines, where each connects to at least one coronal null point.

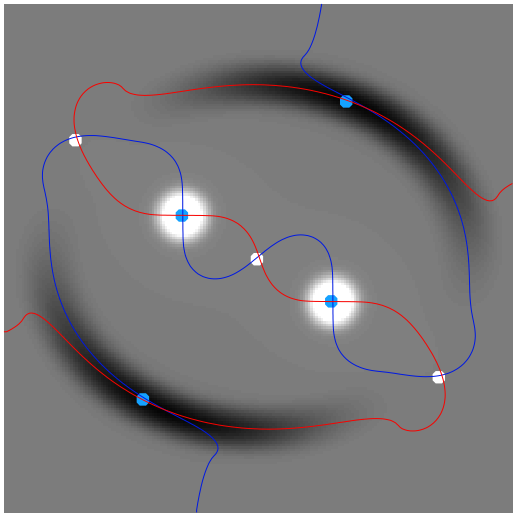

(a)

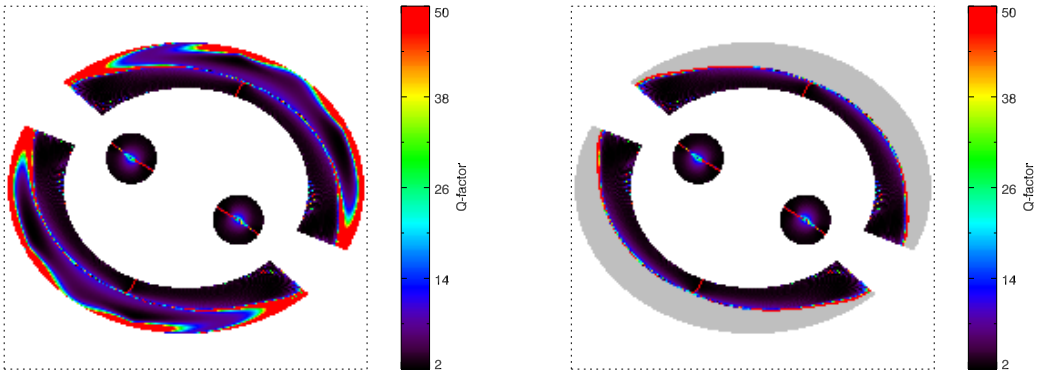

(b) (c)

Figure 3.18: Images for the annular configuration with no source overlap. a) Planar plot of the source configuration, white dots mark null points, where blue dots give the SLP positions. Nullclines for the configuration are plotted as blue and red lines for $B_x = 0$ and $B_y = 0$ respectively. b) The complete Q-map for this source configuration and c) a masked Q-map of the configuration. Where all four test field lines of a grid cell leave the volume, that cell has been shaded grey.

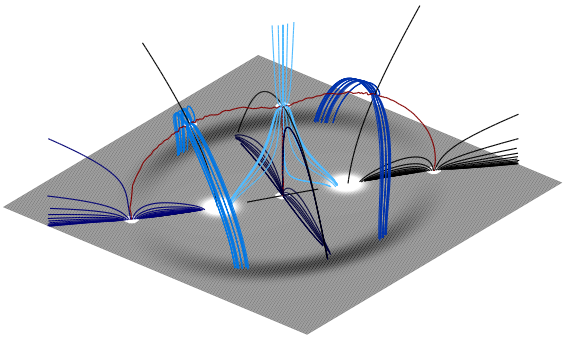

Figure 3.19: Topology of the magnetic skeleton which arises from the configuration with a soft source overlap.

Here, the Q-maps (figures 3.18b, 3.18c) show strong signatures where the central fan walls meet the photospheric plane. The signature associated with the coronal fan wall can be seen across the two circular sources, whilst the separatrix wall from the planar null is visible crossing the arcs of flux. By masking grid cells which have fields lines that terminate at the volume boundaries (figure 3.18c), the positions where the coronal domes project down to the photospheric surface are more readily distinguished, forming a red band along the length of the arcs. Each of the circular sources also displays a trail of heightened Q factors directed towards the null point locations. These lines indicate where the fan surfaces of the outside planar nulls project into the coronal dome interiors.

3.9.2 Soft Source Overlap

This case considers a modification to the source configuration in section 3.9.1 such that the end points of the elliptical arcs now overlap. The overlap of the sources is within the edge region where the additional profile for the flux has been applied by equation 3.21.

The features of the magnetic skeleton under this configuration (figure 3.19) match those from section 3.9.1 with the exception that two of the planar nulls have been

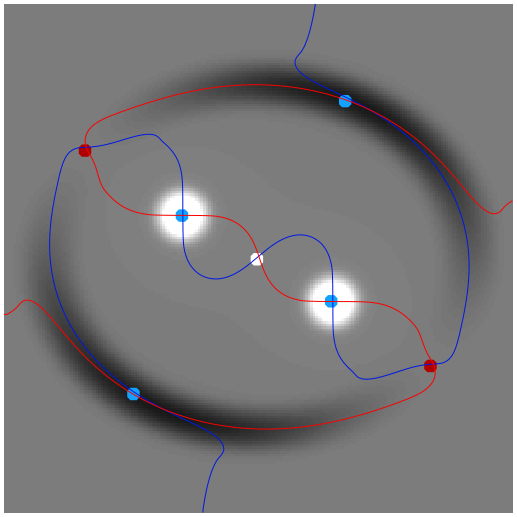

(a)

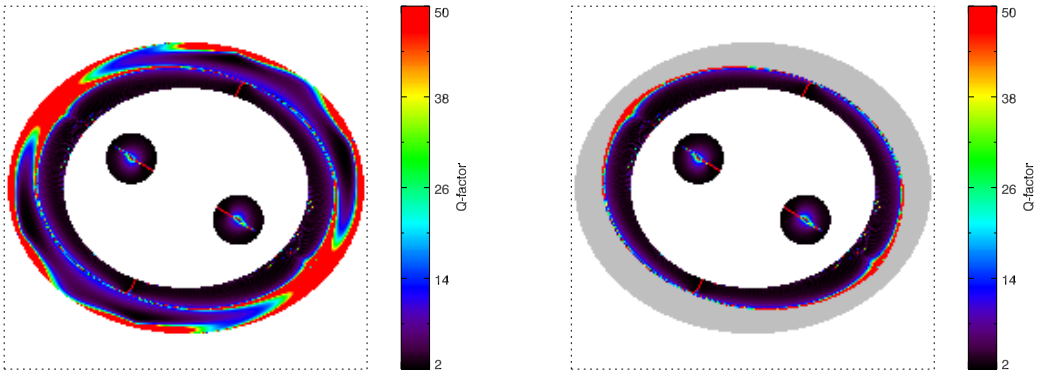

(b) (c)

Figure 3.20: Images for the annular configuration with a soft source overlap. a) Planar plot of the source configuration, white dots mark null points, where blue and red dots give the SLP and NLP positions respectively. Nullclines for the configuration are plotted as blue and red lines for $B_x = 0$ and $B_y = 0$ respectively. b) The complete Q-map for this source configuration and c) a masked Q-map of the configuration. Where all four test field lines of a grid cell leave the volume, that cell has been shaded grey.

replaced by NLPs within the overlapping regions (figure 3.20a), thus replacing two of the separator field lines with separator-like field lines. The separatrix surfaces have also been replaced by separatrix-like surfaces.

Several of the signatures present in the Q-maps for this configuration (figures 3.20b, 3.20c) are the same as those identified in section 3.9.1, hence only the identifiers for the NLPs will be discussed. Recall the result in section 3.7.4, where the NLPs had a slight increase in Q at their location, and their associated separatrices produced diffuse regions in the Q-maps. By again removing the cells which produce only field lines that leave the volume, the regions local to the NLPs can be more readily identified. Across the central circular sources, two heightened bands of Q can be seen, spanning from the centre of the sources, towards the inner boundary of the annulus. These features point towards the NLPs, which exist as small bulges on the annulus mapping. This result agrees with the result produced in section 3.7.4, but the signature of the separatrix-like surfaces is considerably less diffuse in this case.

3.9.3 Hard Source Overlap

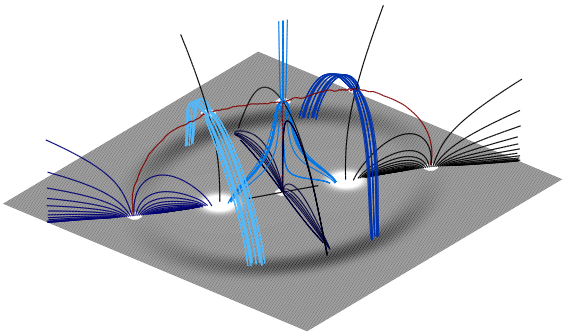

Figure 3.21: Topology of the magnetic skeleton which arises from the configuration with a hard source overlap.

Finally, the arcs of the annulus are extended further, increasing the area of

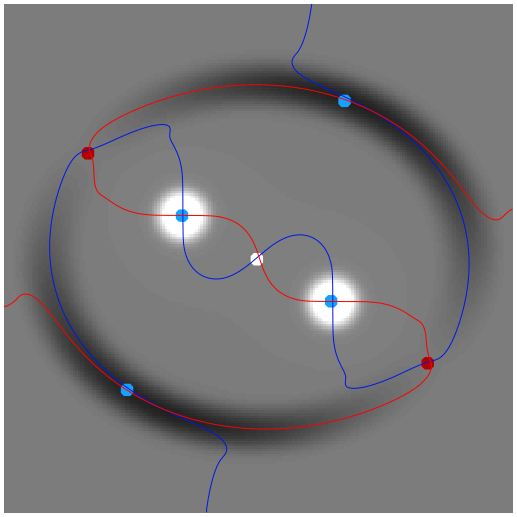

(a)

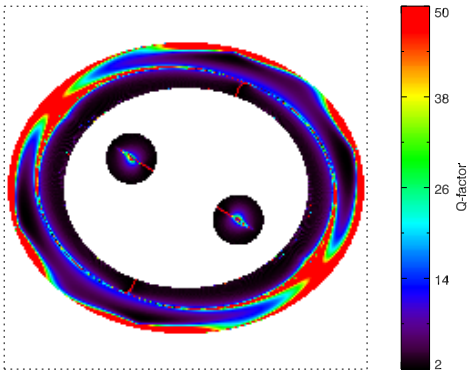

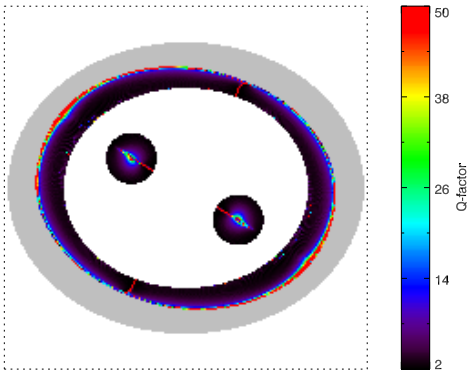

(b) (c)

Figure 3.22: Images for the annular configuration with a hard source overlap. a) Planar plot of the source configuration, white dots mark null points, where blue and red dots give the SLP and NLP positions respectively. Nullclines for the configuration are plotted as blue and red lines, giving $B_x = 0$ and $B_y = 0$ respectively. b) The complete Q-map for this source configuration and c) a masked Q-map of the configuration. Where all four test field lines of a grid cell leave the volume, that cell has been shaded grey.

the overlapping region. The topology from section 3.9.2 is preserved under this configuration (figure 3.21), along with the nullcline crossings (figure 3.22a), though the angle at which the nullclines meet has become much more shallow. The Q-map, however, has some contrasting features. First, the region local to the NLPs has a bulge which is much less pronounced than previously (figures 3.22b, 3.22c), and the signature across the circular sources, that is associated with the separatrix-like surfaces, is much more diffuse.

The diminished signature about the NLP in the Q-map indicates that field lines which extend from this position diverge from one another less than those in the soft-overlapping case. Analysis of the flux distribution shows that the flux is more uniformly spread across this region due to the nature of the overlap. This suggests that the uniformity of the flux distribution has implications on the role an NLP has within the magnetic skeleton.

3.10 Discussion

X-line structures are important sites in the study of reconnection. If an x-line is present in a magnetic field topology, then it is important to ensure that it is represented appropriately. X-lines are easily found as part of the topology in the point-source description but may easily be missed in the continuous source description. The case studies presented in sections 3.7, 3.8 and 3.9 highlight that the inclusion of null-like points prevents x-lines from being omitted from a topological simulation. Whilst discrete sources provide a good first approximation of the topology of a potential magnetic field, continuous sources are a better representation of the photospheric magnetic carpet. This chapter demonstrates that null-like points must be taken into consideration, for continuous source regimes to give a more complete picture of the topological structure.

Section 3.8 illustrated how even in a truly distributed source, rather than a source

overlap (section 3.9), null-like points can still be located, and provide insight into topological properties that may otherwise be missed. The inclusion null-like points in the magnetic skeleton of a topology provides a mechanism for the detection of at least some sub-class of QSLs within a magnetic configuration. Whilst there will almost certainly be cases where a QSL exists in the absence of an NLP, locating NLPs serves to produce a more complete picture of the topological structure. For example, the open separatrix surface (Priest 2014) is bound on each side by the spines of two other coronal null points. For the comparison topologies generated in this chapter, these spine field lines also form the boundaries for two QSLs originating from the null-like points. Whilst this does not separate the topology into any additional flux domains, it means that additional mechanisms, such as slip-running reconnection, would be required for a field line to cross from one side of the open separatrix surface to the other, without reconnecting across the surface itself.

Often models use magnetic sources with a high degree of uniformity, however in a typical quiet (or active) Sun region, one may expect to find a higher degree of irregularity to any magnetic source. The topologies presented in section 3.9 attempt to address this by applying additional functions to govern the distribution of flux along the sources which lie on the arcs of an ellipse. Though there is always an NLP present in the overlapping cases studied in section 3.9, it is posited that non-uniform configurations of magnetic flux will have more NLPs located in their topology, since NLPs have the strongest squashing factors in the least uniform distribution.

The work presented herein uses a potential magnetic field. However, there is no reason to believe that null-like points could only be defined in such a regime. Their definition and properties would be expected to be retained in a force-free magnetic field, or with full MHD simulations. Further work could investigate the inclusion of NLPs under a force-free regime.

Chapter 4

Solar X-ray Bright Points

4.1 Introduction

X-ray Bright Points (XBPs) are small, intense brightenings in X-ray and EUV emissions and many of their statistical properties have previously been studied, as outlined in section 1.2.2. They may manifest in the corona above ephemeral regions, but more commonly occur above cancelling magnetic flux fragments (Harvey 1985). Whilst a model for the formation of ephemeral regions remains unknown (Moreno-Insertis 2012), a converging flux model has been proposed as a mechanism for the formation of an XBP (Priest et al. 1994). Using the converging flux model, it was found that magnetic reconnection is responsible for the XBPs created (Parnell et al. 1994; Neukirch et al. 1997), where plasma is injected into the reconnected field lines which consequently brighten. Longcope (1998) present a model for the interacting flux in an XBP, considering current sheets and reconnection consequences, where the footpoints of the XBP neither emerge or cancel, but just come close enough together to interact.

Whilst many of the statistical properties of XBPs are known, and indeed other catalogues of bright points exist (McIntosh & Gurman 2005), the magnetic activity which takes place locally to the footpoints of the XBPs must also be considered to

fully understand the dynamics of XBPs. However, with the number of bright points present at any given time, manually forming a large statistical study is prohibitive.

This chapter outlines an algorithm for the automatic detection and tracking of XBPs along with the classification of related magnetic events in the photosphere, using line-of-sight magnetograms local to an X-ray bright point (XBP). The aim is to be able to classify the cause of the bright point onset, as well as its demise, automatically. A case study of twenty bright points is formed, and the classification assigned to events by the algorithm is compared to those assigned through visual inspection.

Initially, the methods for collecting an XBP catalogue are outlined in section 4.2. The method for classification of events is then discussed in section 4.3. Section 4.4 forms the case study on a selection of XBPs, where the reliability of the algorithm is then assessed in section 4.5.

4.1.1 SDO Data Collection

The period of observation for collecting this catalogue runs from 00:00 on March 12^{th} to 23:59 on March 16^{th}, 2017. This window was chosen as there were no active regions present on the solar disc. Data from the AIA instrument's 193 Å waveband, and HMI's line-of-sight magnetogram is used at a 90-second cadence. The measurement of the line-of-sight magnetic field at each pixel has an error of ± 10 gauss.

4.2 Collecting an X-ray Bright Point Catalogue

The process for collecting the X-ray bright point catalogue used in this thesis is similar to McIntosh & Gurman (2005) and is as follows. Each AIA 193 Å image (figure 4.1a) has a 101-point box-car smooth applied in both the x and y directions

(figure 4.1b). This smoothed image is then taken to give a typical background intensity and is subtracted from the original, forming a reduced image (figure 4.1c), showing intensity stronger than the background average. Small intensity enhancements are easier to consistently identify in this reduced image (McIntosh & Gurman 2005). The standard deviation, σ_p, of the pixel intensities, I_p, in the image is then calculated, and a mask is applied to the image given by,

$$F_{pixel} = \begin{cases} 1, \text{if } I_p > 3\sigma_p, \\ 0, \text{if } I_p \leq 3\sigma_p. \end{cases} \tag{4.1}$$

This provides an estimate of the significance of the intensity in a pixel, and regions identified as significant are defined as XBP candidates (McIntosh & Gurman 2005). A second mask is then applied to the image, so that regions, where the photospheric surface is inclined at more than 60 degrees to line-of-sight of the observer, can be ignored.

Next, a grouping algorithm is applied to the image, which collects adjacent pixels where $F_{pixel} = 1$ into distinct groups. Each group must then meet a set of criteria as follows, or be rejected from the sample. The total area of the group as calculated by,

$$A = n_p d_x d_y, \tag{4.2}$$

where n_p is the number of pixels in the group, and d_x and d_y is the size of each pixel in the x and y direction respectively, measured in arcseconds. For the AIA instrument, $d_x = d_y = 0.6$. It is then required that 90 arcsec^2 $< A <$ 3000 arcsec^2 else the detection is rejected which serves to eliminate large bright features from the collection, such as those found in an active region, as well as those deemed too small for further study. The second check applied to the group requires that the (approximated) ratio of its semi-major axis to the semi-minor axis, δ_s, be less than 2.5. This ensures that large bright features, such as the coronal loops above active regions, are removed from the sample(McIntosh & Gurman 2005).

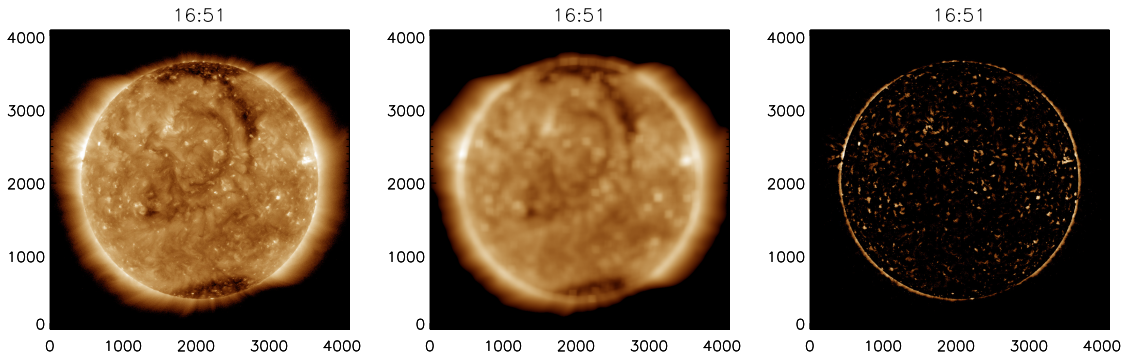

(a) (b) (c)

Figure 4.1: Images showing the solar disc, taken with AIA in the 193 Å waveband on March 12^{th} 2017, with different masks applied. a) The 'original' image, logarithmically scaled intensity between $\ln 25$ and $\ln 1500$. b) The 'original' image with a 101-point box-car average applied, giving the 'smoothed' image. c) The 'original' image minus the 'smoothed' image producing the 'reduced' image showing bright features.

The metadata for each grouping is then assembled. This includes information such as the number of pixels in the group, the coordinate at the centre of the group, and the date and time of the observation.

Finally, each group is assigned an identification number to enable distinct features to be tracked across the solar disc (figure 4.2). The position of each newly detected bright point is then checked against the predicted position due to solar rotation of all bright points detected in the previous half hour (where available). Provided the new detection is within some small radius of this predicted position, the identity numbers are set to be identical to allow the continued tracking of the feature, else a new identification number is assigned. This builds up the catalogue of XBP candidates tracked over time.

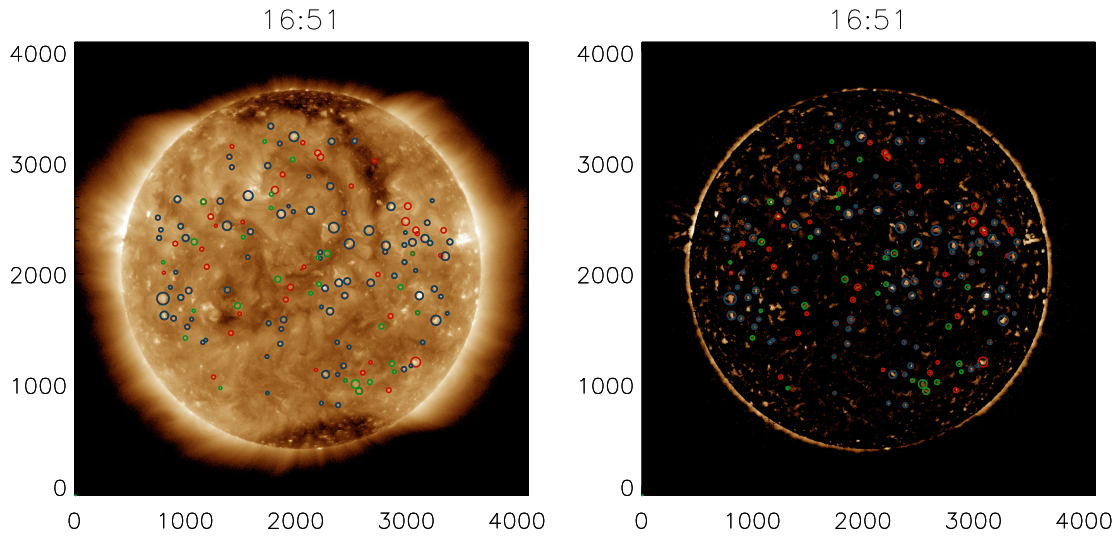

(a) (b)

Figure 4.2: Images taken with AIA in the 193 Å waveband, with the identified XBPs circled. a) The 'original' image and b) the 'reduced' image. Green circles indicate where a new feature is being tracked, blue circles indicate features that have been successfully tracked, and red circles indicate the predicted position of a bright point which has not been detected.

4.3 Event Analysis Method

This section focuses on classifying photospheric magnetic events, such as flux emergence and cancellation, which occur within the region local to an X-ray bright point. Initially, the flux curves of the measured absolute, positive and negative flux of the region are produced, as discussed in section 4.3.1. The method for identifying significant peaks in these curves is then outlined in section 4.3.2. Finally, the method for classifying different magnetic events based on these peaks is provided in section 4.3.3.

4.3.1 Producing Flux Curves

To identify when the magnetic flux in the region local to the footpoints of an XBP is changing, the flux in the region must first be measured. The magnetogram data is collected for the region local to the bright point, which is defined using the maximum size of the bright point over its lifetime in the x and y directions, say Δx and Δy, as identified in the reduced 193 Å data during the collection process. Initially, this size is measured as a number of pixels but is converted to arcseconds as the AIA and HMI instruments have different pixel resolutions. This ensures that the same area is being collected in the HMI data, as has been selected from the AIA data. A radial distance ΔR is defined about the centre of the identified bright point in the 193 Å data. This is done by selecting the larger of Δx and Δy and setting this to be equal to a parameter ΔR (i.e. $\Delta R = max(\Delta x, \Delta y)$). Next, a small value is added to this by,

$$R_m = \Delta R \bmod 15,$$
$$R = \Delta R + (15 - R_m),$$

where mod 15 is included to facilitate later video encoding. Flux within this local region is then collected (figure 4.3a) as the region is tracked with solar rotation.

The data must then be prepared for the calculations to be made. First, the radial distance of each point from the centre of the region, r_i, is calculated by,

$$r_i = \left((x_i - x_0)^2 + (y_i - y_0)^2\right)^{\frac{1}{2}}, \tag{4.3}$$

where x_i and y_i are the x and y co-ordinates of the point respectively, x_0 and y_0 are the co-ordinates at the centre of the region. A 3-point box-car smooth is applied to the image, and the pixel values I_p are then masked (figure 4.3b) dependent on their

radial distance, r_i, from the centre of the local region by,

$$F_{mask} = \begin{cases} I_p, & \text{if } r_i \leq 0.7R, \\ \frac{I_p}{2}\left(\cos\left(\frac{\pi(r_i - 0.7)}{0.25}\right) + 1\right), & \text{if } 0.7R < r_i \leq 0.95R, \\ 0, & \text{if } r_i > 0.95R, \end{cases} \tag{4.4}$$

to produce a circular aperture, centered on the bright point. Thus, flux within $0.7R$ of the centre remains unchanged as this is in the region local to the bright point. Flux that is in the region between $0.7R$ and $0.95R$ is scaled smoothly. This scaling smoothly reduces the contribution of flux as it moves further away from the region, rather than presenting a non-smooth jump as flux leaves the central aperture, which could lead to misidentification by the algorithm. The scaling provides similar benefits for flux entering the region. Finally, flux in the region beyond $0.95R$ is removed and set to zero, as this is outside the local region of the bright point.

The positive flux, f_+, per image is then calculated as the summation of each pixel with a positive flux measure. The negative flux, f_-, is then calculated in a similar manner. The net flux is given by $f_n = f_+ + f_-$, and the absolute flux is given by $f_a = f_+ + |f_-|$. The flux calculations for the region local to XBP03 are shown in figure 4.4.

The gradient of each curve (figure 4.5) is then found, in order to determine when the curves are either increasing or decreasing (i.e. flux is being added to the region or removed). This calculation is done through the linear regression of a 2-hour moving average window. For each time point, data in a $\pm$ 1-hour window is identified, and a simple linear regression is applied to this data. The slope is then taken to be the gradient of the flux at that point.

4.3.2 Peak Detection

When identifying peaks in the flux curve gradients, each curve is handled separately. The approach will be demonstrated for the absolute flux curve, but this can also

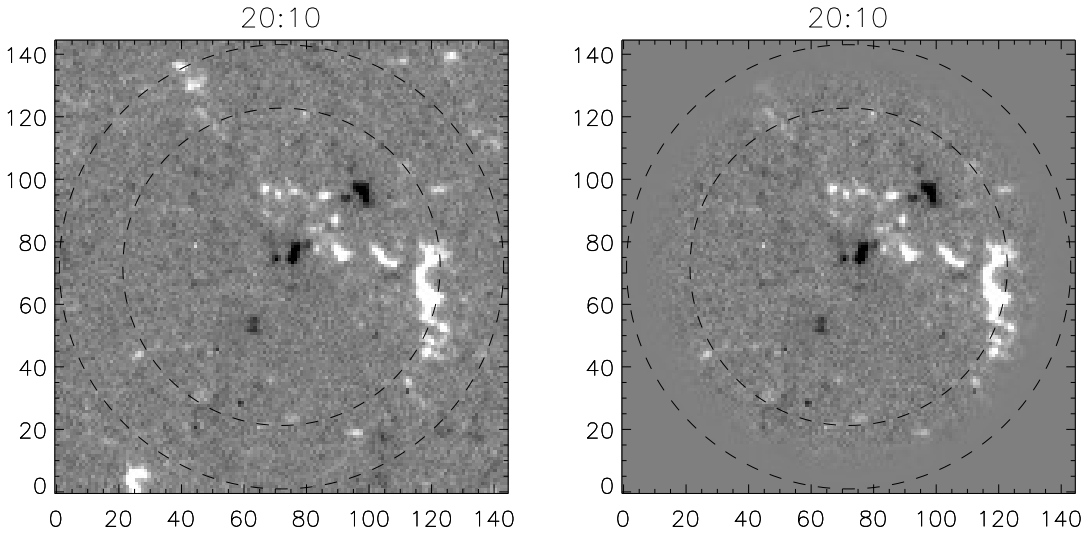

(a) (b)

Figure 4.3: a) Line-of-sight magnetogram image form the HMI instrument on March 12^{th}. b) The same image, but with the mask applied as given by equation 4.4. Contours of where the mask is applied are shown in each image for comparison, where the boundaries are represented by the dashed black lines.

be applied to the positive and negative flux curves in the same way. First, the curve is considered as consisting of two different populations, where the gradient is either positive or negative (as emergence typically happens on shorter timescales than cancellation). The deviation from zero is calculated for each, σ_+ and σ_-, using,

$$\sigma^2 = \frac{1}{N}\sum_{i=1}^{N}\delta_i^2, \tag{4.5}$$

where N is the number of data points where the gradient is positive or negative, and δ_i is the value of the gradient for the point i. This is akin to a standard deviation calculation with the mean taken to be zero. When the data was treated as a single population, often events would be missed due to large emergence events, leading to large deviations and making cancellation events non-significant.

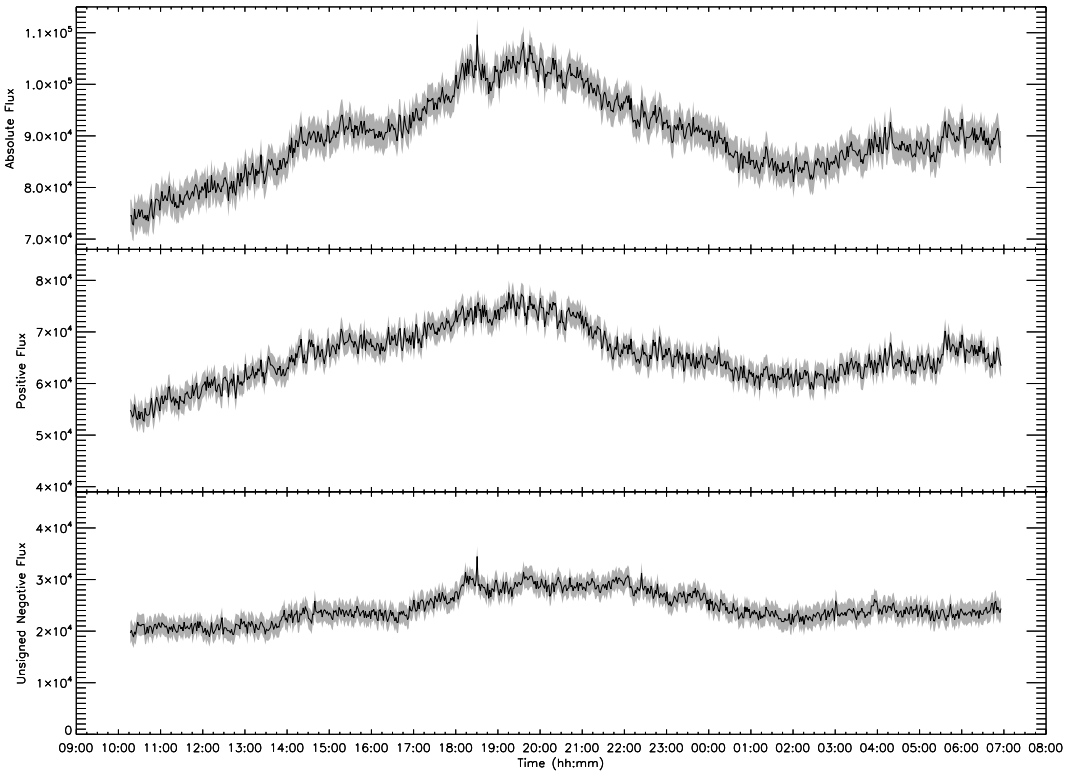

Figure 4.4: Flux curves calculated from the region local to XBP03. The error of each calculation is given by the shaded region about the line.

Once such a region has been found, the largest value within the region is then identified and stored as a significant peak. The tails of each peak are then identified, by scanning forwards (backwards) from the peak value, searching for a gradient which is smaller than all those in the 30 minutes following (preceding) it. Alternatively, if the gradient crosses the t-axis and changes sign, the tail of the peak is taken as the last value of the same sign as the peak value. The distance between the two tails then provides the width of the peak. An example of the final peak graph is shown in figure 4.6, where blue dashed lines represent deviations from zero of the increasing gradient, and red dashed lines are the deviations from zero of the decreasing gradient. Dot-dash lines give the bounds of detected events, with the peaks of each event plotted as solid, vertical lines. Subsequent events have been

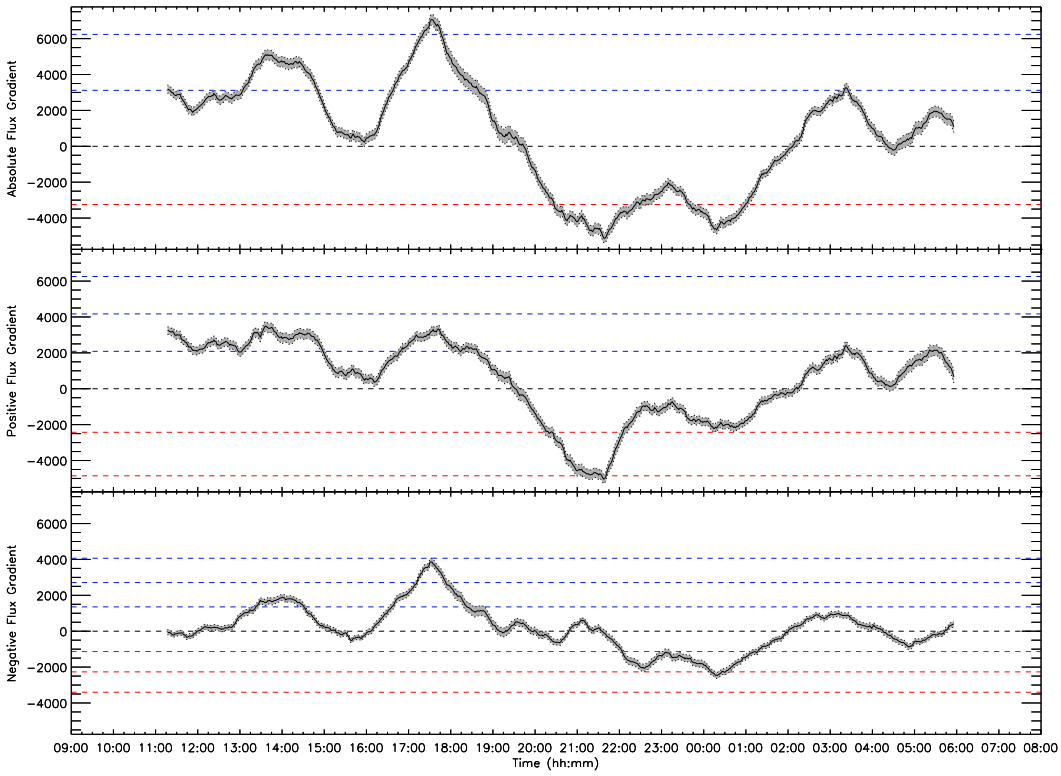

Figure 4.5: Gradients of flux curves calculated from the region local to XBP03. The error associated with each value is given by the shaded region about the line. The red dashed lines give deviations from zero for negative gradients, while the blue dashed lines are deviations from zero of positive gradients.

shaded in an alternating pattern so that adjacent events are more easily distinguishable. The bar at the top of the figure indicates the times for which the bright point was automatically tracked, and the event numbers are indicated as I_x, above the absolute peak that they have been associated with.

Finally, after the width, tails and peak of the curve has been calculated, the peak-region is numerically integrated using the trapezium rule. This provides an estimate of the flux introduced to or removed from the region over the times encompassed by the peak. The second peak detected in XBP03 is analysed here (figure 4.7a). The tails of this peak provide the time frame for the event as running between 15:57 and

19:43 on March 12^{th}. The absolute flux measures (figure 4.7b) at the start (f_0) and end (f_N) of this window are found, and the difference between them is taken using,

$$f_\delta = f_N - f_0, (\pm(\varepsilon_N^2 + \varepsilon_0^2)^{\frac{1}{2}}), \tag{4.6}$$

where ε_N and ε_0 are the measurement errors associated with f_N and f_0 respectively. For this event, this returns a value of $f_\delta = 13,091 \pm 4,399$ G. The value of f_δ approximated by the numerical integration is $f_\delta = 12,275$ G, so the two compare well, validating the approach taken.

4.3.3 Event Identification

Once the peaks have been identified, in the absolute, positive and negative flux gradients, a second procedure is applied to the dataset to relate the absolute flux measurement to the positive and negative flux. Using the result of the previous program, coincident peaks are found by scanning across the events indicated by the absolute flux curve. For a positive (or negative) peak to be associated with the absolute peak, some conditions must first be met. First, the positive peak must fall within the tails of the peak in the absolute flux curve. If this condition is met, the absolute peak is then checked to ensure that it falls within the tails of the positive flux peak. If both conditions hold, then the event is flagged, but otherwise, it is rejected, and another peak value is sought. For a peak in all three curves to be associated, the peaks in the positive and negative curves must both fall within the tails of the absolute flux peak. Secondly, the absolute peak must sit within the tails of both the positive and negative peaks. Finally, the positive peak must fall within the tails of the negative peak. When all these conditions are met, the three peaks are associated as a single event.

In summary, for a positive (negative) peak to be associated with an absolute peak, both peaks must be located within the time-window of the other peak. For peaks in all three curves to be associated, the previous criteria must hold for both

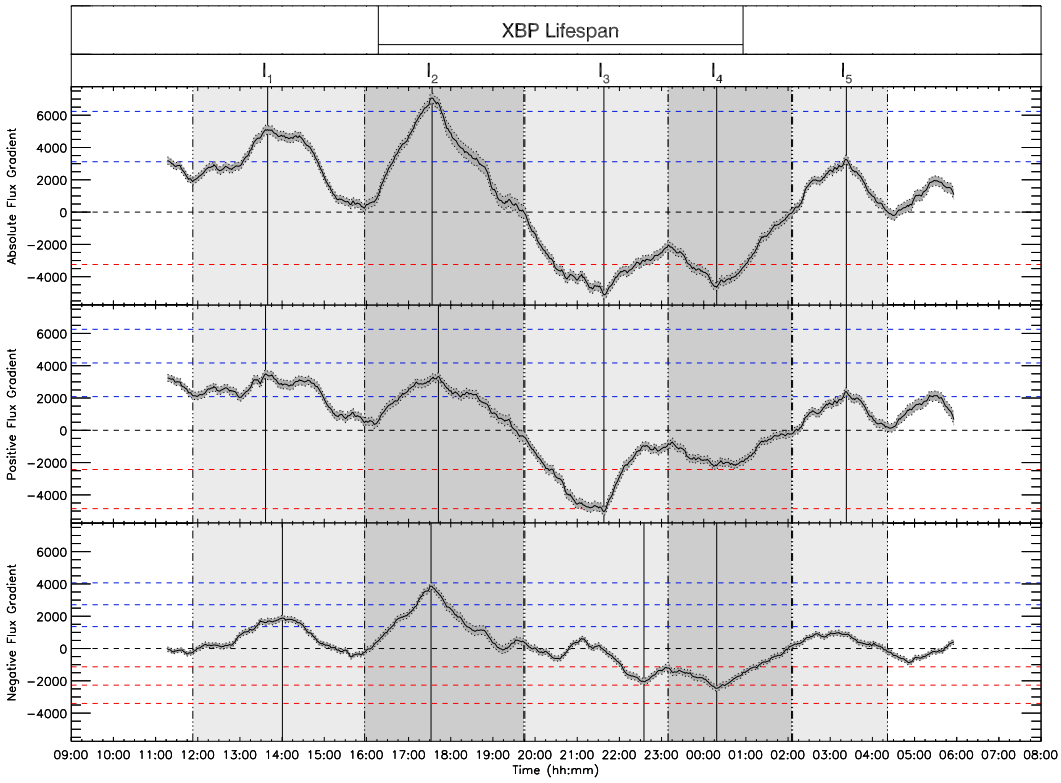

Figure 4.6: Gradients of the absolute, positive and negative flux measures for XBP03. Blue dashed lines represent deviations from zero of the increasing gradient, where red dashed lines are thedeviations from zero of the decreasing gradient. Detected events are bound by vertical dot-dash lines, with the peaks of each event plotted as solid, vertical lines. The bar at the top of the figure indicates the times for which the bright point was automatically tracked.

the positive and negative peak and the positive peak must be located within the window of the negative peak.

Table 4.1 provides the criteria used to classify the different possibilities of events, which can reliably be discerned from the curves. If there is an increase in both the positive and negative flux (and hence the absolute flux) then flux emergence is assumed to have taken place. Emergence events can be considered as two qualitatively

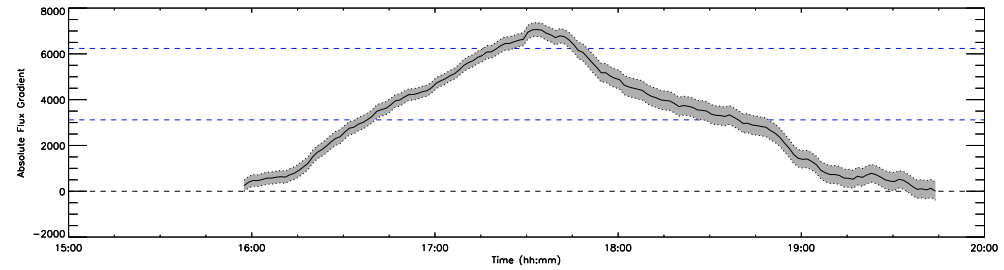

(a)

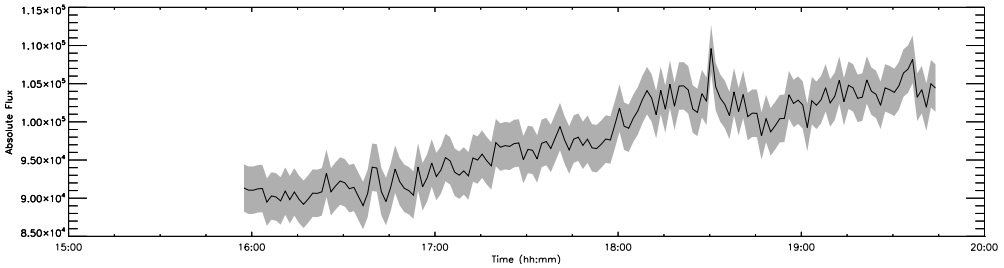

(b)

Figure 4.7: a) Absolute flux gradient for the second detected event of XBP03. b) The absolute flux measure from the magnetogram local to XBP03, during the time window associated with event number two.

different types of events. The first involves the emergence of two concentrated fragments of opposing polarity flux and typically is simply referred to as an emergence event. Alternatively, the emerging flux may form multiple different fragments, which interact with each other during the emergence and may rapidly coalesce with other emerging fragments. Emergence events of this form will be referred to as 'explosive emergence' events.

A decrease in all three of the flux curves is assumed to be due to cancellation. Cancellation events currently only have one classification, as there has been no observed qualitative difference between the instances of cancellation. The increasing and decreasing classifications relate to changes in the flux measurement of a single polarity, along with a corresponding increasing or decreasing absolute flux, due to the drifts of the magnetic fragments present in the local region. A decreasing drift

is recorded either when a large fragment drifts out of the local region and into the annular region, or when an island of flux fragments into smaller clusters. Conversely, an increasing drift is detected when multiple fragments coalesce to form a single island of flux, or when new magnetic flux fragments enter the local region from the annular region. The fragmentation and coalescence of flux leads to these gradients since these events alter the alignment of the flux to the line-of-sight of the spacecraft. As flux fragments, the resultant field is able to spread out more, with less flux directed along the line-of-sight. However, as fragments coalesce, this concentrates the field of these fragments, reducing the spread of the field and focussing it more towards the line-of-sight.

Some combinations of gradients are assigned the 'Mixed' tag. These combinations don't obviously relate to a specific event but may arise when e.g., a combination of events occur at the same time, or if two peaks are spuriously labelled. Possible combinations of gradients that result in a 'Mixed' identification are provided in table 4.2. Mixed events do not identify the event occurring in the region but serve to indicate that something may be happening here which is be too complex to fall into any one category. An example of this may be the cancellation of magnetic fragments, coinciding with a large inward drift of positive flux, which might lead to an increase in absolute and positive flux, but a decrease in negative flux. The event considered may be responsible for, e.g., the extinction of the bright points. When an event like this occurs, it is useful for an observer to be aware that an event happens, rather than simply discounting a convoluted case, potentially leaving no event to indicate the death of the bright point. The final two combinations of gradients shown in table 4.2 may not be possible in reality, but they are included here for completeness.

It should be noted that the criteria defined here are not without fault. Suppose a region exists which contains two opposite polarity islands of flux. Now suppose

Absolute Gradient	Positive Gradient	Negative Gradient	Classification
+	+	+	Emergence
-	-	-	Cancellation
+	+	*n/p*	$+ve$ Increasing
-	-	*n/p*	$+ve$ Decreasing
+	*n/p*	+	$-ve$ Increasing
-	*n/p*	-	$-ve$ Decreasing

Table 4.1: Table of classifications for x-ray bright point events. Here, *n/p* indicates that there is no peak in that curve which is coincident with the other curves.

Absolute Gradient	Positive Gradient	Negative Gradient	Classification
$\pm$	$\pm$	$\mp$	Mixed
$\pm$	$\mp$	$\pm$	Mixed
$\pm$	$\mp$	*n/p*	Mixed
$\pm$	*n/p*	$\mp$	Mixed

Table 4.2: Table of gradient combinations that will lead to an event being tagged as 'Mixed'. Here, *n/p* indicates that there is no peak in that curve which can be considered to be coincident with the other curves.

that both islands begin to fragment over the same period. This results in a general decreasing trend across all three gradients, as the smaller islands of flux allow the magnetic field to fan out more, such that less is aligned with the line-of-sight. Hence, this event would be tagged as cancellation, although no noticeable cancellation occurs. Following this one could easily imagine a scenario where the mutual coalescence of flux would produce an event identified as emergence.

4.4 Selecting a Sample of X-ray Bright Points

A sample of the XBPs detected was taken, to test the ability of the algorithm to identify significant events which occur during their lifetime. To ensure enough observational data was obtained for the study, only bright points which were detected to have a lifetime between 8 and 10 hours have been selected. This rejects bright points which may be so long that they become too complex to analyse. There was also the requirement that a bright point is no more than 300 arcsec from the centre of the solar disc. The observational period of each bright point is also extended 6-hour prior, and 6 hours post the detections in the HMI analysis, with data captured at a 90-second cadence. This provides between 800 and 880 data points for each bright point in the study.

Twenty XBPs were detected to have a lifetime of between 8 and 10 hours, though not all were suitable for the study. Five of the XBPs identified would not have been picked out by an observer, appearing as large diffuse regions where the intensity is increased, hence are rejected and do not form part of the sample. Of the 15 XBPs studied, five detections are due to a significant change in the structure of an existing XBP, hence there is no defining event which marks the onset of the bright point.

The events which lead to the formation and demise of the remaining ten bright points have been visually classified (table 4.3). Four of the bright points form as the result of an emergence event, whilst six of them form as opposing magnetic fragments drift towards one another. Six of the studied bright points are destroyed through the cancellation of their footpoints, whilst one is destroyed through a combination of footpoint cancellation and drifts, and another vanishes as the result of footpoint drifts alone. Two of the XBPs studied are destroyed as the result of an emergence event local to their foot points, where the magnetic field appears to restructure itself into a new configuration.

The following six case studies have been selected for further discussion since they

XBP ID	Onset	Demise
01	Drift	Drift
02	Emergence	Cancellation
03	Emergence	Cancellation
04	Drift	Cancellation
05	Drift	Emergence
09	Emergence	Cancellation & Drift
11	Drift	Cancellation
12	Drift	Cancellation
14	Drift	Cancellation
15	Emergence	Emergence

Table 4.3: Table showing event types responsible for the onset and diffusion of different bright points.

highlight different combinations of events relating to the onset and demise of the bright points. One of the bright points, XBP01, forms as the result of drifting fragments and is subsequently eliminated by drifts. The bright points XBP02, XBP03 are each born of an emergence event, and their demise is due to the cancellation of their footpoints. The bright points XBP04 and XBP14 both form from flux elements drifting towards one another, and their demise occurs due to the cancellation of their footpoints. A combination of events is found to be responsible for the diffusion of XBP09, where the footpoints cancel with one another, but the negative footpoint fragments during this process and a large fragment then drifts away from the local network. Each of the cases is discussed in order of the identification number assigned to them.

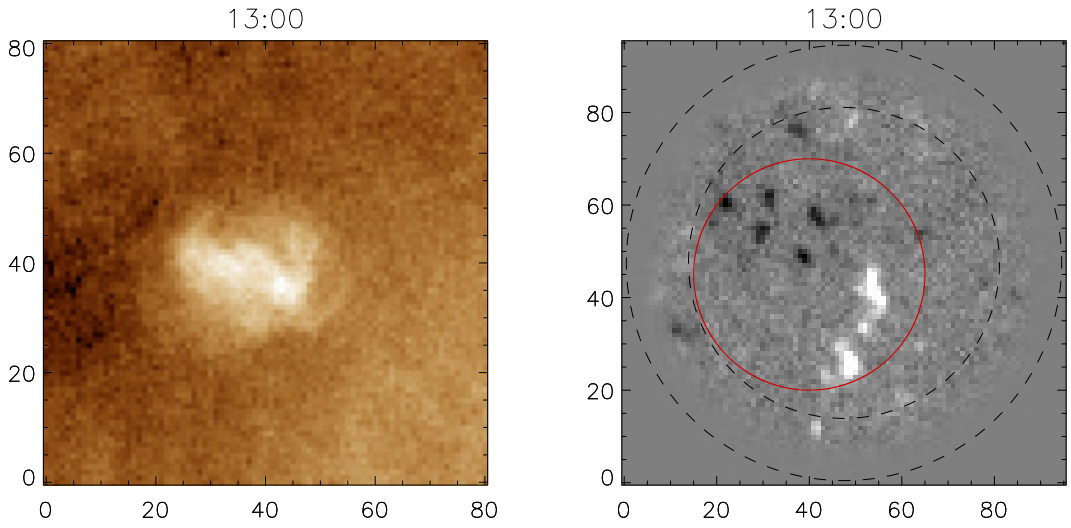

(a) (b)

Figure 4.8: Images of XBP01 taken with a) AIA and b) HMI on March 12^{th}, 2017. The red circle highlights the footpoint fragments of the bright point.

4.4.1 Case Study: XBP01

The first bright point studied from the sample is XBP01 (figure 4.8), which is born and destroyed by drifting magnetic flux. The region where XBP01 is located is observed between 03:18 on March 12^{th} and 00:03 on March 13^{th}. The bright point structure is not present at the onset of the observation but turns on after two opposite polarity sources have drifted towards one another. It is first detected by the program at 09:16 but is visible by eye in the AIA data from 08:00. The program stops tracking the bright point at 18:03 at which point it has become appreciably fainter and smaller. The birth and death of the bright point have been observed within the complete observational window.

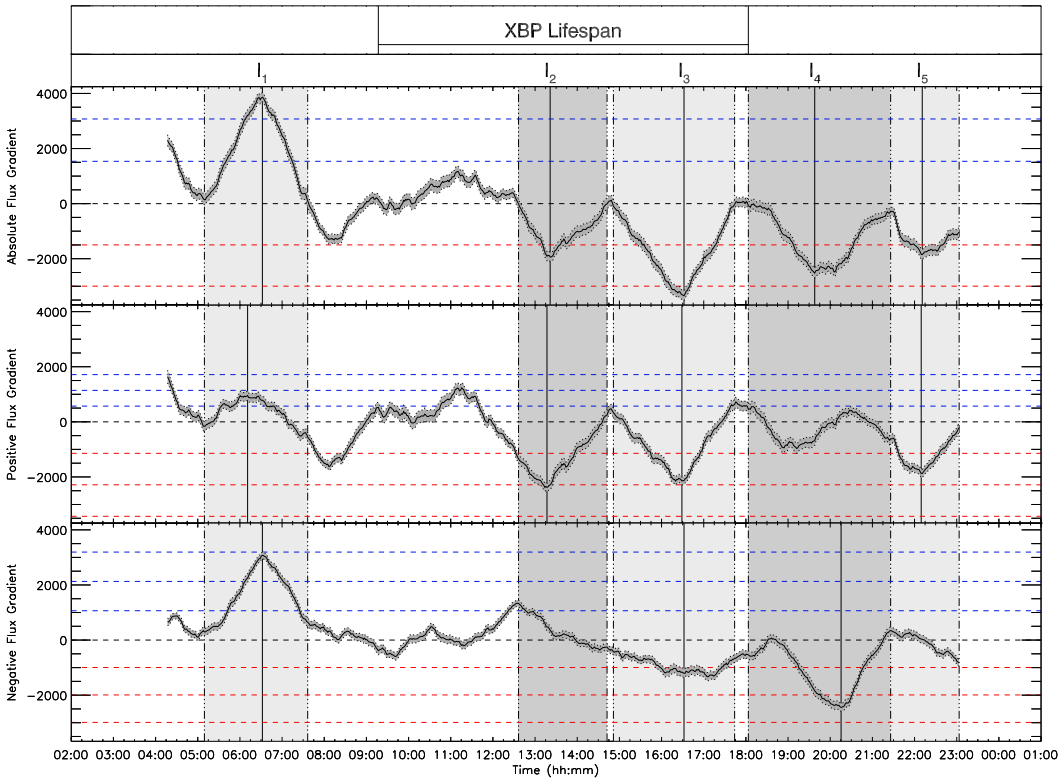

Figure 4.9: Gradients of the absolute, positive and negative flux measures for XBP01. Blue dashed lines represent deviations from zero of the increasing gradient, where red dashed lines are the deviations from zero of the decreasing gradient. Detected events are bound by vertical dot-dash lines, with the peaks of each event plotted as solid, vertical lines and labelled I_1 - I_5. The times that XBP01 was automatically tracked over are indicated by the bar at the top of the figure.

Event Classification

The automatic classifier identifies five unique events within the observational window (figure 4.9). These events are summarised in table 4.4. The first event, I_1, occurs around 06:30, identified as an emergence event, as all three flux curves exhibit a significant positive peak. Inspection of this event finds that an explosive emergence event occurs within close proximity to the sources which goes on to form the bright point footprints (figure 4.10). The emerged sources rapidly cancel and fragment,

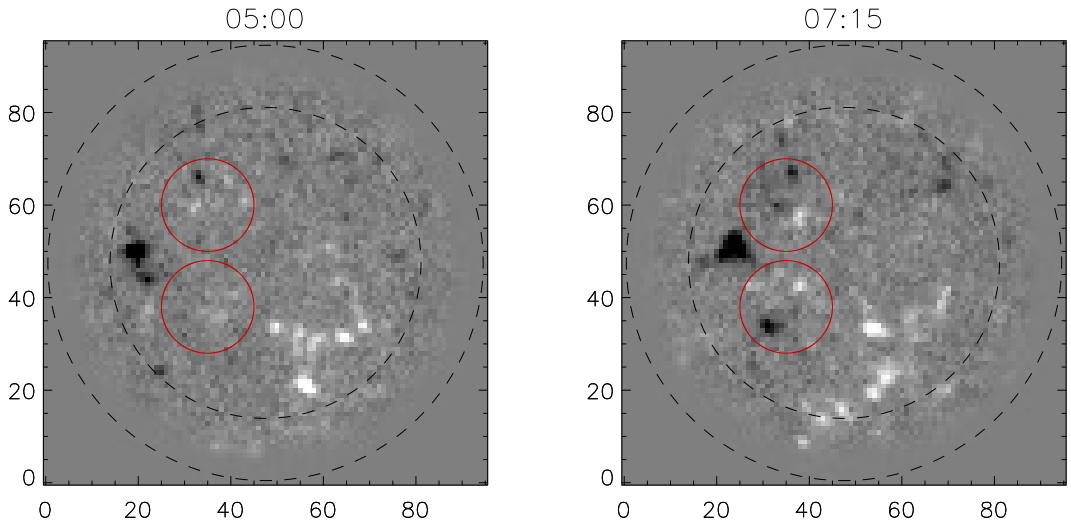

(a) (b)

Figure 4.10: Images showing the emergence of flux for event I_1 in the region local to XBP01. Red circles indicate the regions where flux is emerging.

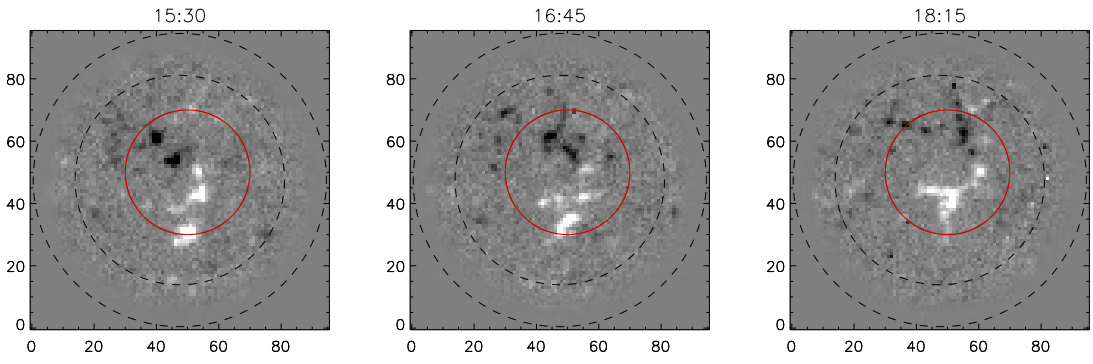

(a) (b) (c)

Figure 4.11: Images showing the cancellation of flux for event I_3 in the region local to XBP01. The red circles indicate where the fragments are interacting and cancelling.

while observations suggest that this event is not responsible for the onset of the bright point. As shown in table 4.3, visual inspection of the local region classifies the onset of the bright point as the result of magnetic fragment drifts. Since these

Event ID	Event Peak Time	Visual	Algorithm
I_1	06:31	Emergence	Emergence
I_2	13:21	Positive Fragmentation	Positive Decreasing
I_3	16:31	Cancellation	Cancellation
I_4	19:37	Negative Fragmentation	Negative Decreasing
I_5	22:10	Positive Fragmentation	Positive Decreasing

Table 4.4: Table showing the times of detected events relating to XBP01, along with the visual classification of the events, and the classification assigned to the events by the algorithm. The ID of each event is also given, which corresponds to the peaks in figure 4.9.

magnetic fragments are already present in the local region, and the motion takes place over several hours, no significant drifting event is automatically identified.

The second event identified, I_2, is labelled as a positive flux decreasing event, occurring around 13:20. Inspection finds that the positive footpoints of the bright point fragment at this time. As discussed earlier, fragmentation of sources can lead to a decrease in the flux measured by a line-of-sight magnetogram, so this result is valid.

The two footpoints of the bright point have been drifting closer to one another since the onset of the bright point. At 15:00, the footpoints have drawn so close together that flux cancellation begins. This event, I_3, is correctly identified as cancellation by the algorithm, which finds the peak about 16:30 (figure 4.11). Coincident with the cancellation, the bright point becomes less intense.

Two more events are identified, I_4 and I_5, labelled as a negative flux decreasing event, followed by a positive flux decreasing event. These events have been confirmed as correct classifications, both associated with the fragmentation of large sources.

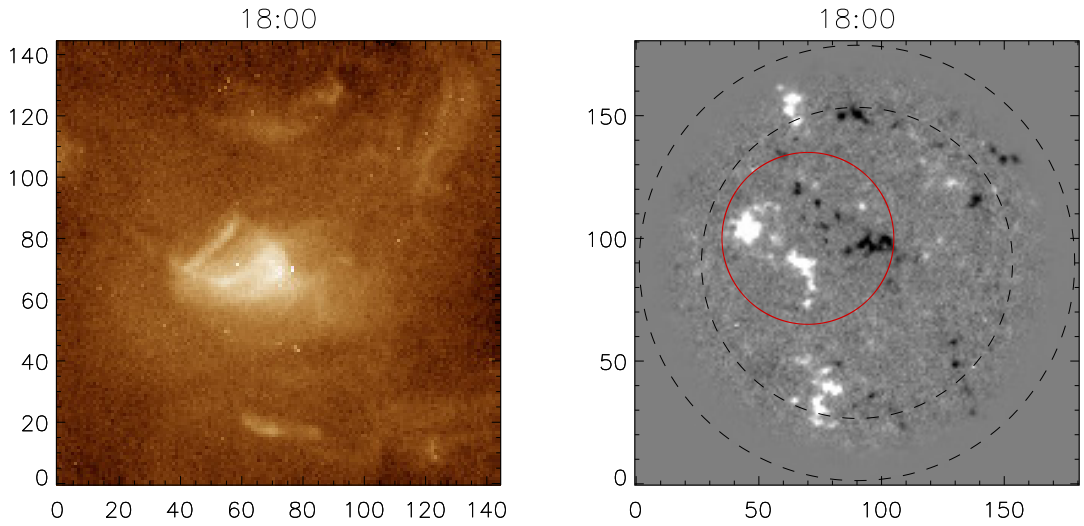

(a) (b)

Figure 4.12: Images of XBP02 taken with a) AIA and b) HMI on March 12^{th}, 2017. The red circle highlights the fragments which are the footpoints of the bright point.

As this fragmentation occurs, and the foot points continue to drift apart, the bright point gradually dims and dies.

The identified events have been summarised in table 4.4, which shows that the algorithm has correctly identified all of the events for this bright point. The emergence and cancellation events which occur are both correctly classified. Where the algorithm has detected decreasing flux drifts, each of these events has been associated with the fragmentation of magnetic islands, with no significant fragments of flux drifting out of the local region and into the annulus at this time.

4.4.2 Case Study: XBP02

The region in which XBP02 (figure 4.12) is located consists of multiple concentrations of magnetic flux. Whilst other bright points are observed to form and die within the window of observation, only XBP02 is studied and discussed in detail

here. This bright point forms as the result of a slow, explosive emergence event. The emerged fragments initially drift apart from one another, spreading across a wider region as two islands of opposite polarity flux. Later in the bright point's life, the opposite polarity fragments begin to drift back towards one another. The bright point becomes extinguished as the two flux concentrations become close enough to allow cancellation, vanishing as the last of the negative flux is eliminated.

The region local to the bright point is observed between 07:57 on March 12^{th} and 05:31 on March 13^{th}. The tracking program first identifies the onset of the bright point at 13:57, which is confirmed visually. The bright point is tracked until 23:31, yet some structure persists beyond this point. The bright point is observed to be completely extinguished by 02:30, as the final fragments of flux are cancelled. Again, the observing window has captured both the birth and death of the bright point.

Event Classification

Seven events are automatically identified for XBP02, totalling two emergence events, three instances of cancellation, along with two events which are identified as drifts (figure 4.13). All of the events which have been identified for this bright point are shown in table 4.5. The first event found, I_1, occurs around 10:18 and is both identified and confirmed to be an emergence event. In fact, there are two explosive emergence events which occur at the same time, both allowing the formation of a distinct bright point (figure 4.14). The emerged flux is quickly cancelled out and the bright points extinguished. Whilst neither are the bright point studied here, the emerged flux interacts with fragments which become the foot points for XBP02.

The next two events, I_2 and I_3, are identified as a positive flux increasing drift, followed by an emergence event, occurring between 12:30 and 16:30. A concentrated source of positive flux is observed drifting in at the top of the observation region,

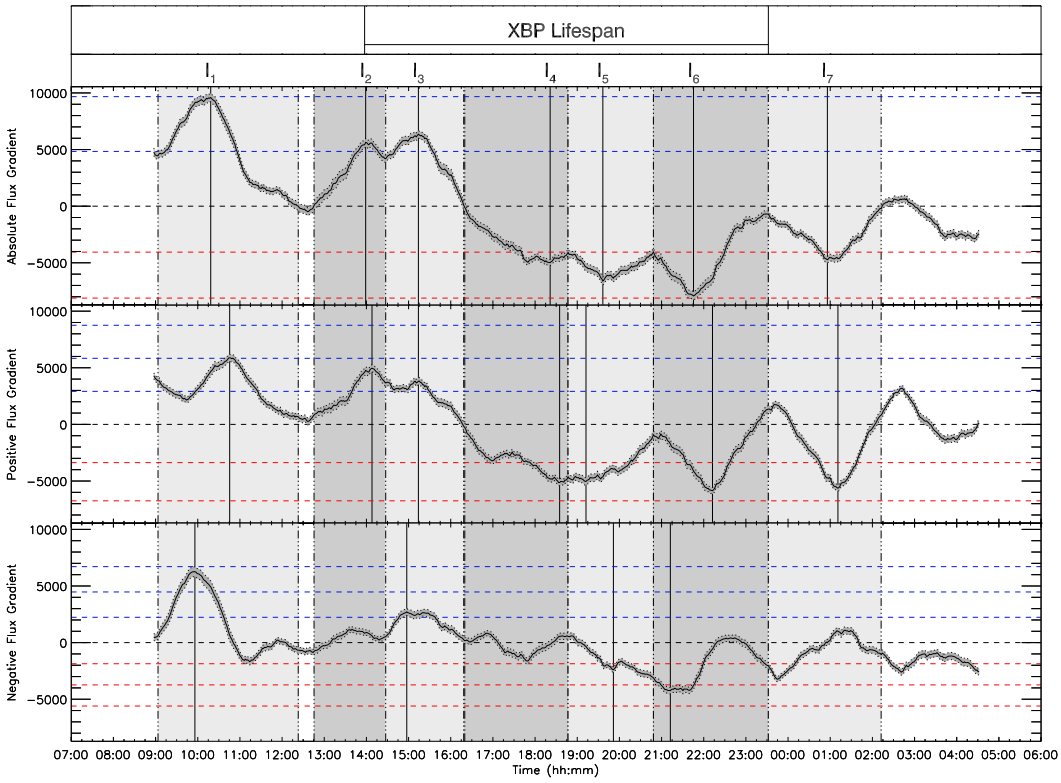

Figure 4.13: Gradients of the absolute, positive and negative flux measures for XBP02. Blue dashed lines represent deviations from zero of the increasing gradient, where red dashed lines are the deviations from zero of the decreasing gradient. Detected events are bound by vertical dot-dash lines, with the peaks of each event plotted as solid, vertical lines and labelled I_1 - I_7. The bar at the top of this figure indicates the times that XBP02 was automatically tracked over.

and the emergence is clearly observable towards the centre. This emergence event, I_3, is responsible for the onset of the bright point and presents as a slow explosive emergence over the time period (figure 4.15). However, together the two events mask the cancelling fragments from the initial emergence event. This can only be a result of the two events together contributing more flux to the region than is lost in the cancellation. Whilst the cancellation is missed by the identifier, the elements cancelled do not contribute to the bright point, so it is a reasonable exception that

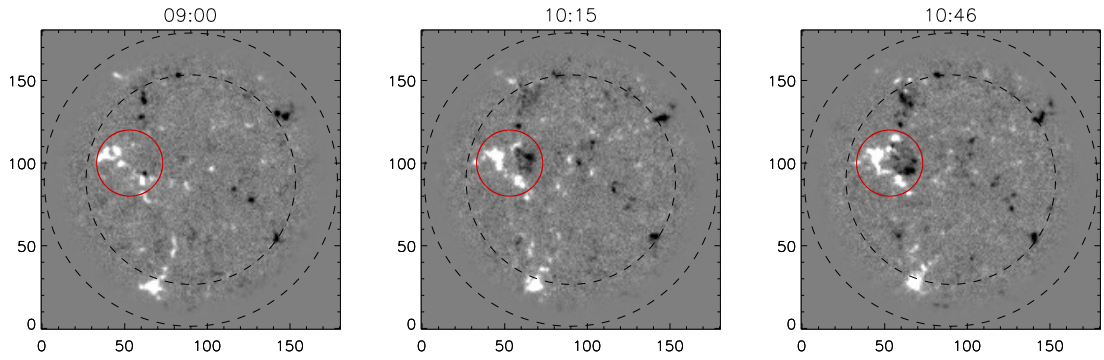

(a) (b) (c)

Figure 4.14: Images showing the first event, I_1, identified as the emergence of flux in the region local to XBP02. The red circles indicate the region where the emerging flux is located.

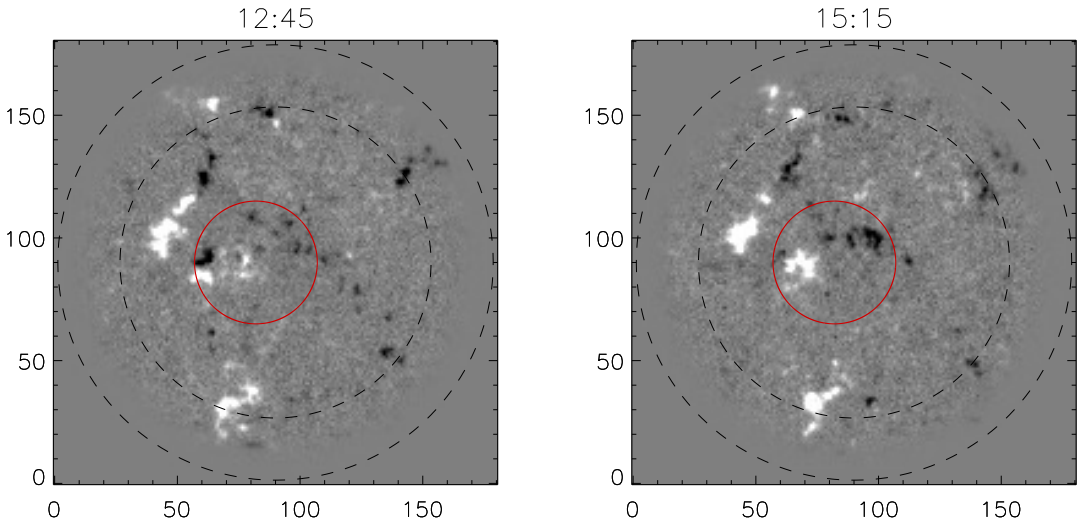

(a) (b)

Figure 4.15: Images showing the second emergence event, I_3, detected in the region local to XBP02. The emerging flux is highlighted by the red circle.

this event is missed in favour of the detection of the event responsible for the onset of the bright point.

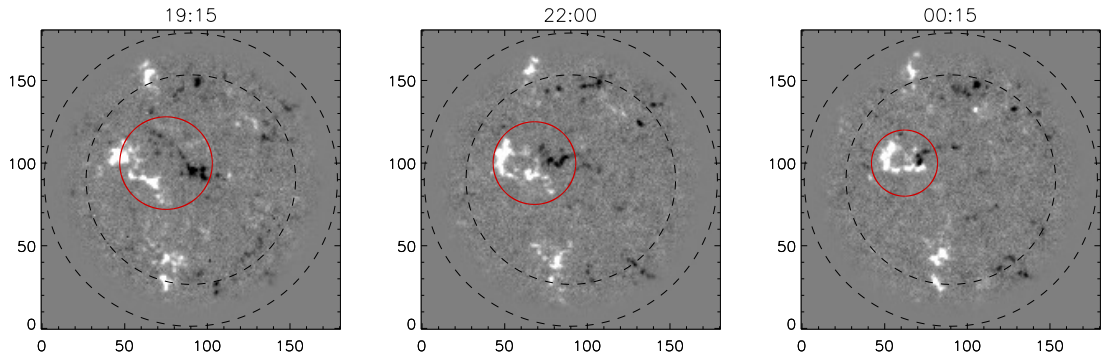

(a) (b) (c)

Figure 4.16: Images showing the cancellation of flux for event I_5 in the region local to XBP02. The region where fragments are interacting and cancelling is enclosed in the red circle.

Event ID	Event Peak Time	Visual	Algorithm
I_1	10:18	Emergence	Emergence
I_2	13:58	Positive Drift In	Positive Increasing
I_3	15:13	Emergence	Emergence
I_4	18:21	Positive Fragmentation	Positive Decreasing
I_5	19:36	Cancellation	Cancellation
I_6	21:45	Continued Cancellation	Cancellation
I_7	00:55	Continued Cancellation	Positive Decreasing

Table 4.5: Table showing the times of detected events relating to XBP02, along with the visual classification of the events, and the classification assigned to the events by the algorithm. The ID of each event is also given, which corresponds to the peaks in figure 4.13.

A positive flux decreasing drift, I_4, is identified at 18:21. Here, no flux leaves the region, but two concentrations which are not part of the bright point network flux experience some fragmentation. This has no bearing on the structure of the bright point.

The following pair of events, I_5 and I_6, are both labelled as cancelling magnetic flux elements, occurring between 18:30 and 22:30. Inspection of the events finds that there is indeed cancellation occurring during this time, along with the fragmentation of both positive and negative flux concentrations external to the bright point (figure 4.16). Two problems present here, the mutual fragmentation of positive and negative concentrations exhibits the same behaviour as cancelling magnetic sources. When one large fragment breaks into multiple smaller fragments, the magnetic field due to these fragments is able to spread out much more than in a single concentrated source. This spreading field means that less is aligned to the line-of-sight of the spacecraft. When two opposite polarity islands begin to fragment at the same time, a decrease in the gradients of both polarities is recorded, which is the same behaviour that arises from a cancellation event. Additionally, two events have been identified, where only one prolonged event is visually identified. Whilst the identification is not without fault, it has served to detect behaviour which is of interest to an observer. The structure of the bright point itself changes little due to this behaviour; rather it changes due to the drifts of its footpoints toward one another.

The final detection, I_7, indicates an instance of positive flux decreasing drift. However, inspection finds that there is continued cancellation occurring at this time, so this result has been recorded as incorrect. This event also coincides with the extinction of the bright point.

These events have been summarised in table 4.5, which compares the classification of the algorithm to the classification of visual inspection. Events I_1 - I_5 have each been correctly identified, whilst I_6 and I_7 are both incorrect detections. The

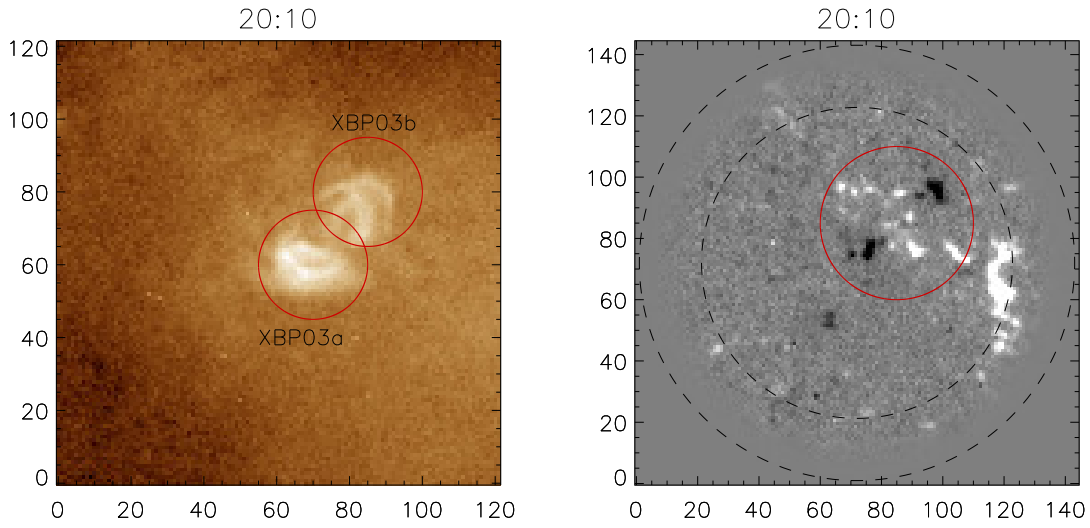

(a) (b)

Figure 4.17: Images of XBP03 taken with a) AIA and b) HMI on March 12^{th}, 2017. The two bright points in the AIA image (a) are labelled and enclosed within red circles, and red circle in the HMI image (b) indicates the footpoints of XBP03.

two incorrect events are the continuation of a previously detected event. The algorithm also failed to identify a cancellation event which was related to the footpoints of this bright point, though numerous other events were occurring at the same time.

4.4.3 Case Study: XBP03

This case studies XBP03 (figure 4.17), covering the time period between 10:16 March 12^{th} and 06:55 March 15^{th}. It too satisfies the condition that the onset and extinction of the bright point are observed within the time range. An initial explosive emergence event is quickly followed by the separate emergence of a clear bipole, with each event forming its own bright point. The bright point structure associated with this detection is the bright point born of the explosive emergence event. For clarity, this bright point will be referred to as XBP03a, as it is the focus of this

Event ID	Event Peak Time	Visual	Algorithm
I_1	13:39	Emergence	Emergence
I_2	17:33	Emergence	Emergence
I_3	21:37	Cancellation	Cancellation
I_4	00:18	Continued Cancellation	Negative Decreasing
I_5	03:22	Emergence	Positive Increasing

Table 4.6: Table showing the times of detected events relating to XBP03, along with the visual classification of the events, and the classification assigned to the events by the algorithm. The ID of each event is also given, which corresponds to the peaks in figure 4.18.

case study. The bright point born of the emerged bipole survives for longer than its counterpart and is present in the extended window of observation. This secondary bright point will be referred to as XBP03b, though a complete study of this bright point is not conducted here. The two bright points are indicated in figure 4.17a.

The tracking program first identifies the bright point XBP03a at 16:16 and stops tracking at 00:55. This time frame encompasses the onset of the bright point, XBP03a, due to an explosive emergence event. The demise of XBP03a is due to the emerged footpoints converging so close that the fragments cancel with one another.

Event Classification

This period of observation has five events identified within it, three of which have been confirmed as correct classifications through visual inspection (figure 4.18). Table 4.6 shows each of the events, along with the classifications assigned visually and by the algorithm. The first event, I_1, is classified as an emergence event, which peaks at 13:45. This first event is the culmination of a cluster of small emergence

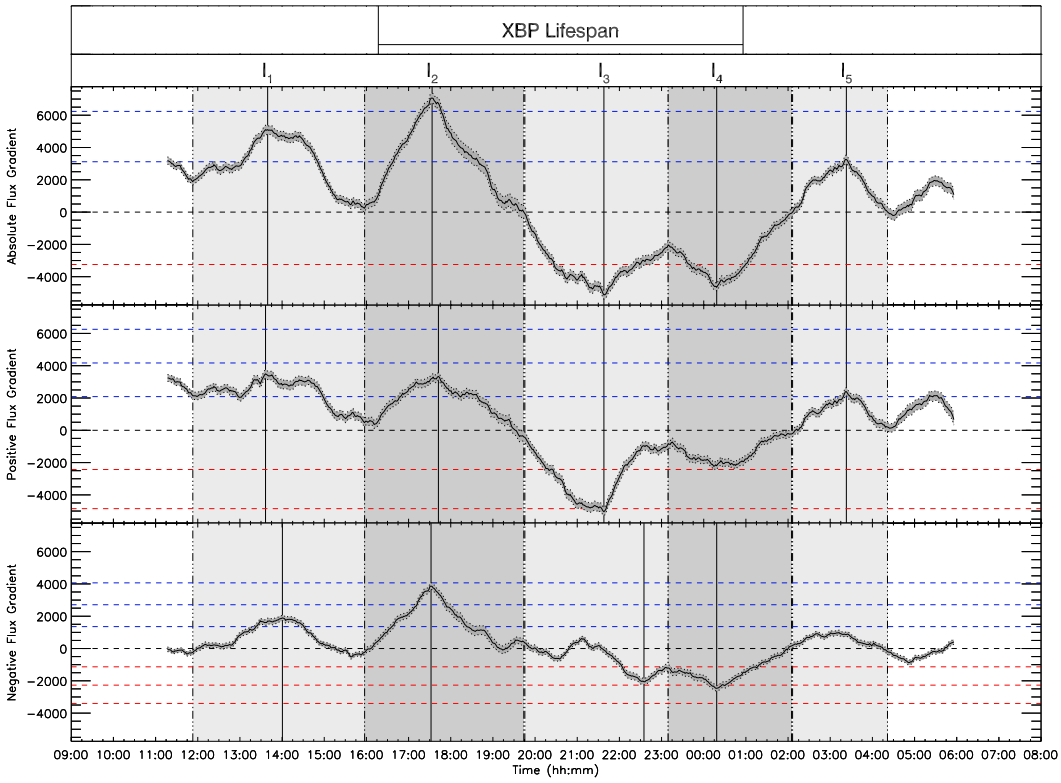

Figure 4.18: Gradients of the absolute, positive and negative flux measures for XBP03. Blue dashed lines represent deviations from zero of the increasing gradient, where red dashed lines are the deviations from zero of the decreasing gradient. Detected events are bound by vertical dot-dash lines, with the peaks of each event plotted as solid, vertical lines and labelled I_1 - I_5. The bar at the top of the figure indicates the times that XBP03 was automatically tracked over.

events close to the centre of the window, which are not responsible for the onset of either XBP03a or XBP03b.

The emergence events that give rise to both the bright points occur in tandem with one another, resulting in the identification of a single event, I_2 (figure 4.19, table 4.6). The event is identified about 17:30, beginning with the explosive emergence of small fragments of flux which coalesce to form several larger fragments. Together, these fragments form the footpoints for XBP03a and begin to converge on one

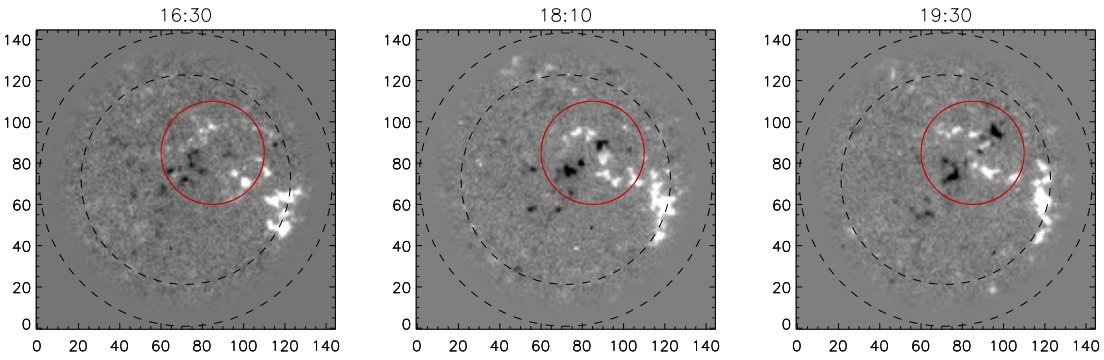

(a) (b) (c)

Figure 4.19: Images showing the emergence of flux in the region local to XBP03, identified as event I_2. The location of the emerging flux is indicated by the red circles.

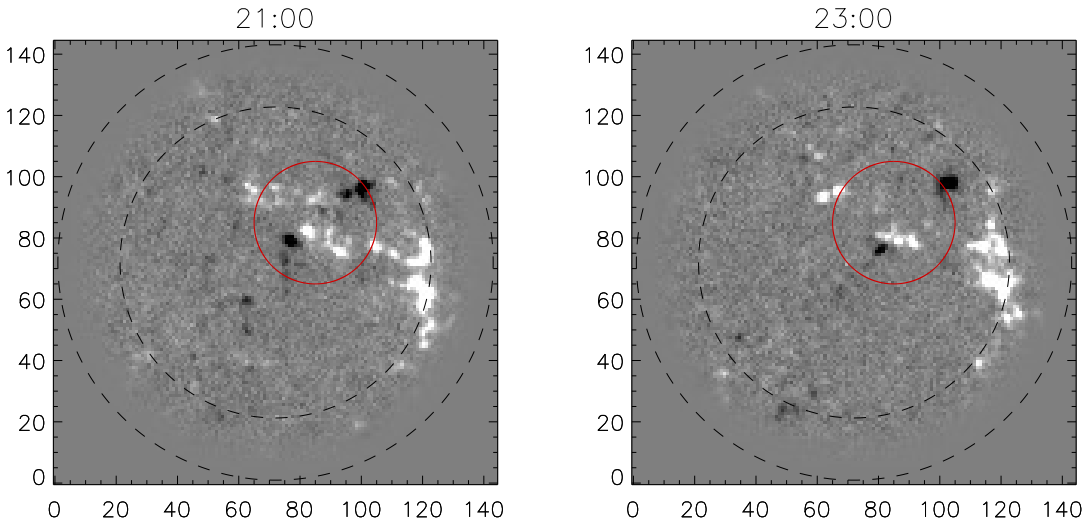

(a) (b)

Figure 4.20: Images showing the cancellation of flux as part of event I_3 in the region local to XBP03. The red circle indicates the location of the cancelling fragments.

another. The second event is the bipole emergence, which adds positive flux to the footpoints of XBP03a, but the negative source interacts with an additional

concentration of flux to form XBP03b. This negative footpoint begins to drift away from the converging source pair of XBP03a.

Following their emergence, the footpoints of XBP03a quickly converge and begin to cancel, which is identified as event I_3 (figure 4.20, table 4.6). The classifier identifies the event about 21:40, and visual inspection confirms the cancellation during this time. However, the event which follows, I_4, is incorrectly classified as an instance of a negative flux decreasing drift. Whilst the negative footpoint of XBP03b does move to the edge of the observation window during this time, it does not enter the masked annular region, and the footpoints of XBP03a are still cancelling with one another. Visual inspection suggests that more of the large concentration of positive flux in the annular region drifts into the local region at this time, contributing enough flux that the cancelling positive flux becomes insignificant. Although the cancellation event has not been identified as spanning the entire period it occurs over, this has the benefit of also noting that there is negative flux drifting out of the region.

The final event, I_5, is identified as a positive flux increasing drift, but inspection suggests that a small emergence event coincides with the cancellation of flux within the faded annulus. However, this event is outside the period in which the bright point XBP03a exists, thus is not strictly a required event.

This collection of events has been summarised in table 4.6, which shows that the algorithm has classified events I_1, I_2 and I_3 as the same event types assigned to them through visual classification. Event I_4 was classified as a negative flux decreasing drift by the algorithm, but visual classification finds that the cancellation occurring in event I_3 continues into this time window. The classification of I_4 is thus incorrect and arises as positive flux drifts into the local region, from the annular region. The final event I_5 was classified as a positive flux increasing drift by the algorithm, whilst visual inspection notes several small emergence events across the region at this time.

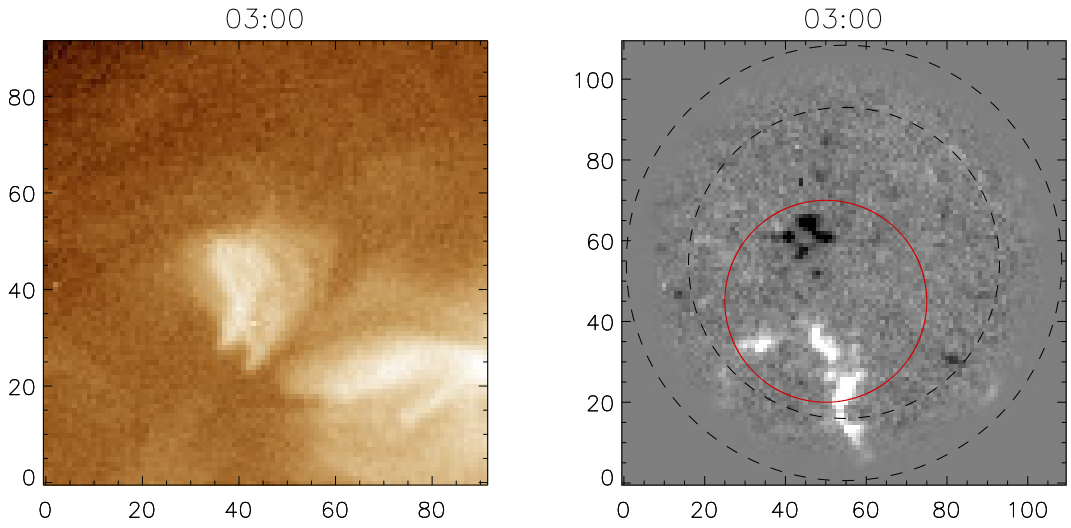

(a) (b)

Figure 4.21: Images of XBP04 taken with a) AIA and b) HMI on March 13^{th}, 2017, and a red circle is used to indicate the footpoints of XBP04.

4.4.4 Case Study: XBP04

This case studies a bright point, XBP04, which arises from the converging drifts of magnetic fragments until they converge to a point where they begin to cancel with one another (figure 4.21). Upon cancellation of the fragments, the bright point is extinguished. The observational window runs from 16:51, March 12^{th} to 14:04, March 13^{th}, where the bright point is automatically tracked between 22:51 and 08:04. Whilst some structure is visible beyond this window, the presence of the bright core of XBP04 is contained within the automatically detected window.

Event Classification

Seven events are identified in the region local to XBP04 (figure 4.22); a single emergence event is identified, along with a single instance of cancellation and numerous drifts. The events are summarised in table 4.7. The onset of the bright point is

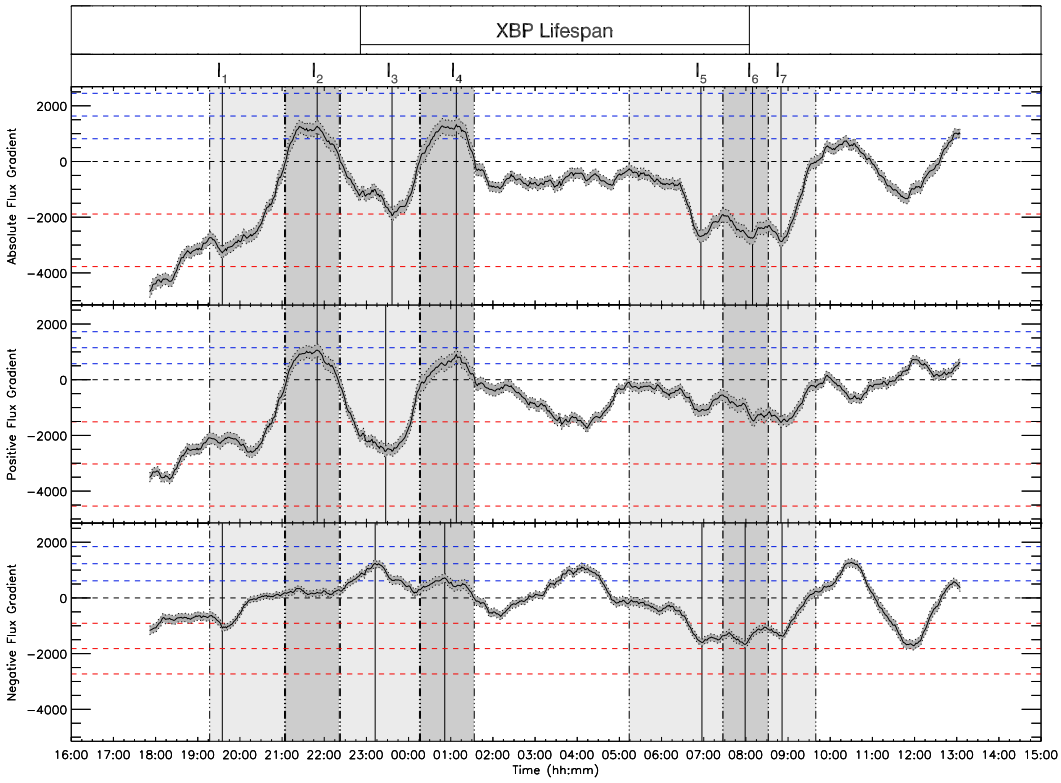

Figure 4.22: Gradients of the absolute, positive and negative flux measures for XBP04. Blue dashed lines represent deviations from zero of the increasing gradient, where red dashed lines are the deviations from zero of the decreasing gradient. Detected events are bound by vertical dot-dash lines, with the peaks of each event plotted as solid, vertical lines and labelled I_1 - I_7. The automatic tracking period of XBP04 is indicated by the bar at the top of the figure.

the result of drifting fragments, though as happened with XBP01 these fragments are already present in the local region at the start of the observation window, so no significant drifting event is identified.

First, a negative flux decreasing drift is identified, I_1, around 19:34 and is confirmed as finding the outward drift of a negative fragment by inspection. At this time, a small concentration of negative flux drifts towards the edge of the region,

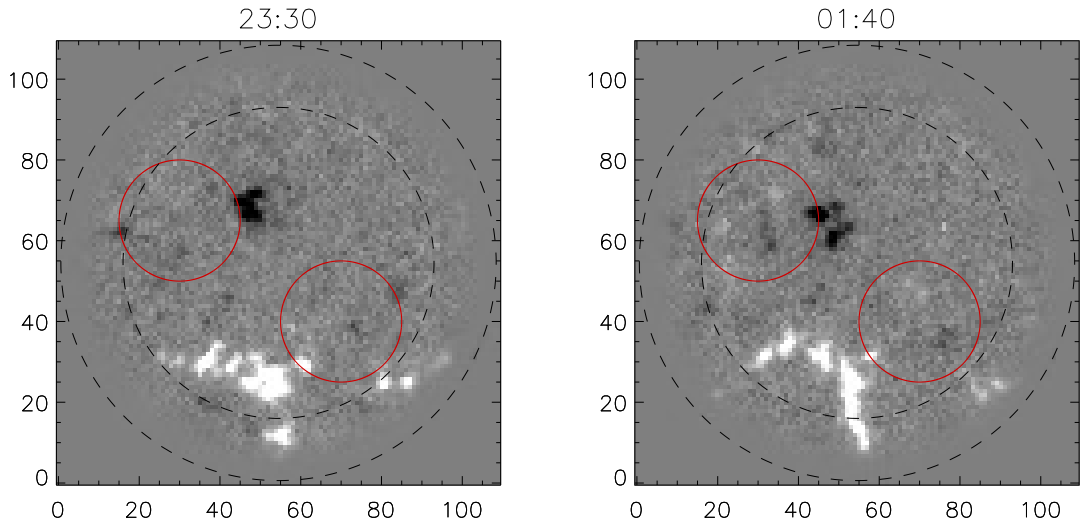

(a) (b)

Figure 4.23: Images showing the emergence of flux in event I_4, in the region local to XBP04. The red circle highlights the emerging fragments.

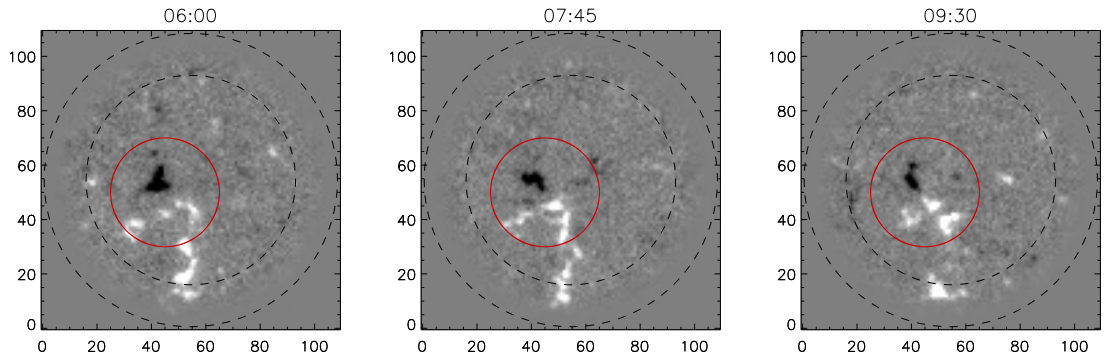

(a) (b) (c)

Figure 4.24: Images showing the cancellation of flux for event I_3 in the region local to XBP04. The cancelling fragments are indicated by the red circle.

fragmenting as it travels, before fragmenting beyond the observable limit in the fading annulus. It should be noted that this event has no bearing on the structure of the bright point, which is not identified at this time. The following event, I_2,

Event ID	Event Peak Time	Visual	Algorithm
I_1	19:34	Negative Drift Out	Negative Decreasing
I_2	21:49	Positive Drift In	Positive Increasing
I_3	23:36	Multiple Events	Mixed Behaviour
I_4	01:07	Emergence	Emergence
I_5	06:55	Cancellation	Negative Decreasing
I_6	08:09	Continued Cancellation	Negative Decreasing
I_7	08:49	Continued Cancellation	Cancellation

Table 4.7: Table showing the times of detected events relating to XBP04, along with the visual classification of the events, and the classification assigned to the events by the algorithm. The ID of each event is also given, which corresponds to the peaks in figure 4.22.

identified at 21:49 is confirmed as a positive drift-in, as flux drifts about the edge of the region, but is also believed to have a negligible effect on the structure of XBP04.

The third event identified, I_3, is somewhat complicated, and is classed as a mixed event occurring at 23:26. Here, an increasing trend is observed in the negative flux in the same window that the positive flux is decreasing. From inspection, it is found that the core of the bright point becomes more intense at this time. This signature arises from the coalescing of the negative fragments forming the footpoints of XBP04, coinciding with the large region of positive flux fragmenting and drifting close to the annular edge. Whilst a mixed event identification is not necessarily an informative classification, logging the event has allowed the change in the bright core to be explained as the result of the negative footpoints coalescing.

An emergence event, I_4, is the next detected, presenting as weak, unrelated explosive events across the region (figure 4.23). One of the events occurs close

to the footpoints of XBP04 and the structure of the bright point warps with the introduction of the new flux. However, the small fragments quickly cancel and coalesce resulting in the structure reverting close to its previous state.

The final three events, I_5 - I_7, form a triplet, all of which can be enclosed within a single, three-hour window, between 06:00 and 09:00. The first two events, I_5 and I_6, are indicated as negative flux decreasing drifts, while the final event is tagged as a cancellation instance (figure 4.24). When the images from HMI are studied, it is clear that cancellation is occurring throughout this time window. This incorrect identification of the first two events is likely the consequence of the large positive concentration close to the edge of the region. The overlap of the drift-in of positive flux and the cancellation between the footpoints of XBP04 initially registers as flux drifts, though a cancellation tag is later assigned. Whilst it may be incorrect initially, the result still alerts an observer to the cancellation of magnetic flux as the likely cause of the bright point's extinction.

Table 4.7 summarises the events identified local to bright point XBP04, and shows that the algorithm's classification of an event matches the visual classification for five of the seven events. As discussed above, the algorithm initially classifies the cancellation event as a negative decreasing drift. Though it does later capture the cancellation event, this detection has not revealed the full extent of the cancellation, as it has been contaminated by additional flux fragments.

4.4.5 Case Study: XBP09

The bright point XBP09 (figure 4.25) is studied across the time period of 01:13, March 14^{th} to 22:09, March 14^{th}. It is first detected automatically at 07:13, shortly after a large emergence event which is clearly responsible. The bright point fades due to the outward drift of its footpoints, coupled with some cancellation, and the automatic tracking stops at 16:09. Shortly after the original bright point is lost, a

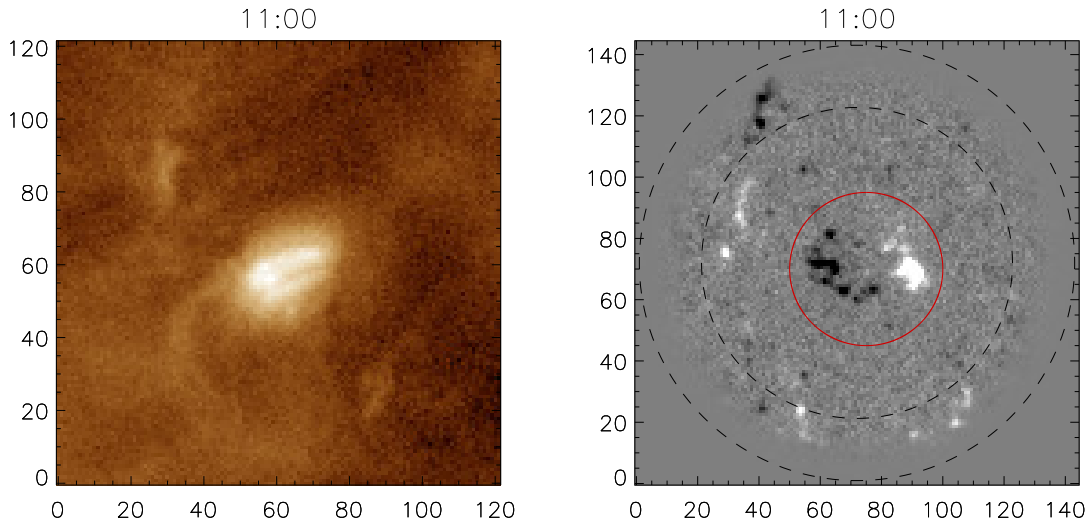

(a) (b)

Figure 4.25: Images of XBP09 taken with a) AIA and b) HMI on March 14^{th}, 2017. The footpoints of XBP09 are indicated by the red circle in image (b).

new one is formed as the positive footpoint drifts towards a new negative fragment.

Event Classification

Four magnetic events are identified during the lifetime of this bright point, where the detections are shown in figure 4.26 and are summarised in table 4.8. This bright point is born from a large emergence event which takes place around 06:30. An initial, slow explosive emergence event, I_1, erupts a large quantity of flux, forming two concentrated islands of opposite polarity (figure 4.27). The compact structure of a bright point forms in response and begins to stretch as the islands drift apart. The event is captured and correctly identified by the classification program, clearly indicating the onset of the bright point.

Next, the classifier suggests that negative flux leaves the local region around 10:30 as event I_2. However, inspection finds fragmentation of a large island of negative

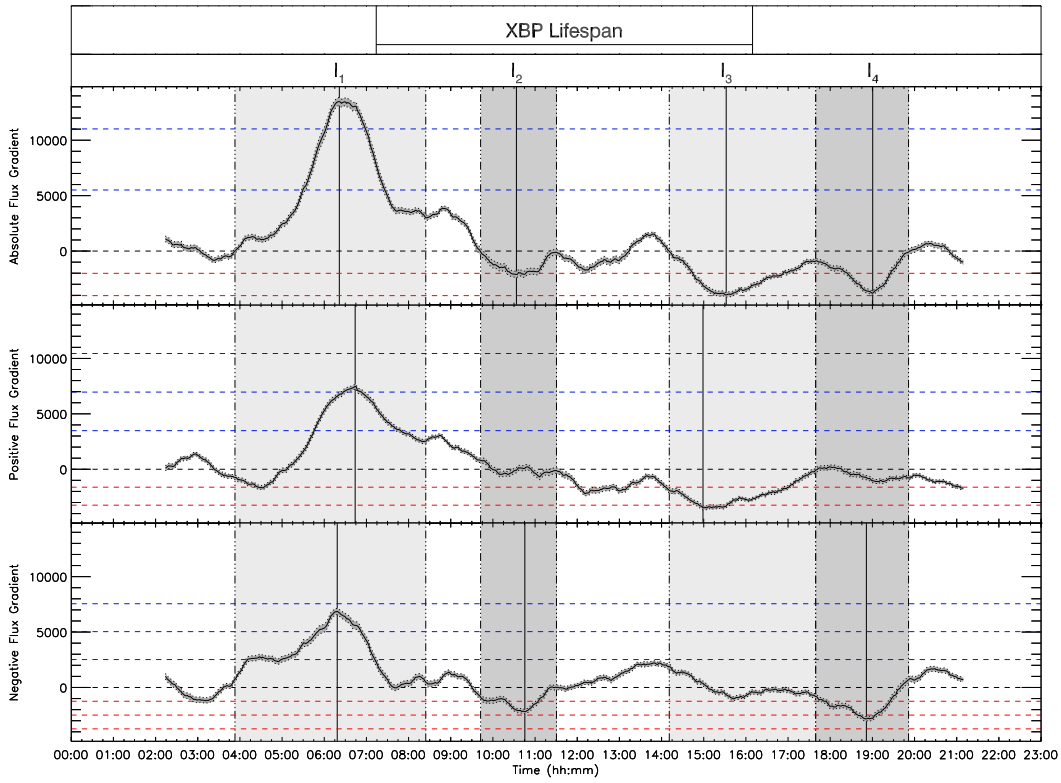

Figure 4.26: Gradients of the absolute, positive and negative flux measures for XBP09. Blue dashed lines represent deviations from zero of the increasing gradient, where red dashed lines are the deviations from zero of the decreasing gradient. Detected events are bound by vertical dot-dash lines, with the peaks of each event plotted as solid, vertical lines and labelled I_1 - I_4. The bar at the top of the figure shows the times that XBP09 was automatically tracked across.

flux, forming numerous concentrated sources. Some of the fragments begin to drift towards the top of the region, where a new negative island has begun to drift in, where the rest begins to converge on the positive island.

The next key event observed is the cancellation of magnetic flux, through the interaction of the footpoints of XBP09 around 12:30. This event has not been identified by the algorithm, which is recorded as a false negative event and is composed of two visually identified contaminating events. First, a large island of negative flux

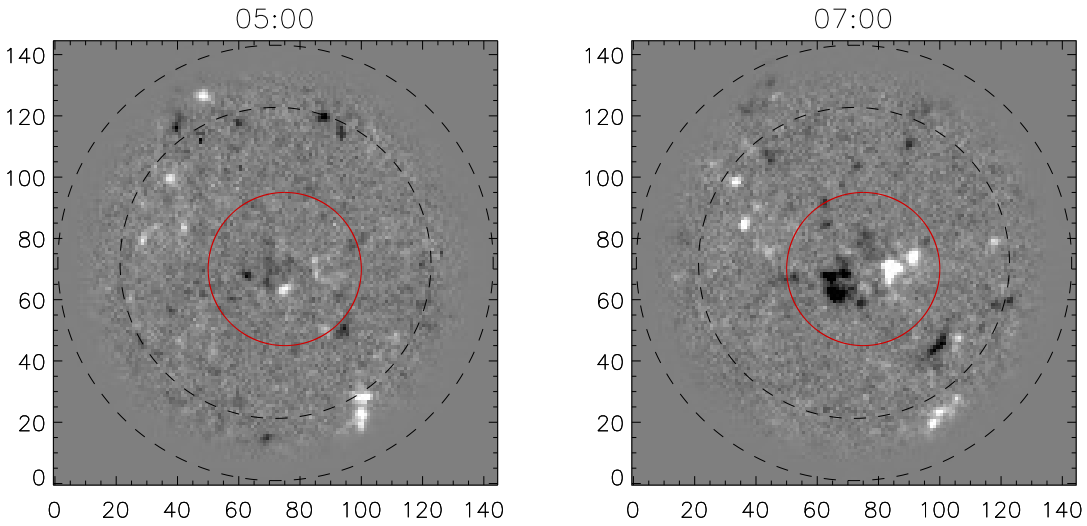

(a) (b)

Figure 4.27: Images showing the emergence of flux in the region local to XBP09 as part of event I_1. The red circle indicates the location of the emerging flux.

Event ID	Event Peak Time	Visual	Algorithm
I_1	06:21	Emergence	Emergence
I_2	10:33	Negative Fragmentation	Negative Decreasing
I_3	15:31	Positive Fragmentation	Positive Decreasing
I_4	19:00	Negative Fragmentation	Negative Decreasing

Table 4.8: Table showing the times of detected events relating to XBP09, along with the visual classification of the events, and the classification assigned to the events by the algorithm. The ID of each event is also given, which corresponds to the peaks in figure 4.26.

has begun to drift into the region, contributing enough flux that an increase in the total negative flux is recorded over this period. Next, a large explosive emergence

event occurs close to the edge of the region, causing newly emerged flux to drift in. This second event is believed to be responsible for dampening the decrease in positive flux recorded during this time.

The final two events, I_3 and I_4, are identified as decreasing flux drifts, one positive and the other negative, spanning from 14:00 to 20:00. Inspection of the HMI data at this time finds there is widespread fragmentation of concentrated islands of flux at this time, confirming the identification of each peak.

Table 4.8 summarises the classification of events associated with XBP09, and the algorithm has correctly classified each event detected local to this bright point. However, a cancellation event was not detected, since multiple events occurred at once. This missed instance of cancellation was directly associated with the footpoints of the bright point, and its detection would have provided both relevant and useful information.

4.4.6 Case Study: XBP14

An observation window between 19:48 on March 14^{th} and 17:25 on March 15^{th} is established for XBP14 (figure 4.28). The tracking program first identifies it at 01:48, tracking it until 11:25, which agrees with the observation of the images produced by AIA, though some small-scale structure persists beyond this time. This bright point is formed by converging flux of opposite polarity and is destroyed through the cancellation, drift and fragmentation of its footpoints.

Event Classification

Four events are identified within the bright point's lifetime, along with four external events (figure 4.29). Study of these external events suggests that they do not play a role in the formation or destruction of the main structure of the bright point, so they will not be discussed completely here. They are included in table 4.9, which

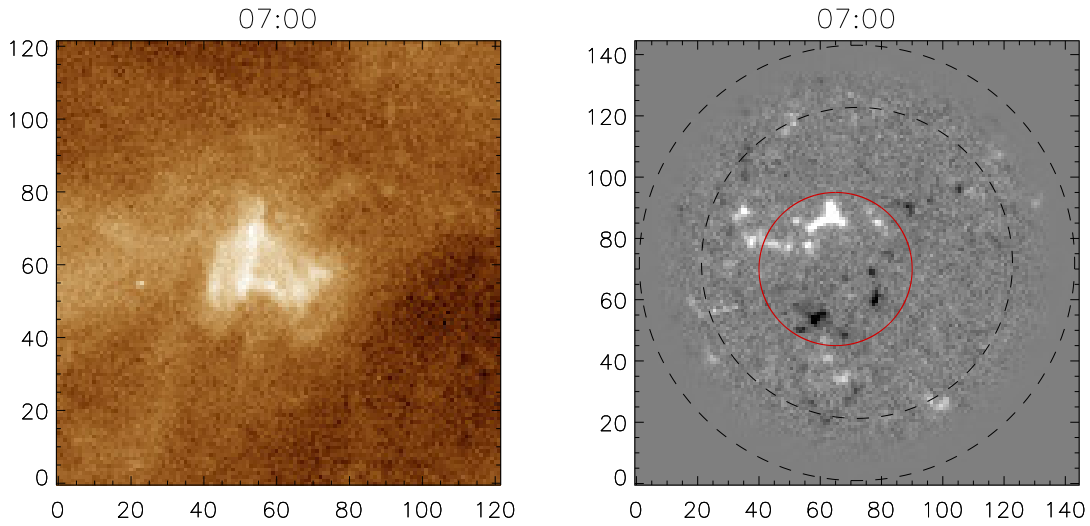

(a) (b)

Figure 4.28: Images of XBP14 taken with a) AIA and b) HMI on March 15^{th}, 2017. The footpoints of XBP14 are enclosed in the red circle in image (b).

provides a complete collection of all the identified events, occurring at 21:57, 12:40, and a double detection at 15:34. The first event detected, I_1, pertains to lots of small-scale cancellation events across the region, though this does not appear to directly interact with fragments which will become the footpoints of the XBP.

The first significant event identified which affects the bright point, I_2, is classed as an emergence event, peaking at 2:43. HMI images show that numerous small-scale explosive emergence events occur across the region at this time. One of the events gives rise to an island of negative flux which later becomes a footpoint for XBP14. As the positive footpoint is not produced by the same emergence event, the formation of the bright point is thus classified as a converging flux scenario.

Emerging flux is also associated with the second significant event to be identified, I_3, where small-scale explosive emergence events are widespread throughout the region (figure 4.30). The emergence occurs around 06:55 and the structure of

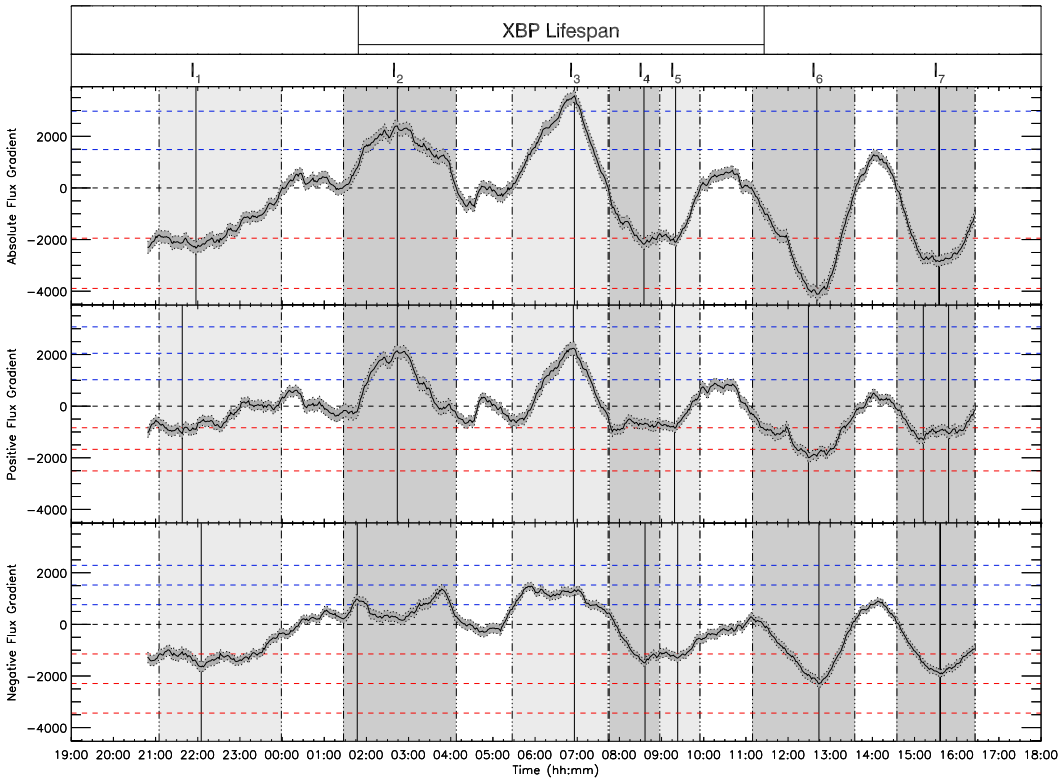

Figure 4.29: Gradients of the absolute, positive and negative flux measures for XBP14. Blue dashed lines represent deviations from zero of the increasing gradient, where red dashed lines are the deviations from zero of the decreasing gradient. Detected events are bound by vertical dot-dash lines, with the peaks of each event plotted as solid, vertical lines and labelled I_1 - I_7. XBP14 was automatically tracked across the time period shown by the bar at the top of the figure.

the bright point changes through the same period, becoming more intense as the emergence peaks.

The next pair of events, I_4 and I_5, are attributed to negative flux decreasing drift and cancellation, occurring between 07:30 and 10:00 (figure 4.31). First, the decreasing negative flux is identified as the result of the fragmentation of the negative footpoints of XBP14. However, the cancellation event is less clear. Inspection of the HMI images suggests that any cancellation during this time is on a small scale,

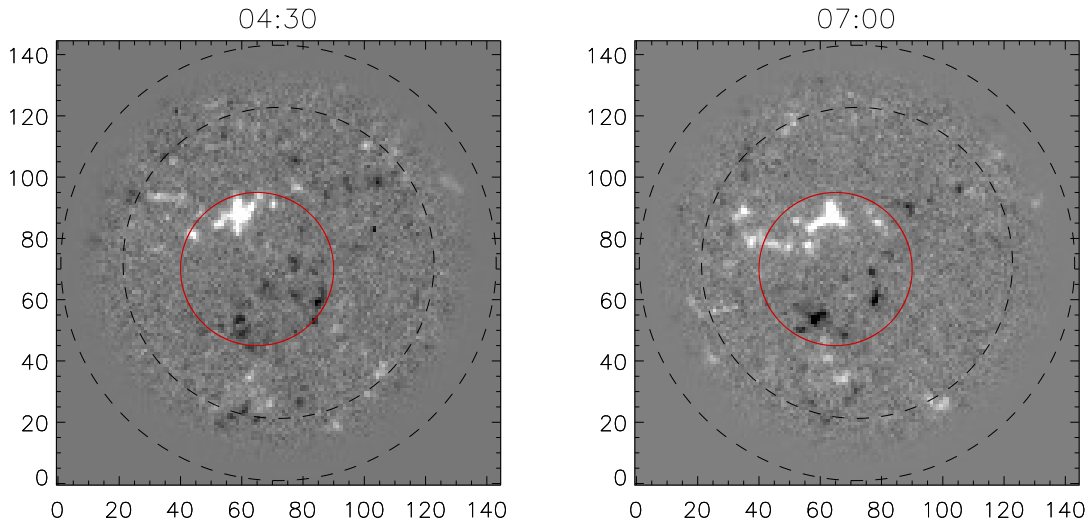

(a) (b)

Figure 4.30: Images showing the emergence of flux in the region local to XBP14 for event I_3. The red circle indicates the location of the emergence.

rather this event is the result of coincident fragmentation of the negative and positive footpoints, thus generating a false positive identification.

The final three events (I_6, I_{7a} and I_{7b}) occur after the bright point has faded but are associated with its footpoints. Here, a series of cancellation events are detected and observed, as negative fragments drift towards the positive islands and cancel out. The dim, remnant structure of the bright point is destroyed as the remaining elements cancel. However, one of these events (either I_7a or I_7b) is a double detection, where two peaks in the positive gradient have been assigned to a single peak in the absolute gradient, so one should be discounted as a false positive.

4.5 Sample Statistics

In this section, the results of all 15 XBPs will be considered from a more global point of view. This sample of XBPs has 76 events associated with it, of which 61

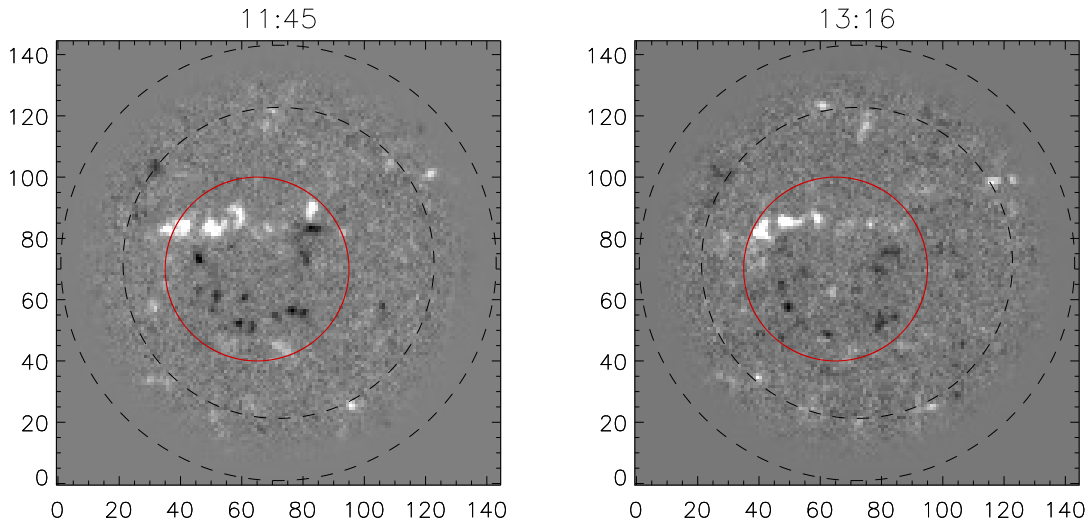

(a) (b)

Figure 4.31: Images showing the cancellation of flux identified as event I_6 in the region local to XBP14. The red circle highlights the region where the fragments are cancelling.

are visually confirmed as correct identifications. Each of these events is given in table 4.10. False positives are events where the algorithm classifies an event in a different manner to the visual identification, occurring 15 times. False negative results are chosen as events where the visual identification finds an event which the algorithm does not, of which 19 are counted. Events where a significant peak presents in either the positive or negative flux gradients, without a corresponding peak in the absolute gradient, also contribute to the false negative count, logged as false negative mixed events. However, of all mixed false negative events, the observer is unable to identify a significant event occurring. Thus, the exclusion of these events, by the algorithm, appears reasonable.

Mixed false negative events are responsible for 40% of the total number of false negative events. These events are logged as the result of a single peak in either

Event ID	Event Peak Time	Visual	Algorithm
I_1	21:57	Cancellation	Cancellation
I_2	02:43	Emergence	Emergence
I_3	06:55	Emergence	Emergence
I_4	08:34	Negative Fragmentation	Negative Decreasing
I_5	09:19	Mutual Fragmentation	Cancellation
I_6	12:40	Cancellation	Cancellation
I_{7a}	15:34	Cancellation	Cancellation
I_{7b}	15:34	Double Detection	Cancellation

Table 4.9: Table showing the times of detected events relating to XBP14, along with the visual classification of the events, and the classification assigned to the events by the algorithm. Two distinct detections have been assigned the IDs I_{7a} and I_{7b}, since they share the peak in the absolute and negative gradients. The ID of each event is also given, which corresponds to the peaks in figure 4.29.

the positive or negative gradient, without a corresponding peak in the absolute gradient. Typically, these events cannot be classified visually as a single event type, and sometimes it is not possible to associate any activity at all. Hence, the conclusion drawn here is that the requirement for a significant peak in the absolute gradient helps to remove unwanted detections.

4.5.1 Emergence and Cancellation

The main goal of this chapter was to automatically detect emergence and cancellation events related to an X-ray bright point. Here, the reliability of the algorithm in

Event Type	Correctly Identified	False Positive	False Negative
Emergence	18	4	5
Cancellation	13	3	4
Increasing Drift	12	3	5
Decreasing Drift	16	5	5
Mixed	2	0	0 (8)
Total	61	15	19 (27)

Table 4.10: Table containing the identifications, false positive and false negative counts for each event type. The false negative mixed events, included in brackets, are events where either the positive or negative flux gradient had a significant peak, without an associated peak in the absolute flux gradient, and where visual inspection is unable to identify an event as the cause for the peak.

respect to this task is considered. Table 4.11 provides a simplified metric for evaluating program performance, comparing visual detections with program detections.

In total, the program identifies 38 distinct events as either emergence or cancellation. By inspecting each of these events visually, 31 of the events are confirmed whilst 7 are found to be incorrect. Thus, this initial investigation suggests that the program is able to correctly interpret an event as either emergence or cancellation 81.5% of the time. Four of the events are false positive detections of emergence, and the other three are of cancellation. Of the false emergence events, three are due to the mutual coalescence of opposite polarity magnetic fragments, where the coalescence changes the profile of the flux such that more of it becomes aligned with the line-of-sight, whilst one is a double detection of a single event. A double detection occurs when a second peak in the gradients is located close to a set of peaks which have already been identified, where an observer may identify only a single event. The

cancellation events represent two double detections and a single instance of mutual fragmentation of sources. Whilst the double detections are correct results, they are undesirable as they may lead to a bright point appearing more active than it is. However, though an observer can recognise a double detection through investigation with relative ease, double detections of events would have a significant impact on the automation of the algorithm across a large number of XBPs.

Recording events through visual inspection finds 40 events related to emergence or cancellation, 9 of which are not detected by the program. This suggests that the program is collecting 77.5% of emergence and cancellation events. The false negative results consist of 5 missed emergence events, and 4 unrecorded instances of cancellation. Two of the emergence events and one of the cancellation events occur close to the boundaries of the observational time window, where the peak is beyond the detectable range. A further three events occur close to the edge of the photospheric region being studied, near or on the faded annular region. These three events are believed to have minimal impact on the XBP footpoints, so would be undesirable detections if recorded. The final three events, two of cancellation and one of emergence, are events which interact with the XBP footpoints. However, two of the events are associated with false positive detections of drifts, so only one event is truly missed. The missed event relates to the cancellation of a pair of small flux fragments, with the large footpoint of the XBP being studied.

It is also sensible to consider how many of the 31 correctly identified events relate directly to the XBP in the region being studied. Analysis finds that just 3 out of 18 emergence events are attributed to the emergence of flux which has little or no impact on the footpoints of the XBP. Of the 13 cancellation events, only 1 involves the cancellation of magnetic fragments which are not footpoints of the XBP. Thus, 87% of the correctly identified events are desirable. If 27 of the events detected are desired, while only 3 of the missed events are ones which need to be correctly

identified, the program is capable of collecting 27 of 30 (90%) desirable events.

In summary:

- of events identified as cancellation or emergence, 81.5% are correct
- 87% of correctly identified emergence and cancellation events relate directly to an XBP
- the program correctly identifies 77.5% of all emergence and cancellation events in the region local to an XBP
- the program correctly collects 90% of all cancellation and emergence events which relate directly to an XBP

		Program	
		D	N
Visual	D	31	9
	N	7	*n/a*

Table 4.11: Table counting emergence and cancellation events detected (D) both visually and by the program with those not detected (N) by either the program or the observer. When neither the program nor the observer detect an event, nothing is logged as it is difficult to characterise such times as discrete events.

4.6 Discussion

This study has drawn statistics from the automatic detection of 15 XBPs. Whilst classifying the drift, fragmentation and coalescence of flux elements remains problematic, instances of flux emergence and cancellation are handled well. It is found

that 80% of events identified as emergence or cancellation are also observed as such through inspection. Approximately 86% of the events that would be identified by an observer are also captured by the program.

A high proportion of events which occur beyond the lifetime of the XBP are incorrectly classified. However, in the absence of an XBP, these events may not be suitably contained by the annulus, with elements of the event located in the annulus itself, leading to the misidentification.

Harvey (1985) found that more than twice as many XBPs occur as the result of 'the encounter of existing network elements' than those resulting from emerging flux elements. Ten of the XBPs which formed the study in this thesis had an event which was clearly responsible for the onset and diffusion of the bright point (table 4.3). Here it is found that 40% of the bright points were born of emerging photospheric flux, but the other 60% were due to the drift of opposite polarity magnetic fragments. Whilst the ratio of the two onset event types found from this case study is closer to unity, these are small number statistics, hence some discretion is required.

Considering the events responsible for the demise of the bright points, 60% of XBPs were found to demise as the result of the cancellation of the magnetic fragments acting as their photospheric footpoints. 20% of bright points were destroyed through a significant restructuring due to the emergence of new flux fragments local to the XBP's footpoints. 10% of XBPs diffuse as the result of opposite polarity flux fragments drifting apart from one another. The final 10% were due to a combination of both cancelling and drifting footpoints (XBP09).

Golub et al. (1977) found that separation between the footpoints of an XBP increased over the course of its lifetime. However, this study finds only one bright point (accounting for 10%) which demises as the result of footpoint drifts. In 70% of cases, the footpoints are found to converge on one another, where cancellation between the fragments then occurs. The findings of this study are in closer agreement

with Harvey (1985), as the majority of bright points in this study demise as the result of cancelling magnetic features.

Whilst no distinction is made at this time between explosive and bipolar emergence events, it would be useful to identify properties which could be used as classifiers of the two types of event.

4.6.1 Future Development

Several avenues for the development of the algorithm are considered here. In the future, it would be useful to address these points to make the algorithm more robust.

There was an issue with double detections, where the algorithm found two events but only one was visually identifiable. To improve the algorithms ability to distinguish two peaks as a single event, it may be sensible to measure the depth of the trough between them. First, require that two peaks are associated distinct events and that the time windows associated with these events meet at the same trough. Consider the maximum value for the gradient at each peak, say P_1 and P_2, and assign the value of the gradient at the smallest value in the trough as t. The following criteria could then be applied as,

$$\frac{P_1 - t}{P_1} > \beta, \frac{P_2 - t}{P_2} > \beta,$$

where β is the a value given to the threshold. The value of β would then have to be fine-tuned to minimise the double peak detections, whilst also maximising the number of correctly identified distinct events.

The algorithm currently classifies instances of flux fragmentation and flux drifting out of the local region as a single class (decreasing drifts). Fragmentation of flux elements could be distinguished from flux elements drifting out of the region, by also calculating the flux present in a masked annulus region about the local region. As magnetic fragments enter (leave) the annulus, the flux measure would increase (decrease) accordingly. This increase (decrease) could then be related to a decrease

(increase) in the local region, to establish whether flux has entered (left) the annulus having moved from (to) the local region.

In an alternative approach, pixels corresponding to each fragment could be grouped together, and their position tracked to determine when they have left the annulus and drifted into the region. If the fragments could be grouped in such a manner, their flux contribution could either be neglected entirely or used to account for the increase/decrease in the flux of the local region. The algorithm could also check the number of fragment groups present in the local region. If the number of groups in the region increases, without any of the tracked fragments leaving this annulus, this could be used to indicate the fragmentation of flux sources. However, such an increase in the number of fragments may also present due to an explosive emergence event. Criteria would need to be defined for successful grouping. How many pixels must the fragment be spread over, to be considered as one worth tracking? Should a fragment only be included if it carries a large amount of magnetic flux, in order to rule out spurious, low-level elements?

The emergence of magnetic flux is detected as an increasing gradient in all three flux curves, which is the same behaviour exhibited by instances where magnetic fragments of both polarities are coalescing at the same time. The problem of identifying mutual coalescence of opposite polarity fragments could be addressed using the integrated flux values of the event peaks. Where the integrated values of the positive and negative flux are close to one another, this may indicate an emergence or cancellation event. Where the two values are significantly different to one another, it may be sensible to infer that the opposite polarity flux elements are simply coalescing or fragmenting at the same time. However, this could still become contaminated by complex periods where multiple events occur at once. There may also be instances where the amount of flux emerged of each polarity is significantly different. These events would now be missed, labelled as a mutual coalescence event, rather than

emergence.

Events which occur beyond the detected lifetime of an XBP, or within the masked annulus region, are often incorrectly classified by the algorithm. Another addition would be the removal of events which are unrelated to the XBP, based on the time at which they occur and where they occur in the local region. For example, the requirement that the event time-window must overlap the identified time window of the bright point's lifetime could be added. This would then remove any events where the tails of the event peak are not within the main observational period.

The spatial filtering of events presents a somewhat greater challenge. By improving the definition of the local region, it may be possible to remove more events which are unrelated to the XBP. There may be cases where it is more appropriate to define an elliptical annulus about an XBP, rather than a circular one. For example, where a circular annulus is applied to an elliptical bright point, the semi-minor axis of the bright point has additional space captured around it which would allow unrelated events to contaminate the identifications. Finding an elliptical annulus which best fits a given XBP would ensure that its footpoints are suitably centred in the observation window, whilst also capturing a region which is so compact that it only encloses the XBP.

Chapter 5

Conclusions and Future Work

5.1 Summary

This thesis has studied the topological structure and behaviour of the coronal magnetic field due to a variety of flux source configurations in the photosphere. Applications have principally been directed at quiet Sun magnetic fields.

Comparisons of topological structures in a discrete and continuous source regime, as explored in chapter 2, found that the topology produced by a configuration of discrete sources is qualitatively representative of that produced by continuously distributed sources. Similar topological structures and bifurcation behaviour was found to be present for source configurations modelled in both regimes. However, the discrete source model does not provide a good representation of configurations where continuously distributed sources overlap. Here, the discrete source model finds null points in locations where magnetic sources overlap in the continuous source case. This has implications in cases, such as active regions, where the flux is highly contiguous.

One of the case studies found a coronal dome which was bound within the separatrix dome of a planar null point. During the scenario, the spine of the coronal null point bifurcates with the fan of the separatrix dome through a spine-fan bifurcation.

This allows the spine of the coronal null point to extend into the coronal volume, with a magnetic separator located along its length. This scenario may be applicable as a characteristic model of a polar plume, where closed flux opens up to extend out into the coronal volume.

The study focussed on topologies where at least one coronal null point was present. Topological states analogous to those found previously by Brown & Priest (1999) and Beveridge et al. (2002) existed throughout many of the cases considered, but also with a coronal equivalent of the enclosed state. The case where three coronal null points were present (section 2.5) was similar to the open separatrix surface case discussed by Platten et al. (2014) and Priest (2014). However, it was found that additional separatrix surfaces were present, dividing the volume into additional domains of connectivity, removing the 'open' property of the central surface.

The overlapping region between two continuously distributed sources was studied further in chapter 3. The definition of a new topological feature, the null-like point, is proposed to prevent the exclusion of x-line structures from the topological simulations. If an x-line is present in a magnetic field topology, then it is important to ensure that it is represented appropriately, as these structures are important for the study of magnetic reconnection. This chapter demonstrates that for continuous source regimes to give a more complete picture of topological structures, null-like points must be located as they provide a mechanism for locating a sub-class of quasi-separatrix layers in a magnetic topology. It is also then possible to locate separator-like field lines, where the QSLs intersect other separatrix and separatrix-like surfaces. These field lines are important in the study of reconnection, as their trajectory is aligned with a heteroclinic connection between an NLP and either a null point or another NLP.

The open separatrix surface (Priest 2014), as discussed in section 3.8, is bound on each side by the spines of two other coronal null points. For comparison topologies

generated in this section, these spine field lines also form the boundaries for two QSLs originating from the null-like points. Whilst this does not separate the topology into any additional flux domains, it means that additional mechanisms, such as slip-running reconnection, would be required for a field line to cross from one side of the open separatrix surface to the other, without reconnecting across the surface itself. Thus, the open separatrix is not truly 'open', and the addition of the null-like points has provided a more complete picture of the magnetic topology due to the source configuration.

In the future, it would be useful to locate null-like points in more complex models and in fields extrapolated from photospheric magnetograms, along with extending to force-free and MHD simulations.

An algorithm for the automatic detection and classification of magnetic events local to X-ray bright points (XBPs) was explored in chapter 4. A sample of 15 XBPs was collected, for which the algorithm was able to correctly identify 90% of all observable emergence and cancellation events which had direct interactions with the footpoints of the associated XBP. Golub et al. (1977) found that separation between the footpoints of an XBP increases over the course of its lifetime. However, this study found that only one bright point (accounting for 10% of those observed) dispersed as the result of footpoint separation. The majority of cases studied here (accounting for 70%) ended as the result of the direct cancellation of the magnetic footpoints. This study's findings are in stronger agreement with Harvey (1985), as the majority of bright points in this study were observed to demise due to cancelling magnetic features.

The algorithm does need further development to reduce the number of erroneous event classifications. The ability to resolve single events from double peaks would be a strong addition. The algorithm could also be improved by being able to distinguish instances of mutual coalescence (fragmentation) from the emergence (cancellation)

of flux elements.

5.2 Future Work

5.2.1 Polar Plume Breakout Model

Chapter 2 of this thesis presented a topology where a coronal null point was initially closed off from the background coronal field. Investigation of perturbations to the source configuration used may find similar behaviour. It would also be useful to compare this source configuration to the photospheric field beneath a polar plume structure. This could be achieved by finding a period where a large coronal hole dips low enough to provide a reasonable view of the line-of-sight photospheric flux.

Trans-equatorial coronal holes would also provide an opportunity for a study of this nature to be completed. The STEREO satellites may be able to see the plume in these regions, and SDO would provide a top-down view of the plume, along with the photospheric flux beneath it.

In the future, Solar Orbiter will provide line-of-sight coverage of the Sun's poles which has not previously been available. This will provide a better top-down view of the polar plumes, along with line-of-sight magnetogram data of the footpoints of the plume, which would be invaluable for the study.

5.2.2 Null-like Points

In the future, it would be useful to locate null-like points in the topologies from force-free models and full MHD simulations. Initially, a small force-free perturbation from a potential field configuration could be used, which could be expanded to more extreme cases such as the magnetic field local to sunspots and active regions.

It would also be useful to locate null-like points in the extrapolated topologies of photospheric magnetograms. Work would initially focus on regions of the quiet

Sun, such as the region local to an X-ray bright point. This could then be extended by searching for null-like points in active region models, though this would require the magnetograms to be pre-processed, for example, by smoothing the data and removing flux values below the error level of the instrument.

5.2.3 X-ray Bright Points

The algorithm presented in Chapter 4 produces several incorrect identifications in the detection and classification. The principal problem which presents is the detection of double event peaks which are visually observed as a single event. It may be possible to reduce the impact of this effect, by grouping peaks with a shallow trough into a single event, as is done when the events are inspected visually. This would remove erroneous events and may also allow the events to be correctly identified. A method which could be applied to address this problem is outlined in section 4.6.1.

Fragmentation of flux elements also needs to be distinguished from flux elements drifting out of the region. This could be achieved by calculating the flux present in a masked annulus region to determine whether 'leaving flux' enters the annulus region or not. Alternatively, by applying a grouping algorithm, fragments which are located in the annulus could be tracked to determine when/if they drift into the local region, or drift out of the region entirely. Instances where opposite polarity sources are coincidentally fragmenting also needs to be identifiable. Again, application of a grouping algorithm may allow fragmentation and coalescence to be identified.

Removing events which are unrelated to the XBP, based on when and where they occur in the focal region would also be a useful addition. By requiring that the event time-window overlaps the identified time window of the bright point's lifetime, it would be possible to remove these unrelated events.

It may also be possible to remove unrelated events by improving the definition of the local region. There may be cases where it is more appropriate to define an

elliptical annulus about an XBP, rather than a circular one. Applying a circular annulus to an elliptical bright point adds additional space along the semi-minor axis of the bright point, allowing unrelated events to contaminate the identifications. Finding an elliptical annulus which best fits a given XBP would ensure that its footpoints are suitably centred in the observation window and capture a region which is so compact that it only encloses the XBP.

Chapter 4 has collected a sample of 15 XBPs. It is not possible to derive meaningful statistical properties relating to the formation and diffusion of an X-ray bright point from such a small sample. Once the above improvements have been addressed, the algorithm could then be applied to a larger sample of thousands of bright points (which the detection algorithm is capable of finding), so that a more complete statistical study could be completed. The study could also then be expanded to consider the energy released by an XBP over its lifetime, whether this energy release can be related to changes in the line of sight magnetogram data, but also study the effect that XBP footpoint motions have on the Poynting flux.

5.2.4 X-ray Bright Point: Topology Extrapolation

In the future, it would be useful to extrapolate topologies which include NLPs from magnetogram data local to XBPs and a method for this task is outlined here. First, the magnetogram has a 3-point box-car smooth applied to it, where the definition of the local region is then used to mask pixels in an annulus region as outlined in Chapter 4. Next, any pixel values which are within the instrument error are set to zero. Using the methods of Chapter 2, magnetic null points and NLPs can be located in the magnetogram and a potential field topology can be generated from these points. In total, 23 null points are found, along with 4 coronal null points and 41 null-like points. Figure 5.1a shows XBP09 in SDO/AIA 193 Å waveband data and figure 5.1b shows the region local to this bright point as captured by

SDO/HMI in a line-of-sight magnetogram. Figures 5.1c, 5.1d provide two of the separatrix-like structures generated from null-like points which are located on the large negative island of flux. Together, these two surfaces appear to form a bound on the extent of the bright point (by comparison to figure 5.1a), where the bright point then fills the space in the valley between them. This highlights the importance of searching for NLPs when considering topology, as two of the key features in this scenario arise from NLPs. While further investigation is needed, this proof of concept demonstrates that the basic approach outlined here, can be applied to data driven boundary conditions.

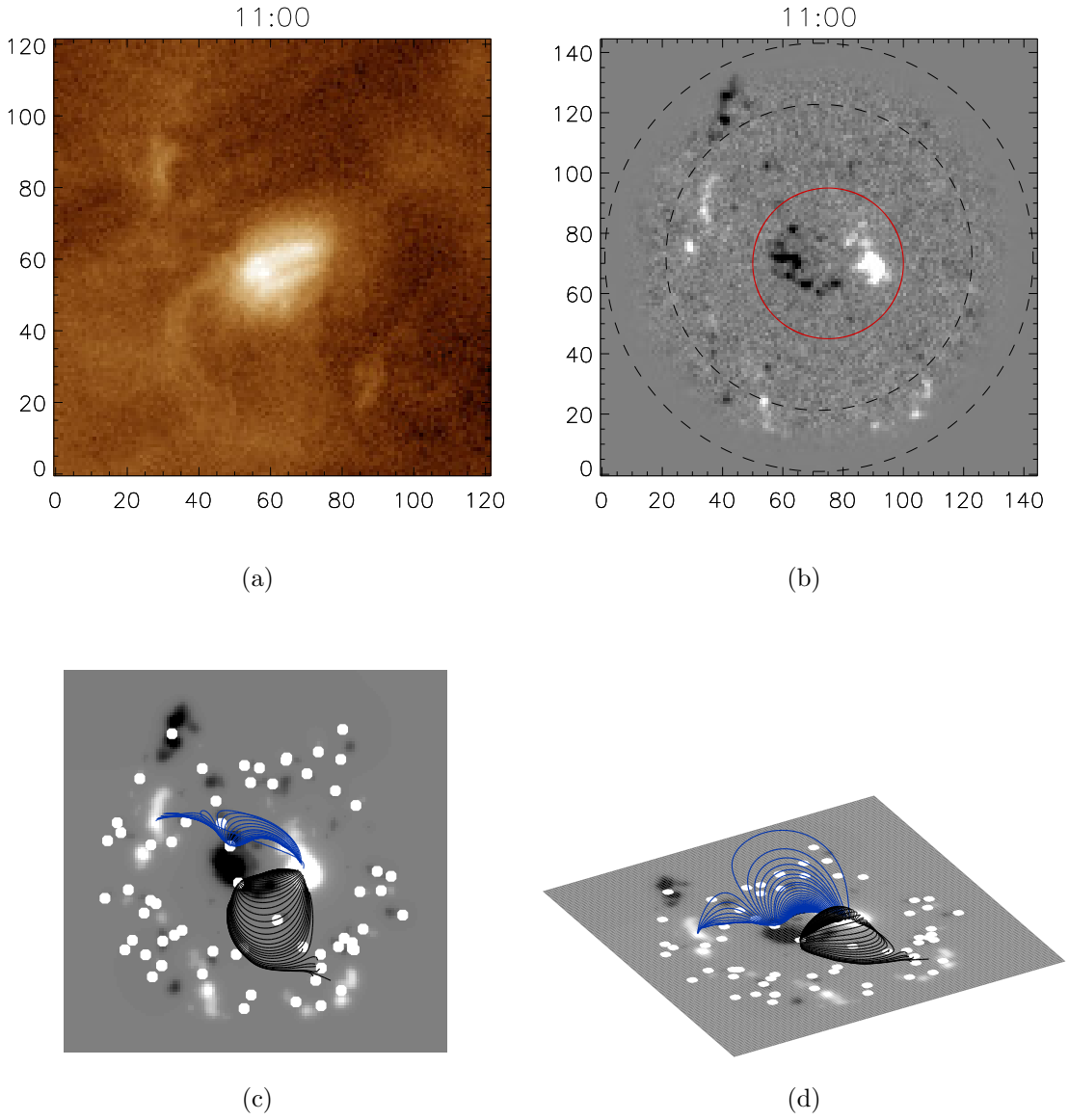

Figure 5.1: a) Figure showing XBP09 in a 193 Å waveband image from SDO/AIA. b) Line-of-sight magnetogram of the photospheric region local to XBP09 captured with SDO/HMI. c) A top-down view of the topology due to the nullpoints found in subfigure (b). Only two of the separatrix-like surfaces are shown to highlight the topological structures local to XBP09. Nullpoints and NLPs are represented by white circles. d) Figure showing the same topology as subfigure (c) but from a different viewing angle.

Bibliography

Antiochos, S. K. 1998, *Astrophys. J. Letters*, 502, L181

Aulanier, G., Pariat, E., & Démoulin, P. 2005, *Astron. Astrophys.*, 444, 961

Aulanier, G., Pariat, E., Démoulin, P., & DeVore, C. R. 2006, *Solar Physics*, 238, 347

Baum, P. J. & Bratenahl, A. 1980, *Solar Physics*, 67, 245

Beveridge, C., Priest, E. R., & Brown, D. S. 2002, *Solar Physics*, 209, 333

Bhatnagar, A. & Livingston, W. 2005, Fundamentals Of Solar Astronomy, Vol. 6

Brown, D. S., Parnell, C. E., Deluca, E. E., Golub, L., & McMullen, R. A. 2001b, Solar Physics, 201, 305

Brown, D. S., Parnell, C. E., Deluca, E. E., McMullen, R. A., & Golub, L. 1999, in Astronomical Society of the Pacific Conference Series, Vol. 184, Third Advances in Solar Physics Euroconference: Magnetic Fields and Oscillations, ed. B. Schmieder, A. Hofmann, & J. Staude, 81–85

Brown, D. S., Parnell, C. E., DeLuca, E. E., et al. 2002, Advances in Space Research, 29, 1093

Brown, D. S. & Priest, E. R. 1999, Proceedings of the Royal Society of London Series A, 455, 3931

Brown, D. S. & Priest, E. R. 2000, *Solar Physics*, 194, 197

Brown, D. S. & Priest, E. R. 2001a, Astronomy and Astrophysics, 367, 339

Close, R. M., Parnell, C. E., & Priest, E. R. 2004, Solar Physics, 225, 21

Cowley, S. W. H. 1973, Radio Science, 8, 903

Démoulin, P., Bagalá, L. G., Mandrini, C. H., Hénoux, J. C., & Rovira, M. G. 1997, *Astron. Astrophys.*, 325, 305

Demoulin, P., Henoux, J. C., & Mandrini, C. H. 1994, *Astron. Astrophys.*, 285, 1023

Démoulin, P., Hénoux, J. C., Priest, E. R., & Mandrini, C. H. 1996, Astronomy and Astrophysics, 308, 643

Dwivedi, B. N. & Parker, F. b. E. N. 2007, Dynamic Sun

Edwards, S. J. & Parnell, C. E. 2015, *Solar Physics*, 290, 2055

Foukal, P. V. 2004, Solar Astrophysics, 2nd, Revised Edition, 480

Freed, M. S., Longcope, D. W., & McKenzie, D. E. 2015, *Solar Physics*, 290, 467

Gary, G. A. 1989, *Astrophys. J. Supple.*, 69, 323

Glendinning, P. 1994, Stability, Instability and Chaos

Golub, L., Davis, J. M., & Krieger, A. S. 1979, *Astrophys. J. Letters*, 229, L145

Golub, L., Krieger, A. S., Harvey, J. W., & Vaiana, G. S. 1977, *Solar Physics*, 53, 111

Golub, L., Krieger, A. S., Silk, J. K., Timothy, A. F., & Vaiana, G. S. 1974, Astrophysical Journal, 189, L93

Golub, L., Krieger, A. S., & Vaiana, G. S. 1976a, *Solar Physics*, 49, 79

Golub, L., Krieger, A. S., & Vaiana, G. S. 1976b, *Solar Physics*, 50, 311

Golub, L. & Pasachoff, J. M. 2009, The Solar Corona

Green, S. F. & Jones, M. H. 2015, An Introduction to the Sun and Stars

Guckenheimer, J. & Holmes, P. 1986, Nonlinear Oscillations, Dynamical Systems and Bifurcations of Vector Fields

Habbal, S. R., Ronan, R. S., Withbroe, G. L., Shevgaonkar, R. K., & Kundu, M. R. 1986, *Astrophys. J.*, 306, 740

Hagenaar, H., Schrijver, C., & De Rosa, M. 2008, in Astronomical Society of the Pacific Conference Series, Vol. 383, Subsurface and Atmospheric Influences on Solar Activity, ed. R. Howe, R. W. Komm, K. S. Balasubramaniam, & G. J. D. Petrie, 343

Hale, G. E. & Nicholson, S. B. 1925, *Astrophys. J.*, 62, 270

Harra, L. K. & Mason, K. O. 2004, Space Science (Imperial College Press)

Harrison, R. A. 1996, *Solar Physics*, 166, 441

Hart, A. B. 1954, *Mon. Not. Roy. Astron. Soc.*, 114, 17

Harvey, K. L. 1985, Australian Journal of Physics, 38, 875

Harvey, K. L. & Martin, S. F. 1973, *Solar Physics*, 32, 389

Hudson, T. S. & Wheatland, M. S. 1999, *Solar Physics*, 186, 301

Inverarity, G. W. & Priest, E. R. 1999, *Solar Physics*, 186, 99

Kankelborg, C. C., Walker, II, A. B. C., Hoover, R. B., & Barbee, Jr., T. W. 1996, *Astrophys. J.*, 466, 529

Kumar, P., Karpen, J. T., Antiochos, S. K., et al. 2018, *Astrophys. J.*, 854, 155

Lang, K. R. 2001, The Cambridge Encyclopedia of the Sun, 268

Lau, Y.-T. & Finn, J. M. 1990, *Astrophys. J.*, 350, 672

Lemen, J. R., Title, A. M., Akin, D. J., et al. 2012, *Solar Physics*, 275, 17

Longcope, D. W. 1996, Solar Physics, 169, 91

Longcope, D. W. 1998, *Astrophys. J.*, 507, 433

Longcope, D. W. & Beveridge, C. 2007, The Astrophysical Journal, 669, 621

Longcope, D. W. & Cowley, S. C. 1996a, Physics of Plasmas, 3, 2885

Maclean, R. C., Beveridge, C., Longcope, D. W., Brown, D. S., & Priest, E. R. 2005, Proceedings of the Royal Society of London Series A, 461, 2099

Maclean, R. C., Beveridge, C., & Priest, E. R. 2006a, *Solar Physics*, 238, 13

Maclean, R. C., Hornig, G., Priest, E. R., & Beveridge, C. 2006b, *Solar Physics*, 235, 259

Mandrini, C. H., Démoulin, P., Rovira, M. G., de La Beaujardière, J.-F., & Hénoux, J. C. 1995, *Astron. Astrophys.*, 303, 927

Masson, S., Pariat, E., Aulanier, G., & Schrijver, C. J. 2009, *Astrophys. J.*, 700, 559

McIntosh, S. W. & Gurman, J. B. 2005, *Solar Physics*, 228, 285

Moreno-Insertis, F. 2012, in Astronomical Society of the Pacific Conference Series, Vol. 455, 4th Hinode Science Meeting: Unsolved Problems and Recent Insights, ed. L. Bellot Rubio, F. Reale, & M. Carlsson, 91

Moreno-Insertis, F., Galsgaard, K., & Ugarte-Urra, I. 2008, *Astrophys. J. Letters*, 673, L211

Morton, K. W. & Mayers, D. F. 2005, Numerical Solution of Partial Differential Equations

Neukirch, T., Dreher, J., & Birk, G. T. 1997, Advances in Space Research, 19, 1861

Pariat, E., Antiochos, S. K., & DeVore, C. R. 2009, *Astrophys. J.*, 691, 61

Parnell, C. E., Priest, E. R., & Golub, L. 1994, *Solar Physics*, 151, 57

Pesnell, W. D., Thompson, B. J., & Chamberlin, P. C. 2012, *Solar Physics*, 275, 3

Platten, S. J., Parnell, C. E., Haynes, A. L., Priest, E. R., & Mackay, D. H. 2014, *Astron. Astrophys.*, 565, A44

Priest, E. R. 2014, Magnetohydrodynamics of the Sun

Priest, E. R. & Démoulin, P. 1995, Journal of Geophysical Research, 100, 23443

Priest, E. R. & Forbes, T. G. 1992, *J. Geophys. Res.*, 97, 1521

Priest, E. R. & Forbes, T. G. 2000, Magnetic Reconnection, 612

Priest, E. R., Parnell, C. E., & Martin, S. F. 1994, *Astrophys. J.*, 427, 459

Priest, E. R. & Titov, V. S. 1996, Philosophical Transactions of the Royal Society of London Series A, 354, 2951

Scherrer, P. H., Bogart, R. S., Bush, R. I., et al. 1995, *Solar Physics*, 162, 129

Schindler, K., Hesse, M., & Birn, J. 1988, *J. Geophys. Res.*, 93, 5547

Schou, J., Scherrer, P. H., Bush, R. I., et al. 2012, *Solar Physics*, 275, 229

Schrijver, C. J. & Title, A. M. 2002, *Solar Physics*, 207, 223

Schwabe, M. 1843, Astronomische Nachrichten, 20, 283

Seehafer, N. 1986, *Solar Physics*, 105, 223

Stix, M. 2004, The Sun : An Introduction

Title, A. M., Tarbell, T. D., Topka, K. P., et al. 1989, *Astrophys. J.*, 336, 475

Titov, V. S. 2007, *Astrophys. J.*, 660, 863

Titov, V. S. & Démoulin, P. 1999a, *Astron. Astrophys.*, 351, 707

Titov, V. S. & Démoulin, P. 1999b, in Astronomical Society of the Pacific Conference Series, Vol. 184, Third Advances in Solar Physics Euroconference: Magnetic Fields and Oscillations, ed. B. Schmieder, A. Hofmann, & J. Staude, 76–80

Titov, V. S., Démoulin, P., & Hornig, G. 1999, in ESA Special Publication, Vol. 448, Magnetic Fields and Solar Processes, ed. A. Wilson & et al., 715

Titov, V. S., Forbes, T. G., Priest, E. R., Mikić, Z., & Linker, J. A. 2009, *Astrophys. J.*, 693, 1029

Titov, V. S. & Hornig, G. 2002, Advances in Space Research, 29, 1087

Titov, V. S., Hornig, G., & Démoulin, P. 2002, Journal of Geophysical Research (Space Physics), 107, 1164

Tousey, R. 1973, in Space Research Conference, Vol. 2, Space Research Conference, ed. M. J. Rycroft & S. K. Runcorn, 713–730

Vaiana, G. S., Krieger, A. S., Speybroeck, L. P., & Zehnpfennig, T. 1970, Bul. Am. Phys. Soc., 15, 611

Woods, T. N., Eparvier, F. G., Hock, R., et al. 2012, *Solar Physics*, 275, 115

Yeh, T. 1976, *J. Geophys. Res.*, 81, 2140